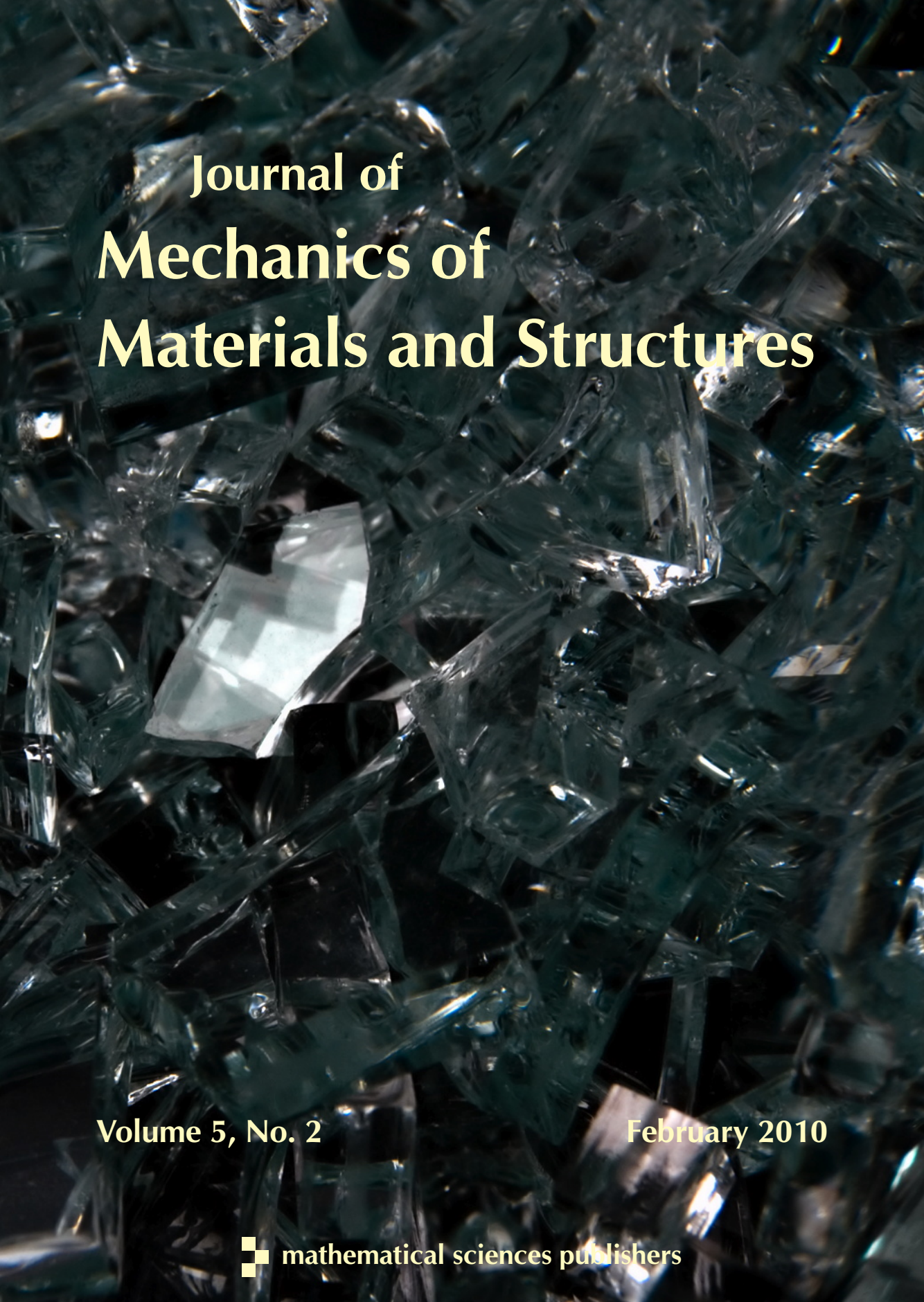

Journal of Mechanics of Materials and Structures

Volume 5, No. 2 February 2010

mathematical sciences publishers

JOURNAL OF MECHANICS OF MATERIALS AND STRUCTURES

http://www.jomms.org

Founded by Charles R. Steele and Marie-Louise Steele

Cover design: Alex Scorpan

Cover photo: Mando Gomez, www.mandolux.com

See inside back cover or http://www.jomms.org for submission guidelines.

JoMMS (ISSN 1559-3959) is published in 10 issues a year. The subscription price for 2010 is US $500/year for the electronic version, and $660/year (+$60 shipping outside the US) for print and electronic. Subscriptions, requests for back issues, and changes of address should be sent to Mathematical Sciences Publishers, Department of Mathematics, University of California, Berkeley, CA 94720–3840.

JoMMS peer-review and production is managed by EditFLOW™ from Mathematical Sciences Publishers.

PUBLISHED BY

mathematical sciences publishers

http://www.mathscipub.org

A NON-PROFIT CORPORATION

Typeset in LaTeX

JOURNAL OF MECHANICS OF MATERIALS AND STRUCTURES
Vol. 5, No. 2, 2010

A CRITICAL ANALYSIS OF INTERFACE CONSTITUTIVE MODELS FOR THE SIMULATION OF DELAMINATION IN COMPOSITES AND FAILURE OF ADHESIVE BONDS

ANTON MATZENMILLER, SEBASTIAN GERLACH AND MARK FIOLKA

Delamination in layered composites and debonding in adhesive joints are modeled and analyzed using interfacial mechanics, consisting of interface elements for the kinematical assumption and traction-separation equations for the constitutive model. Material equations are presented for the inelastic behavior of pure and ductile-modified epoxy resins, used for the matrix phase of the composite and in a chemically modified form for the adhesive in bonded structures.

Two different modeling approaches are proposed. The first is a brittle fracture model with a stress-based failure criterion and rate-dependent strength parameters together with a mixed-mode energy criterion for the interaction of the three different modes of failure. The second makes use of an elastic-plastic approach with a traction-separation equation for ductile materials and rate-dependent yield stresses.

Standard tests for the delamination of layered composites under various modes of failure are simulated by making use of the interface element for bonding/debonding. The model for the inelastic behavior of a thin layer of the structural adhesive is validated up to fracture for various modes of failure due to pure and combined loading in the normal and shear directions. Therefore, the relevant part of the experimental setup for the testing is meshed with finite elements and the results of the simulation are compared to the corresponding test data.

1. Introduction

Delamination in layered composites and debonding in adhesive joints are caused by crack initiation and growth, since epoxy resin is often used as the matrix material of the reinforced composite and in a chemically modified form as the adhesive for the bonding of structural components. With regard to the mathematical description of both failure mechanisms, that is, the separation of the laminae and the breaking of the adhesive layer in the joints, interfacial mechanics may be employed with interface elements for the kinematics and traction-separation equations of the constitutive formulation. Therefore, constitutive equations for the inelastic behavior of pure and ductile-modified epoxy resins are needed in

Keywords: adhesive models, structural bonding, delamination, crash analysis, interface element, traction-separation model, adhesively bonded joints, simulation of failure, plasticity, mixed-mode fracture.

Parts of the experimental results presented stem from the research project [Schlimmer et al. 2008], coordinated and financed by the Forschungsvereinigung Stahlanwendung e.V., Düsseldorf, with resources from the Stiftung Stahlanwendungsforschung, Essen. The participants of this project are the Institut für Werkstofftechnik, Universität Kassel, the Institut für Mechanik, Universität Kassel, the Laboratorium für Werkstoff- und Fügetechnik, Universität Paderborn, the Lehrstuhl für Technische Mechanik, Universität Paderborn, the Institut für Füge- und Schweißtechnik, Universität Braunschweig, the Fraunhofer Institut für Fertigungstechnik, Bremen, the Fraunhofer Institut für Werkstoffmechanik, Freiburg, and the Fraunhofer Institut für Kurzzeitdynamik, Freiburg.

addition to the interface elements for the effective modeling of the cohesive zone in the crashworthiness analysis of layered composites as well as adhesively bonded structures.

In order to prevent sudden brittle fracture at low strain magnitudes, typical adhesives, made of epoxy resin, are toughened by admixing tiny particles of elastomeric substances in order to make the duromeric matrix more ductile. These structural adhesives become strain rate dependent and withstand large deformations. They are used in the bonded joints of car bodies. Tests on bulk specimens of toughened adhesives show permanent deformations after unloading, if the material is strained beyond a critical limit.

The theory of interfacial mechanics is well suited for the modeling and analysis of delamination in layered composite structures and failure of adhesive joints in assembled components. The characteristic feature of interfacial mechanics is the use of only those three stress components, which act on the interface and, thus, on the plane of failure. The constitutive equations are formulated in terms of the displacement discontinuities across the interface.

The failure analysis of adhesive joints in assembled structures requires a fine discretization of the adhesive layer in the thickness direction in order to describe the state of stress precisely. However, for the crashworthiness analysis of complete vehicle bodies, tiny finite elements are undesirable, since they require a small critical time step for the simulation of the entire structure with explicit integration schemes for the equations of motion. Crash simulation with solid elements for thin adhesive layers in complete car body models is numerically still too elaborate, if no additional measures, like mass-scaling, are taken to increase the critical step length of time. Thus, interface elements with very small or zero thickness are superior for the modeling of thin adhesive layers. Then, the critical time step is no longer controlled by the Friedrichs–Levy criterion of the solid elements for the adhesive layer but rather by the neighbouring shell or solid elements, applied for the adjacent steel structures.

Two different modeling approaches for the delamination of layered materials and joints with thin adhesive layers are taken from the literature. The first is a fracture model, founded on the work of Barenblatt [1959] and Dugdale [1960], with a stress-based failure criterion and rate-dependent strength parameters together with a mixed-mode energy criterion for the interaction of the three different modes of failure. The second makes use of an elastic-plastic description with a traction-separation equation for ductile materials as proposed by Su et al. [2004].

Due to the similarity between thin layers in structural components and laminated fiber composites, analysis using interface models can be used in both cases. The finite element calculation of fracture or delamination of specimens in different modes of failure under quasistatic and crash loading is demonstrated with various numerical examples.

2. Cohesive zone models

The experimental investigations performed in [Schlimmer et al. 2008] at joints, bonded with crash-resistant adhesives, show that the fracture of the bonding is dominated by cohesive failure, that is, the crack initiation and growth takes place within the cohesive zone (see Section 5). Modelling with one element through the thickness of the adhesive layer is numerically sufficient for the purposes of crashworthiness analysis of complex structural assemblages, because only the effective mechanical behavior of the bonding is important for the vehicle simulation, not the complete three-dimensional fine stress resolution

in the adhesive layer. Modelling with interface elements is justified, since the compliant adhesive bond between the stiff sheet metal is nearly inextensible and shear rigid in the plane tangential to the adhesive layer. Thus, interfacial mechanics are an efficient approach to modeling adhesive layers as they are widely accepted for the delamination analysis of layered composite structures.

2A. ***Interface element.*** Interface elements were originally developed for the description of the delamination process in composite materials [Beer 1985; Mi et al. 1998; Schellekens and de Borst 1993]. Contrary to the usual finite element concept, the primary kinematical variable of the interface element is the displacement jump vector $\boldsymbol{\Delta}$ instead of the strain tensor, as is typical for volumetric continuum elements. The element has three degrees of freedom at each node and consists of a total of eight nodes with four nodes on the upper and lower sides of the interface. The displacement field in the length and transverse directions of the interface is assumed to be bilinear. Full integration with four Gauss points is performed. The element has no stiffness in the membrane direction. Pronounced locking effects could not be observed so far.

2B. ***Mixed-mode extension of the Hillerborg fracture model.*** The constitutive behavior for fracture of the adhesive is formulated between the interface stresses t_i and the displacement jumps Δ_i, which represent the differences of the displacement components in the normal and tangential directions of the two neighbouring surfaces of the adherents. For the description of the softening behavior in interfaces various models have been presented in the literature; for example, Barenblatt [1959] developed a damage model for brittle interfaces. The traction-separation equations are formulated for the three failure modes of fracture mechanics by means of the dissipated energy during the opening of the interface:

$$\mathcal{G}_{\mathrm{Ic}} = \int t_3 \, d\Delta_3, \qquad \mathcal{G}_{\mathrm{IIc}} = \int t_1 \, d\Delta_1, \qquad \mathcal{G}_{\mathrm{IIIc}} = \int t_2 \, d\Delta_2, \tag{2-1}$$

where $\mathcal{G}_{\mathrm{Ic}}$, $\mathcal{G}_{\mathrm{IIc}}$, and $\mathcal{G}_{\mathrm{IIIc}}$ are the critical energy release rates of the three well-known modes of fracture. The interface traction as a function of the crack opening in the process zone is unknown and must be supposed unless better experimental information is available, as given by [Andersson and Stigh 2004]. Different assumptions for the distribution of the traction-separation equation are discussed in the literature. An example is the bilinear model of Hillerborg et al. [1976] for brittle interfaces, which combines linear elasticity with brittle fracture (see Figure 1).

The adhesive joint behaves linearly elastically up to the stress maximum:

$$\boldsymbol{t} = \boldsymbol{K}\boldsymbol{\Delta}, \quad \text{with} \quad \boldsymbol{K} = \begin{bmatrix} K_n & 0 & 0 \\ 0 & K_t & 0 \\ 0 & 0 & K_t \end{bmatrix}. \tag{2-2}$$

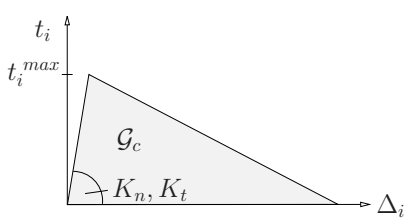

Figure 1. Bilinear course of interface traction versus displacement discontinuity.

The same relation holds with reduced stiffness values for unloading and reloading, if the interface has started softening. The failure initiation of the interface is determined here by a mixed-mode stress criterion [Brewer and Lagace 1988]:

$$\sqrt{\left(\frac{t_1}{t_1^{\max}}\right)^2+\left(\frac{t_2}{t_2^{\max}}\right)^2+\left(\frac{\langle t_3\rangle}{t_3^{\max}}\right)^2}=1. \tag{2-3}$$

The interaction of the three different modes of fracture is accounted for by a mixed-mode energy criterion [Whitcomb 1986]:

$$\left(\frac{\mathcal{G}_I}{\mathcal{G}_{\mathrm{Ic}}}\right)^n+\left(\frac{\mathcal{G}_{\mathrm{II}}}{\mathcal{G}_{\mathrm{IIc}}}\right)^n+\left(\frac{\mathcal{G}_{\mathrm{III}}}{\mathcal{G}_{\mathrm{IIIc}}}\right)^n=1. \tag{2-4}$$

The implementation of the model into a commercial finite element code and the application of the mixed-mode formulation with a bilinear stress-strain diagram were presented first by Dávila and Camanho [2001] (see also [Pinho et al. 2006]). In the present paper, the model is extended to rate-dependency and implemented into the commercial FE code LS-DYNA [DYNA 2006], since structural adhesives show rate-dependent material behavior even under the moderate strain rates encountered in the crashworthiness analysis of bonded structural components — see the test data in Section 5A.

In order to take rate-dependent material behavior into account, the mixed-mode fracture model is extended here according to the proposal by Johnson and Cook [1983] for a rate-dependent yield limit. Its application to the brittle fracture model is based on the scaling of the failure stress components $(t_i^{\max})_0$ of the rate-independent limit case with the logarithm of the rate of the effective displacement discontinuity $\dot{\Delta}_v$, defined as

$$t_1^{\max}=(t_1^{\max})_0\left(1+C\left\langle\ln\frac{\dot{\Delta}_v}{\dot{\Delta}_0}\right\rangle\right),\qquad t_3^{\max}=(t_3^{\max})_0\left(1+C\left\langle\ln\frac{\dot{\Delta}_v}{\dot{\Delta}_0}\right\rangle\right), \tag{2-5}$$

with the material parameter C, and in the Macaulay brackets $\langle\cdot\rangle$ the reference value of the jump velocity $\dot{\Delta}_0$, which must be identified from the experimental results:

$$\dot{\Delta}_v=\sqrt{\dot{\Delta}_1^2+\dot{\Delta}_2^2+\dot{\Delta}_3^2}. \tag{2-6}$$

It is assumed that the rates of the effective displacement discontinuity $\dot{\Delta}_v$ below the reference value $\dot{\Delta}_0$ do not contribute to the rate-dependency of the strength parameters for the adhesive.

2C. ***Tvergaard–Hutchinson fracture model.*** Tvergaard and Hutchinson proposed one of the first interface failure models for the analysis of fractures in the cohesive zone. The model is widely accepted and used for cohesive zone analysis, since it is available in commercial finite element codes (for example, LS-DYNA [DYNA 2006]). The model of Tvergaard and Hutchinson [1994], based on the ductile fracture concept of Dugdale [1960], possesses a trilinear distribution of the interface traction with regards to the effective crack opening displacement, which is taken as a measure for the damage Λ (see Figure 2), defined as

$$\Lambda=\sqrt{\left(\frac{\Delta_1}{\Delta_1^{\max}}\right)^2+\left(\frac{\langle\Delta_3\rangle}{\Delta_3^{\max}}\right)^2},$$

where $\Delta_1^{\max}$ and $\Delta_3^{\max}$ are the critical crack opening displacements in the tangential and normal directions. However, no permanent displacement jumps in the sense of plasticity are taken into account. Interaction

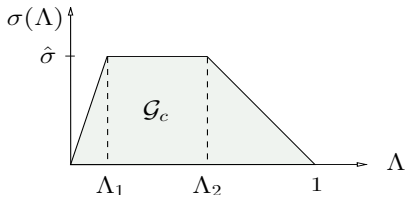

Figure 2. Trilinear course of interface stress σ versus damage Λ.

of fracture modes I and II is inherent in the formulation, which may be extended to mode III in an analogous manner.

The components t_i of the stress vector on the interface are derived from a free energy density function [Tvergaard and Hutchinson 1996, equation (1.2)] where the parameter for the damage Λ is defined by means of the components Δ_1 and Δ_3 of the displacement discontinuity vector. The interface stresses are given by the derivatives of the free energy density function with respect to the associated components Δ_i of the crack opening:

$$t_3 = \frac{\sigma(\Lambda)}{\Lambda}\frac{\Delta_3}{\Delta_3^{\max}}, \qquad t_1 = \frac{\sigma(\Lambda)}{\Lambda}\frac{\Delta_3^{\max}}{\Delta_1^{\max}}\frac{\Delta_1}{\Delta_1^{\max}}. \tag{2-7}$$

Hence, the critical energy release rate $\mathcal{G}_c$ becomes:

$$\mathcal{G}_c = \tfrac{1}{2}\hat{\sigma}\,\Delta_3^{\max}(1 - \Lambda_1 + \Lambda_2). \tag{2-8}$$

2D. ***Elastic-plastic interface model.*** Su et al. [2004] developed an elastic-plastic interface model with softening, which accounts for elastic and irreversible inelastic displacement jumps prior to failure. In this paper the model is improved with respect to hardening and softening and is extended to rate-dependency. It is applied to the analysis of joints, bonded with toughened ductile adhesives under combined loading of shear and tension. Unlike in [Su et al. 2004], the model is validated here for the case of combined tension and shear loading. No information about the model's performance for combined loading is given in [Su et al. 2004]. The constitutive behavior is formulated between the three components of the interface stress vector t_i and the components of the displacement jump vector across the adherent layer Δ_i. Based on the additive decomposition of the displacement jump vector into elastic and plastic parts, $\boldsymbol{\Delta} = \boldsymbol{\Delta}^e + \boldsymbol{\Delta}^p$, the elasticity assumption for the calculation of the interface stress vector leads to

$$\boldsymbol{t} = \boldsymbol{K}\boldsymbol{\Delta}^e = \boldsymbol{K}(\boldsymbol{\Delta} - \boldsymbol{\Delta}^p), \tag{2-9}$$

with the two-dimensional elastic stiffness tensor $\boldsymbol{K}$ of the interface as given in (2-2). The interface stress vector $\boldsymbol{t}$ may be decomposed into normal and tangential parts, $\boldsymbol{t}_n = (\boldsymbol{t}\cdot\boldsymbol{n})\boldsymbol{n}$ and $\boldsymbol{t}_t = \boldsymbol{t} - \boldsymbol{t}_n$. The effective shear stress $\tau = \sqrt{\boldsymbol{t}_t \cdot \boldsymbol{t}_t}$ in the interface is the resultant stress of the two tangential traction components. The elastic domain is bounded by two yield curves with functions $f^{(1)}$ and $f^{(2)}$ for a two surface plasticity interface model. The yield conditions in the normal (1) and shear (2) modes are

$$f^{(1)} = t_n - Y^{(1)} \le 0, \tag{2-10}$$

$$f^{(2)} = \tau + \mu t_n - Y^{(2)} \le 0, \tag{2-11}$$

with the yield stress in the normal, $Y^{(1)}$, and tangential, $Y^{(2)}$, directions. The variable μ in (2-11) can be interpreted as the friction parameter of the Coulomb model, describing the interaction between stresses in the normal and tangential directions at yielding.

The rate of the plastic displacement jump is defined by the flow rule:

$$\dot{\boldsymbol{\Delta}}^P = \sum_{i=1}^{2} \lambda^{(i)} \boldsymbol{m}^{(i)} \tag{2-12}$$

with an associated flow vector in tension $\boldsymbol{m}^{(1)} = \boldsymbol{n}^{(1)}$ and a nonassociated flow vector in shear

$$\boldsymbol{m}^{(2)} = \frac{\boldsymbol{t}_t}{\tau} \neq \boldsymbol{n}^{(2)},$$

where $\boldsymbol{n}^{(i)}$ is the normal to the yield surface $f^{(i)}$. The variable $\lambda^{(i)}$ is the plastic multiplier in the flow rule for mode (i). It has nothing to do with the Λ of Section 2C in the Tvergaard–Hutchinson model.

Hardening or softening due to either mode of yielding is introduced into the model by means of evolution equations for the change of the current yield stresses $Y^{(i)}$ in [Su et al. 2004]. Here, the yield stresses are given as

$$Y^{(i)} = \hat{Y}^{(i)}(\bar{\gamma}) \tag{2-13}$$

in each mode of plastic flow as a function of the equivalent plastic displacement jump $\bar{\gamma}$, introduced as the weighted sum of the time integrated plastic multipliers $\gamma^{(i)}$:

$$\bar{\gamma} := \sqrt{(\gamma^{(1)})^2 + \beta(\gamma^{(2)})^2}, \tag{2-14}$$

with β as an appropriately identified mode interaction parameter, and where

$$\gamma^{(i)} := \int_0^t \lambda^{(i)}(\tau)\, d\tau. \tag{2-15}$$

For the analysis of the peel and KS-II (see Section 5D) tests, the experimental data in Figure 9 are approximated by piecewise linear yield curves for tension ($\alpha = 0$) and slow, uniform loading in pure torsion ($\alpha = \infty$):

$$Y^{(1)} = \hat{Y}^{(1)}(\Delta_n^P) = Y_0^{(1)} + H^{(1)}(\bar{\gamma})\Delta_n^P, \qquad Y^{(2)} = \hat{Y}^{(2)}(\Delta_t^P) = Y_0^{(2)} + H^{(2)}(\bar{\gamma})\sqrt{\beta}\,\Delta_t^P. \tag{2-16}$$

The kinematical variables $\Delta_n^P = \Delta_3^P$ and $\Delta_t^P = \sqrt{(\Delta_1^P)^2 + (\Delta_2^P)^2}$ are respectively the normal and resultant shear components of the plastic displacement jump vector $\boldsymbol{\Delta}^P$. The material quantities $H^{(1)}$ and $H^{(2)}$ are the hardening parameters $H^{(1)}_{\text{hard}}$ and $H^{(2)}_{\text{hard}}$ identified as the inclinations of the yield curves in the hardening range. Likewise, $H^{(1)}_{\text{soft}}$ and $H^{(2)}_{\text{soft}}$ denote the slopes of the straight lines through the data in the successive softening range. Three different cases can be distinguished for the hardening quantities $H^{(i)}(\bar{\gamma})$, depending on the state of the effective plastic displacement jump $\bar{\gamma}$:

$$H^{(i)}(\hat{\gamma}) = \begin{cases} H^{(i)}_{\text{hard}} & \text{if } \bar{\gamma} < \bar{\gamma}_{\text{crit}}, \\ H^{(i)}_{\text{soft}} & \text{if } \bar{\gamma}_{\text{crit}} \leq \bar{\gamma} < \bar{\gamma}_{\text{fail}} \text{ and } f^{(i)} > 0, \\ 0 & \text{if } \bar{\gamma} \geq \bar{\gamma}_{\text{fail}}. \end{cases} \tag{2-17}$$

In the first case, the equivalent plastic displacement jump $\bar{\gamma}$ is smaller than the given critical displacement jump $\bar{\gamma}_{\text{crit}}$ and the adhesive layer is still in the state of hardening. If the variable $\bar{\gamma}$ is greater than the critical displacement jump, then softening of the adhesive takes place. The interface fails when the variable $\bar{\gamma}$ is equal to the displacement jump at failure $\bar{\gamma}_{\text{fail}}$, which follows from the softening moduli $H^{(1)}_{\text{soft}}$ and $H^{(2)}_{\text{soft}}$. Note that the softening moduli are included in the model as material parameters and $\bar{\gamma}_{\text{fail}}$ is calculated from them.

In this paper the elastic-plastic traction-separation equation is extended to rate-dependency by defining the initial yield stresses $Y^{(1)}_0$ and $Y^{(2)}_0$ in the normal and tangential directions similar to the proposal of Johnson and Cook [1983] for a rate-dependent yield limit:

$$Y^{(1)} = Y^{(1)}_0\left(1 + C\left\langle \ln \frac{\dot{\Delta}_v}{\dot{\Delta}_0}\right\rangle\right) + H^{(1)}_{\text{hard}}\Delta^P_n, \qquad Y^{(2)} = Y^{(2)}_0\left(1 + C\left\langle \ln \frac{\dot{\Delta}_v}{\dot{\Delta}_0}\right\rangle\right) + H^{(2)}_{\text{hard}}\Delta^P_t. \tag{2-18}$$

The material parameter C and the reference rate of the displacement jump $\dot{\Delta}_0$ must be determined experimentally. The variables $Y^{(i)}_0$ are the initial yield stresses according to (2-16) for the two modes of plastic flow and the variable $\dot{\Delta}_v$ is the rate of the effective displacement jump as given in (2-6).

3. Time step control for explicit integration of equations of motion

The size of the critical time step for the conditionally stable explicit schemes has to be estimated for the numerical time integration of the equations of motion. The inverse of the largest eigenfrequency of the linear system of second order ordinary differential equations limits the maximum allowable time step, which is slightly reduced and then used for the step-by-step integration of the nonlinear system of the equations of motion. The largest eigenfrequency of the linear system is usually not known, since it is practically impossible to repeatedly solve the associated eigenvalue problem with a large number of degrees of freedom for the finite element mesh of a vehicle in a crashworthiness analysis. Therefore, approximate solutions, mainly based on the analysis of the individual finite element, must be used for a conservative estimate of an efficient time step.

A conservative estimate of the critical step length for the spatially discretized equations of motion for the complete structure is computed from the largest value $\omega_{\max}$ of the set of maximum eigenfrequencies of all individual finite elements e: $\omega^{\text{system}}_{\max} \le \max_e(\omega^e_{\max})$, where $\omega^e_{\max}$ is the maximum frequency of the e-th element subjected to zero traction boundary conditions [Irons 1970; Hughes et al. 1979]. The maximum eigenvalue of solid elements is often approximated by the bar wave velocity c and the smallest distance Δl of two arbitrary nodes within the element, leading to the critical time step $\Delta t_{\text{crit}} = \Delta l/c$. If only one solid element over the thickness d_k is used for the spatial modeling of thin adhesive layers, the smallest distance Δl between adjacent nodes is equal to d_k. The criterion above leads to an inefficiently small critical time step, since the length of any edge in any of the finite elements must currently be at least 5 mm for the crash analysis of complete vehicle bodies to guarantee a reasonable run time in practice. Therefore, we resort to another estimate for the critical size of the time step.

The distributed springs, symbolizing the stiffness, provided by an eight node interface element connect the masses of the top and bottom planes in Figure 3, left.

Both planes may consist of shell elements, describing the adjoining sheet metal or the surfaces of solid elements, used for the modeling of more bulky structural parts. The masses of both surfaces mainly

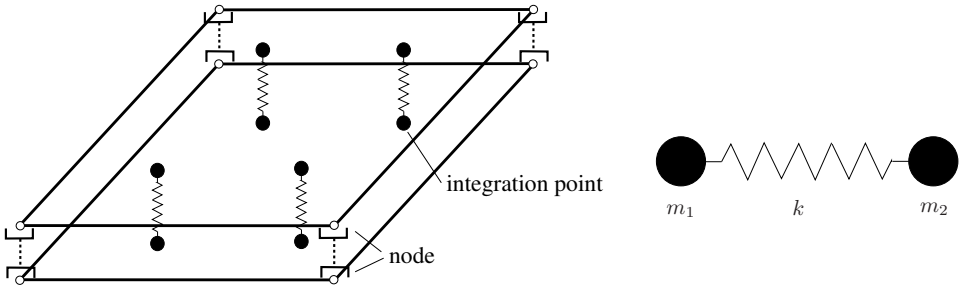

Figure 3. Left: interface element symbolized by distributed springs. Right: spring-mass system.

come from the bonded steel components and, to a small extent, from the adhesive layer. Figure 3, right, shows a node with mass m_1 in the top plane and a neighbouring node with mass m_2 in the bottom surface, connected by a discrete spring with stiffness k, which is computed by numerical quadrature at the integration points of the interface element. The parameter k equals the product of the shear or normal stiffness times a quarter of the element area in the case of an eight node interface element. The critical time step for the spring-mass system is given by:

$$\Delta t_{\text{crit}} = 2\sqrt{\frac{m_1 m_2}{m_1+m_2}\frac{1}{k}}. \tag{3-1}$$

Note from this equation that the thickness d_k of the adhesive layer does not enter the estimate of the critical time step for the interface element. It may be shown by numerical investigation that the critical time step of the solid elements for the steel parts is not further limited by this estimate for the interface elements.

4. Numerical examples for delamination analysis

The interface elements, along with the traction-separation equations of mixed-mode fracture and elasto-plasticity, were coded into the finite element program FEAP [FEAP 2002] and the commercial code LS-DYNA [DYNA 1998; DYNA 2006] as user defined material models. The performance of the different approaches are demonstrated by means of the double cantilever beam (DCB) and fixed ratio mixed-mode (FRMM) tests for delamination, all run with FEAP. The values of the elastic interface stiffness terms K_n and K_t serve more or less as penalty parameters in the case of delamination analysis and are kept in a reasonable range, where the stiffness does not obstruct the condition number of the stiffness matrix in implicit analysis [Fiolka and Matzenmiller 2007] or the time step of the explicit runs.

4A. ***DCB test.*** The double cantilever beam (DCB) test, shown schematically in Figure 4, is a widely used interlaminar fracture test of fiber-reinforced structures to analyze crack growth in mode I. The material parameters E_{11}, E_{22}, G_{12}, G_{13}, and ν_{12} of the orthotropic elasticity model for the DCB specimen, made of fiber-reinforced composite material, are given in Table 1 together with the material constants for mode I of the Hillerborg fracture model.

For the analysis of the delamination test, two kinds of elements are used: the three-dimensional interface element (see Section 2A) and a locking-free solid-shell element [Fiolka and Matzenmiller 2007].

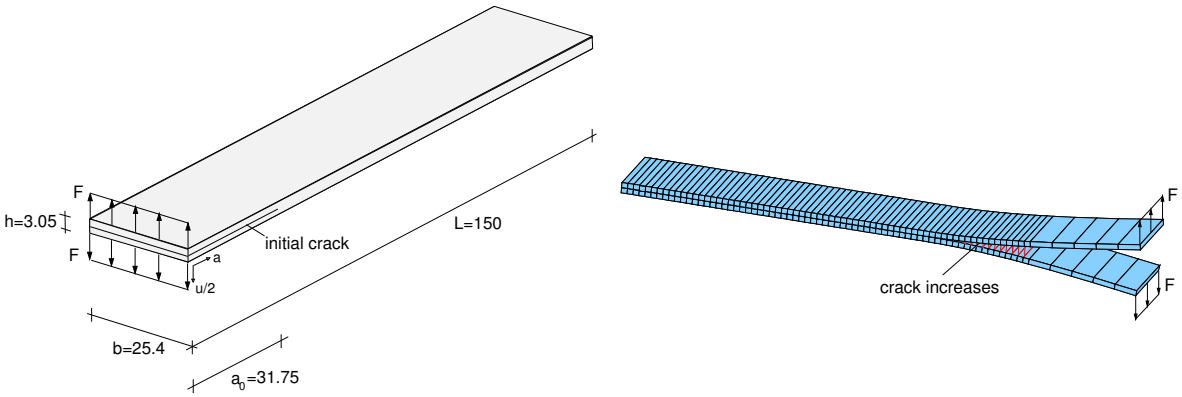

Figure 4. DCB test setup and finite element model.

The convergence study reveals that 140 interface elements along the length of the uncracked specimen of 118.25 mm are sufficient for the accurate resolution of the load-deflection diagram. A total of 290 solid-shell elements are taken for the double cantilever [Fiolka 2007].

Figure 5, left, displays the experimental data from [Aliyu and Daniel 1985] and the analytical solution from [Mi et al. 1998] together with the finite element simulation. The numerical and the experimental results are identical until the load peak is reached, where the crack begins to increase. During the delamination process, the forces in the numerical and the analytical solutions match very well. Further finite element simulations have shown that the shape of the traction-separation equation, here taken as bilinear or trilinear as in the Tvergaard–Hutchinson model, has only a small influence on the force-displacement curve.

The interface stiffness parameters K_n and K_t are chosen to be sufficiently large enough in Table 1, since practically the same result is obtained as in Figure 5, left, for the numerical case, if K_n and K_t are reduced to 12000 N/mm^3 or increased to 30000 N/mm^3; see Figure 5, right.

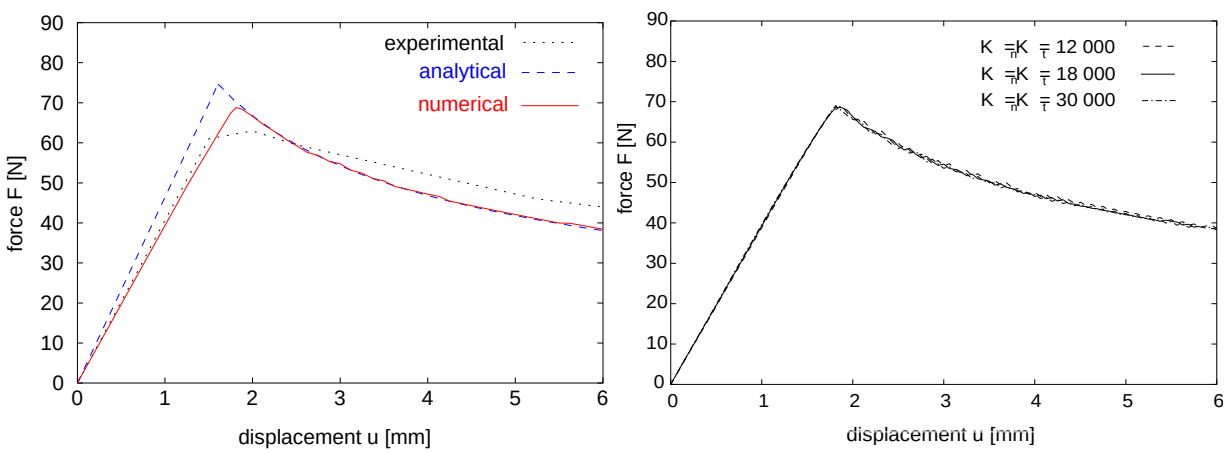

Figure 5. Left: Experimental data and simulation results of the mixed-mode fracture model for the DCB test. Right: Results for various interface stiffness values K_n and K_t of the mixed-mode fracture model for the DCB test from [Fiolka 2007, page 115].

Elasticity moduli	$E_{11} = 138000\,\mathrm{N/mm^2}$	$E_{22} = 8960\,\mathrm{N/mm^2}$
Shear moduli	$G_{12} = 7100\,\mathrm{N/mm^2}$	$G_{23} = 3446\,\mathrm{N/mm^2}$
Poisson's ratio	$\nu_{12} = 0.3$	
Elastic interface stiffness	$K_n = 18000\,\mathrm{N/mm^3}$	$K_t = 18000\,\mathrm{N/mm^3}$
Maximal interface stress	$t_3^{\max} = 51.7\,\mathrm{N/mm^2}$	
Energy release rate	$\mathcal{G}_{\mathrm{Ic}} = 222\,\mathrm{Nm/m^2}$	

Table 1. Material parameters for orthotropic elasticity model of composite and bilinear interface model of DCB test from [Teßmer 2000; Fiolka 2007].

Elasticity moduli	$E_{11} = 130000\,\mathrm{N/mm^2}$	$E_{22} = 8000\,\mathrm{N/mm^2}$
Shear moduli	$G_{12} = 6000\,\mathrm{N/mm^2}$	$G_{23} = 3000\,\mathrm{N/mm^2}$
Poisson's ratio	$\nu_{12} = 0.27$	
Elastic interface stiffness	$K_n = 100000\,\mathrm{N/mm^3}$	$K_t = 100000\,\mathrm{N/mm^3}$
Maximal interface stress	$t_1^{\max} = 48.0\,\mathrm{N/mm^2}$	$t_3^{\max} = 48.0\,\mathrm{N/mm^2}$
Energy release rates	$\mathcal{G}_{\mathrm{Ic}} = 257\,\mathrm{Nm/m^2}$	$\mathcal{G}_{\mathrm{IIc}} = 856\,\mathrm{Nm/m^2}$
Interaction parameter	$n = 2$	

Table 2. Material parameters of orthotropic elasticity model for composite layer and interface model for FRMM test.

4B. ***FRMM test.*** Among the mixed-mode bending tests, the FRMM test in Figure 6 is a common benchmark for the investigation of interlaminar fracture and for the determination of the mixed-mode properties for the delamination process in fiber-reinforced composite structures. The layered composite is notched at the free end over a length of $a_0 = 45$ mm and clamped at the other end. The material parameters of the FRMM specimen, made of carbon fiber-reinforced epoxy resin [Chen et al. 1999], are given in Table 2. The parameters for the elastic interface stiffness are chosen in accordance with the earlier considerations. A transverse load is applied at the free edge of the upper layer. The length of the finite elements is chosen as 0.87 mm in the direction of the crack growth after a convergence study of the mesh size has been undertaken on the experience of the DCB test. Hence, 148 volume-shell elements and 69 interface elements are used in total.

The simulation results are compared to the experimental data and the analytical solution in Figure 7, left. The Hillerborg mixed-mode model approximates the experimental load-displacement curve fairly well for an interaction parameter of $n = 2$ in (2-4). However, the Tvergaard–Hutchinson model

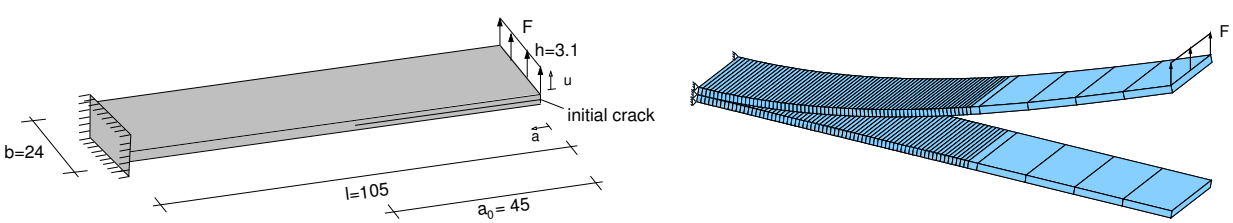

Figure 6. FRMM test setup.

underestimates the experimental load-displacement curve, because the critical energy release rate $\mathcal{G}_c$ in (2-8) takes only the mode I part into account. Again, it can be shown that the shape of the graph from the traction-separation equation has only a minor effect on the load-displacement relation — see Figure 7, right, where the force-displacement curve with $\lambda_1 = \lambda_2 = 0.1$ (the bilinear shape) is compared to the one with $\lambda_1 = 0.2$ and $\lambda_2 = 0.6$ (the trilinear shape in Figure 2).

5. Failure analysis of adhesive bonds

The proposed interface models are used for the simulation of the mechanical behavior of adhesively bonded joints until failure of the adhesive layer occurs. Therefore, the bonded tube test, the peel test, and the KS-II test are simulated with LS-DYNA and explicit time integration. The numerical results are compared to the experimental data. The thickness of the adhesive layers is between 0.25 and 0.30 mm for all specimens.

5A. ***Experimental results for toughened adhesives.*** Structural adhesives are crash-resistant, toughened plastic polymers, nowadays used in bonding applications. The material behavior of crash-resistant adhesives such as Betamate 1496, SikaPower 490-6, EP 12, or Terokal 5070 was comprehensively examined in an earlier research project [Schlimmer et al. 2002]. A typical characteristic behavior of toughened adhesives is plastic flow under shear as well as hydrostatic loading, as can be measured in tension and torsion tests of adhesively bonded tubes. The constitutive response in shear of a crash-resistant adhesive under slow loading, complete unloading, and reloading was investigated in [Schlimmer 2003] with a shear strain rate of $\dot{\gamma}_{xy} = 2 \cdot 10^{-3}\,\mathrm{s}^{-1}$. The shear stress-shear strain from the test is shown in Figure 8, where permanent strains $\gamma_{xy,bl}$ remain in the specimen, if the external load exceeded the yield limit before unloading took place. The hysteresis loops due to cyclic loading are neglected in the elastoplastic approach and the linear elastic response with the shear modulus G_s is fitted to the unloading/reloading paths.

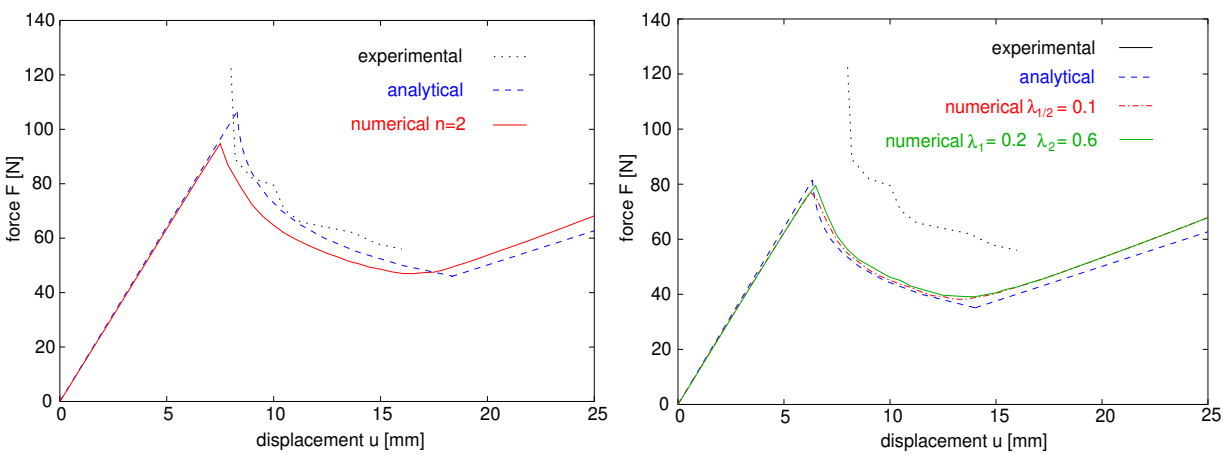

Figure 7. Left: Experimental data and simulation results of the Hillerborg mixed-mode interface model for FRMM test. Right: Experimental data and simulation results of the Tvergaard–Hutchinson mixed-mode interface model for the DCB test.

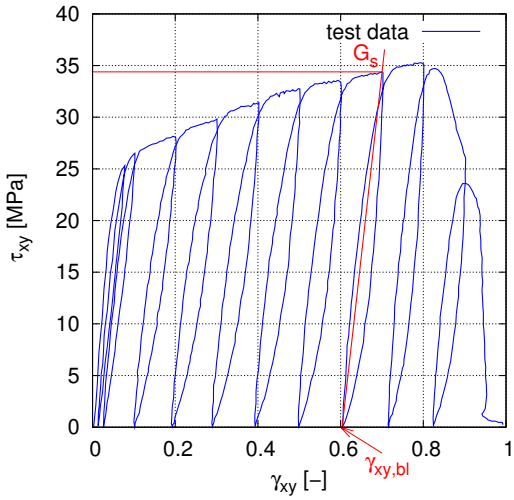

Figure 8. Stress-strain diagram of crash-resistant adhesive EP 12 under cyclic loading from [Schlimmer 2003].

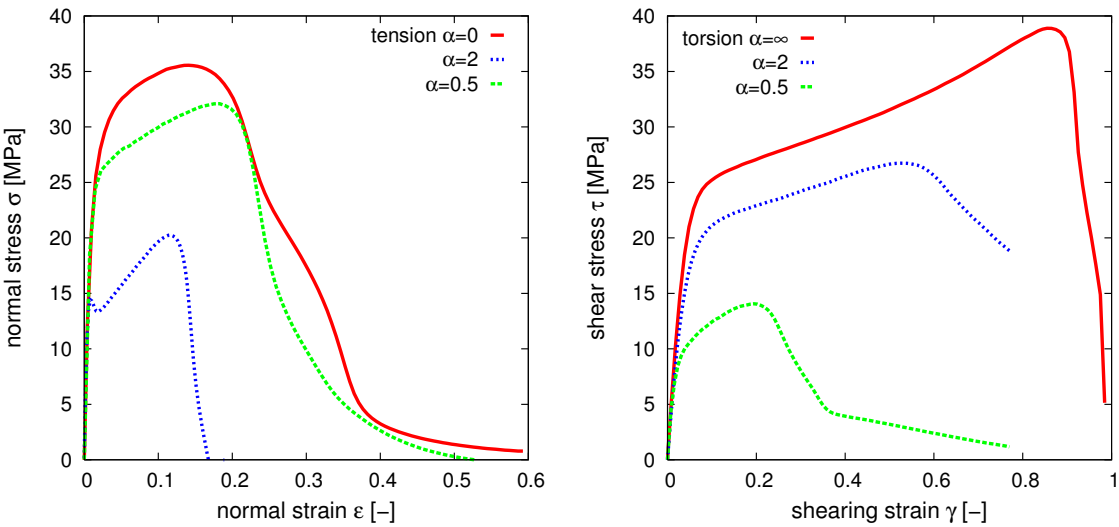

Figure 9. Experimental results of pure tension, pure torsion, and combined tension-torsion tests of adhesively bonded tubes from [Schlimmer 2003].

The material behavior in Figure 9 is typical for an adhesive layer between two bonded steel tubes under uniaxial tension and torsion loading. The experimental data for the stress-strain diagrams have been provided by Schlimmer [2003]. The combined tension-torsion tests are characterized by the ratio $\alpha = \gamma/(2\epsilon)$ of normal to shear strains ϵ and γ. In Figure 9 the results of pure tension ($\alpha = \infty$) and torsion ($\alpha = 0$) tests and two combined tension-torsion experiments with $\alpha = 0.5$ and $\alpha = 2.0$ are shown.

The rate dependency of the yield stress or stress at failure is investigated by means of tension tests at butt-jointed specimens and of shear tests at thick shear lap specimens [Schlimmer et al. 2008]. The

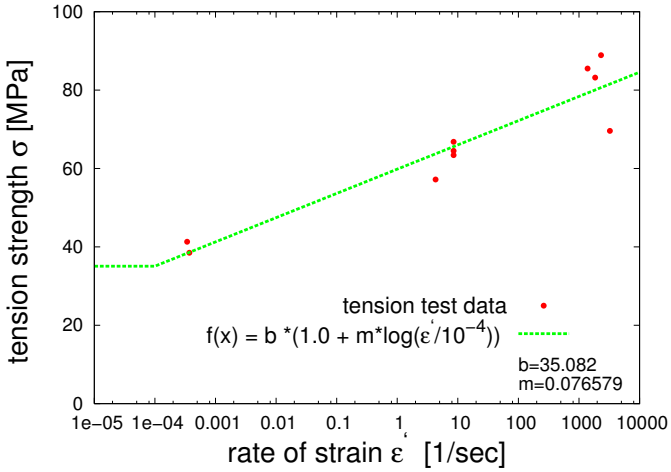

Figure 10. Experimental data for rate-dependent tensile strength of adhesively bonded joints and least square fit of model response for butt-jointed specimen from [Jendrny 2005; Schlimmer et al. 2008].

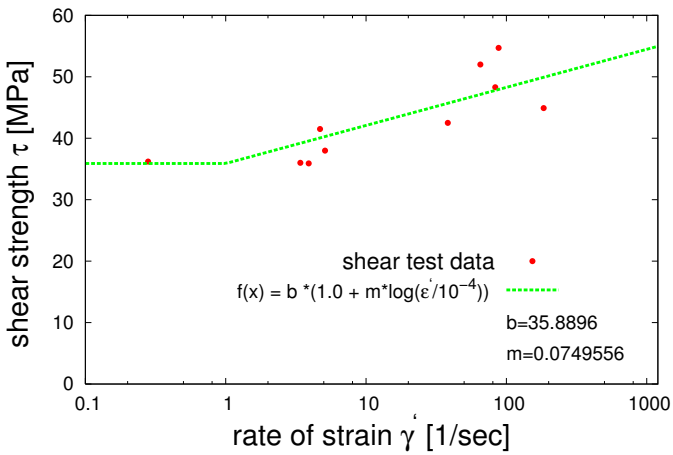

Figure 11. Experimental data for rate-dependent shear strength of adhesively bonded joints and least square fit of model response for thick shear lap specimen from [Jendrny 2005; Schlimmer et al. 2008].

results are summarized in Figures 10 and 11 together with the least square fit to the data of the functions in (2-5).

5B. ***Numerical analysis of bonded tubes.*** The bonded tube test above consists of two hollow metal cylinders, joined at the cross section by an adhesive layer of Betamate 1496 V. An axial force or a torque is applied at the upper end of the structure, while the far end of the lower cylinder is kept fixed (see Figure 12). The parameters of the elastic-plastic interface model, discussed above, are determined by fitting the model response to the data [Schlimmer et al. 2002] from the pure tension and pure torsion tests of the bonded tubes. These are given in Table 3. The elastic interface stiffness parameters K_n and K_t

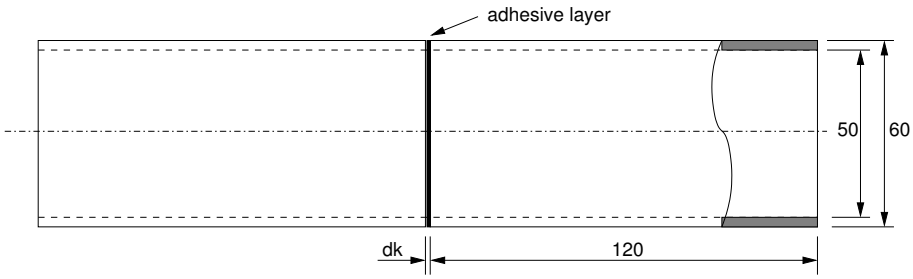

Figure 12. Bonded tubes with geometrical data.

coincide with the measured stiffness values for the adhesive layer with thickness of 0.3 mm. Dividing the elasticity modulus and shear modulus of the adhesive layer by the thickness delivers the values chosen for K_n and K_t in Table 3. The combined tension-torsion tests for $\alpha = 0.5$ and $\alpha = 2.0$ are used as validation examples. The adhesive layer is meshed by 28 interface elements in the circumferential direction of the tube. Figure 13 shows the experimental data from [Schlimmer et al. 2002] and the simulation results of the stress-strain curves from the elastoplastic interface model in Section 2D.

The results of the finite element simulation agree sufficiently with the experimental data in the pure tension and pure torsion tests, which are performed for the identification of the constitutive parameters. The stress-strain curves in Figure 13 show that the different yield limits in the normal and tangential directions correspond to the experimental data. The hardening of the adhesive layer is approximated fairly well by the linear course of the graph from the model, whereas the displacement jump at the failure of the adhesive bond is not so well represented in the load cases of combined tension and torsion.

Although the model is very flexible, allowing independent approximations of yielding due to tension and shear, its capability to describe the postcritical behavior is very limited. It does not permit representing the initiation of softening and the state of failure separately. There is only one variable β (see (2-14)), which may be identified such that either the initiation of softening at $\bar{\gamma}_{\text{crit}}$ or the failure at $\bar{\gamma}_{\text{fail}}$ takes place in tension and shear at the same time in both modes of plastic flow. In this paper the determination of the parameter β is a compromise between the onset of softening and the occurrence of complete failure. In conclusion, the model has only two parameters β and $\bar{\gamma}_{\text{crit}}$ (see Table 3) to describe the points of maximum stress at the critical discontinuity and zero stress at failure $\overline{\gamma}_{\text{fail}}$ for both modes of yielding. The combined tension-torsion tests for $\alpha = 0.5$ and $\alpha = 2.0$ serve as examples for

Elastic interface stiffness	$K_n = 6500\,\text{N/mm}^3$	$K_t = 2500\,\text{N/mm}^3$
Yield limits	$Y_0^{(1)} = 30.0\,\text{MPa}$	$Y_0^{(2)} = 26.0\,\text{MPa}$
Hardening modulus	$H_{\text{hard}}^{(1)} = 210\,\text{MPa/mm}$	$H_{\text{hard}}^{(2)} = 450\,\text{MPa/mm}$
Softening modulus	$H_{\text{soft}}^{(1)} = 580\,\text{MPa/mm}$	$H_{\text{soft}}^{(2)} = 5000\,\text{MPa/mm}$
Coulomb friction parameter	$\mu = 0.55$	
Interaction parameter	$\beta = 0.039$	
Critical displacement jump	$\bar{\gamma}_{\text{crit}} = 0.035\,\text{mm}$	

Table 3. Material parameters of elastic-plastic interface model.

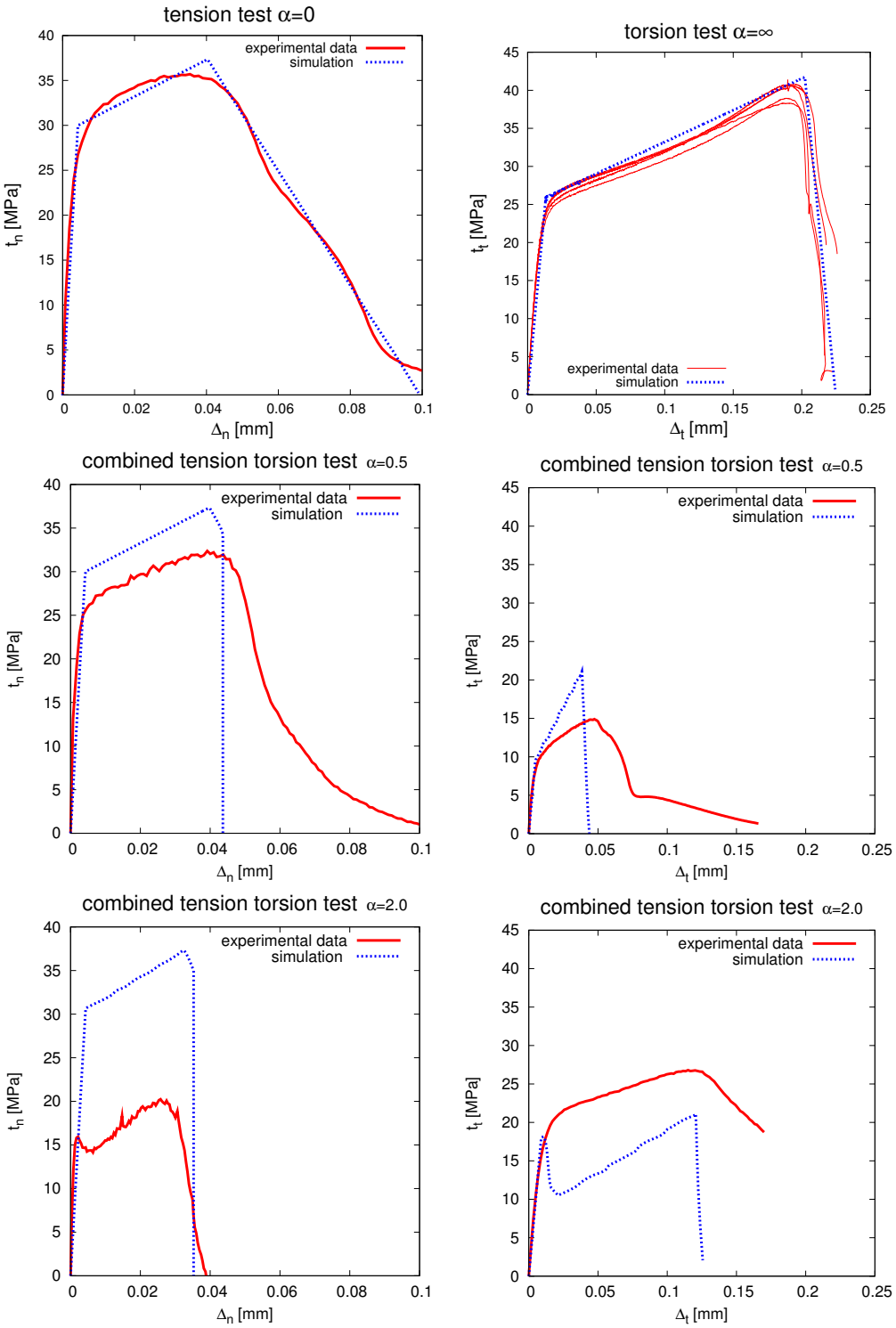

Figure 13. Comparison between experimental data and simulation results of elastic-plastic interface model for tension, torsion, and combined loading tests of bonded tubes.

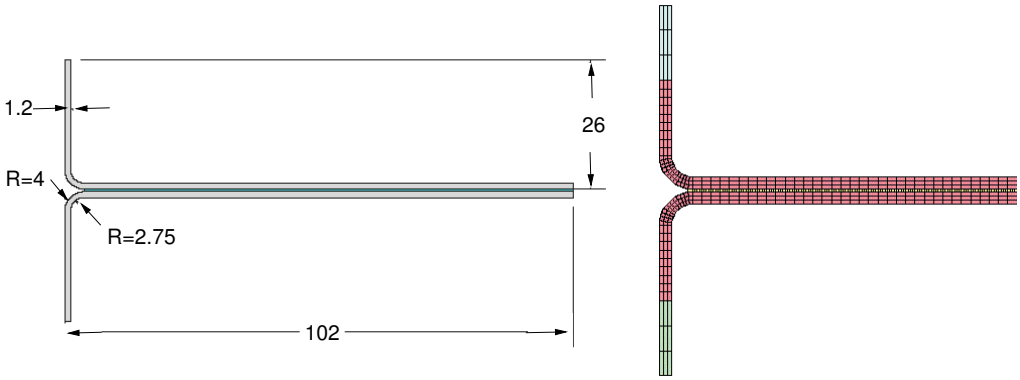

Figure 14. Geometry of peel test specimen and FE mesh of front part.

the validation of the model's hypotheses in describing the plastic flow in nonuniaxial situations. The prediction of the mechanical behavior from the simulation using LS-DYNA for these combined loading tests is not satisfactory for the special adhesive Betamate 1496. The mode interaction behavior should be improved for this adhesive, as should the simple assumption for the flow vector $\boldsymbol{m}^{(2)} = \boldsymbol{t}_t$ in mode II (see (2-12)).

5C. ***Numerical analysis of peel test.*** The first series of specimens with inhomogeneous stress distributions and fracture to be examined for adhesive joints is the peel test. It resembles the DCB specimen (see Figure 14), where two metal sheets with width $b = 25$ mm are glued together with the crash resistant adhesive Betamate 1496 V and torn apart by forces at the ends normal to the bonding. However, the metal sheets deform plastically during the peeling process, whereas in the DCB test the laminae bend only within the elastic range.

The peel test is analyzed with the mixed-mode fracture model and the elastic-plastic interface approach for the adhesive. Rate-independent material models are used for the adhesive and conventional Prandtl–Reuss plasticity theory of the von Mises type for the steel of the sheet metal. The material constants from Table 3 are taken for the plasticity model of the adhesive and from Table 4 for the isotropic, ideal plastic description of the adherends and the mixed-mode fracture model. The constitutive parameters of the latter in Table 4 are determined on the basis of fracture tests for modes I and II by Brede and Hesebeck [2005].

Elasticity modulus steel	$E = 209000\,\mathrm{N/mm^2}$	
Poisson's ratio steel	$\nu = 0.3$	
Yield limit steel	$Y_0 = 350\,\mathrm{N/mm^2}$	
Elastic interface stiffness	$K_n = 6500\,\mathrm{MPa/mm}$,	$K_t = 6500\,\mathrm{MPa/mm}$
Maximal interface stress	$t_n^{\max} = 20.0\,\mathrm{MPa}$,	$t_t^{\max} = 39.5\,\mathrm{MPa}$
Energy release rate	$\mathcal{G}_{\mathrm{Ic}} = 5400\,\mathrm{Nm/m^2}$	$\mathcal{G}_{\mathrm{IIc}} = \mathcal{G}_{\mathrm{IIIc}} = 23000\,\mathrm{Nm/m^2}$
Interaction parameter	$n = 2$	

Table 4. Material parameters of steel sheets and mixed-mode cohesive zone model from [Brede and Hesebeck 2005].

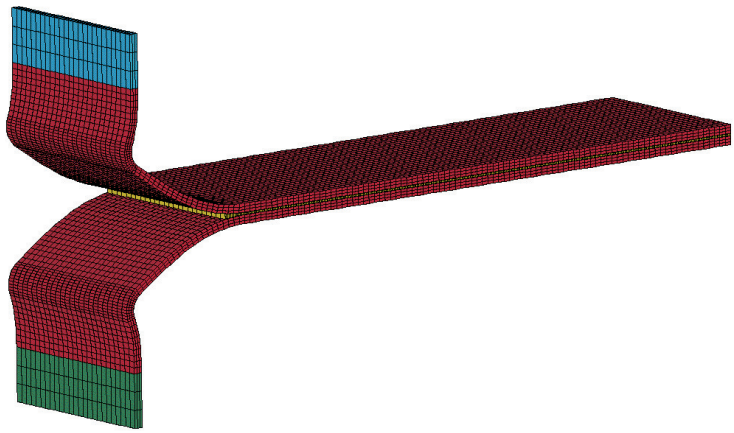

Figure 15. FE model of deformed shape of peel test specimen.

The FE model of the peel test consists of 473 interface elements along the length and 25 in the cross direction of the adhesive layer. Three linear solid elements are taken through the thickness of each steel sheet and 137 in the length direction. With an element size of about 1.1 mm for the hexahedron of the steel and 0.275 mm for the interface elements of the adhesive, the finite element mesh may be considered as converged in practice. The boundary value problem is solved with the commercial code LS-DYNA [DYNA 2006], extended by the user interface element with the constitutive models above, and explicit time integration. The test is simulated with a constant velocity boundary condition of 140 mm/s at the upper end. The deformed specimen is shown in Figure 15.

The comparison of the simulation results with the experimental data from [Schlimmer et al. 2008] is presented in Figures 16 and 17 by means of the load-displacement curves. The typical features of these are the peak force at the beginning, when the crack starts to open, and the decrease of the resultant force value during the advancing peel process. The simulations with the mixed-mode model (Figure 16) and the elastic-plastic interface approach (Figure 17) lead to different peak values of the force in the cases with data from [Schlimmer 2003; Brede and Hesebeck 2005]. The mixed-mode model with these data clearly overestimates the maximum load carrying capacity of the specimen; obviously, the force during the peeling process is significantly greater than that of the corresponding experimental data (Figure 16).

The excessively high load carrying capacity in the simulation with the mixed-mode model, shown in blue (upper dotted curve) in Figure 16, is mainly due to the loss of adhesion bonding at the surface of the adherends in the experiments as outlined in [Schlimmer et al. 2008, chapter 3.1.7]. However, the material data for the energy release rates in Table 4 are determined in [Brede and Hesebeck 2005] for cohesive fracture at a much higher load carrying capacity. In summary, they may be too large, since the area under the experimentally measured diagrams of the stress versus crack opening displacement is, according to the tests in [Schlimmer 2003], about 3240 Nm/m^2 in the case of pure tension, $\alpha = 0$ in Figure 13a, and 12900 Nm/m^2 in the case of torsion, $\alpha = \infty$ for pure shearing in Figure 13b. If these values are taken for the critical energy release rates $\mathcal{G}_{\mathrm{Ic}}$ and $\mathcal{G}_{\mathrm{IIc}}$ with the maximal interface stresses adjusted to $t_n^{\max} = 35.0$ MPa and $t_t^{\max} = 39.0$ MPa, the red (solid) curves in Figure 16 follow from the simulation with the mixed-mode fracture model [Schlimmer et al. 2002; Schlimmer 2003]. In the third run, the energy release rates are lowered to $\mathcal{G}_{\mathrm{Ic}} = 1300$ Nm/m^2 and $\mathcal{G}_{\mathrm{IIc}} = 10000$ Nm/m^2 as inversely identified in

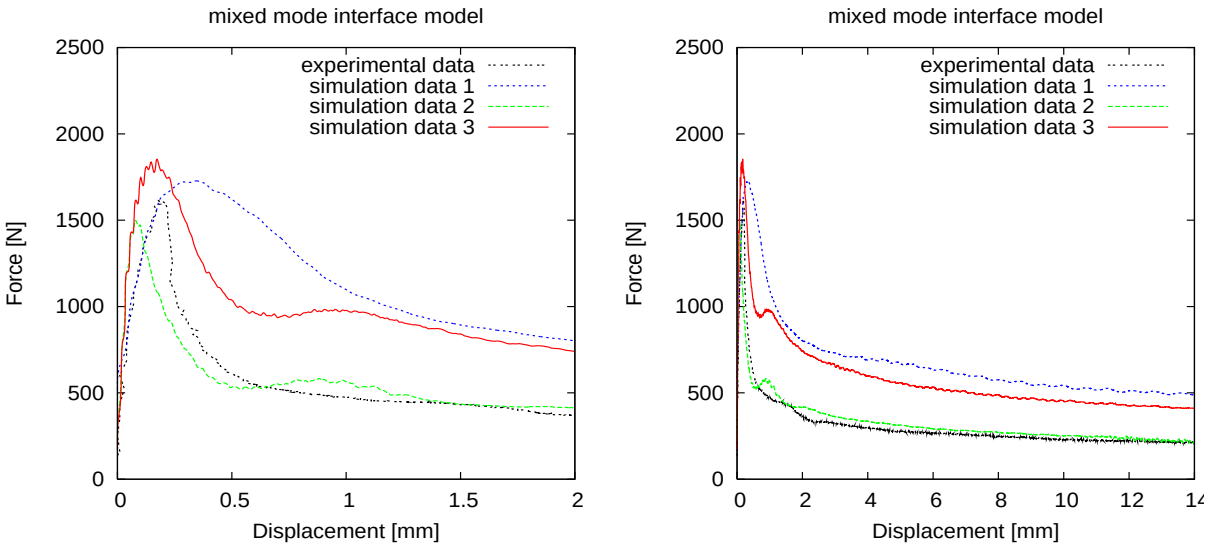

Figure 16. Results of the peel test computed with mixed-mode interface model and compared to experimental data. Simulation data #1 is from [Brede and Hesebeck 2005], #2 from [Schlimmer et al. 2008], and #3 from [Schlimmer 2003].

[Schlimmer et al. 2008], where the maximal stresses are changed slightly to $t_n^{\max} = 43.0\,\text{MPa}$ and $t_t^{\max} = 39.0\,\text{MPa}$. Shown in green (light-colored dashed graph), this solution approximates the test data best.

The data in Figure 17 suggest that the elastic-plastic interface model approximates the maximum resultant force of the experiment very well, but the peak is slightly shifted towards the left. The forces of the interface model during the peeling process coincide with the experimental data (see Figure 17).

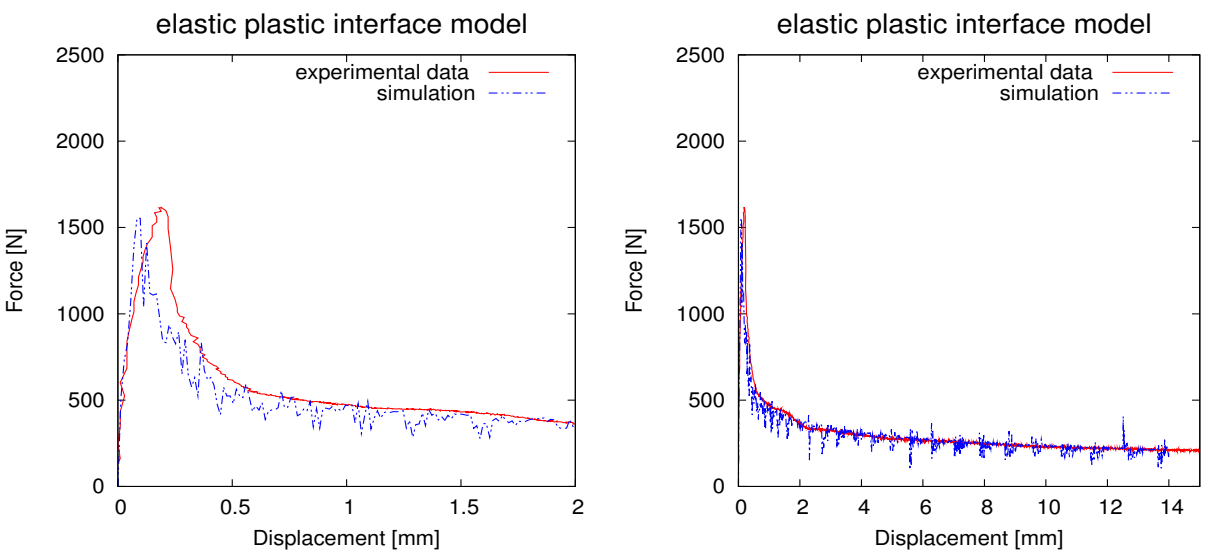

Figure 17. Comparison of experimental data for peel test with the response of the elastic-plastic interface model.

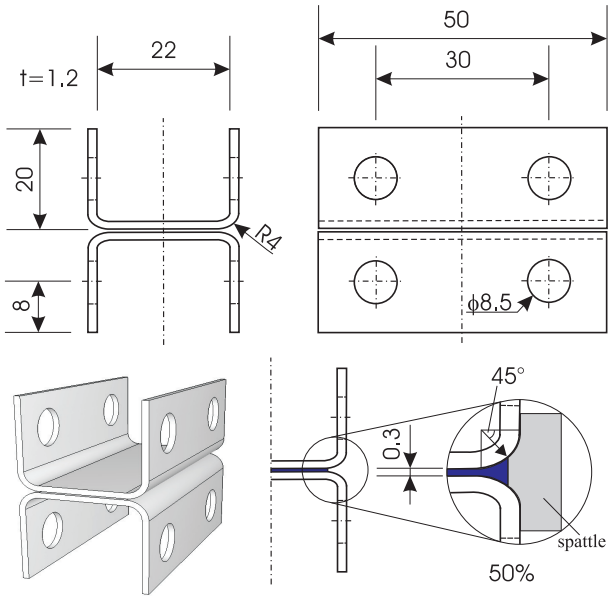

Figure 18. Geometry of KS-II test specimen, and underfilling (lower right).

5D. ***KS-II test.*** Hahn et al. [1999] developed an experimental setup to investigate the mechanical behavior of adhesively bonded joints under tensile and shear loading (see Figures 18 and 19). The purpose of the test is to characterize and evaluate the behavior of bonding techniques under different mechanical stress conditions. Two U-shaped steel components are joined together with an adhesive similar to a flange in an automotive application (see Figure 18). The dimensions of the adhesive layer are 23 mm by 16 mm with a thickness of 0.3 mm. The underfilling of 50% at the edge of the adhesive layer is shown in Figure 18, right.

The test specimen can be pulled apart with different clamping devices under various angles of loading with respect to the normal on the adhesive layer (see Figure 19). Four different load angles are chosen

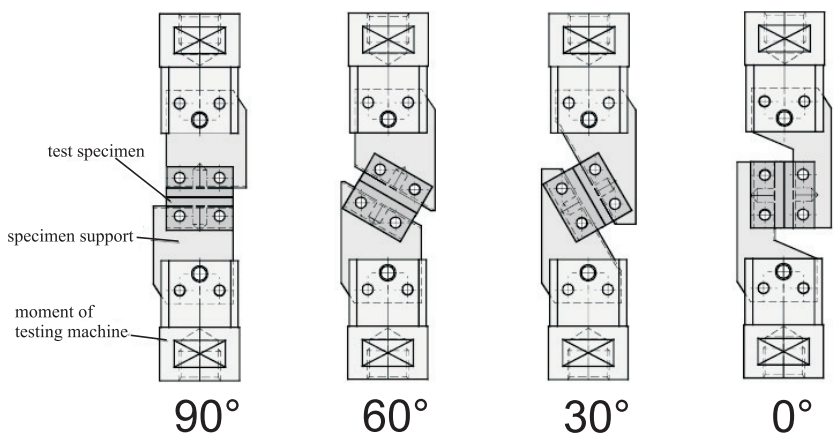

Figure 19. Test control unit and load cases.

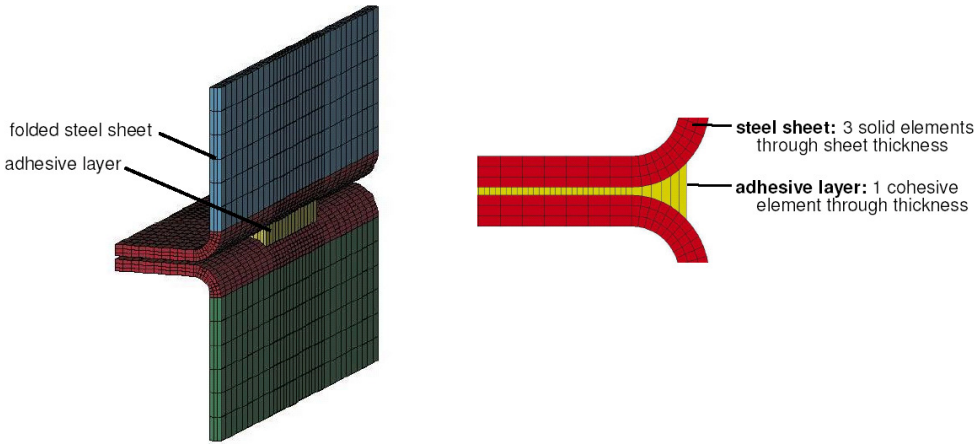

Figure 20. Finite element idealization of symmetric half model.

with 0° for pure shear loading, 90° for normal loading, and the two intermediate angles 30° and 60° for combined tension and shear stressing. The loading is applied in terms of prescribed nodal velocities on the far ends of the U-shaped profiles, which are mounted on steel support jaws, treated as rigid in the FE model. In order to investigate the influence of the rate-dependency, analysis and experimental testing have been performed for loading velocities of $v = 1.0$ m/s, in addition to the quasistatic one with $v = 10$ mm/min. The displacement is measured 15 mm below the upper and lower edges of the specimen on the line of symmetry.

In the numerical analysis, only the symmetrical half of the specimen is analyzed, as shown in Figure 20, left. Since the validation of the substitute element for the bonding was the primary intent, both the adhesive layer and the adherent steel parts are meshed fairly finely with the interface elements in the region of the bonding. The adhesive bond is meshed with 16 interface elements lengthwise and 46 interface elements crosswise. However, outside of this area the steel parts in the clamping devices are modeled as rigid bodies, where the loading in terms of prescribed nodal velocities is applied. Special attention has to be given to the filling at the outer edge of the adhesive layer around the corner from the steel parts (see the right side of Figure 20). Due to the increased thickness, the strains in the filling are smaller and, thus, local failure takes place later.

Each load case has been investigated with both constitutive models mentioned above for the adhesive. The material parameters of the mixed-mode fracture model are determined on the basis of fracture tests (see Table 4 for the mechanical properties). The material parameters for the elastic-plastic model in Table 3 are identified from the data from experimental tests at bonded tubes with a fairly homogeneous state of stress in the adhesive layer under tension and torsion. These are used in the analysis of the KS-II test.

The results of the analysis are plotted as the total internal force in the load direction versus the local displacement in Figures 21–24 and compared to the data measured in the experiments [Schlimmer et al. 2008]. The local displacements in the experiment are computed as the difference of the displacement vectors for two marked points on the clamped legs of the upper and lower U-shaped steel parts. In the finite element analysis, the local displacement is defined as the discontinuity between the displacements of the rigid bodies for parts of the upper and lower steel components. The force in the load direction on the ordinate of the diagrams is calculated in the theoretical investigation from the stresses in the adhesive

layer by summing them over the entire area. It is generally impossible to measure with a device the force in the adhesive layer without influencing its properties with embedded particles. Therefore, the force cannot be recorded close to the glued interface in the current test setup and a measurement cell is put into the top of the upper clamping device. Due to the inertial effects of the mass for the steel parts between the adhesive layer and the measurement cell, the measured forces differ from the total internal force, transferred through the adhesive joint between the lower and upper steel components. It is difficult to estimate the deviation of the internal force in the measurement device from the resultant on the cut through the adhesive layer. Despite the unknown error between the measured force in the clamping device and the stress resultant on the adhesive layer we compare the measured force from the test to the calculated resultant in the joint and plot both quantities over the local displacements in Figures 21–24.

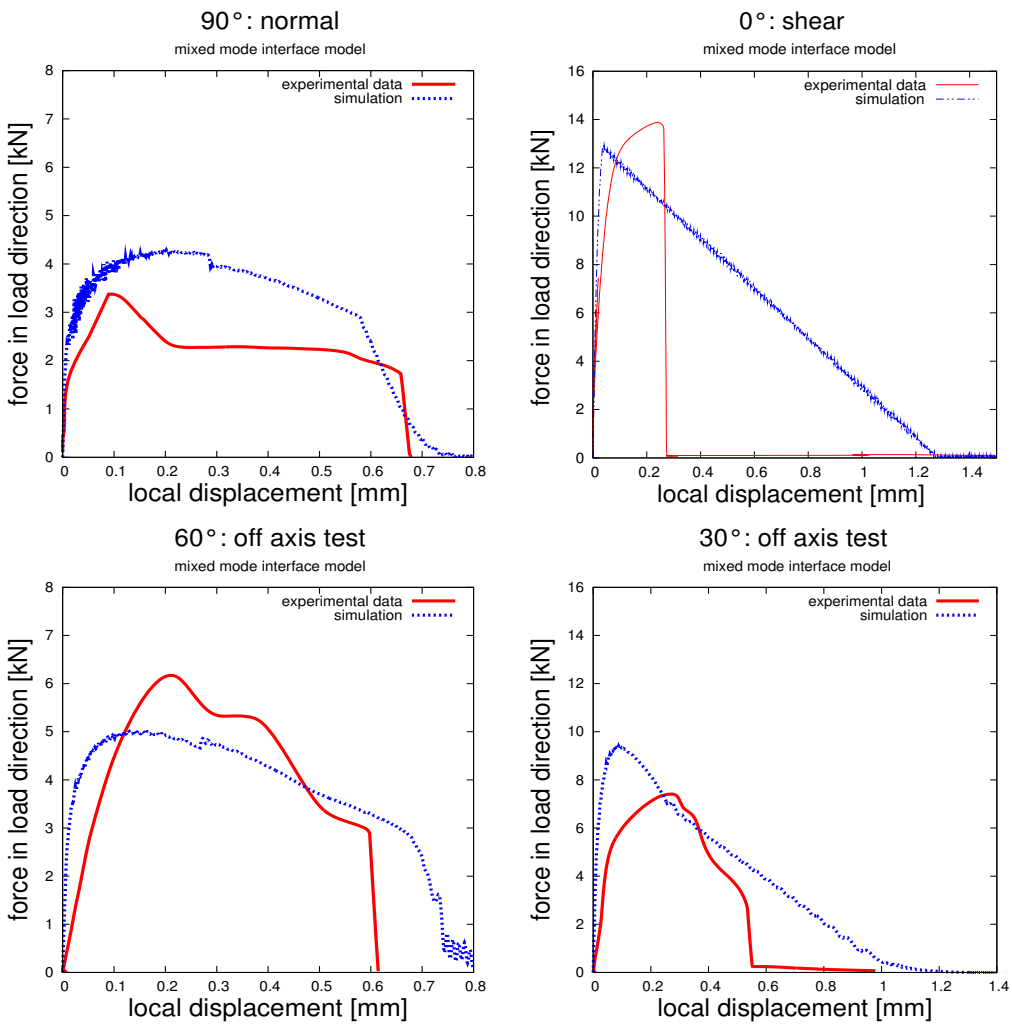

Figure 21. Comparison between experimental data and simulation results with mixed-mode interface model for quasistatic loading: tension and shear tests with angles 90° and 0° (top) and off-axis tests with angles 60° and 30° (bottom).

5E. ***Quasistatic loading of KS-II test.*** The numerical analysis of the KS-II test shows that the failure mechanism of the specimen is very complex. The thickness of the adherents is only 1.2 mm and, therefore, the relatively thin sheet metals are bent in two directions during the loading process. Additionally, the thickness of the bonding layer varies at the edges of the U-shaped adherents due to the filling of the joint (see Figure 20). Because of these phenomena, the state of stress and strain in the adhesive layer is very inhomogeneous. Therefore, the onset of failure takes place in the center very locally and spreads out continuously throughout the entire bonded area.

The maximum load carrying capacity depends on the off-axis angle and is largest in the cases of shear loading and minimal under normal loading. The peak values of the forces from the experimental and numerical analyses are of the same order of magnitude for both models (see Figures 21 and 22). However,

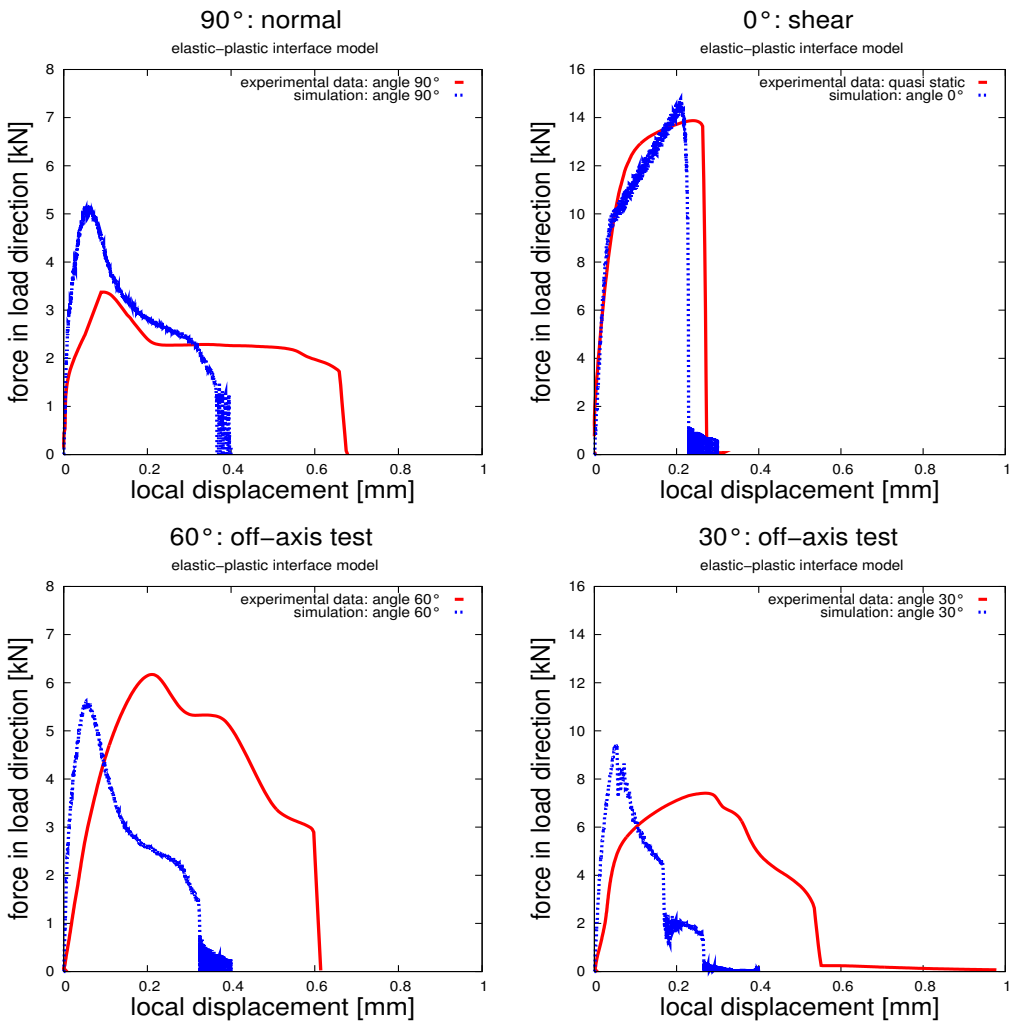

Figure 22. Comparison between experimental data and simulation results with elastic-plastic interface model for quasistatic loading: tension and shear tests with angles 90° and 0° (top) and off-axis tests with angles 60° and 30° (bottom).

the courses of the load-deflection diagrams from the test and the simulation in the case of shear loading (0°) differ in the postcritical range. As in the mixed-mode approach, the elastic-plastic interface model describes the mechanical behavior of the bonded joint in all four load cases reasonably well (Figure 22). The load-deflection diagrams of the load cases 30°, 60°, and 90° are more ductile in the test than in the simulations. The predicted peak values in all cases are in the range of the experimental data. The corresponding local displacement jumps between the two clamping devices are underestimated at both critical states, namely at the location of the maximum force and at complete failure in most load cases.

5F. ***Dynamic loading of KS-II test.*** The rate-dependent material behavior of the adhesive layer becomes significant in crash analyses. The rate dependency of the models, presented in (2-18), is quantitatively

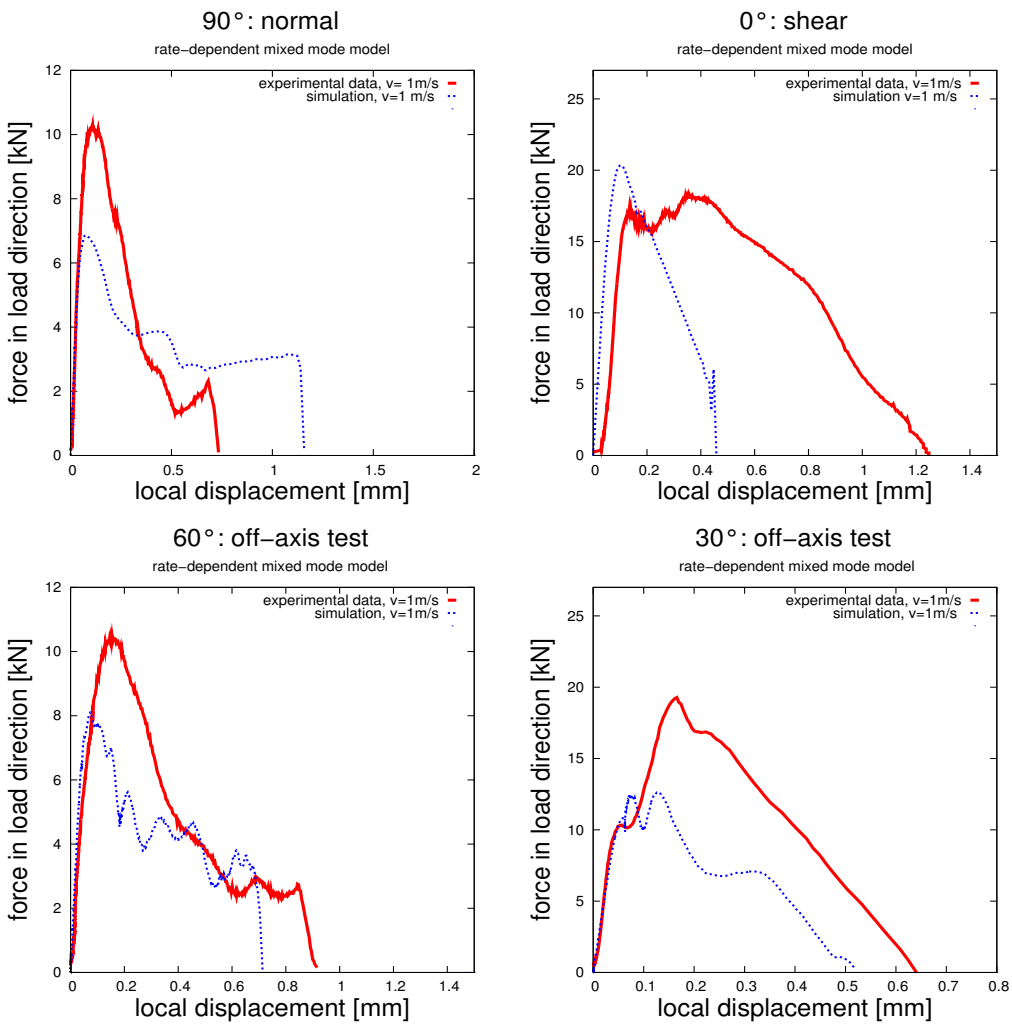

Figure 23. Comparison between experimental data and simulation results with mixed-mode model for velocity $v = 1.0$ m/s: tension and shear test with angles 90° and 0° (top), and off-axis tests with angles 60° and 30° (bottom).

defined with the reference value $\dot{\Delta}_0 = 10^{-4}$ 1/s and with the parameter C, which is set equal to the slope of the graph for the linear regression in Figures 10 and 11: $C = m = 0.076$. Because of the rate-dependent influence of the adhesive, the KS-II specimens are tested dynamically. The tests are performed with tensile loading under four different off-axis angles as given above. The load-displacement curves are determined from the measured data for the displacements and the internal forces versus time. The experimental results from the tests in [Schlimmer et al. 2008] are shown in Figures 23 and 24 for a loading velocity of $v = 1.0$ m/s. Due to the rate-dependency of the adhesive, the peak value of the force increases clearly with a larger loading velocity in comparison to the ones of the quasistatic cases in Figures 21 and 22.

The mechanical behavior of the KS-II specimen under pure normal and combined loading with respect

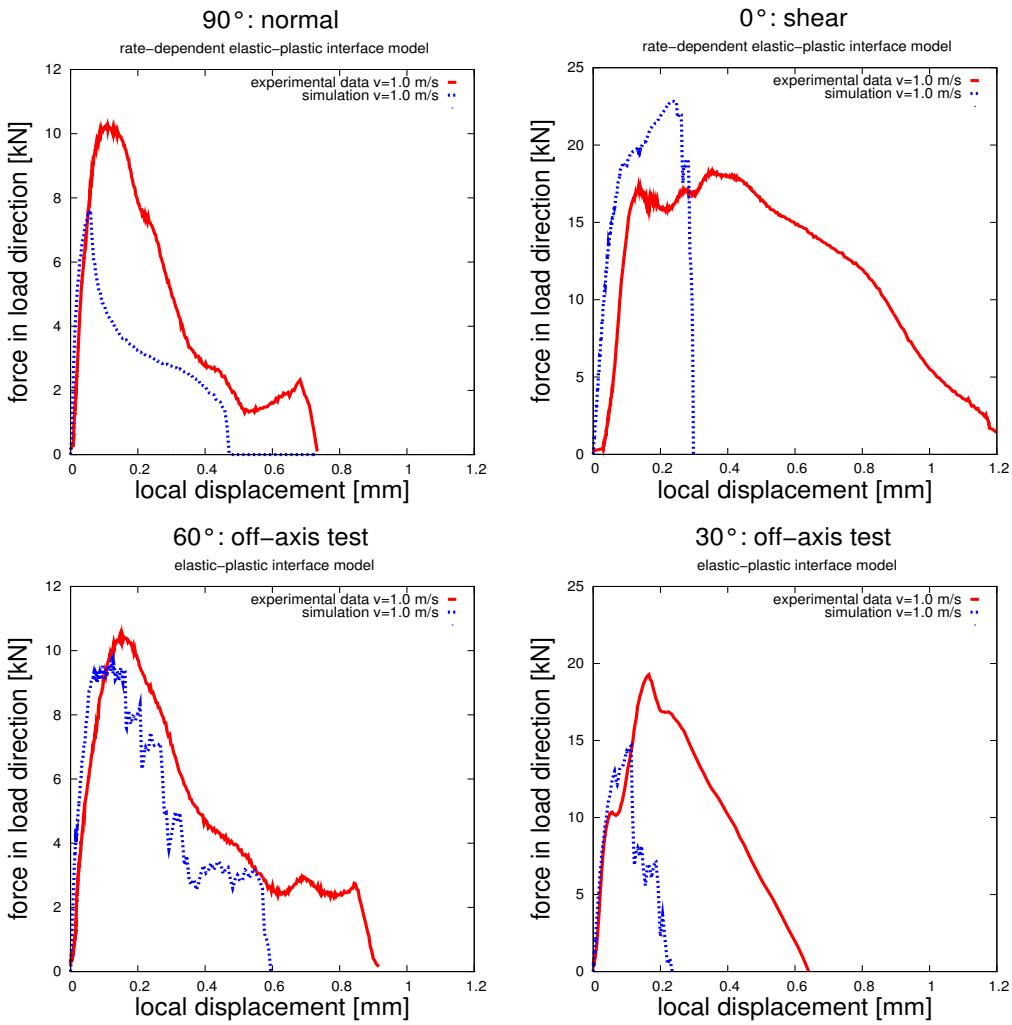

Figure 24. Comparison between experimental data and simulation results with elastic-plastic interface model for velocity $v = 1.0$ m/s: tension and shear test with angles 90° and 0° (top), and off-axis tests with angles 60° and 30° (bottom).

to the direction of the adhesive layer is investigated in Figure 23 by comparing the finite element results of the mixed-mode fracture model to the experimental data. The theoretical solution and the test data are in fairly good agreement.

The results of the numerical analysis with Anand's traction-separation equations, extended to rate-dependency, are graphically represented in Figure 24 for the four loading angles and a velocity of $v = 1.0\,\text{m/s}$ for the separation of the two steel parts. The experimental data are added to the predicted load-displacement curves. In the case of shear loading, the ultimate forces in the experiment and the simulation agree well, but complete failure is detected at a much smaller relative displacement in the analysis with the traction-separation model than in the test. For the case of combined loading, the maximum forces differ more than in the diagrams for shear loading; however, the postcritical parts of the force-displacement curves agree better. A more reliable validation of the test data with the theoretical results is under way. One source of error is the force, measured far away from the adhesive layer, as already mentioned, and compared to the stress resultant of the adhesive layer. In contrast to the quasistatic case the entire test control unit should be modeled from the lower clamping part up to the measurement device for the force in the case of dynamical loading. The internal force, calculated at the position of the measurement cell, must be compared to the experimentally found value.

Another uncertainty is the exact reproduction of equal mechanical properties for the adhesive layer. The liquid glue solidifies under heating of the entire specimen in the successive curing process. It is difficult to guarantee a specified quality of the adhesive bond with strength and fracture strain within a small interval of tolerance.

6. Summary and outlook

The similarities of interface models for the analysis of delamination and fracture of adhesive layers between relatively stiff parts have been outlined and discussed with regard to the validation of simulated results from experimental tests. Two different approaches for the modeling of thin adhesive layers under crash loading conditions have been briefly outlined. An existing mixed-mode fracture model is extended to account for rate-dependent strength and damage and failure of the adhesive bond. Alternatively, an elastic-plastic interface model with a traction-separation equation can be used to describe the effective bonding behavior. Although the interface elements may be massless an estimate of the critical time step for the interface elements can be given.

Comparison of the simulation results and the experimental data demonstrates the model's ability to capture the experimentally observed major effects of rate-dependent damage and failure. The numerical approximation of the experimental data must be still improved, for example, by modeling the entire control unit and by better matching the experimental data. In order to draw conclusions from the simulation at hand for the crashworthiness analysis of vehicle bodies, the finite-element idealization for the KS-II test has to be simplified by reducing the number of elements considerably.

In addition to the development of an application oriented substitute model for the adhesive layer, the determination of adequate constitutive parameters for more effective substitute models is another important task of the current research project. Finally, the models developed so far should be applied to the simulation of a B-pillar in a car body, which will be investigated experimentally by another research partner.

Acknowledgments. We gratefully acknowledge the provision of test data by Prof. Michael Schlimmer, of the University of Kassel, Prof. Ortwin Hahn, of the University of Paderborn, and Dr. Markus Brede, of the Fraunhofer-Institut für Fertigungstechnik und Angewandte Materialforschung (IFAM), Bremen, as well as helpful discussions with Dr. Olaf Hesebeck, also of IFAM.

References

[Aliyu and Daniel 1985] A. A. Aliyu and I. M. Daniel, "Effects of strain rate on delamination fracture toughness of graphite/epoxy", pp. 336–348 in *Delamination and debonding of materials* (Pittsburgh, PA, 1983), edited by W. S. Johnson, ASTM Special Technical Publication **876**, American Society for Testing and Materials, Philadelphia, PA, 1985.

[Andersson and Stigh 2004] T. Andersson and U. Stigh, "The stress-elongation relation for an adhesive layer loaded in peel using equilibrium of energetic forces", *Int. J. Solids Struct.* **41**:2 (2004), 413–434.

[Barenblatt 1959] G. Barenblatt, "The formation of equilibrium cracks during brittle fracture: General ideas and hypotheses. Axially-symmetric cracks", *J. Appl. Math. Mech.* **23**:3 (1959), 622–636.

[Beer 1985] G. Beer, "An isoparametric joint/interface element for finite element analysis", *Int. J. Numer. Methods Eng.* **21**:4 (1985), 585–600.

[Brede and Hesebeck 2005] M. Brede and O. Hesebeck, "Verformungs- und Versagensverhalten von Klebverbindungen: Grundversuche für das Kohäsivzonenmodell", Bericht 1-13-D-2005-09-0, Fraunhofer-Institut für Fertigungstechnik und Angewandte Materialforschung (IFAM), Bremen, for Research Project P676 of the Foundation "Stahlanwendungsforschung", FOSTA (Forschungsvereinigung Stahlanwendung e.V.), Düsseldorf, 2005.

[Brewer and Lagace 1988] J. C. Brewer and P. A. Lagace, "Quadratic stress criterion for initiation of delamination", *J. Compos. Mater.* **22**:12 (1988), 1141–1155.

[Chen et al. 1999] J. Chen, M. Crisfield, A. J. Kinloch, E. P. Busso, F. L. Matthews, and Y. Qiu, "Predicting progressive delamination of composite material specimens via interface elements", *Mech. Compos. Mater. Struct.* **6**:4 (1999), 301–317.

[Dávila and Camanho 2001] C. G. Dávila and P. P. Camanho, "Decohesion elements using two and three-parameter mixed-mode criteria", Technical report 20020010916, NASA Langley Research Center, Hampton, VA, 2001, Available at http://tinyurl.com/NASA-20020010916. Presented at the American Helicopter Society, Hampton Roads Chapter, Structure Specialists' Meeting, Williamsburg, VA, 2001.

[Dugdale 1960] D. S. Dugdale, "Yielding of steel sheets containing slits", *J. Mech. Phys. Solids* **8**:2 (1960), 100–104.

[DYNA 1998] J. O. Hallquist, *LS-DYNA theoretical manual*, Livermore Software Technology Corporation, Livermore, CA, May 1998, Available at http://www.dynamax-inc.com/manuals/theory.pdf.

[DYNA 2006] *LS-DYNA keyword user's manual*, Version 971, Livermore Software Technology Corporation, Livermore, CA, 2006, Available at http://www.dynasupport.com/news/ls-dyna-971-manual-pdf.

[FEAP 2002] R. L. Taylor, *FEAP, a finite element analysis program: theory manual*, Version 7.4, University of California, Berkeley, CA, 2002, Available at http://www.ce.berkeley.edu/feap.

[Fiolka 2007] M. Fiolka, *Theorie und Numerik volumetrischer Schalenelemente zur Delaminationsanalyse von Faserverbundlaminaten*, Ph.D. thesis, Institute of Mechanics, Department of Mechanical Engineering, University of Kassel, 2007, Available at http://tinyurl.com/ThesisMarkFiolka.

[Fiolka and Matzenmiller 2007] M. Fiolka and A. Matzenmiller, "On the resolution of transverse stresses in solid-shells with a multi-layer formulation", *Commun. Numer. Methods Eng.* **23**:4 (2007), 313–326.

[Hahn et al. 1999] O. Hahn, J. R. Kurzok, and M. Oeter, "Prüfvorschrift für die LWF KS-2-Probe", Laboratorium für Werkstoff- und Fügetechnik, Universität Paderborn, 1999.

[Hillerborg et al. 1976] A. Hillerborg, M. Modéer, and P.-E. Petersson, "Analysis of crack formation and crack growth in concrete by means of fracture mechanics and finite elements", *Cem. Concr. Res.* **6**:6 (1976), 773–781.

[Hughes et al. 1979] T. J. R. Hughes, K. S. Pister, and R. L. Taylor, "Implicit-explicit finite elements in nonlinear transient analysis", *Comput. Methods Appl. Mech. Eng.* **17–18**:1 (1979), 159–182.

[Irons 1970] B. M. Irons, "Applications of a theorem on eigenvalues to finite element problems", Technical report CR/132/70, University of Wales, Department of Civil Engineering, Swansea, 1970.

[Jendrny 2005] J. Jendrny, "Grundversuche an Klebstoffen und Klebverbindungen", Bericht 1-11-D-2005-01-0, Laboratorium für Werkstoff- und Fügetechnik (LWF), Universität Paderborn, for Research Project P676 of the Foundation "Stahlanwendungsforschung", FOSTA (Forschungsvereinigung Stahlanwendung e.V.), Düsseldorf, 2005.

[Johnson and Cook 1983] G. R. Johnson and W. H. Cook, "A constitutive model and data for metals subjected to large strains, high strain rates and high temperatures", pp. 541–547 in *Proceedings of the 7th International Symposium on Ballistics* (The Hague, 1983), Royal Institution of Engineers in the Netherlands, The Hague, 1983.

[Mi et al. 1998] Y. Mi, M. A. Crisfield, G. A. O. Davies, and H. B. Hellweg, "Progressive delamination using interface elements", *J. Compos. Mater.* **32**:14 (1998), 1246–1272.

[Pinho et al. 2006] S. T. Pinho, L. Iannucci, and P. Robinson, "Formulation and implementation of decohesion elements in an explicit element code", *Compos. A Appl. Sci. Manuf.* **37**:5 (2006), 778–789.

[Schellekens and de Borst 1993] J. C. J. Schellekens and R. de Borst, "On the numerical integration of interface elements", *Int. J. Numer. Methods Eng.* **36**:1 (1993), 43–66.

[Schlimmer 2003] M. Schlimmer, "Grundlagen zur Berechnung des mechanischen Verhaltens von strukturellen Klebverbindungen des Fahrzeugbaus", pp. 107–133 in *Mechanisches Fügen und Kleben: Tagungsband 10. Paderborner Symposium Fügetechnik* (Paderborn, 2003), edited by O. Hahn, University of Paderborn, Laboratorium für Werkstoff- und Fügetechnik, Paderborn, 2003.

[Schlimmer et al. 2002] M. Schlimmer, O. Hahn, and O.-D. Hennemann, "Methodenentwicklung zur Berechnung und Auslegung geklebter Stahlbauteile für den Fahrzeugbau", Technischer Bericht AiF-Projekt P 593/07/2002, FOSTA (Forschungsvereinigung Stahlanwendung e.V.), Düsseldorf, 2002.

[Schlimmer et al. 2008] M. Schlimmer, A. Matzenmiller, R. Mahnken, O. Hahn, K. Dilger, P. Gumbsch, K. Thoma, and O.-D. Hennemann, "Methodenentwicklung zur Berechnung von höherfesten Stahlklebverbindungen des Fahrzeugbaus unter Crashbelastung", Final report of Research Project P676, FOSTA (Forschungsvereinigung Stahlanwendung e.V.), Düsseldorf, 2008.

[Su et al. 2004] C. Su, Y. J. Wei, and L. Anand, "An elastic-plastic interface constitutive model: application to adhesive joints", *Int. J. Plast.* **20**:12 (2004), 2063–2081.

[Teßmer 2000] J. Teßmer, *Theoretische und algorithmische Beiträge zur Berechnung von Faserverbundschalen*, Ph.D. thesis, Leibniz Universität Hannover, Institut für Baumechanik und Numerische Mechanik, 2000.

[Tvergaard and Hutchinson 1994] V. Tvergaard and J. W. Hutchinson, "Toughness of an interface along a thin ductile layer joining elastic solids", *Philos. Mag. A* **70**:4 (1994), 641–656.

[Tvergaard and Hutchinson 1996] V. Tvergaard and J. W. Hutchinson, "On the toughness of ductile adhesive joints", *J. Mech. Phys. Solids* **44**:5 (1996), 789–800.

[Whitcomb 1986] J. D. Whitcomb, "Parametric analytical study of instability-related delamination growth", *Compos. Sci. Technol.* **25**:1 (1986), 19–48.

Received 23 Jan 2008. Accepted 26 Aug 2009.

ANTON MATZENMILLER: amat@ifm.maschinenbau.uni-kassel.de
Institute of Mechanics, Department of Mechanical Engineering, University of Kassel, Mönchebergstraße 7, 34109 Kassel, Germany

SEBASTIAN GERLACH: sebastian.gerlach@gmx.de
Institute of Mechanics, Department of Mechanical Engineering, University of Kassel, Mönchebergstraße 7, 34109 Kassel, Germany

MARK FIOLKA: Mark_Fiolka@gmx.de
Institute of Mechanics, Department of Mechanical Engineering, University of Kassel, Mönchebergstraße 7, 34109 Kassel, Germany

JOURNAL OF MECHANICS OF MATERIALS AND STRUCTURES
Vol. 5, No. 2, 2010

COMPUTATIONAL STUDIES OF COLLAGEN FIBRIL BIOMINERALS USING A VIRTUAL INTERNAL BOND MODEL WITH EXTRINSIC LENGTH SCALE

GANESH THIAGARAJAN AND KAVITA DESHMUKH

Mineralized type-I collagen fibrils are made up of mineral hydroxyapatite and type-I collagen and are known to have good mechanical properties. Hydroxyapatite by itself is stiffer and collagen is relatively weaker. The development of a multiscale virtual internal bond model (VIB) used to model the material behavior and failure of such biocomposites was described in an earlier paper by the authors. An explicit finite element based framework using a two parameter fracture-constitutive VIB model, with an extrinsic length scale, was used in this study.

The model used in this study is a nano sized dahlite mineral crystal commonly found in collagen fibrils. Two important computational implementation characteristics are presented here; namely the effect of a material parameter used in the VIB model and the effect of thickness of the material at the nanoscale on the failure behavior. The effect of the thickness is studied in order to demonstrate the extrinsic length scale capability of the VIB model at nano length scales.

1. Introduction

Recent research in biomedical engineering has shown evidence that the growth and development of biological tissues is also related to the mechanical loadings on and history of the tissue. Many types of biological materials, such as bone, exhibit a hierarchical structure consisting of several levels [Katz 1976; 1980; Weiner and Wagner 1998]. The mineralized collagen fibril is one of the fundamental constructs of bone, dentin, and mineralized tendons. There are three major components of a mineralized collagen fibril; the collagen molecule, minerals, and water [Weiner and Wagner 1998]. The proportion of the three components varies for different types of tissues. The collagen molecule, which is the major protein component in the fibrils, is predominantly made of type-I collagen. The triple helical structure of the collagen molecule has an average diameter of 1.23 nm and is about 300 nm long [Weiner and Traub 1992]. The mineral component of the mineralized collagen fibril in bone consists of plate-shaped crystals of carbonated apatite [Weiner and Traub 1992]. The apatite crystals are also known as dahlite and are known to be 10 nm wide and 0.61 nm thick [Landis et al. 1996]. The diameter of the mineralized collagenous fibril, at the next hierarchical level, is of the order of 80–100 nm.

The physical structure of mineralized collagenous fibril is complex and many forms have been proposed. Apatite crystals are arranged in parallel arrays in a collagenous framework to form mineralized collagen fibrils. Orgel et al. [2000; 2001] confirmed that collagen molecules show a quasihexagonal packing in the lateral plane and conform to the Hodge–Petruska quarter stagger model [Petruska and

Keywords: finite element analysis, collagen, biomineralization, nanomechanical behavior, dentin, parametric studies.
Thiagarajan thanks the National Center for Supercomputing Applications (NCSA) for computational resources and was partially funded by the National Science Foundation Grant CMS 748085.

Hodge 1964] in the axial plane, with a periodicity of 67 nm (the D period). The length of the molecule is 4.46 D (300 nm) and there are gap regions of 0.54 D. Each collagen molecule is divided into 4 segments of length D and a fifth segment of length 0.46 D. The 67 nm periodicity of the collagen molecule is made up of a 40 nm hole region and a 27 nm overlap region [Weiner and Traub 1992].

Significant advances in the development of experimental capabilities in recent years have made possible the study of biological tissues at the micro and nano scales. These advances provide the motivation for developing models at these scales and provide a mechanism to validate the models experimentally.

For mineral platelets, the implementation aspects of the scaled finite element (FE) framework in combination with the virtual internal bond (VIB) model have been demonstrated in [Thiagarajan et al. 2007]. The paper outlined a new scaled FE scheme, which facilitated study of the mechanical behavior of mineralized collagen fibrils and their constituents. A two parameter VIB model, set up in an explicit FE environment using ABAQUS, was used in the study. The effect of ABAQUS/Explicit specific parameters, when applied to quasistatic loading, has been studied and presented. The factors include the mass scaling factor (MSF) and scaled time specification (ST) in a scaled FE framework. A good understanding of how the two parameters (MSF and ST) affect the analysis has provided input into the selection of the parameters for further studies. The quasistatic nature of the explicit FE simulations was also studied.

The model used in the study was a nano sized dahlite mineral crystal which is commonly found in collagen fibrils. Two important implementation characteristics were explored: first, the usage of scaled dimensions and material properties at the micro and nano length scales and, second, the scaling of loading time without the loading becoming dynamic in nature. Using energy studies it was shown that the simulations remain quasistatic in nature.

1.1. ***Minerals in collagen fibrils.*** Mineralization processes and the arrangement of minerals in collagen fibrils and fibers are areas of extensive ongoing research [Tong et al. 2003; Chang et al. 2005; Veis 2005]. Eppell et al. [2001] performed atomic force microscopy studies on mature bovine cortical bone mineralites and report that the minerals are plate-like in shape with thickness ranging from 12 to 115 nm (mean 37 nm), width ranging from 27 to 172 nm (mean 64 nm), and length ranging from 43 to 226 nm (mean 90 nm). They also point out that the large mineralites could be located at the outer surface of the fibrils and 98% of the minerals are less than 2 nm thick with mean dimensions of $12\,\text{nm} \times 10\,\text{nm} \times 0.61\,\text{nm}$. Kinney et al. [2003] used a small angle x-ray scattering technique and suggested that the thickness of the mineralite crystals in human teeth, in general, is approximately 5 nm.

1.2. ***Observed mechanical relations at the mineral level.*** In addition to the crystallite dimensions two more important factors influence the mechanical behavior at the fibril level. They are the mineral density in the fibril and the arrangement of mineral particles in the collagen matrix of the fibril [Rho et al. 1998; Weiner and Wagner 1998]. Currey [1990] suggested that as mineralization increases the elastic modulus increases. Mineral crystals in collagen have the effect of increasing the stiffness and fracture stress but reducing the fracture strain [Tong et al. 2003]. For example, the lack of the intrafibrillar minerals results in reduced elastic modulus and hardness of dentin [Kinney et al. 2003; Balooch et al. 2008].

Mineralization geometry models: Mineralization is known to initiate primarily in the gap regions. Hence, the geometric order of the gaps in the lateral direction is important in determining the mineralization pattern and geometry. Two hypotheses of the manner in which the channels are formed are concentric

channel arrangement [Hulmes et al. 1995; Perumal et al. 2008] and a three dimensional packing model that arranges the gaps as lateral channels or holes that are one molecule thick (∼15 Å) and extend an unknown distance in the transverse direction [Weiner and Traub 1992]. Tong et al. [2003] have suggested that the channels run for a distance of at least 10 nm in the transverse direction. Hulmes et al. [1995] have discussed radial packing and order arrangements in collagen fibril and had proposed that the gaps in the collagen fibril run as concentric channels around a central fibril core. Jager and Fratzl [2000] have discussed three possible arrangements of minerals in the fibril, namely, crystals occupying only the gap zones, crystals growing into the overlap zone, and longer crystal sizes (∼100 nm) extending beyond the overlap zone and having a staggered arrangement.

1.3. ***Objectives of the study.*** This paper presents the details of the next steps in the scaled FE study of mineral platelets, namely the effect of various VIB material model parameters and the effect of the mineral geometry. The VIB model, in its present stage, has two parameters — A and B. Parameter A is related to the elastic modulus of the material and has a constant value since the material itself is not being changed. The effect of varying the parameter B on the stresses and failure behavior is studied and presented in this paper. Secondly, the effect of geometry on the mineral crystal behavior is studied by varying the thickness of the mineral platelet and performing scaled FE studies.

The VIB model does not have an intrinsic length scale and consequently an extrinsic length scale must be adopted in order to represent the fracture energy of the material. The extrinsic length scale effect, when the VIB model is implemented in this scaled FE framework, is demonstrated using the thickness studies presented in this paper. The output variables studied are the notch tip stress and the strain values in the loading direction. Failure patterns have also been observed and presented for various combinations of the parameters.

2. Materials and methods

Biocomposites, specifically type-I collagen fibrils, have good mechanical properties. Hence, the overall objective of the research was to develop a new FE based framework by which the mechanical behavior of mineralized collagen fibrils could be studied. Firstly, the nature and issues pertaining to the modeling of nano sized mineral platelets must be addressed followed by the mechanical modeling of tissues that contain only type-I collagen such as the rat tail tendon, the structural model of which is described in [Orgel et al. 2006]; the next step would be to develop models for a collagen fibril, and finally the collagen fibril model would be statistically combined to develop the FE framework for collagen fibers. This paper addresses the implementation issues related to the modeling of a single platelet.

2.1. ***Virtual internal bond (VIB) model basics.*** The VIB model is a multiscale model that combines the behavior at the atomistic and the continuum length scales. In the VIB model [Thiagarajan et al. 2004a; 2004b], the continuum is considered as a spatial distribution of material points at the continuum level, as shown in Figure 1. The material points are represented by the integration points in a FE scheme. Each individual material point is hypothesized to represent collectively the behavior of underlying atoms. At the atomistic length scale the interaction between the atoms is represented by cohesive bonds described by a two body pair potential (see Figure 1), which results in a cohesive type interaction between material points at the continuum level.

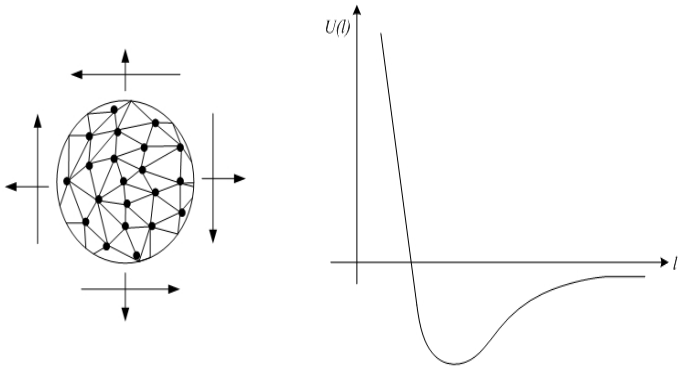

Figure 1. Atomic representation of a material point (left) and potential energy function (right).

The Cauchy–Born rule of crystal elasticity relates the motion of atoms to the continuum deformation and its measures. This rule assumes that the atomic motion, from the undeformed to the deformed configuration, under a homogeneous deformation, can be defined as a unique mapping. At the continuum level, the deformation gradient $\boldsymbol{F}$ defines such a mapping. The interaction at the atomistic level may be described through interaction potentials. In a polycrystalline material, the material behavior is isotropic due to the random orientation of grains. Such behavior can be modeled by a random spatial distribution of cohesive bonds using the VIB model. While biocomposites are a complex material, in this study it is assumed that they can be modeled as material points interconnected by cohesive bonds. The details of the original implementation of the VIB model can be found in [Thiagarajan et al. 2004a; 2004b].

2.2. ***VIB model framework and its suitability.*** The VIB model is described within the framework of hyperelastic continuum mechanics. The initial and the deformed configurations are defined using the Lagrangian coordinates $X = X_I$ and the Eulerian coordinates $x = x(X, t) = x_i(X_I, t)$, respectively. In this paper, capital letter subscripts are used for the initial configuration while lower case subscripts are used for the deformed configuration. In the Lagrangian description the deformation gradient can be expressed as follows:

$$F = \frac{\partial x}{\partial X} \qquad \text{or} \qquad F_{iI} = \frac{\partial x_i}{\partial X_I}, \tag{1}$$

and the Green–Lagrange strain tensor may then be defined as $E = \frac{1}{2}(F^T F - I)$, where I is the second-order identity tensor.

The atomistic bond can be described by a potential energy function $U(l)$ where l is the bond length (see Figure 1). Consider an arbitrary microstructural bond at angles θ and ϕ, where θ is the angle of the bond orientation with respect to the vertical positive 2-axis, and ϕ is the angle in the horizontal plane with respect to the positive 1-axis. The unit vector along this direction is given as

$$\xi = (\sin\theta\cos\phi, \sin\theta\sin\phi, \cos\theta)$$

with respect to the undeformed configuration. The stretch of this bond can be related to the continuous deformation as $l = l_o\sqrt{1 + 2\xi_I E_{IJ}\xi_J}$. The macroscopic strain energy density function is derived using

the Cauchy–Born rule as follows, thus linking the two scales:

$$\Phi(E_{IJ}) = \langle U(l) \rangle, \tag{2}$$

where, $\langle\ \rangle$ represents the weighted average with respect to the bond density function D_d and $U(l)$ is the bond potential energy function. Assuming that all bonds have the same initial length l_o, the weighted average is given as

$$\langle \cdots \rangle = \int_0^{2\pi} \int_0^{\pi} \cdots D_d(\theta, \phi) \sin\theta \, d\theta \, d\phi. \tag{3}$$

The term $D_d(\theta, \phi) \sin\theta \, d\theta \, d\phi$ represents the number of bonds per unit volume between the bond angles $(\theta, \theta + d\theta)$ and $(\phi, \phi + d\phi)$.

2.3. ***Constitutive equations and cohesive force law.*** From the strain energy density function Φ given in (2), the symmetric second Piola–Kirchhoff stress S_{IJ} and the elastic modulus C_{IJKL} can be derived as follows:

$$S = \frac{\partial \Phi}{\partial E} \quad \text{or} \quad S_{IJ} = \frac{\partial \Phi}{\partial E_{IJ}}, \qquad C_{IJKL} = \frac{\partial^2 \Phi}{\partial E_{IJ} \partial E_{KL}}. \tag{4}$$

The modulus derived from this potential satisfies the major and minor symmetries,

$$C_{IJKL} = C_{JIKL} = C_{IJLK} = C_{KLIJ},$$

as well as the Cauchy symmetry, $C_{IJKL} = C_{IKJL}$. For isotropic material this results in only one independent elastic constant due to the fact that the Cauchy symmetry is satisfied by the fourth order isotropic elasticity tensor only for the case of $\lambda = \mu$, where λ and μ are the two Lamé's constants. Consequently, the VIB model as used in this work represents a Poisson's ratio of 0.25. The Poisson's ratio of the VIB model meshes well with the analytical modeling effort by Jager and Fratzl [2000] in their development of a mechanical model for mineralized collagen fibrils, wherein they also replaced the anisotropic nonlinear collagen by an effective elastic material with a Poisson's ratio of 0.25, which was also used by Akiva et al. [1998] in their modeling effort.

In order to represent the potential $U(l)$, in this paper the two parameter cohesive force law, as shown in (5), is used:

$$U'(l) = A(l - l_o)e^{-(l-l_o)/B}. \tag{5}$$

$U'(l)$ is the cohesive force and is the derivative of the bond potential energy with respect to the bond length l. The constant A can be related to the material shear modulus by (5) and represents the initial slope of the curve. The parameter B is related to the strain at which the cohesive stress is reached.

2.4. ***VIB and scaled-FE modeling.*** Modeling the behavior of nano structures using traditional finite elements necessitates the usage of material models that appropriately represent the behavior at the nanoscale. Hence, traditional elasticity, plasticity, fracture, and damage based constitutive models may not be suitable. There are a number of requirements. For example, it has been hypothesized [Gao and Ji 2003; Gao et al. 2003] that failure of nanostructural materials is governed by critical surface energy and not necessarily by stress concentrations at crack tips. It is difficult for FE material models to incorporate this feature. In order to address these issues a new framework of a scaled FE modeling effort was presented in [Thiagarajan et al. 2007] by using the scaled material property and dimension (property scaling and dimension scaling) values at the different length scales. Another advantage of dimension scaling is that in simulations using ABAQUS/Explicit, the solution results in reduced clock times for the simulation. It was shown that as length scales decrease the simulation times also decreases.

2.5. ***Geometric and VIB model parametric study.*** To further characterize the mechanical behavior of mineralites, scaled FE studies on specific sized mineral platelets are performed using the VIB material model. A parametric study is conducted using a notched rectangular plate model subjected to uniaxial tensile displacement based loading. The parameters studied were the VIB model parameter B and the thickness of the mineral platelet t.

Parametric variation: The basic model studied is shown in Figure 2 which shows a mineral crystal size of 50 nm $\times$ 25 nm $\times$ t nm. The dimensions chosen for this study are based on the values published in [Weiner and Wagner 1998]. Dahlite crystals can be represented as rectangular plate shaped materials with a length of 50 nm and a width of 25 nm. Transmission electron microscopy and small angle x-ray scattering of these minerals have demonstrated a fairly uniform thickness for these minerals. The thickness varied from 1.5 nm in mineralized tendons to 4 nm for some mature bone types. Although no known measurements exist for the elastic modulus of these minerals extracted from bone, the measured elastic modulus of synthetic powdered carbonated apatite is reported in the same reference as 109 GPa.

Variation of thickness: It was shown in [Thiagarajan et al. 2007] that for a mineral platelet with an elastic modulus of 100 GPa the value of the critical thickness h^* comes to about 30 nm. The critical thickness has been defined as the thickness below which flaws in the material are hypothesized to not affect the failure behavior. However, in this study of dahlite mineral, the crystal thickness of 30 nm is very high and hence is not considered. The values reported in [Weiner and Wagner 1998] have been used as a reference and thus thickness values of 1 nm, 4 nm, and 10 nm have been studied.

2.5.1. *Variation of VIB model parameter B.* The cohesive force law, which represents the interaction between two atoms in a structure, given by Equation (5) for $U'(l)$, has two parameters A and B. The parameter A represents the initial slope of the curve and is directly related to the elastic modulus of the material. The parameter B represents the strain at which the cohesive stress (the maximum stress) is reached. A higher value of B gives a higher cohesive stress value as shown in Figure 3. A higher value

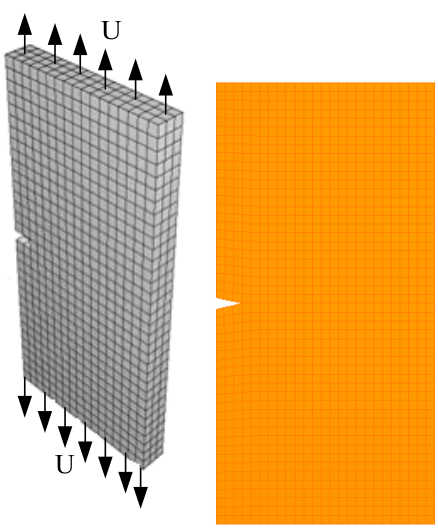

Figure 2. The basic model of mineral crystal with loading shown.

of cohesive stress results in a greater surface energy required for the separation of surfaces in a body. Hence, from the perspective of the failure at the continuum level, it can be inferred that a higher value of B represents a greater surface energy required for separation of two surfaces. Since there are no known experimental measurements of the surface energy γ (N/m^2) for dahlite crystals, a parametric study has been conducted here with different values of B.

As outlined in [Thiagarajan et al. 2007], the value of the parameter B, using a γ value of 1 N/m^2, for a 4 nm thick plate was 0.055. However, due to the uncertainties in the determination of the surface energy and the theoretical failure stress values, the B value is clearly not a deterministic one. Hence, the parametric study conducted here used four different values of B namely, 0.0005, 0.005, 0.05, and 0.1. Figure 3 shows the cohesive force curves for the dahlite material properties:

$$\left(A = \frac{4G}{\pi D_o^2 l_o} = \frac{4 \times 100{,}000\,\text{sPa}}{\pi} \approx 127,000\,\text{sPa}\right),$$

where sPa is a scaled Pascal unit, with different B values. It can be seen that the cohesive stress values, given by $\sigma_{\max} = AB/e$, are equal to 23.6, 236, 2336, and 4672 sPa for B values of 0.0005, 0.005, 0.05, and 0.1 respectively. In Figure 3 the curve representing a B value of 0.0005 is seen as a flat line due to the difference in the order of stress values represented by the y-axis. The cohesive stress values of the crack tip element are presented in a later section. A total of 12 different cases are thus studied, and presented in this paper, using three different thickness and four different B values.

2.5.2. *Loading, material properties, and other issues.* The loading applied in all the twelve simulations in the study presented in this section is a displacement based uniaxial loading in the vertical direction. A specified displacement is given at both ends of the mineral as shown in Figure 2.

The time scaling (ST) concept is used in all the simulations. It was shown in [Deshmukh 2006] that a displacement application time of $1.2e^{-1}$ seconds for the millimeter size model was equivalent to a displacement application time of $1.2e^{-7}$ seconds for the nanometer size model. The scaled time concept

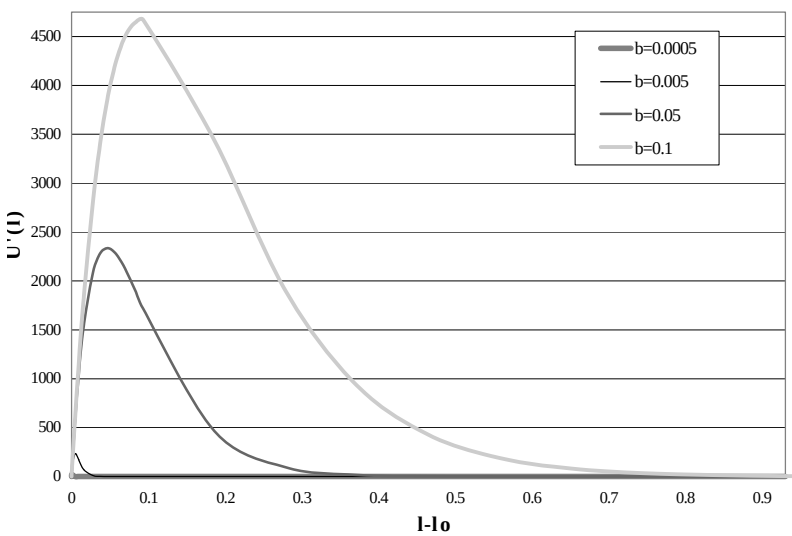

Figure 3. Cohesive force law with different values of B.

demonstrated that the problem does not become a dynamic one as a result of loading applied in a very short time. As the geometric size of the model is in the nanometer range, the time of load application in all these studies is $1.2e^{-7}$ seconds.

The MSF, an ABAQUS/Explicit based parameter, is not a variable in these studies. Based on the results outlined in [Deshmukh 2006] the value chosen here is 10,000. The values of $A = 4G/\pi$ and the density of the mineral are 50.9×10^3 sPa and 3.18×10^{-21} skg/nm^3 (skg = scaled kilogram), respectively.

3. Results and discussions

This section presents a comparison of the stress and strain values at the notch tip for the twelve different case studies. Stress and strain contours and graphical plots of the variation of stress and strain in the element at the tip of the notch are presented.

Notch tip stress variation: The variation of the vertical (axial) stress S_{22} with time for different values of the material parameter B are presented in Figures 4–7. Each graph shows the variation of the stress for the three thickness values for a given value of B. From the graphs, the following observations can be made:

- For B values of 0.1, 0.05, and 0.005, as the thickness increases the failure stress values increases.
- However, for $B = 0.0005$, all the three thicknesses fail at the same time and with the same peak stress value. All three thicknesses fail at $1.0e^{-9}$ seconds with a stress of approximately 64 MPa.

Failure pattern: The failure patterns of the basic model were studied for the thicknesses 1 nm, 4 nm, and 10 nm for the four different B values. The failure patterns for the models have been shown by depicting the axial strain contours at one time step before a total collapse was observed. Figures 8–11 show the axial strain contour and deformed shapes for B values of 0.0005, 0.005, 0.05, and 0.1, respectively. The actual time step of depiction in each case is different.

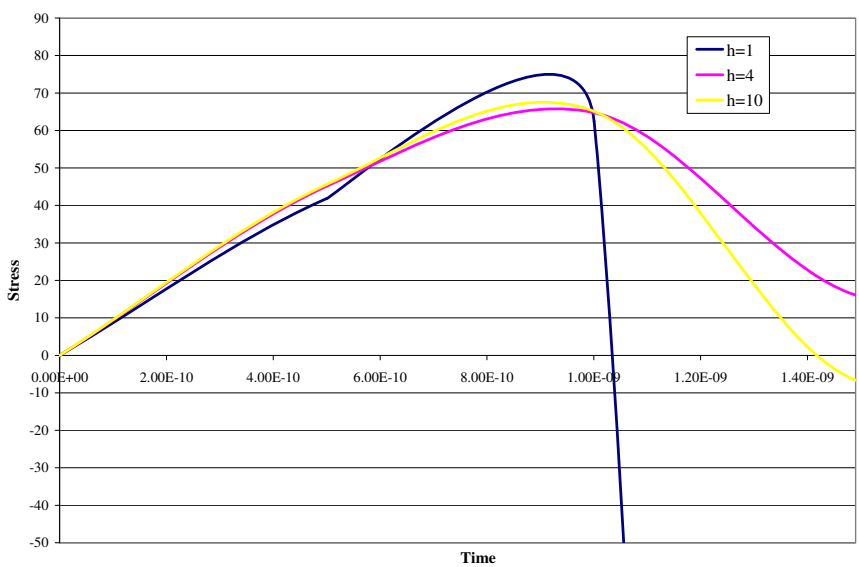

Figure 4. Variation of S_{22} with time for $B = 0.0005$.

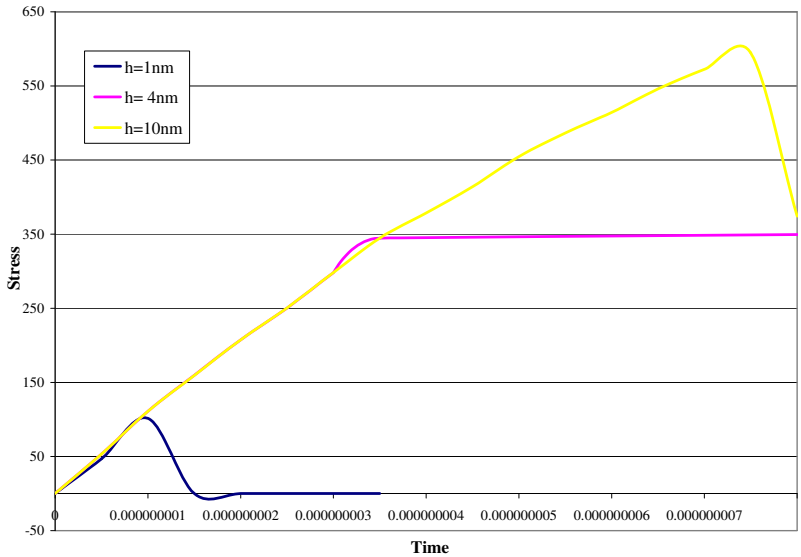

Figure 5. Variation of S_{22} with time for $B = 0.005$.

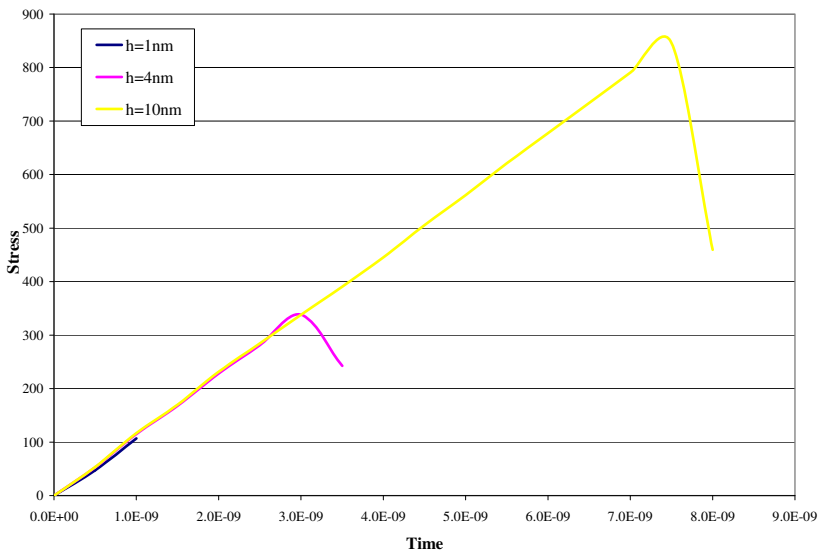

Figure 6. Variation of S_{22} with time for $B = 0.05$.

Failure types: There are two types of failure that can be observed from the contour plots shown. The first type is referred to as a *general failure* and the second type is termed the *stress concentration failure*.

- A general failure is defined as occurring when the whole model tends to collapse. It is proposed here that this type of failure occurs when the stresses in a majority of the elements reach close to the peak or the cohesive stress values at the same time, resulting in a subsequent loss of stiffness in almost all the elements.

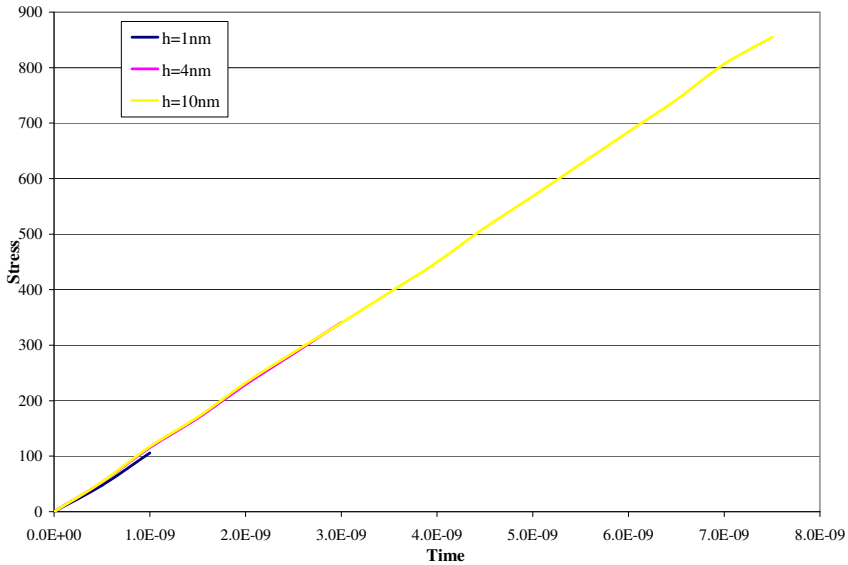

Figure 7. Variation of S_{22} with time for $B = 0.1$.

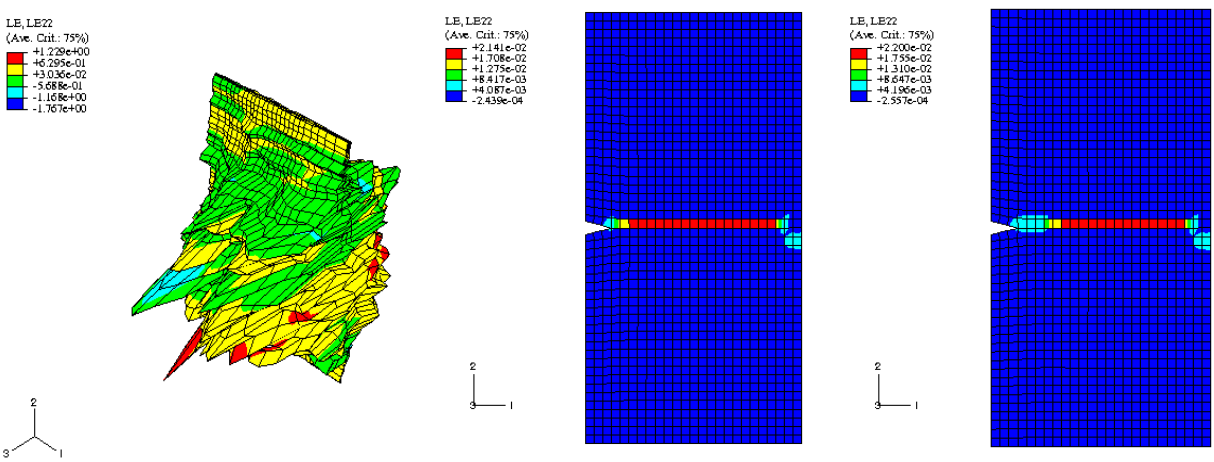

$h = 1$ nm $h = 4$ nm $h = 10$ nm

Figure 8. Strain contours showing the failure pattern for $B = 0.0005$.

- Stress concentration failure or a crack propagation failure is defined as one in which the cohesive stress is reached only at those elements near the crack tip. The rest of the elements in the model are in a state of stress well below the cohesive stress value. Consequently, the subsequent loss of stiffness occurs only in a limited number of elements along which the crack propagation occurs.

Observations: For each B value, it can be seen that as the thickness decreased from 10 nm to 1 nm the failure became a general failure. For thicker platelets, with thicknesses 4 nm and 10 nm, the failure was due to stress concentration at the notch tip. The observations suggest that for thinner platelets the failure is general and not due to the presence of the notch, whereas in thicker platelets the presence of the notch

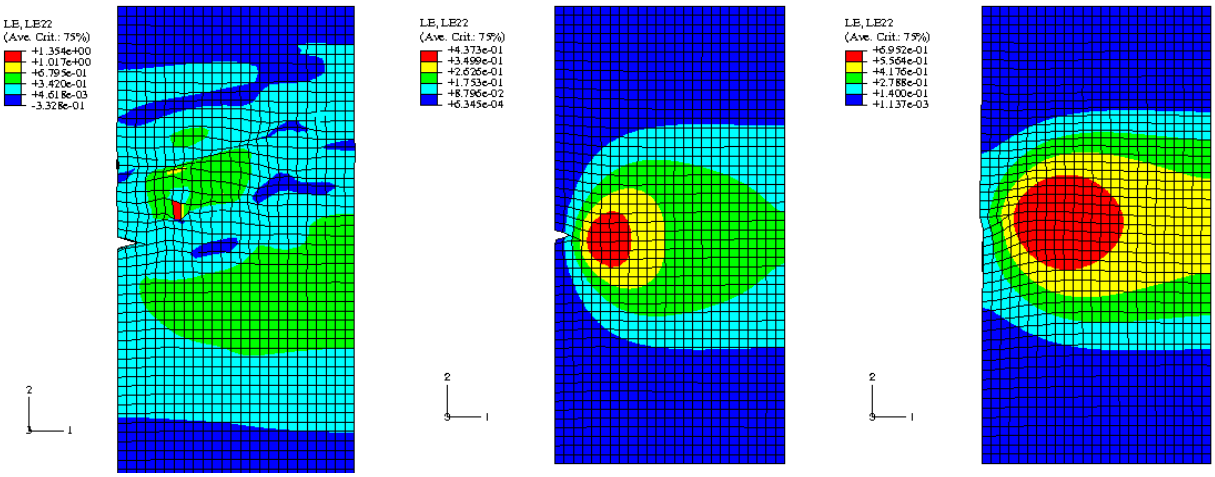

$h = 1$ nm $h = 4.25$ nm $h = 10$ nm

Figure 9. Strain contours showing the failure pattern for $B = 0.005$.

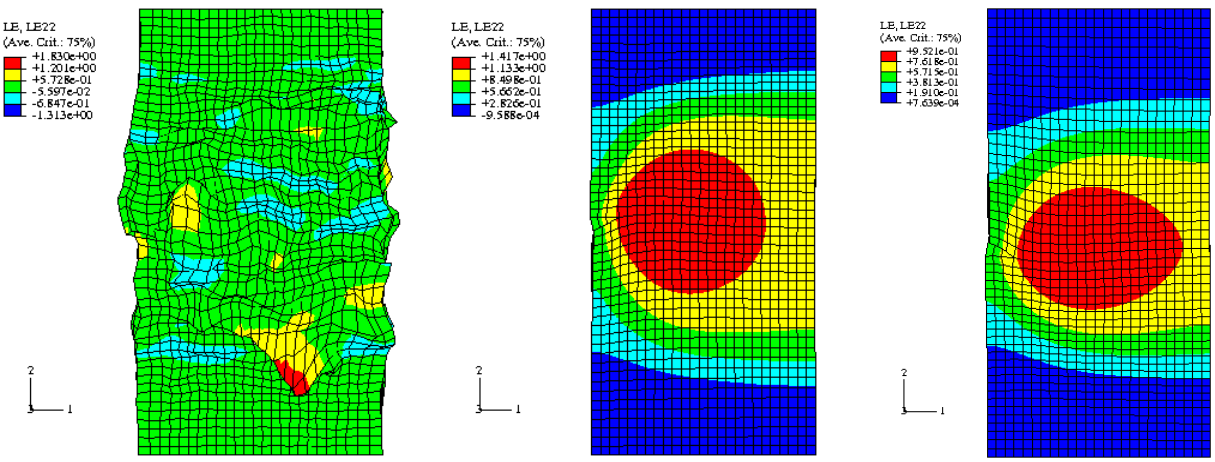

$h = 1$ nm $h = 4.25$ nm $h = 10$ nm

Figure 10. Strain contours showing the failure pattern for $B = 0.05$.

results in a stress concentration type failure of the platelet. The observed failure pattern suggests that, for a particular thickness, the change in the B value does not change the manner in which the platelet fails. The behavior exhibited by the model results lend to the extrinsic length scale of the scaled VIB FE framework.

Stress-strain-time observations: This section presents select results of axial stress and strain and the times of failure for the different parameter values. These results are presented form in Table 1 on the next page. The following observations can be made from that table.

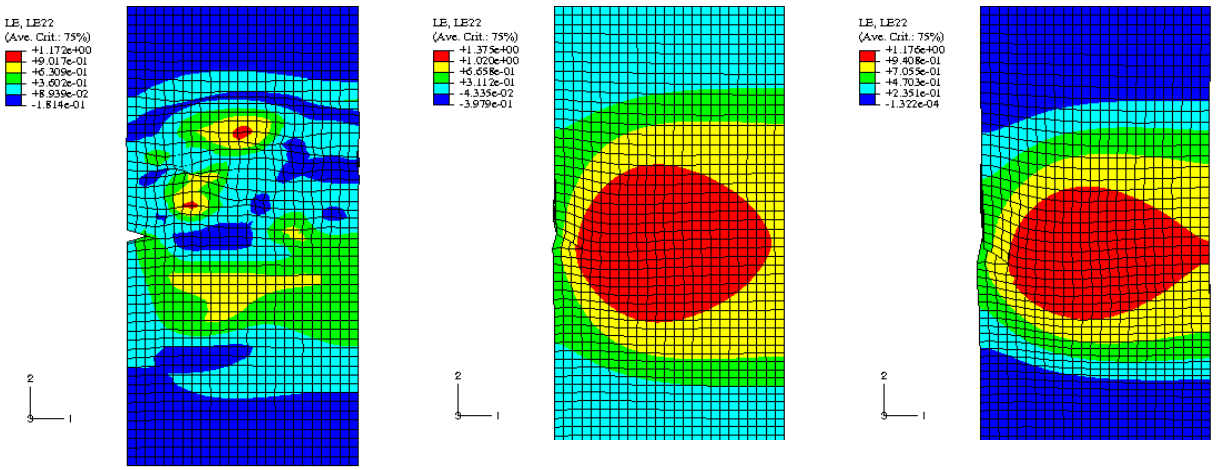

$h = 1$ nm $h = 4.25$ nm $h = 10$ nm

Figure 11. Strain contours showing the failure pattern for $B = 0.1$.

- Specific B value: As thickness increases the stress and the time of failure increases. The increase in the time of failure indicates that the model is capable of taking a higher displacement at the ends before failure occurs.
- Specific thickness value: For a specific thickness as the B value decreases the cohesive stress (failure stress) value decreases as expected.
- For all the thicknesses the failure stress and time for a B value of 0.0005 remained the same, unlike for the other B values. For 1 nm thickness the failure was of a general type while for thicknesses of 4 nm and 10 nm it was of a stress concentration type. This observation appears to indicate an

Thickness	B	Time of failure	Stress at notch tip (MPa)	Strain at notch tip
1 nm	0.0005	1×10^{-9}	62.403	0.000412
	0.005	1×10^{-9}	104.16	0.000359
	0.05	1×10^{-9}	106.732	0.00035
	0.1	1×10^{-9}	105	0.00035
4 nm	0.0005	1×10^{-9}	64.7658	0.000463
	0.005	3.5×10^{-9}	344.594	0.405
	0.05	3.5×10^{-9}	338	0.372
	0.1	3.5×10^{-9}	341	0.0014
10 nm	0.0005	1×10^{-9}	65.1243	0.000472
	0.005	7.5×10^{-9}	594.624	0.0113
	0.05	7.5×10^{-9}	846.09	0.00513
	0.1	7.5×10^{-9}	854.97	0.0114

Table 1. Stress-strain-time of failure with change in thickness.

interesting suggestion that since the surface energy values for the material are not known a priori, a low B value in the range of 0.0005 could be a reasonable value to be chosen for any further studies using minerals such as dahlite.

4. Conclusions

This paper has described a novel methodology, outlined, applied, and demonstrated issues involving scaled finite element virtual internal bond (VIB) modeling in an explicit finite element (FE) framework. The previous study [Thiagarajan et al. 2007] illustrated two FE implementation related characteristics, firstly that scaled properties can be used at the lower levels along with scaled dimensions and secondly that the loading time can be appropriately scaled without the loading becoming a dynamic loading. The scaled time aspect is significant as it allows for computations to be completed in real time which is about three to six orders faster than with traditional frameworks.

The parametric studies done and presented in this paper, using four different B values and three different thicknesses for a total of twelve combinations, suggest that the B values for minerals such as the one studied here should be in the range of 0.0005.

The mesh size of a model plays an important role in the failure behavior of that particular model. The failure of any VIB model is represented by separation of the adjacent nodes near the crack tip which is caused due to localization of the strain in that region. Ji and Gao [2004] showed that for a material with $E = 100\,\text{GPa}$ and $\gamma = 1\,\text{J/m}^2$ with $B = 0.06$ the localization zone is 3.5 nm wide. Since fracture simulation in the VIB model is often contained within one strip of the mesh, the mesh size has to be of the order of the localization zone. In the models that have been studied, the mesh size is of the order of the scale itself. Hence, in the cases of millimeter and micrometer models, as the mesh size is very large compared to the localization zone, the localization zone of nanometer length scale is seen in the model as a high stress zone near the notch tip which in turn results in a crack formation. In the nanometer scale model, since the mesh size is of the same order as the localization zone, the model shows a uniform distribution of the high stress resulting in the possibility that the model can fail anywhere, not necessarily at the notch tip. To have a nanometer mesh size in a millimeter or micrometer model will require prohibitively large computational times for this simulation.

References

[Akiva et al. 1998] U. Akiva, H. D. Wagner, and S. Weiner, "Modelling the three-dimensional elastic constants of parallel-fibred and lamellar bone", *J. Mater. Sci.* **33**:6 (1998), 1497–1509.

[Balooch et al. 2008] M. Balooch, S. Habelitz, J. H. Kinney, S. J. Marshall, and G. W. Marshall, "Mechanical properties of mineralized collagen fibrils as influenced by demineralization", *J. Struct. Biol.* **162**:3 (2008), 404–410.

[Chang et al. 2005] D. Chang, G. Falini, S. Fermani, C. Abbott, and J. Moradian-Oldak, "Supramolecular assembly of amelogenin nanospheres into birefringent microribbons", *Science* **307**:5714 (2005), 1450–1454.

[Currey 1990] J. D. Currey, "Physical characteristics affecting the tensile failure properties of compact bone", *J. Biomech.* **23**:8 (1990), 837–844.

[Deshmukh 2006] K. P. Deshmukh, "Nano finite element modeling of the mechanical behavior of biominerals using a multi-scale (virtual internal bond) model", M.S. Thesis, University of Missouri, Kansas City, 2006.

[Eppell et al. 2001] S. J. Eppell, W. Tong, J. Katz, L. Kuhn, and M. J. Glimcher, "Shape and size of isolated bone mineralites measured using atomic force microscopy", *J. Orthopaedic Res.* **19**:6 (2001), 1027–1034.

[Gao and Ji 2003] H. Gao and B. Ji, "Modeling fracture in nanomaterials via a virtual internal bond method", *Eng. Fract. Mech.* **70**:14 (2003), 1777–1791.

[Gao et al. 2003] H. Gao, B. Ji, I. Jager, E. Artz, and P. Fratzl, "Materials become insensitive to flaws at nanoscale: lessons from nature", *Proceedings of the National Academy of Science* **100**:10 (2003), 5597–5600.

[Hulmes et al. 1995] D. J. Hulmes, T. J. Wess, D. J. Prockop, and P. Fratzl, "Radial packing, order, and disorder in collagen fibrils", *Biophys. J.* **68**:5 (1995), 1661–1670.

[Jager and Fratzl 2000] I. Jager and P. Fratzl, "Mineralized collagen fibrils: a mechanical model with a staggered arrangement of mineral particles", *Biophys. J.* **79**:4 (2000), 1737–1746.

[Ji and Gao 2004] B. Ji and H. Gao, "A study of fracture mechanisms in biological nano-composites via the virtual internal bond model", *Mater. Sci. Eng. A* **366**:1 (2004), 96–103.

[Katz 1976] J. L. Katz, "Hierarchical modeling of compact haversian bone as a fiber reinforced material", *Adv. Bioeng., ASME* (1976), 17–18. New York City.

[Katz 1980] J. L. Katz, "Anisotropy of Young's modulus of bone", *Nature* **283**:5742 (1980), 106–107.

[Kinney et al. 2003] J. H. Kinney, S. Habelitz, S. J. Marshall, and G. W. Marshall, "The importance of intrafibrillar mineralization of collagen on the mechanical properties of dentin", *J. Dental Res.* **82**:12 (2003), 957–961.

[Landis et al. 1996] W. J. Landis, K. J. Hodgens, J. S. Min, J. Arena, S. Kiyonaga, M. Marko, C. Owen, and B. F. McEwen, "Mineralization of collagen may occur on fibril surfaces: evidence from conventional and high-voltage electron microscopy and three-dimensional imaging", *J. Struct. Biol.* **117**:1 (1996), 24–35.

[Orgel et al. 2000] J. P. Orgel, T. J. Wess, and A. Miller, "The in situ conformation and axial location of the intermolecular cross-linked non-helical telopeptides of type I collagen", *Structure* **8**:2 (2000), 137–142.

[Orgel et al. 2001] J. P. R. O. Orgel, A. Miller, T. C. Irving, R. F. Fischetti, A. P. Hammersley, and T. J. Wess, "The in situ supermolecular structure of type I collagen", *Structure* **9**:11 (2001), 1061–1069.

[Orgel et al. 2006] J. P. R. O. Orgel, T. C. Irving, A. Miller, and T. J. Weiss, "Microfibrillar structure of type I collagen in situ", *Proc. Natl. Acad. Sci. USA* **103**:24 (2006), 9001–9005.

[Perumal et al. 2008] S. Perumal, O. Antipova, and J. P. R. O. Orgel, "Collagen fibril architecture, domain organization and triple-helical conformation govern its proteolysis", *Proceedings of the National Academy of Sciences* **105**:8 (2008), 2824–2829.

[Petruska and Hodge 1964] J. A. Petruska and A. J. Hodge, "A subunit model for the tropocollagen macromolecule", *Proceedings of the National Academy of Sciences* **51**:5 (1964), 871–876.

[Rho et al. 1998] J. Y. Rho, L. Kuhn-Spearing, and P. Zioupos, "Mechanical properties and the hierarchical structure of bone", *Med. Eng. Phys.* **20**:2 (1998), 92–102.

[Thiagarajan et al. 2004a] G. Thiagarajan, K. J. Hsia, and Y. Huang, "Finite element implementation of virtual internal bond model for simulating crack behavior", *Eng. Fract. Mech.* **71**:3 (2004), 401–423.

[Thiagarajan et al. 2004b] G. Thiagarajan, Y. Y. Huang, and K. J. Hsia, "Fracture simulation using an elasto-viscoplastic virtual internal bond model with finite elements", *J. Appl. Mech.* (*ASME*) **71**:6 (2004), 796–804.

[Thiagarajan et al. 2007] G. Thiagarajan, K. Deshmukh, Y. Wang, A. Misra, J. L. Katz, and P. Spencer, "Nano finite element modeling of the mechanical behavior of biocomposites using multi-scale (virtual internal bond) material models", *J. Biomed. Mater. Res. A* **83**:2 (2007), 332–344.

[Tong et al. 2003] W. Tong, M. J. Glimcher, J. L. Katz, and S. J. Eppell, "Size and shape of mineralites in young bovine bone measured by atomic force microscopy", *Calcified Tissue* **72** (2003), 592–598.

[Veis 2005] A. Veis, "A window on biomineralization", *Science* **307** (2005), 1419–1420.

[Weiner and Traub 1992] S. Weiner and W. Traub, "Bone structure: from angstroms to microns", *FASEB J.* **6** (1992), 879–885.

[Weiner and Wagner 1998] S. Weiner and H. D. Wagner, "The material bone: structure-mechanical function relations", *Annu. Rev. Mater. Sci.* **28** (1998), 271–298.

Received 7 Nov 2008. Revised 13 Aug 2009. Accepted 17 Aug 2009.

GANESH THIAGARAJAN: ganesht@umkc.edu
School of Computing and Engineering, University of Missouri, Kansas City, MO 64110, United States

KAVITA DESHMUKH: kavita81@gmail.com
School of Computing and Engineering, University of Missouri, Kansas City, MO 64110, United States

JOURNAL OF MECHANICS OF MATERIALS AND STRUCTURES
Vol. 5, No. 2, 2010

THE SIMULATION OF STOCHASTICALLY EXCITED VISCOELASTIC SYSTEMS AND THEIR STABILITY

VADIM D. POTAPOV

An efficient method for the analysis of nonlinear elastic and viscoelastic systems under the action of parametric forces in the form of Gaussian random stationary processes is suggested. The spectral densities of the input random stationary processes are assumed to be in the form of rational functions. The method is based on the simulation of stochastic processes and the numerical solution of differential equations, describing the motion of the system. Considering a sample of solutions, statistical characteristics of trajectories can be found. The effect of the parameters of the input random processes on the indicated statistical characteristics is investigated. Special attention is devoted to investigation of the stability of the unperturbed motion of elastic and viscoelastic systems. To analyze the stability of the unperturbed motion of the system the motion due to perturbations of the initial conditions is considered. The method of the stability investigation is based on the numerical solution of differential equations, describing the perturbed motion of the system, and the calculation of the top Lyapunov exponents. The method results in the estimation of the stability with respect to statistical moments of different orders. In some cases the superposition of a stochastic noise on the deterministic periodic excitation can have a stabilizing effect on the motion of elastic and viscoelastic systems.

1. Introduction

The behavior of nonlinear mechanical systems subjected to random loads in the form of random stationary processes, was considered in [Dimentberg 1980; 1988; Simiu 2002], which contain an extensive review of investigations in the indicated direction. As a rule, these investigations were developed under various restrictions imposed on the character of the stationary processes. For example, sometimes these processes were assumed as narrow-band; in this case the method used for the solution was similar to the method of the harmonic balance. In other cases the level of the nonlinearity was assumed to be small, and then the method of stochastic averaging was applied [Dimentberg 1980; 1988]. For the estimation of the reliability of nonlinear systems in [Simiu 2002] the Melnikov stochastic process was used.

Some questions on the stability of elastic and viscoelastic systems, subjected to random loads in the form of random stationary processes, were considered in [Potapov 1999]. A numerical method was suggested for nonlinear problems using the method of canonical expansions of stationary processes. The present paper is devoted to a numerical analysis of nonlinear oscillation of viscoelastic systems under stochastic excitation in the form of a Gaussian stationary process with a rational spectral density. The analysis is based on numerical simulation of the input stationary process, on a numerical solution of

Keywords: stochastics, viscoelasticity, nonlinear oscillations, stability, simulation, top Lyapunov exponents, random stationary processes.

Financial support by the Russian Foundation of Basic Researches under grant N 09-01-00267 is gratefully acknowledged by the author.

the differential equations which describe the motion of the system, and, in the case of the stability investigation of this motion, on the calculation of the top Lyapunov exponent. In the example of a plate subjected to a random stationary load acting in the middle plane, peculiarities in the application of the proposed method are considered. Particular attention is devoted to the interaction of deterministic periodic and stochastic excitations from the stability point of view of the motion. It is shown that in some cases the superposition of a colored noise can have a stabilizing effect on an unstable deterministic system.

2. Statement of the problem

The dynamic behavior of a viscoelastic system with regard to finite deflections, provided that strains are small, is described by a system of nonlinear integrodifferential equations with partial derivatives. Using different methods, for example, the method of finite elements, the method of finite differences, the Bubnov–Galerkin method, et cetera, this system can be replaced by a system of ordinary integrodifferential equations. The relaxation kernels of the material are assumed as degenerate. This means that they can be presented in the form

$$R(t,\tau)=\sum_{i=1}^{m} f_i(t)\varphi_i(\tau).$$

We increase the dimensions of the phase space and replace the system of integrodifferential equations with a system of nonlinear first-order differential equations:

$$\dot{z}=\boldsymbol{F}\big(z,\alpha(t),t\big), \tag{1}$$

where z is the vector of unknowns, $\alpha(t)=\alpha^*(t)+\alpha^o(t)$, $\alpha^*(t)$ is a deterministic function, $\alpha^o(t)$ is a random stationary process, and t is the time. A dot indicates the derivative with respect to time t.

The random stationary process $\alpha^o(t)$ is assumed to be a Markov process, which is a result of passing the Gaussian white noise through a linear filter of the m-th order. That is, the function $\alpha^o(t)$ is the solution of the stochastic differential equation

$$\alpha^{o^{(m)}}+d_1\alpha^{o^{(m-1)}}+\cdots+d_{m-1}\dot{\alpha}^o+d_m\alpha^o=h\xi(t), \tag{2}$$

where d_k $(k=1,2,\ldots,m)$ and h are constants, and $\xi(t)$ is the Gaussian white noise.

For the analysis of the behavior of the system the method of statistical simulation is used, which is based on the numerical solution of differential equations (by the Runge–Kutta method) in combination with a numerical method of obtaining the realizations of random stationary processes.

3. Oscillations of the plate under the action of a random load in the middle of the plane

As an illustration of the present method let us consider transverse oscillations of a thin rectangular viscoelastic plate hinged along all edges and subjected to a uniformly distributed load applied to two opposite edges in the plate plane (see Figure 1). It is assumed that the opposite edges remain parallel to each other during the motion of the plate.

If the material of the plate is isotropic and the Poisson coefficient is constant with respect to time μ, then the equations of the plate oscillations for the case of finite deflections of von Karman type is written

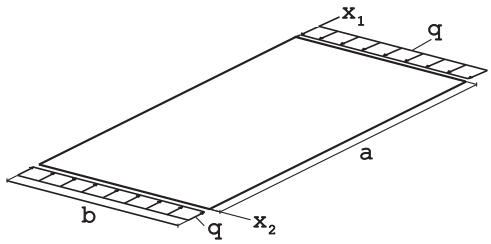

Figure 1. The rectangular plate under loads applied to the middle of the plane.

in the following form [Vol'mir 1967]:

$$D(1-\boldsymbol{R})\nabla^4 w - h(\Phi_{,22}w_{,11} - 2\Phi_{,12}w_{,12} + \Phi_{,11}w_{,22}) = -\gamma\,\ddot{w} - k\dot{w}, \tag{3}$$

$$\frac{1}{E}\nabla^4\Phi = (\boldsymbol{I}-\boldsymbol{R})(w_{,12}^2 - w_{,11}w_{,22}), \tag{4}$$

where w is the deflection of the plate, Φ is the function of stresses, acting in the middle of the surface of the plate, h is the thickness of the plate, γ is the mass per unit area of the plate, k is the damping coefficient, ∇^4 is the biharmonic operator, E is the Young modulus, and $\boldsymbol{R}$ is the relaxation operator.

If the form of the plate is close to square and the initial conditions have the form

$$w(t,x_1,x_2)\big|_{t=0} = f_0 \sin\frac{\pi}{a}x_1 \sin\frac{\pi}{b}x_2, \qquad \dot{w}(t,x_1,x_2)\big|_{t=0} = v_0 \sin\frac{\pi}{a}x_1 \sin\frac{\pi}{b}x_2, \tag{5}$$

then the deflection of the plate can be found in a similar form:

$$w(t,x_1,x_2) = f(t)\sin\frac{\pi}{a}x_1 \sin\frac{\pi}{b}x_2. \tag{6}$$

Really, even for the initial conditions given by (5), the solution of (3) and (4) has a more complicated form. However, since we focus on the qualitative aspect of the problem rather than the quantitative one, we restrict the consideration to the first approximation of the function $w(t,x_1,x_2)$, given by (6).

Substituting (6) in the right-hand side of (4) and solving it with respect to the function Φ, we obtain

$$\Phi(t,x_1,x_2) = \frac{1}{32}E(1-\boldsymbol{R})f^2(t)\left(\frac{a^2}{b^2}\cos\frac{2\pi}{a}x_1 + \frac{b^2}{a^2}\cos\frac{2\pi}{b}x_2\right) - \frac{qx_1^2}{2h}. \tag{7}$$

It is not difficult to prove that the boundary conditions concerning the parallelism of opposite edges are fulfilled [Potapov 1999].

To find the plate deflection amplitude $f(t)$ let us use the Bubnov–Galerkin method. To this end we multiply both sides of (3) by $\sin(\pi/a)x_1 \sin(\pi/b)x_2$ and integrate the resultant relation over the plate area. Then we obtain the integrodifferential equation

$$z'' + 2\varepsilon z' + (1-\boldsymbol{R})z - \alpha z + \frac{3}{4}(1-\mu^2)\frac{a^4+b^4}{(a^2+b^2)^2}z(1-\boldsymbol{R})z^2 = 0. \tag{8}$$

Here $z = f/h$, $2\varepsilon = k/(\gamma\omega)$, and ω is the fundamental frequency of plate oscillations, given by

$$\omega^2 = \frac{D}{\gamma}\left(\frac{\pi^2}{a^2}+\frac{\pi^2}{b^2}\right)^2, \qquad \alpha = \frac{\pi^2 q}{Db^2}\left(\frac{\pi^2}{a^2}+\frac{\pi^2}{b^2}\right)^{-2},$$

where the prime denotes the derivative with respect to dimensionless time $t_1 = \omega t$.

If $a = b$ and $\mu = 0.3$, then Equation (8) acquires the form

$$z'' + 2\varepsilon z' + (1 - \boldsymbol{R})z - \alpha z + 0.34125z(1 - \boldsymbol{R})z^2 = 0. \tag{9}$$

Suppose that the material of the plate is standard. Then the relaxation kernel $R(t - \tau)$ has an exponential form, $R(t - \tau) = \chi L e^{-\chi(t-\tau)}$, where χ and L are constant.

We introduce the new variables

$$z_1 = z, \qquad z_2 = z', \qquad z_3 = \int_0^t \chi L e^{-\chi(t-\tau)} z(\tau)\, d\tau, \qquad z_4 = \int_0^t \chi L e^{-\chi(t-\tau)} z^2(\tau)\, d\tau,$$

and we replace the integrodifferential equation (9) by the system of first-order differential equations

$$\begin{aligned} z_1' &= z_2, & z_2' &= -2\varepsilon z_2 - (1 - \alpha)z_1 + z_3 - 0.34125 z_1(z_1^2 - z_4), \\ z_3' &= \chi L z_1 - \chi z_3, & z_4' &= \chi L z_1^2 - \chi z_4. \end{aligned} \tag{10}$$

The solution of these equations should satisfy the initial conditions

$$z_1(0) = \frac{f_0}{h}, \qquad z_2(0) = \frac{v_0}{h}, \qquad z_3(0) = z_4(0) = 0.$$

Let us express the function $\alpha(t)$ in the form of the sum $\alpha(t) = \alpha_0 + \alpha_1 \sin \omega t + \alpha^o(t)$, where α_0 and α_1 are deterministic constants, ω is the frequency of the deterministic periodic part of the load, $\alpha^o(t)$ is a stationary random process with zero mathematical expectation, $\langle \alpha^o(t) \rangle = 0$, and the correlation function

$$K(t_1 - t_2) = \sigma^2 \exp(-\delta |t_1 - t_2|) \left[\cos \theta (t_1 - t_2) + \frac{\delta}{\theta} \sin \theta (t_1 - t_2) \right], \tag{11}$$

where σ^2 is the dispersion of the process and δ and θ are parameters, characterizing the scale of the correlation and the frequency of the implicit periodicity respectively. Angle brackets denote the operation of the mathematical expectation.

The spectral density $S(\omega)$ in this case has the form

$$S(\omega) = \frac{2\sigma^2 \delta}{\pi} \frac{\delta^2 + \theta^2}{(\omega^2 - \theta^2 - \delta^2)^2 + 4\delta^2 \omega^2}.$$

The considered random process is differentiable.

Equation (2) is written in the following way [Vol'mir 1967; Shalygin and Palagin 1986]:

$$\ddot{\alpha}^o - a_2 \dot{\alpha}^o - a_1 \alpha^o = b_2 \sigma \xi(t), \tag{12}$$

where $a_1 = -(\delta^2 + \theta^2)$, $a_2 = -2\delta$, $b_2 = \sqrt{2(\delta^2 + \theta^2)}$, and $\xi(t)$ is the Gaussian white noise, simulated by the expression

$$\xi(t) = \sqrt{\frac{2\delta}{\Delta}} \epsilon_\Delta(t).$$

Here $\epsilon_\Delta(t) = \epsilon_i$, and $t \in [i\Delta, (i+1)\Delta]$, where ϵ_i is a sequence of normally distributed uncorrelated numbers with zero mean value and $\langle \epsilon^2 \rangle = 1$; $\Delta = \Delta t$ is the time step.

Let us consider some results for the viscoelastic plate, obtained at $\varepsilon = 0.1$, $L = 0.5$, $\chi = 0.1$, $\delta = 0.5$, $\theta = \omega = 1.4$, and $\Delta t = 0.1$ by means of the numerical solution of (10) by the fourth-order Runge–Kutta

method. The number of increments n and initial conditions in all cases were assumed to be the same, namely, $n = 10^4$ and $z_1(0) = 1.0$, $z_2(0) = z_3(0) = z_4(0) = 0$.

Figure 2 shows the most typical trajectories of the plate motion on the phase plane $z_1 \sim z_2$. For each of these trajectories the limits of the variation of values z_1 and z_2 are indicated. These results can be explained as follows.

If the load is deterministic and constant with time, then the quantity z, corresponding to an equilibrium state of the plate, can be found from the cubic equation

$$(1 - \alpha_0)z + 0.34125z^3 = 0. \tag{13}$$

If $\alpha_0 < 1$, then this equation has only one root, $z = 0$, which corresponds to the unbent equilibrium configuration of the plate, and this state is known to be stable. If $\alpha_0 > 1$, then (13) has three roots,

$$z_{(1)} = 0, \qquad z_{(2),(3)} = \pm\sqrt{\frac{\alpha_0 - 1}{0.34125}}.$$

It can be shown that the solution $z_{(1)}$ is unstable and nontrivial while solutions $z_{(2)}$ and $z_{(3)}$ are stable. The quantity $\alpha_0 = 1$ is critical for an elastic plate.

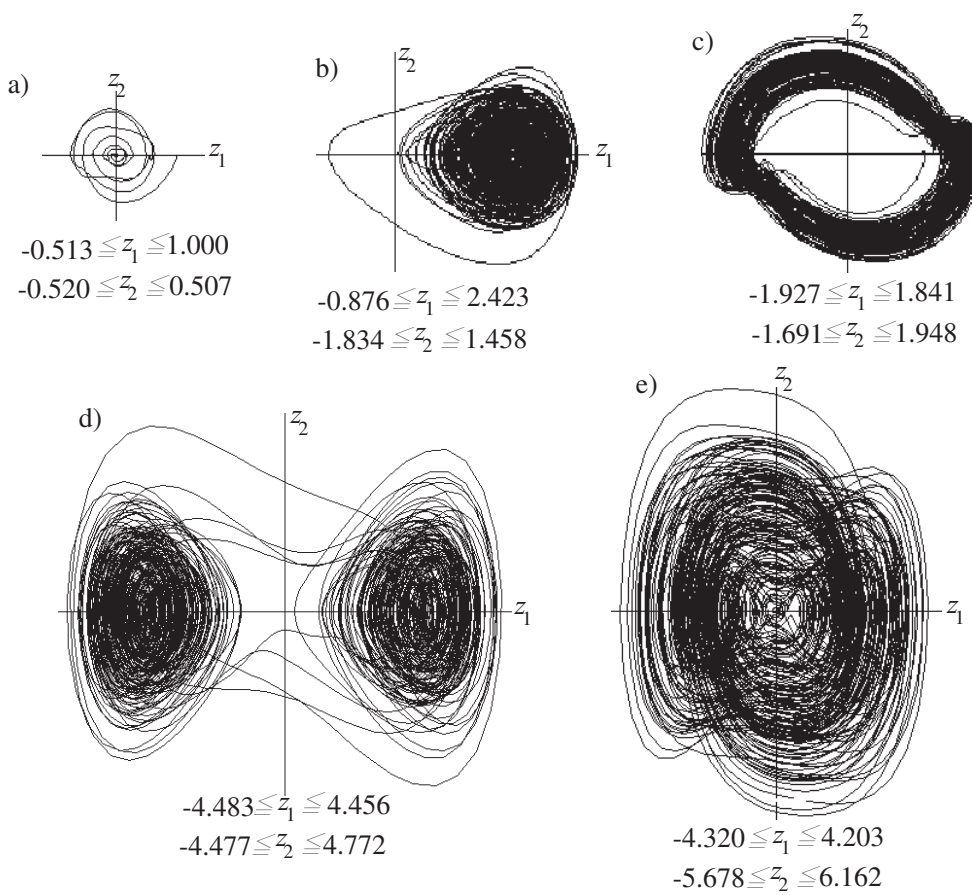

Figure 2. Trajectories of the viscoelastic plate motion in the phase plane.

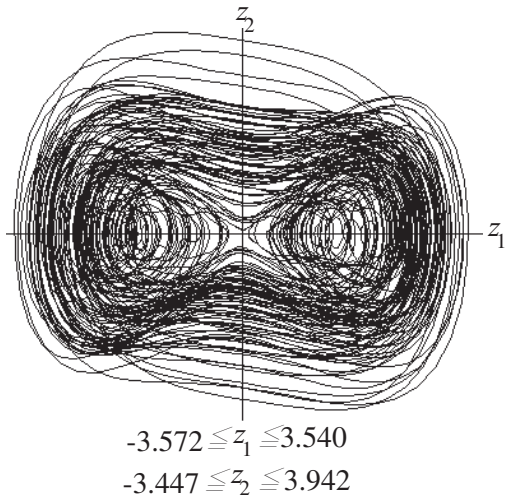

Figure 3. The trajectory of the elastic plate motion in the phase plane.

The situation is similar in a viscoelastic plate, but in this case the critical value of the parameter α_0 is equal to $1 - \bar{R}$, where

$$\bar{R} = \int_0^\infty R(\theta)\, d\theta.$$

The results for the dynamic (deterministic or stochastic) statement of the problem are similar. Indeed, if parameters α_0, α_1, and σ are sufficiently small, then, obviously, oscillations are performed in the neighborhood of the trivial equilibrium state. This statement is confirmed by the plots in Figure 2a, obtained at $\alpha_0 = 0$, $\alpha_1 = 1.0$, and $\sigma^2 = 0.09$, and dampened with time.

But if the same parameters α_0, α_1, and σ are sufficiently large, then the plate motion becomes much more diverse. The plate can oscillate in the neighborhood of a certain equilibrium (see Figure 2b at $\alpha_0 = 1.0$, $\alpha_1 = 0$, and $\sigma^2 = 0.04$) or jump between two equilibria (see Figure 2c at $\alpha_0 = 0.5$, $\alpha_1 = 1.0$, and $\sigma^2 = 0.01$; and Figure 2d at $\alpha_0 = 0.5$, $\alpha_1 = 0.5$, and $\sigma^2 = 0.25$); moreover, in some cases the plate motion is chaotic (see Figure 2e at $\alpha_0 = 1.0$, $\alpha_1 = 1.0$, and $\sigma^2 = 0.25$). It should be said that in such cases with increasing time the solution of the nonlinear equations becomes steady-state and different initial conditions may lead to different steady-state solutions.

The effect of the viscous properties of the material on the behavior of the plate can be estimated with help of the trajectory, shown in Figure 3, obtained with the same input data and the same realization of the process $\alpha^o(t)$, as in Figure 2d, and of the charts of variation deflections z_1 with time (see Figure 4), which correspond to the same elastic and viscoelastic plates. In Figure 5 the histograms of the value z_1 are shown corresponding to the same input data and obtained at $n = 10^5$ ($\langle z_1 \rangle$ and σ_1 are the mean value and the mean square scattering of z_1, respectively). As seen the viscous properties of the material lead to the noticeable modification of the trajectories on the phase plane and with time. A more detailed analysis of these trajectories shows that the motion of the elastic plate is chaotic (unstable) while that of the viscoelastic plate is asymptotically stable. These histograms have the same form for different times if they are far enough from initial time $t = 0$; this fact verifies the stationary state of the plate motion.

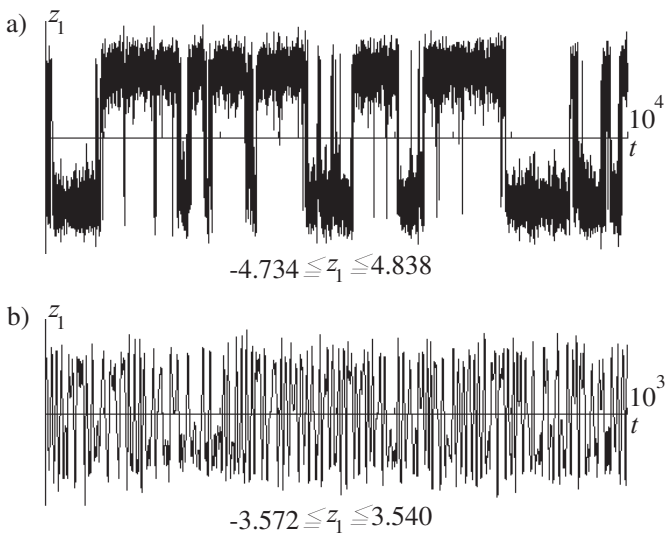

Figure 4. Realizations of the generalized displacement $z_1 = f(t)$ in the (a) viscoelastic and (b) elastic plates.

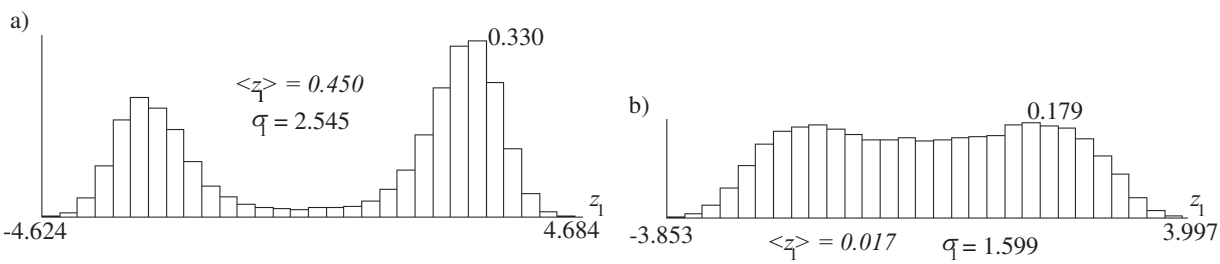

Figure 5. Histograms of the value z_1 for the (a) viscoelastic and (b) elastic plates.

4. Stability of the unperturbed motion of the system

For the analysis of the stability of the unperturbed motion of the system, described by Equation (9), let us consider the perturbed motion, caused by perturbations of the initial conditions.

In the case of perturbed motion the solution of (1) has the form $\boldsymbol{y} = \boldsymbol{z} + \delta\boldsymbol{z}$, that is,

$$\dot{\boldsymbol{y}} = \boldsymbol{F}\big(\boldsymbol{y}, \alpha(t), t\big), \tag{14}$$

where $\boldsymbol{z} = \{z_1, z_2, \ldots, z_n\}^T$ is the vector of unknowns, corresponding to the unperturbed motion of the system; the vector $\boldsymbol{y} = \{y_1, y_2, \ldots, y_n\}^T$, corresponding to the perturbed motion; and the vector of perturbations $\delta\boldsymbol{z} = \{\delta z_1, \delta z_2, \ldots, \delta z_n\}^T$. Let us expand the right-hand side of (14) by the Taylor series in the neighborhood of the solution $\boldsymbol{z}(t)$:

$$\boldsymbol{F}\big(\boldsymbol{z} + \delta\boldsymbol{z}, \alpha(t), t\big) = \boldsymbol{F}\big(\boldsymbol{z}, \alpha(t), t\big) + \boldsymbol{F}'\big(\boldsymbol{z}, \alpha(t), t\big)\delta\boldsymbol{z} + \cdots .$$

Restricting this expansion to the two first terms and taking into account (1), we obtain a linearized equation:

$$\delta\dot{\boldsymbol{z}} = \boldsymbol{F}'\big(\boldsymbol{z}, \alpha(t), t\big)\delta\boldsymbol{z}. \tag{15}$$

The solution of the equation should satisfy the initial condition $\delta\boldsymbol{z}(0) = \delta\boldsymbol{z}_0$, $\delta\boldsymbol{z}_0 = \{\delta z_{01}, \delta z_{02}, \ldots, \delta z_{0n}\}^T$.

For the estimation of the stability of the system the method of top Lyapunov exponents is used, which is calculated for each pair consisting of a realization $\alpha(t)$ and the corresponding realization of the process $z(t)$. Further, the stability is treated as stability with respect to the statistical moments.

- The solution $\boldsymbol{\delta z}(t) \equiv 0$ is called p-stable if, for any $\varepsilon > 0$, a $\Delta > 0$ can be found such that at $t \geq 0$ and $|\delta z_i(0)| < \Delta$ $(i = 1, 2, \ldots, n)$, where n is the number of first-order differential equations in (15) and $|\langle \delta z_i^p(t)\rangle| < \varepsilon$.
- The solution $\boldsymbol{\delta z}(t) \equiv 0$ is called asymptotically p-stable if it is p-stable and, in addition, for a small enough $|\delta z_i(0)|$ $(i = 1, 2, \ldots, n)$,

$$\lim_{t\to\infty} \big|\langle \delta z_i^p(t)\rangle\big| = 0.$$

At $p = 1$ stability takes place in the mean (with respect to the mathematical expectation), and at $p = 2$ there is stability in the mean square.

The growth of the vector $\boldsymbol{\delta z}(t)$ can be estimated with the help of the top Lyapunov exponent λ, which is defined by the expression

$$\lambda = \lim_{t\to\infty} \frac{1}{t} \ln \frac{\|\boldsymbol{\delta z}(t)\|}{\|\boldsymbol{\delta z}(0)\|},$$

where $\|\boldsymbol{\delta z}(t)\|$, $\|\boldsymbol{\delta z}(0)\|$ is the norm of the vector $\boldsymbol{\delta z}(t)$ in a Euclidean space at time t and at initial time $t = 0$.

The value λ can be found numerically with help of the method proposed in [Benettin et al. 1980a; Benettin et al. 1980b]. With this purpose in mind let us divide a large enough time interval $[0, t]$ into m equal intervals, so $\Delta t = t_{j+1} - t_j$ $(j = 1, 2, \ldots, m)$.

Let us assume that (15) is deterministic and that at $t = t_j$ the norm of the vector $\|\boldsymbol{\delta z}(t_j)\|$ is of unit length. Using this vector as the vector of initial conditions, let us obtain the solution of the system (15) for time t_{j+1} with the norm $\|\boldsymbol{\delta z}(t_{j+1}\| = d_{j+1}$. Continuing the solution of the system (15) with new initial conditions $\delta z_{i0}(t_{j+1})/d_{j+1}$, we will find the sequence of values d_j, and then the top Lyapunov exponent can be found as the limit

$$\lambda = \lim_{m\to\infty} \frac{1}{m\,\Delta t} \sum_{i=1}^{m} \ln d_j. \tag{16}$$

Because the system of equations for the statistical moments of functions $\delta z_i(t)$ in the case of colored noises $\alpha^o(t)$ cannot be obtained in a closed form, let us find it using the method of statistical simulation [Potapov 1997; 1999].

The estimation of statistical moments $\langle \delta z_i^p\rangle$ for times t_j can be obtained as the result of a statistical averaging of the values $\langle \delta z_i^p\rangle$, found from (15) for a sufficiently large number of realizations q:

$$\langle \tilde{\delta} z_i^p(t_j)\rangle = \frac{1}{q} \sum_{m=1}^{q} [\delta z_i^p(t_j)]^{(m)}, \tag{17}$$

where $[\delta z_i^p(t_j)]^{(m)}$ is the quantity $\delta z_i^p(t_j)$ corresponding to m-th realization of the solution of (15).

Assume that the norm of the vector

$$\langle \boldsymbol{\delta z}^p(t_k)\rangle = \left\{\langle \delta z_1^p(t_k)\rangle, \langle \delta z_2^p(t_k)\rangle, \ldots, \langle \delta z_n^p(t_k)\rangle\right\}^T$$

in the Euclidean space for time t_k is of unit length. The norm of the vector $\langle \boldsymbol{\delta z}(t)^p\rangle$ becomes equal to $\tilde{d}_{k+1}$ at time $t_{k+1} = t_k + \Delta$. Furthermore, the system of equations (15) is solved for each realization of the matrix $\boldsymbol{F}'(z, \alpha(t), t)$ with initial conditions

$$\delta z_{i0}(t_{k+1}) = \frac{\delta z_i(t_{k+1})}{(\tilde{d}_{k+1})^{1/p}}.$$

Repeating the stated procedure we obtain the sequence of values $\tilde{d}_k$, with the help of which the estimation of the top Lyapunov exponent can be found:

$$\tilde{\Lambda} = \lim_{l\to\infty} \frac{1}{l\Delta} \sum_{k=1}^{l} \ln \tilde{d}_k.$$

Let us illustrate the investigation of the stability of geometric nonlinear systems by the example of the above plate.

Equation (9), linearized with respect to perturbations δz, has the following form:

$$\delta z'' + 2\varepsilon\delta z' + [(1 - \alpha - \boldsymbol{R}) + 0.34125(3z^2 - 2z\boldsymbol{R}z)]\delta z - \delta z\boldsymbol{R}z^2 = 0. \tag{18}$$

We introduce the new variables

$$z_5 = \delta z, \qquad z_6 = \delta z', \qquad z_7 = \int_0^t \chi L e^{-\chi(t-\tau)}\delta z(\tau)\,d\tau, \qquad z_8 = \int_0^t \chi L e^{-\chi(t-\tau)} z(\tau)\delta z(\tau)\,d\tau;$$

hence we can write (18) as a system of first-order differential equations

$$\begin{aligned} z_5' &= z_6, & z_6' &= -2\varepsilon z_6 - (1-\alpha)z_5 + z_7 - 0.34125(3z_1^2 z_5 - 2z_1 z_8 + z_4 z_5),\\ z_7' &= \chi L z_5 - \chi z_7, & z_8' &= \chi L z_1 z_5 - \chi z_8. \end{aligned} \tag{19}$$

If the plate is subjected to a deterministic periodic load, then at some values of the input parameters the motion of the plate can be chaotic [Guckenheimer and Holmes 1996].

This is confirmed by the trajectory of the motion of the elastic plate on the phase plane $z_1 \sim z_2$, shown in Figure 6a, which is obtained at $\varepsilon = 0, 1$; $\alpha_0 = 0.5$; $\alpha_1 = 2.0$; $\omega = 1, 4$; $\Delta t = 0.1$; and number of increments $n = 10^4$. The value of the top Lyapunov exponent at $t = 6.10^4$ is $\lambda = 0.165$ (see Figure 7a), which confirms the instability of the plate.

If we impose on the deterministic load a random noise in the form of a Gaussian stationary process $\alpha^o(t)$ with characteristics $\sigma^2 = 0.01$, $\delta = 0.5$, and $\theta = 1.4$, then the plate becomes stable with respect to statistical moments of the first, $\lambda_1 = -0.082$ (see Figure 7b), and second, $\lambda_2 = -0.164$ (see Figure 7c), orders. These estimates of the top Lyapunov exponents are obtained as a result of averaging the results of 20 realizations at $t = 6.10^4$. One of realizations of the trajectories on the phase plane in this case, obtained at $n = 10^4$, is shown in Figure 6b.

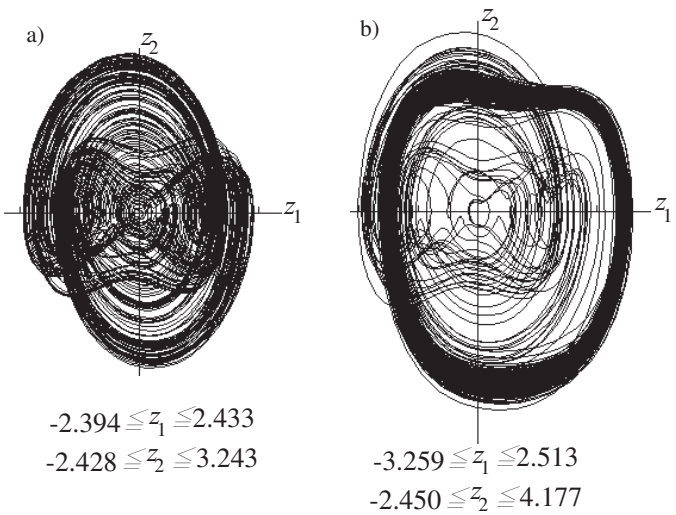

Figure 6. Trajectories of the elastic plate motion in the phase plane under (a) deterministic and (b) stochastic treatments of the problem.

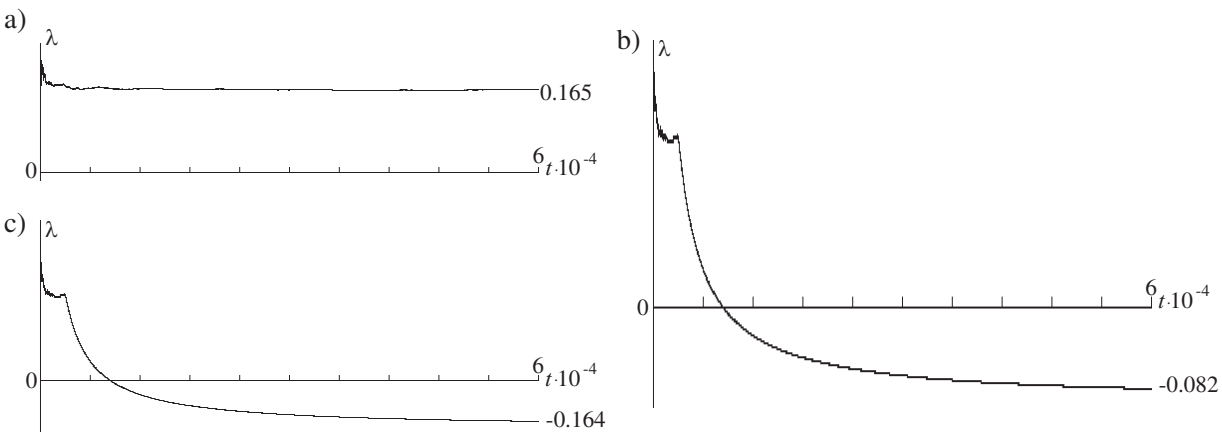

Figure 7. Changes in the estimate of the top Lyapunov exponent for the elastic plate under (a) deterministic and (b and c) stochastic treatments of the problem.

If we increase the time interval to 10^5, the same values result in quantities $\lambda_1 = -0.088$ and $\lambda_2 = -0.180$. At finally, if the number of realizations is assumed to be equal to 40, then at $t = 10^5$ we will find $\lambda_1 = -0.087$ and $\lambda_2 = -0.177$.

If the material of the plate has a small viscosity, then the indicated effect remains. This is confirmed by the data, shown in the tables at the top of the next page. The results shown in Table 1 are obtained for the plate under the action of a deterministic load, with and without random noise (with characteristics $\sigma^2 = 0.01$, $\delta = 0.5$, and $\theta = 1.4$). These quantities of the top Lyapunov exponents are found as a result of data processing of 40 realizations at $t = 10^5$.

The presented results show that the calculation of top Lyapunov exponent estimates demands a lot of steps with respect to time. In such situations questions about the exactness of the numerical solution

L	χ	λ
0	0	0.166
0.1	0.1	0.156
0.5	0.1	0.131
0.1	0.5	0.151
0.5	0.5	−0.149

L	χ	$\lambda_1^{(4)}$	$\lambda_2^{(4)}$	$\lambda_1^{(5)}$	$\lambda_2^{(5)}$
0	0	−0.087	−0.177	−0.085	−0.179
0.1	0.1	−0.086	−0.172	−0.086	−0.167
0.5	0.1	0.132	0.260	0.132	0.259
0.1	0.5	0.140	0.273	0.136	0.284
0.5	0.5	−0.146	−0.291	−0.146	−0.291

Table 1. Results obtained for the plate under the action of a deterministic load (left) and under a deterministic load and random noise with $\sigma^2 = 0.01$, $\delta = 0.5$, and $\theta = 1.4$.

arise. In order to verify the results obtained with the help of the fourth-order Runge–Kutta method, the $\lambda_1^{(4)}$ results are shown in Table 1; these are found with the help of the fifth-order Runge–Kutta–Fehlberg results, $\lambda_1^{(5)}$ [Fehlberg 1969; Butcher 2003]. Because the algorithm of this method is not widely known we will give a scheme for the numerical solution of the ordinary differential equation $dz/dt = f(t, z)$:

$$z_{n+1} = z_n + h\sum_{i=1}^{s} b_i k_i, \qquad k_i = f\left(t_n + c_i h, x_n + h\sum_{j=1}^{s} a_{ij}k_j\right).$$

This method is defined by the Butcher tableau, which shows the coefficients of the method as follows:

c_1	a_{11}	a_{12}	...	a_{1s}
c_2	a_{21}	a_{22}	...	a_{2s}
⋮	⋮	⋮	⋱	⋮
c_s	a_{s1}	a_{s2}	...	a_{ss}
	b_1	b_2	...	b_s

These coefficients for the Runge–Kutta–Fehlberg version are equal to

0						
1/4	1/4					
3/8	3/32	9/32				
12/13	1932/2197	−7200/2197	7296/2197			
1	439/216	−8	3680/513	−845/4104		
1/2	−8/27	2	−3544/2565	1859/4104	−11/40	
	16/135	0	6656/12825	28561/56430	−9/50	2/55

The comparison of the corresponding results shows that the fourth-order Runge–Kutta method gives sufficiently correct results.

The stabilizing effect of the unstable system was discovered for the first time in the investigation of the stability of the first-order differential equation [Leibowitz 1963; Hasminskiĭ 1980]

$$\dot{X} = (b + \sigma\xi)X, \tag{20}$$

where b and σ are constants, and ξ is a Gaussian white noise, introduced by Ito.

The trivial solution of Equation (20) is stable at $b < \sigma^2/2$, which has been considered as physically contradictive [Hasminskiĭ 1980]. On this basis the conclusion was made that the white noise in Ito's sense is "physically unrealizable".

If $\xi(t)$ is a white noise in Stratonovich's sense, then the effect of the stabilization disappears [Hasminskiĭ 1980], and it has been remarked that the unstable deterministic system $\dot{x} = bx$ ($b > 0 -$ const.) cannot be stabilized by a physically realizable perturbation of its parameter.

However, Hasminskiĭ [1980] has shown that for higher-order systems of differential equations Stratonovich white noise can stabilize an unstable deterministic system. In particular, the trivial solution of the second-order equation $\ddot{z} + (k + \sigma\chi)\dot{z} + \omega^2 z = 0$, where k and ω^2 are constants, at definite quantities of the parameter σ can be stable, although the same solution of the deterministic equation (at the same magnitudes of values k and ω^2) $\ddot{z} + k\dot{z} + \omega^2 z = 0$ is unstable.

It should be said that white noises in both Ito's and Stratonovich's senses are mathematical idealizations, which cannot be realized physically (as physical processes with unlimited power doesn't exist). From this point of view the smoothing in the mean square process, used in the present paper, can be considered a physically realizable process.

Arnold et al. [1983] showed that deterministic differential equations can be stabilized (in sense of the almost sure stability) by stochastic wide-band stationary processes. The result, obtained for the plate in the present paper, demonstrates that a physically realizable (colored) noise can render a stabilizing effect (in sense of stability with respect to statistical moments) in the analysis of the stability of elastic and viscoelastic systems, the motion of which is described by nonlinear differential equations.

5. Conclusion

In the present paper an effective method of investigation of nonlinear oscillations and the stability of elastic and viscoelastic systems at stochastic excitations is proposed. Loads are assumed to be in the form of Gaussian random stationary processes with rational spectral densities (colored noises). The method is based on the numerical simulation of random processes, the numerical solution of differential equations, describing the motion of the considered system, and on the calculation of the top Lyapunov exponent. It is shown that the viscous properties of the material have an essential effect on its nonlinear oscillations. It is remarked that in some cases the addition of a stochastic noise on the deterministic periodic excitation can have a stabilizing effect on the motion of elastic and viscoelastic plates.

References

[Arnold et al. 1983] L. Arnold, H. Crauel, and V. Wihstutz, "Stabilization of linear systems by noise", *SIAM J. Control Optim.* **21**:3 (1983), 451–461.

[Benettin et al. 1980a] G. Benettin, L. Galgani, A. Giorgilli, and J.-M. Strelcyn, "Liapunov characteristic exponents for smooth dynamical systems and for Hamiltonian systems; a method for computing all of them. 1: Theory", *Meccanica* (*Milano*) **15**:1 (1980), 9–20.

[Benettin et al. 1980b] G. Benettin, L. Galgani, A. Giorgilli, and J.-M. Strelcyn, "Liapunov characteristic exponents for smooth dynamical systems and for Hamiltonian systems; a method for computing all of them. 2: Numerical application", *Meccanica* (*Milano*) **15**:1 (1980), 21–30.

[Butcher 2003] J. C. Butcher, *Numerical methods for ordinary differential equations*, Wiley, Chichester, 2003.

[Dimentberg 1980] M. F. Dimentberg, Нелинеиные стохастические задачи механических колебании, Nauka, Moscow, 1980.

[Dimentberg 1988] M. F. Dimentberg, *Statistical dynamics of nonlinear and time-varying systems*, Mechanical Engineering Research Studies. Engineering Dynamics Series **5**, Research Studies Press, Taunton, 1988.

[Fehlberg 1969] E. Fehlberg, "Klassische Runge–Kutta-Formeln fünfter und siebenter Ordnung mit Schrittweiten-Kontrolle", *Computing* (*Arch. Elektron. Rechnen*) **4**:2 (1969), 93–106.

[Guckenheimer and Holmes 1996] J. Guckenheimer and P. Holmes, *Nonlinear oscillations, dynamical systems, and bifurcations of vector fields*, Springer, New York, 1996.

[Hasminskiĭ 1980] R. Z. Hasminskiĭ, *Stochastic stability of differential equations*, Monographs and Textbooks on Mechanics of Solids and Fluids: Mechanics and Analysis **7**, Sijthoff & Noordhoff, Alphen aan den Rijn, 1980.

[Leibowitz 1963] M. A. Leibowitz, "Statistical behavior of linear systems with randomly varying parameters", *J. Math. Phys.* **4**:6 (1963), 852–858.

[Potapov 1997] V. D. Potapov, "Numerical method for investigation of stability of stochastic integro-differential equations", *Appl. Numer. Math.* **24**:2-3 (1997), 191–201.

[Potapov 1999] V. D. Potapov, *Stability of stochastic elastic and viscoelastic systems*, Wiley, Chichester, 1999.

[Shalygin and Palagin 1986] A. C. Shalygin and Y. I. Palagin, *Applied methods of statistical simulation*, Mashinostroenie, Leningrad, 1986.

[Simiu 2002] E. Simiu, *Chaotic transitions in deterministic and stochastic dynamical systems: applications of Melnikov processes in engineering, physics, and neuroscience*, Princeton University Press, Princeton, NJ, 2002.

[Vol'mir 1967] A. S. Vol'mir, Устоичивость деформируемых систем, Nauka, Moscow, 1967. In Russian; translated as *Stability of deformable systems*, Ft. Belvoir Defense Technical Information Center, 1970.

Received 3 Dec 2008. Revised 22 Jun 2009. Accepted 20 Aug 2009.

VADIM D. POTAPOV: potapov@micnmic.msk.ru
Department of Structural Mechanics, Moscow State University of Means Communication, Obraztsov street, 15, Moscow 127994, Russia

JOURNAL OF MECHANICS OF MATERIALS AND STRUCTURES
Vol. 5, No. 2, 2010

FUNDAMENTAL SOLUTIONS FOR AN INHOMOGENEOUS CROSS-ANISOTROPIC MATERIAL DUE TO HORIZONTAL AND VERTICAL PLANE STRAIN LINE LOADS

CHENG-DER WANG, JIA-YAN HOU AND WEI-JER WANG

This work derives the fundamental solutions for displacements and stresses due to horizontal and vertical line loads acting in a continuously inhomogeneous plane strain cross-anisotropic full space with Young's and shear moduli varying exponentially with depth. The governing equations can be obtained by combining the generalized Hooke's law, the strain-displacement relationships, and the equilibrium equations. Then, utilizing Fourier transforms, the governing equations are transformed into ordinary differential equations. Additionally, by using the variation of parameters, the solutions of the displacements in the Fourier domain are found. However, the stress solutions in the same domain can also be found by employing the stress-strain-displacement relationships. Eventually, performing inverse Fourier transforms by means of the numerical integration program QDAGI, the displacements and stresses induced by horizontal and vertical plane strain line loads can be calculated. The solutions indicate that the displacements and stresses are profoundly influenced by the nondimensional inhomogeneity parameter, the type and degree of material anisotropy, the types of loading, and the nondimensional horizontal distance. The proposed solutions are identical to those of Wang and Liao after suitable integration, as derived in an appendix, when the full space is a homogeneous cross-anisotropic material. A series of parametric studies are conducted to demonstrate the present solutions, and to elucidate the effects of aforementioned factors on the vertical normal stress. The results reveal that estimates of displacement and stress should take the inhomogeneity into account when studying cross-anisotropic materials under applied line loads.

Introduction

Many natural soils, such as flocculated clays, varved silts, or sands, are often deposited through a geologic process of sedimentation over a long period of time. The effects of deposition, overburden, desiccation, et cetera, can cause both anisotropic and inhomogeneous deformability. The mechanical responses of anisotropic materials with spatial gradients in composition, called anisotropic functionally graded materials, are important in many fields of applied mechanics. Hence, an elastic loading problem for a continuously inhomogeneous plane strain cross-anisotropic full space with Young's and shear moduli varying exponentially with depth is considered in this article.

The solution of a point load acting in the interior of a full space is called the fundamental solution or the Green's function solution. This kind of solution is employed in the boundary integral equation method (or boundary element method) for solving elastostatic boundary value problems [Hu et al. 2007]. However,

Keywords: inhomogeneity, cross-anisotropic full space, horizontal and vertical plane strain line loads, Fourier transforms, fundamental solutions of displacements and stresses, numerical integrations.

We acknowledge the financial support of the National Science Council (Taiwan) under Grant No. 96-2628-E-239-022-MY3.

theoretical treatment of both inhomogeneous and anisotropic characteristics in materials frequently poses mathematical difficulties. Therefore, a plane strain state on the y-axis of a cartesian coordinate system is assumed throughout this study, which means the inhomogeneous cross-anisotropic medium is subjected to two-dimensional horizontal/vertical line loads, P_x/P_z (force/length). Furthermore, the magnitudes and distributions of displacements and stresses in materials due to these applied loads have always played an important role in the design of foundations. In the past, a great deal of study was contributed to estimate the displacements and stresses in isotropic media with Young's or shear modulus varying with depth according to the power law, the linear law, the exponential law, et cetera. A very detailed survey of the solutions related to soil/rock mechanics and foundation engineering for inhomogeneous isotropic/cross-anisotropic media is given in [Wang et al. 2003]. However, some recent investigations are not included in that survey, and will be mentioned here. Some relevant articles about inhomogeneous isotropic media are [Chen et al. 2001; Gray et al. 2001; Doherty and Deeks 2002; 2003c; 2003a; 2003b; 2005; 2006; Martin 2004; Martin et al. 2002; Cihan 2003], and some about inhomogeneous anisotropic media are [Azis and Clements 2001; Wang et al. 2003; 2006; Wang and Tzeng 2009]. Azis and Clements [2001] studied the solutions of boundary value problems for static deformations of inhomogeneous anisotropic elastic materials. The elastic moduli varied continuously with three cartesian coordinates, and three plane strain boundary value problems for inhomogeneous isotropic/cross-anisotropic media were illustrated. Wang et al. [2003] presented semianalytical solutions for displacements and stresses by employing the Hankel integral transforms in a cylindrical coordinate system with the assumption of axial symmetry about the z-axis, owing to a vertical point load in a continuously inhomogeneous cross-anisotropic half space with Young's and shear moduli varying exponentially with depth (Ee^{-kz}, $E'e^{-kz}$, and $G'e^{-kz}$). The planes of cross-anisotropy were horizontal, and the resulting integrals involved products of Bessel functions of the first kind, an exponential, a polynomial; some of them cannot be given in a closed form. Hence, numerical techniques proposed by Longman [1956b; 1956a] and Davis and Rabinowitz [1984] were adopted. The point load solutions in the Hankel domain for the half space were obtained by superposing the solutions of two full spaces, one with a point load in its interior and the other with opposite traction of the first full space along the boundary surface plane. Subsequently, Wang et al. [2006] integrated the point load solutions of [Wang et al. 2003] to get solutions for the displacements and stresses along the centerline, induced by a uniform vertical circular load acting in the interior of an inhomogeneous cross-anisotropic half space with Young's and shear moduli varying exponentially with depth. In addition, Wang and Tzeng [2009] generated the solutions for the same medium for conical and parabolic vertical circular loads.

In this article, the fundamental solutions of displacements and stresses subjected to horizontal and vertical line loads for an inhomogeneous plane strain cross-anisotropic medium with Young's and shear moduli varying exponentially with depth (Ee^{-kz}, $E'e^{-kz}$, and $G'e^{-kz}$) are derived. Note that, in order to consider the important effect of a horizontal force on the inhomogeneous cross-anisotropic medium, the axisymmetric assumption cannot be utilized. In other words, the solutions of Wang et al. [2003] cannot be applied to solve for the displacements and stresses resulting from the actions of horizontal forces, or those from asymmetrically shaped loads, such as strip loads. Hence we use cartesian coordinates for performing Fourier transforms. However, past investigations suggest that considering anisotropic deformability together with inhomogeneity can make the problems too complicated to allow closed-form solutions for the displacement and stress; therefore, we resort to numerical integration using QDAGI.

The present solutions indicate that the displacements and stresses are governed by the nondimensional inhomogeneity parameter (kz), the type and degree of material anisotropy (E/E', G'/E', and ν/ν'), the types of line loading (P_x and P_z, force/length), and the nondimensional horizontal distance (x/z). The proposed solutions are identical with those of [Wang and Liao 1999] by integration, as derived in the Appendix of this article, when the full space is a homogeneous cross-anisotropic medium owing to infinite horizontal and vertical line loads. Finally, a parametric study is conducted to demonstrate the obtained solutions and to elucidate the effect of aforementioned factors on the vertical normal stress. The results reveal that the inhomogeneous characteristics should be taken into account in the case of cross-anisotropic soil/rock masses under plane strain horizontal/vertical line loads.

1. Governing equations for an inhomogeneous plane strain cross-anisotropic medium due to line loads

In this study, solutions for the displacements and stresses caused by horizontal/vertical line loads in a continuously inhomogeneous plane strain cross-anisotropic full space are derived. Figure 1 depicts a cartesian coordinate system in which the z-axis is the axis of rotation associated with elastic symmetry, and the x-y plane is the cross-anisotropic plane. The cross-anisotropic medium has inhomogeneous elastic properties according with the assumptions of [Wang et al. 2003]. The Young's and shear moduli vary exponentially with depth, but the two Poisson's ratios remain constants. Hence, the expression of stress-strain for an inhomogeneous cross-anisotropic medium under the plane strain assumption is

$$\begin{bmatrix} \sigma_{xx} \\ \sigma_{zz} \\ \tau_{xz} \end{bmatrix} = \begin{bmatrix} C_{11} & C_{13} & 0 \\ C_{13} & C_{33} & 0 \\ 0 & 0 & C_{44} \end{bmatrix} \begin{bmatrix} \varepsilon_{xx} \\ \varepsilon_{zz} \\ \gamma_{xz} \end{bmatrix} e^{-kz}, \tag{1}$$

where k is referred to as the inhomogeneity parameter, and it has dimensions of inverse length. The product kz represents the nondimensional inhomogeneity parameter; here z is coordinate (increasing

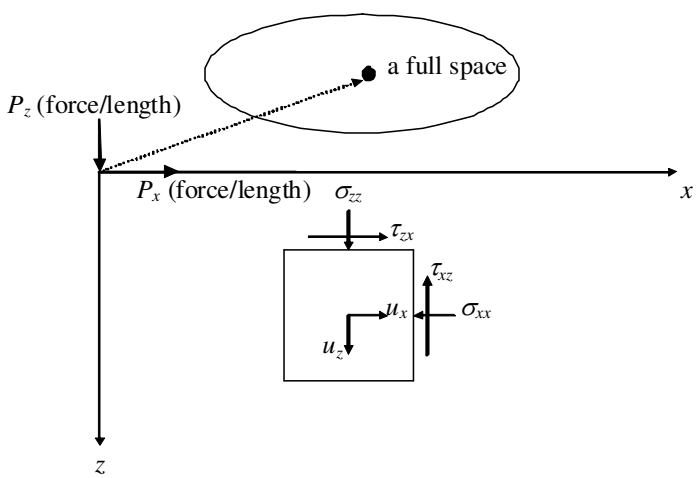

Figure 1. Horizontal/vertical line load P_x/P_z acting in an inhomogeneous plane strain cross-anisotropic full space.

downward) in the direction of the axis of rotation associated with elastic symmetry. The matrix entries C_{11}, C_{13}, C_{33}, and C_{44} are elastic moduli or elasticity constants of the medium, and can be expressed in terms of five independent elastic constants E, E', ν, ν', and G' as

$$C_{11} = \frac{E\left(1 - \frac{E}{E'}\nu'^2\right)}{(1+\nu)\left(1 - \nu - \frac{2E}{E'}\nu'^2\right)}, \quad C_{13} = \frac{E\nu'}{1 - \nu - \frac{2E}{E'}\nu'^2}, \quad C_{33} = \frac{E'(1-\nu)}{1 - \nu - \frac{2E}{E'}\nu'^2}, \quad C_{44} = G', \quad (2)$$

where

- E and E' are Young's moduli in the plane of cross-anisotropy and in the direction normal to it, respectively;
- ν and ν' are Poisson's ratios characterizing the lateral strain response in the plane of cross-anisotropy to a stress acting parallel or normal to it, respectively; and
- G' is the shear modulus in planes normal to the plane of cross-anisotropy.

Since it is often convenient in soil mechanics to consider compressive stresses as positive, this convention is adopted in this article. The normal and shear stresses act in an element as shown in Figure 1, and the stresses are all of positive sign [Poulos and Davis 1974]. The differences between the homogeneous cross-anisotropic elastic constants [Wang and Liao 1999] and the inhomogeneous ones [Wang et al. 2003] in this work are listed in Table 1. For an inhomogeneous cross-anisotropic material as described by (1), only three engineering elastic constants (E, E', and G') are exponentially dependent on the nondimensional inhomogeneity parameter kz; however, two Poisson's ratios (ν and ν') remain constants. In addition, according to the nondimensional inhomogeneity parameter k, three distinct situations exist:

- $kz > 0$ indicates a hardened surface, where E, E', and G' decrease with increasing depth (for example, graded ceramic coatings on metallic substrates [Giannakopoulos and Suresh 1997]).
- $kz = 0$ indicates the conventional homogeneous condition.
- $kz < 0$ indicates a soft surface, where E, E', and G' increase with increasing of depth: for example, modulus variations measured as a function of depth beneath the earth's surface for soils and rocks [Giannakopoulos and Suresh 1997].

Homogeneous	Inhomogeneous
E	Ee^{-kz}
E'	$E'e^{-kz}$
ν	ν
ν'	ν'
G'	$G'e^{-kz}$

Table 1. Differences between homogeneous [Wang and Liao 1999] and inhomogeneous [Wang et al. 2003] cross-anisotropic elastic constants.

The expressions of the strain-displacement relations for small strain in a cartesian coordinate system are [Poulos and Davis 1974]:

$$\varepsilon_{xx} = -\frac{\partial u_x}{\partial x}, \qquad \varepsilon_{zz} = -\frac{\partial u_z}{\partial z}, \qquad \gamma_{xz} = -\frac{\partial u_x}{\partial z} - \frac{\partial u_z}{\partial x}, \tag{3}$$

where u_x and u_z are the displacements in the x and z directions, as shown in Figure 1. A positive normal strain corresponds with a decrease in length, whereas a positive shear strain represents an increase in the right angle, and a negative shear strain denotes a decrease in the right angle [Poulos and Davis 1974].

By considering the equilibrium of the element shown in Figure 1 in a cartesian coordinate system, the following equilibrium equations are obtained [Poulos and Davis 1974]:

$$\frac{\partial \sigma_{xx}}{\partial x} + \frac{\partial \tau_{xz}}{\partial z} - P_x \delta(x)\delta(z) = 0, \qquad \frac{\partial \tau_{xz}}{\partial x} + \frac{\partial \sigma_{zz}}{\partial z} - P_z \delta(x)\delta(z) = 0, \tag{4}$$

where δ is the Dirac delta function, and P_x and P_z (force/length) are the horizontal and vertical infinite line loads acting at the origin in an inhomogeneous cross-anisotropic full space.

Combining (1) and (3), and substituting them into (4), the Navier–Cauchy equations for an inhomogeneous plane strain cross-anisotropic medium can be regrouped as

$$\begin{aligned}
&\left(C_{11}\frac{\partial^2}{\partial x^2} + C_{44}\frac{\partial^2}{\partial z^2} - kC_{44}\frac{\partial}{\partial z}\right)u_x + \left((C_{13}+C_{44})\frac{\partial^2}{\partial x \partial z} - kC_{44}\frac{\partial}{\partial x}\right)u_z + P_x\delta(x)\delta(z) = 0,\\
&\left((C_{13}+C_{44})\frac{\partial^2}{\partial x \partial z} - kC_{13}\frac{\partial}{\partial x}\right)u_x + \left(C_{44}\frac{\partial^2}{\partial x^2} + C_{33}\frac{\partial^2}{\partial z^2} - kC_{33}\frac{\partial}{\partial z}\right)u_z + P_z\delta(x)\delta(z) = 0.
\end{aligned} \tag{5}$$

2. Fundamental solutions of displacements in the Fourier domain

In order to solve the governing equations as expressed in (5), the Fourier transforms relating to the x coordinate of the components of displacement are

$$\frac{1}{\sqrt{2\pi}}\int_{-\infty}^{\infty}\begin{Bmatrix} u_x(x,z) \\ u_z(x,z)\end{Bmatrix} e^{-i\alpha x}dx = \begin{Bmatrix} \overline{u}_x(\alpha,z) \\ \overline{u}_z(\alpha,z)\end{Bmatrix}, \tag{6}$$

where α is the Fourier transformed parameter.

However, the Dirac delta function has the property $\int_{-\infty}^{\infty}\delta(x)dx = 1$. Hence, (5) becomes a system of ordinary differential equations:

$$\begin{aligned}
&\left(-\alpha^2 C_{11} + C_{44}\frac{d^2}{dz^2} - kC_{44}\frac{d}{dz}\right)\overline{u}_x + \left(i\alpha(C_{13}+C_{44})\frac{d}{dz} - i\alpha k C_{44}\right)\overline{u}_z = -\frac{P_x}{\sqrt{2\pi}}\delta(z),\\
&\left(i\alpha(C_{13}+C_{44})\frac{d}{dz} - i\alpha k C_{13}\right)\overline{u}_x + \left(-\alpha^2 C_{44} + C_{33}\frac{d^2}{dz^2} - kC_{33}\frac{d}{dz}\right)\overline{u}_z = -\frac{P_z}{\sqrt{2\pi}}\delta(z).
\end{aligned} \tag{7}$$

The homogeneous solutions of (7) are found by solving the ordinary differential equations

$$\begin{aligned}
\overline{u}_x(H) &= A_1 e^{(k+u_1)z/2} + A_2 e^{(k-u_1)z/2} + A_3 e^{(k+u_2)z/2} + A_4 e^{(k-u_2)z/2},\\
\overline{u}_z(H) &= B_1 e^{(k+u_1)z/2} + B_2 e^{(k-u_1)z/2} + B_3 e^{(k+u_2)z/2} + B_4 e^{(k-u_2)z/2},
\end{aligned} \tag{8}$$

where

$$u_1, u_2 = \sqrt{\frac{2\alpha^2 t + k^2 C_{33}C_{44} \mp 2\alpha\sqrt{\alpha^2 t^2 - 4(\alpha^2 C_{11} + k^2 C_{13})C_{33}C_{44}^2}}{C_{33}C_{44}}},$$

with $t = C_{11}C_{33} - C_{13}^2 - 2C_{13}C_{44}$. (The top sign is used for u_1.)

The coefficients B_i can be eliminated in favor of the A_i by substituting (8) into (7). This reduces equations (8) to

$$\overline{u}_x(H) = A_1 e^{(k+u_1)z/2} + A_2 e^{(k-u_1)z/2} + A_3 e^{(k+u_2)z/2} + A_4 e^{(k-u_2)z/2},$$
$$\overline{u}_z(H) = S_1 A_1 e^{(k+u_1)z/2} + S_2 A_2 e^{(k-u_1)z/2} + S_3 A_3 e^{(k+u_2)z/2} + S_4 A_4 e^{(k-u_2)z/2},$$

where

$$S_1 = \frac{-2i\alpha\big(C_{13}(k-u_1) - C_{44}(k+u_1)\big)}{4\alpha^2 C_{44} + C_{33}(k^2 - u_1^2)}, \qquad S_2 = \frac{-2i\alpha\big(C_{13}(k+u_1) - C_{44}(k-u_1)\big)}{4\alpha^2 C_{44} + C_{33}(k^2 - u_1^2)},$$
$$S_3 = \frac{-2i\alpha\big(C_{13}(k-u_2) - C_{44}(k+u_2)\big)}{4\alpha^2 C_{44} + C_{33}(k^2 - u_2^2)}, \qquad S_4 = \frac{-2i\alpha\big(C_{13}(k+u_2) - C_{44}(k-u_2)\big)}{4\alpha^2 C_{44} + C_{33}(k^2 - u_2^2)}.$$

Next, the particular solutions of (7) can be found by defining two displacement functions:

- For $z \geq 0$ (recall that the sign of z is downward positive):

$$\overline{u}_x(P) = C_1 e^{(k+u_1)z/2} + C_2 e^{(k-u_1)z/2} + C_3 e^{(k+u_2)z/2} + C_4 e^{(k-u_2)z/2},$$
$$\overline{u}_z(P) = D_1 e^{(k+u_1)z/2} + D_2 e^{(k-u_1)z/2} + D_3 e^{(k+u_2)z/2} + D_4 e^{(k-u_2)z/2}.$$

- For $z < 0$: $\overline{u}_x(P) = 0$, $\overline{u}_z(P) = 0$.

The undetermined coefficients C_i and D_i $(i = 1, \ldots, 4)$ can be obtained by variation of parameters:

$$C_1, C_2 = \frac{-4\Big(\big(\frac{1}{4}C_{33}(k\pm u_1)^2 - \frac{1}{2}C_{33}k(k\pm u_1) - \alpha^2 C_{44}\big)P_x - i\alpha\big(\frac{1}{2}(C_{13}+C_{44})(k\pm u_1) - kC_{44}\big)P_z\Big)}{\sqrt{2\pi}\,C_{33}C_{44}u_1(u_1^2 - u_2^2)},$$

$$C_3, C_4 = \frac{-4\Big(\big(\frac{1}{4}C_{33}(k\pm u_2)^2 - \frac{1}{2}C_{33}k(k\pm u_2) - \alpha^2 C_{44}\big)P_x - i\alpha\big(\frac{1}{2}(C_{13}+C_{44})(k\pm u_2) - kC_{44}\big)P_z\Big)}{\sqrt{2\pi}\,C_{33}C_{44}u_2(u_1^2 - u_2^2)},$$

$$D_1, D_2 = \frac{-4\Big(-i\alpha\big(\frac{1}{2}(C_{13}+C_{44})(k\pm u_1) - kC_{13}\big)P_x + \big(\frac{1}{4}C_{44}(k\pm u_1)^2 - \frac{1}{2}C_{44}k(k\pm u_1) - \alpha^2 C_{11}\big)P_z\Big)}{\sqrt{2\pi}\,C_{33}C_{44}u_1(u_1^2 - u_2^2)},$$

$$D_3, D_4 = \frac{-4\Big(-i\alpha\big(\frac{1}{2}(C_{13}+C_{44})(k\pm u_2) - kC_{13}\big)P_x + \big(\frac{1}{4}C_{44}(k\pm u_2)^2 - \frac{1}{2}C_{44}k(k\pm u_2) - \alpha^2 C_{11}\big)P_z\Big)}{\sqrt{2\pi}\,C_{33}C_{44}u_2(u_1^2 - u_2^2)}.$$

The general solutions are obtained as sums of homogeneous and particular solutions:

- For $z \geq 0$:

$$\overline{u}_x(G) = (A_1 + C_1)e^{(k+u_1)z/2} + (A_2 + C_2)e^{(k-u_1)z/2} + (A_3 + C_3)e^{(k+u_2)z/2} + (A_4 + C_4)e^{(k-u_2)z/2},$$
$$\overline{u}_z(G) = (S_1A_1 + D_1)e^{(k+u_1)z/2} + (S_2A_2 + D_2)e^{(k-u_1)z/2} + (S_3A_3 + D_3)e^{(k+u_2)z/2} + (S_4A_4 + D_4)e^{(k-u_2)z/2}.$$

- For $z < 0$:

$$\overline{u}_x(G) = A_1 e^{(k+u_1)z/2} + A_2 e^{(k-u_1)z/2} + A_3 e^{(k+u_2)z/2} + A_4 e^{(k-u_2)z/2},$$
$$\overline{u}_z(G) = S_1 A_1 e^{(k+u_1)z/2} + S_2 A_2 e^{(k-u_1)z/2} + S_3 A_3 e^{(k+u_2)z/2} + S_4 A_4 e^{(k-u_2)z/2}.$$

In these four equations, we assume $k+u_1$ and $k+u_2$ are positive and $k-u_1$ and $k-u_2$ are negative, so we can utilize the two infinite boundary conditions ($z \to \infty$ and $-\infty$) of displacements to solve for the undetermined constants A_i. The final expressions for the general solutions $\overline{u}_x(\alpha, z)$ and $\overline{u}_z(\alpha, z)$ in the Fourier domain are as follows:

- For $z \geq 0$:

$$\begin{aligned}
\overline{u}_x(\alpha, z) &= \frac{4}{\sqrt{2\pi}\, C_{33}C_{44}(u_1^2 - u_2^2)} \\
&\quad \times \left(\left(\left(\tfrac{1}{4}C_{33}(k-u_1)^2 - \tfrac{1}{2}C_{33}k(k-u_1) - \alpha^2 C_{44}\right) P_x - i\alpha \left(\tfrac{1}{2}(C_{13}+C_{44})(k-u_1) - kC_{44}\right) P_z \right) \frac{e^{(k-u_1)z/2}}{u_1} \right. \\
&\quad \left. - \left(\left(\tfrac{1}{4}C_{33}(k-u_2)^2 - \tfrac{1}{2}C_{33}k(k-u_2) - \alpha^2 C_{44}\right) P_x - i\alpha \left(\tfrac{1}{2}(C_{13}+C_{44})(k-u_2) - kC_{44}\right) P_z \right) \frac{e^{(k-u_2)z/2}}{u_2} \right), \\
\overline{u}_z(\alpha, z) &= \frac{4}{\sqrt{2\pi}\, C_{33}C_{44}(u_1^2 - u_2^2)} \\
&\quad \times \left(\left(-i\alpha \left(\tfrac{1}{2}(C_{13}+C_{44})(k-u_1) - kC_{13}\right) P_x + \left(\tfrac{1}{4}C_{44}(k-u_1)^2 - \tfrac{1}{2}C_{44}k(k-u_1) - \alpha^2 C_{11}\right) P_z \right) \frac{e^{(k-u_1)z/2}}{u_1} \right. \\
&\quad \left. - \left(-i\alpha \left(\tfrac{1}{2}(C_{13}+C_{44})(k-u_2) - kC_{13}\right) P_x + \left(\tfrac{1}{4}C_{44}(k-u_2)^2 - \tfrac{1}{2}C_{44}k(k-u_2) - \alpha^2 C_{11}\right) P_z \right) \frac{e^{(k-u_2)z/2}}{u_2} \right).
\end{aligned}$$

- For $z < 0$:

$$\begin{aligned}
\overline{u}_x(\alpha, z) &= \frac{4}{\sqrt{2\pi}\, C_{33}C_{44}(u_1^2 - u_2^2)} \\
&\quad \times \left(\left(\left(\tfrac{1}{4}C_{33}(k+u_1)^2 - \tfrac{1}{2}C_{33}k(k+u_1) - \alpha^2 C_{44}\right) P_x - i\alpha \left(\tfrac{1}{2}(C_{13}+C_{44})(k+u_1) - kC_{44}\right) P_z \right) \frac{e^{(k+u_1)z/2}}{u_1} \right. \\
&\quad \left. - \left(\left(\tfrac{1}{4}C_{33}(k+u_2)^2 - \tfrac{1}{2}C_{33}k(k+u_2) - \alpha^2 C_{44}\right) P_x - i\alpha \left(\tfrac{1}{2}(C_{13}+C_{44})(k+u_2) - kC_{44}\right) P_z \right) \frac{e^{(k+u_2)z/2}}{u_2} \right), \\
\overline{u}_z(\alpha, z) &= \frac{4}{\sqrt{2\pi}\, C_{33}C_{44}(u_1^2 - u_2^2)} \left(\frac{2i\alpha[C_{13}(k-u_1) - C_{44}(k+u_1)]}{4\alpha^2 C_{44} + C_{33}(k^2 - u_1^2)} \left(-Q_{x1}P_x + i\alpha Q_{z1} P_z \right) \frac{e^{(k+u_1)z/2}}{u_1} \right. \\
&\quad \left. - \frac{2i\alpha[C_{13}(k-u_2) - C_{44}(k+u_2)]}{4\alpha^2 C_{44} + C_{33}(k^2 - u_2^2)} \left(-Q_{x2}P_x + i\alpha Q_{z2} P_z \right) \frac{e^{(k+u_2)z/2}}{u_2} \right),
\end{aligned}$$

where in the last expression we used the abbreviations $Q_{xi} = \left(\tfrac{1}{4}C_{33}(k+u_i)^2 - \tfrac{1}{2}C_{33}k(k+u_i) - \alpha^2 C_{44}\right)$ and $Q_{zi} = \left(\tfrac{1}{2}(C_{13}+C_{44})(k+u_i) - kC_{44}\right)$, for $i = 1, 2$.

The desired solutions for the displacements $u_x(x,z)$ and $u_z(x,z)$ in the inhomogeneous plane strain cross-anisotropic full space can be obtained by taking the inverse Fourier transforms with respect to α:

$$\begin{bmatrix} u_x(x,z) \\ u_z(x,z) \end{bmatrix} = \frac{1}{\sqrt{2\pi}} \int_{-\infty}^{\infty} \begin{bmatrix} \overline{u}_x(\alpha,z) \\ \overline{u}_z(\alpha,z) \end{bmatrix} e^{i\alpha x} d\alpha. \tag{9}$$

3. Fundamental solutions of stresses in the Fourier domain

The horizontal normal stress $\overline{\sigma}_{xx}(\alpha,z)$, the vertical normal stress $\overline{\sigma}_{zz}(\alpha,z)$, and the shear stress $\overline{\tau}_{xz}(\alpha,z)$ can be derived by combining (1) and (3) and performing the Fourier transforms; the result is

$$\overline{\sigma}_{xx}(\alpha,z) = -i\alpha C_{11}\overline{u}_x(\alpha,z) - C_{13}\frac{d\overline{u}_z(\alpha,z)}{dz}, \quad \overline{\sigma}_{zz}(\alpha,z) = -i\alpha C_{13}\overline{u}_x(\alpha,z) - C_{33}\frac{d\overline{u}_z(\alpha,z)}{dz},$$

$$\overline{\tau}_{xz}(\alpha,z) = -C_{44}\left(\frac{d\overline{u}_x(\alpha,z)}{dz} + i\alpha\overline{u}_z(\alpha,z)\right).$$

Thus, for example, the stresses for $z \geq 0$ are

$$\begin{aligned}
\overline{\sigma}_{xx}(\alpha,z) \;=\; & \frac{e^{(k-u_1-u_2)z/2}}{2\sqrt{2\pi}\,C_{33}C_{44}u_1u_2(u_1^2-u_2^2)} \\
& \times \Big(2i\alpha\big(-u_1e^{u_1z/2}\{C_{13}C_{44}(k-u_2)^2 - C_{13}^2(k^2-u_2^2) + C_{11}[4\alpha^2C_{44} + C_{33}(k^2-u_2^2)]\} \\
& \quad + u_2e^{u_2z/2}\{C_{13}C_{44}(k-u_1)^2 - C_{13}^2(k^2-u_1^2) + C_{11}[4\alpha^2C_{44} + C_{33}(k^2-u_1^2)]\}\big)P_x \\
& \quad + \big(-u_1(k+u_2)C_{44}e^{u_1z/2}[4\alpha^2C_{11} + C_{13}(k-u_2)^2] \\
& \quad + u_2(k+u_1)C_{44}e^{u_2z/2}[4\alpha^2C_{11} + C_{13}(k-u_1)^2]\big)P_z\Big),
\end{aligned} \tag{10}$$

$$\begin{aligned}
\overline{\sigma}_{zz}(\alpha,z) \;=\; & \frac{e^{(k-u_1-u_2)z/2}}{2\sqrt{2\pi}\,C_{33}C_{44}u_1u_2(u_1^2-u_2^2)} \times \Big(2i\alpha\big(-u_1C_{44}e^{u_1z/2}[4\alpha^2C_{13} + C_{33}(k-u_2)^2] \\
& \quad + u_2C_{44}e^{u_2z/2}[4\alpha^2C_{13} + C_{33}(k-u_1)^2]\big)P_x \\
& + \big(-u_1e^{u_1z/2}\{-4\alpha^2C_{13}^2(k-u_2) + 4\alpha^2C_{13}C_{44}(k+u_2) + C_{33}(k-u_2)[4\alpha^2C_{11} + C_{44}(k^2-u_2^2)]\} \\
& \quad + u_2e^{u_2z/2}\{-4\alpha^2C_{13}^2(k-u_1) + 4\alpha^2C_{13}C_{44}(k+u_1) + C_{33}(k-u_1)[4\alpha^2C_{11} + C_{44}(k^2-u_1^2)]\}\big)P_z\Big),
\end{aligned} \tag{11}$$

$$\begin{aligned}
\overline{\tau}_{xz}(\alpha,z) \;=\; & \frac{e^{(k-u_1-u_2)z/2}}{2\sqrt{2\pi}\,C_{33}u_1u_2(u_1^2-u_2^2)} \times \Big(\big(-u_1(k+u_2)e^{u_1z/2}[4\alpha^2C_{13} + C_{33}(k-u_2)^2] \\
& \quad + u_2(k+u_1)e^{u_2z/2}[4\alpha^2C_{13} + C_{33}(k-u_1)^2]\big)P_x \\
& \quad + 2i\alpha\big(-u_1e^{u_1z/2}[4\alpha^2C_{11} + C_{13}(k-u_2)^2] \\
& \quad + u_2e^{u_2z/2}[4\alpha^2C_{11} + C_{13}(k-u_1)^2]\big)P_z\Big).
\end{aligned} \tag{12}$$

Finally, the stresses $\sigma_{xx}(x,z)$, $\sigma_{zz}(x,z)$, and $\tau_{xz}(x,z)$ in the physical domain are determined by inverse Fourier transformation:

$$\begin{bmatrix} \sigma_{xx}(x,z) \\ \sigma_{zz}(x,z) \\ \tau_{xz}(x,z) \end{bmatrix} = \frac{1}{\sqrt{2\pi}} \int_{-\infty}^{\infty} \begin{bmatrix} \overline{\sigma}_{xx}(\alpha,z) \\ \overline{\sigma}_{zz}(\alpha,z) \\ \overline{\tau}_{xz}(\alpha,z) \end{bmatrix} e^{i\alpha x} d\alpha. \tag{13}$$

However, from (9) and (13), the formulation of displacements $u_x(x, z)$ and $u_z(x, z)$ and stresses $\sigma_{xx}(x, z)$, $\sigma_{zz}(x, z)$, and $\tau_{xz}(x, z)$ in a continuously inhomogeneous cross-anisotropic full space have very complicated integrals, which cannot be given in an exact closed form; hence, numerical inversion of the Fourier transforms is required. The detailed numerical integrations required to estimate the vertical normal stress are elucidated in the next section.

4. An illustrative example

From (10)–(13), the numerical inversion of Fourier transforms for stress fields can be performed by using the routines of QUADPACK. QUADPACK can be utilized for the numerical computation of definite one-dimensional integrals [Piessens et al. 1983; Barros and Mesquita 1999]. There are routines for adaptive and nonadaptive integration, finite, semiinfinite and fully infinite integration regions, integrands with singularities, and integrands with $\sin x$ or $\cos x$. Therefore, the values of (13) can be accurately calculated by employing the numerical integration subroutine QDAGI between the limits $-\infty$ and ∞. In this investigation, the displacements, (9), owing to horizontal/vertical line loadings in the full space are only meaningful if evaluated as the displacements of one point relative to another point, with both points located neither at the origin of loading nor at infinity [Poulos and Davis 1974]. Hence, in this section, a parametric study is conducted to clarify the effect of inhomogeneity, the type and degree of material anisotropy, and the loading types on the most interesting quantity in geotechnical engineering, namely, the vertical normal stress (σ_{zz}).

Two illustrative examples, horizontal and vertical line loads acting in the inhomogeneous plane strain cross-anisotropic full space, are given to show the effect of the nondimensional inhomogeneity parameter kz; the degree of material anisotropy specified by the ratios E/E', G'/E', and ν/ν'; and the loading types P_x/P_z (force/length) on σ_{zz}, respectively. In this investigation, the values of the nondimensional inhomogeneity parameter kz (z is downward positive in this numerical analysis) are theoretically assumed to be -0.3, -0.2, -0.1, and 0 (homogeneous). As mentioned previously, the situation $kz < 0$ (-0.3, -0.2, -0.1) corresponds to soft surface, where E, E', and G' increase with the depth. This situation would be suitable for the earth materials, such as soils and rocks. Regarding the typical ranges of cross-anisotropic parameters, Gazetas [1982] summarized experimental data for deformational cross-anisotropy of clays and sands. He concluded that the ratio E/E' for clays ranges from 0.6 to 4, and was as low as 0.2 for sands. However, for the heavily overconsolidated London clay, the range of E/E' was 1.35–2.37, and that of the ratio G'/E' was 0.23–0.44 [Ward et al. 1965; Gibson 1974; Lee and Rowe 1989; Tarn and Lu 1991; Wang et al. 2008]. The ratio ν/ν' is hypothetically assumed to be within the range 0.75–1.5 in this study. Therefore, the anisotropic ratios (E/E', G'/E', and ν/ν') of elastic constants for seven different soils are listed in Table 2.

The influence of inhomogeneity and of the degree and type of soil anisotropy on the vertical normal stress due to a horizontal line load acting in the cross-anisotropic material is explored first. Figure 2 plots the effect of the nondimensional inhomogeneity parameter kz (equal to -0.3, -0.2, -0.1, or 0) on the nondimensional vertical normal stress ($z\sigma_{zz}/P_x$) versus the nondimensional horizontal distance (x/z), induced by a horizontal line load (P_x) for isotropic soil 1 and for each of the cross-anisotropic soils 2–7. In order to examine the accuracy of the numerical integration by using QDAGI, comparisons are carried out with the extension of the homogeneous point load solutions of [Wang and Liao 1999] ($kz = 0$). That

Soil type	E/E'	G'/E'	ν/ν'	Soil type	E/E'	G'/E'	ν/ν'
1	1	0.385	1				
2	1.35	0.385	1	5	1	0.44	1
3	2.37	0.385	1	6	1	0.385	0.75
4	1	0.23	1	7	1	0.385	1.5

Table 2. Anisotropic ratios of elastic constants for different soil types. Soil 1 is isotropic, while the others exhibit cross-anisotropy. In each case, $E = 50$ MPa and $\nu = 0.3$.

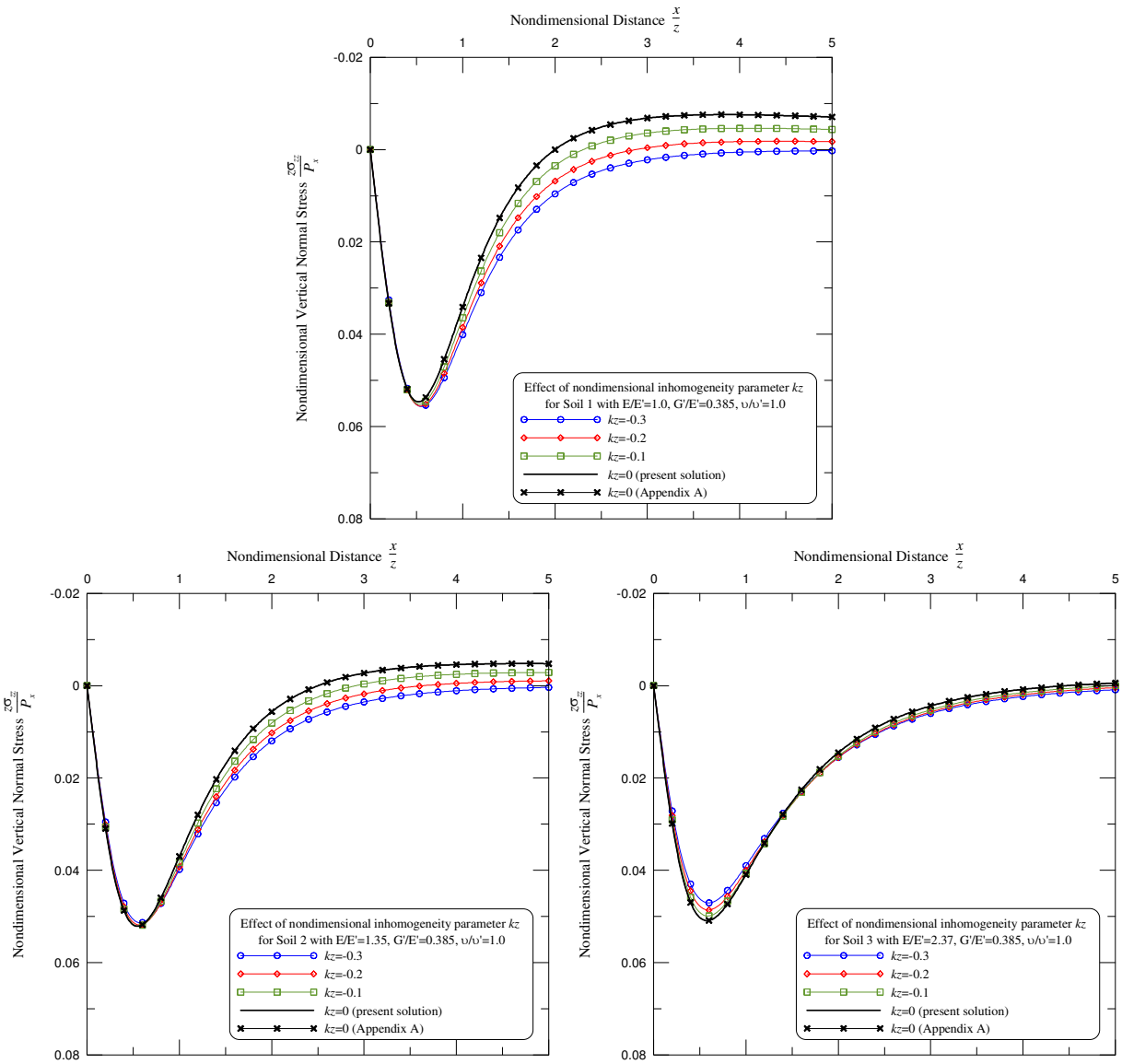

Figure 2. Effect of the inhomogeneity parameter kz on the vertical normal stress (σ_{zz}) induced by a horizontal line load (P_x) for soil types 1–3. (Continued on next page.)

means the horizontal/vertical point load solutions for the stress components of [Wang and Liao 1999] in a cartesian coordinate system for a homogeneous cross-anisotropic full space should be extended to those of line load solutions by suitable integration. The new solutions are also expressed in the Appendix, and formulae (A.1)–(A.3) are the checking criteria for the present solutions, (10)–(13), in the case of the nondimensional inhomogeneity parameter $kz = 0$. From Figure 2, the calculated results from the present solutions for soils 1–7 are in excellent agreement with those of in the Appendix. In addition, we see that when the nondimensional horizontal distance x/z is less than 0.5, the nondimensional vertical normal stresses ($z\sigma_{zz}/P_x$) are almost the same irrespective of the variation of kz for the isotropic medium

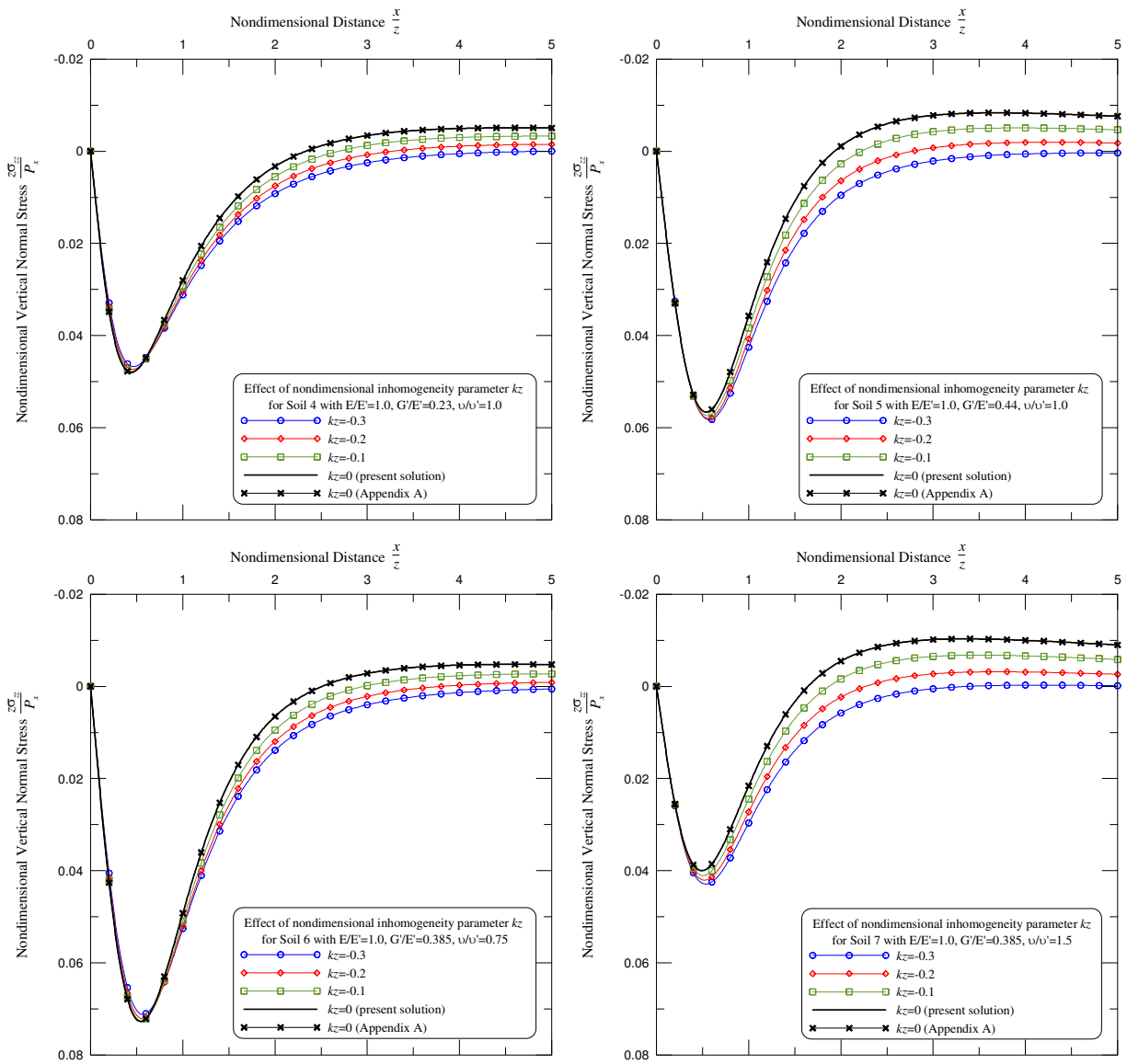

Figure 2 (continued). Effect of the inhomogeneity parameter kz on the vertical normal stress (σ_{zz}) induced by a horizontal line load (P_x) for soil types 4–7.

(soil 1). However, with increasing $x/z > 1.5$, the vertical normal stress would be transferred by tension except for $kz = -0.3$, and the induced stress follows, decreasing steadily as kz goes from -0.3 to 0. It is apparent that the nondimensional inhomogeneity parameter kz does have a great influence on σ_{zz}.

With an increase in E/E' from 1 for soil 1 to 1.35 for soil 2 and then to 2.37 for soil 3, the magnitude and region of the induced tensile stress is gradually reduced. In each figure, $z\sigma_{zz}/P_x$ converges with increasing x/z.

A similar trend, except for the magnitude, holds for the comparison of soils 1, 4 and 5, with G'/E' decreasing from 0.385 for soil 1 to 0.23 for soil 4, and increasing to 0.44 for soil 5.

However, $z\sigma_{zz}/P_x$ becomes larger within the very small loaded distance of x/z (< 1) with a decrease in ν/ν' from 1 for soil 1, to 0.75 for soil 6, and becomes smaller in the case of increasing ν/ν' (from 1 for soil 1 to 1.5 for soil 7). Thus, it is clear from Figure 2 that the induced vertical normal stress by a horizontal line load in a plane strain cross-anisotropic material strongly relies on the nondimensional inhomogeneity parameter kz and the nondimensional horizontal distance x/z.

Figures 3–5 depict the effect of soil anisotropy (E/E', G'/E', and ν/ν') on the vertical normal stress (σ_{zz}) induced by a horizontal line load (P_x) for three groups of soils: 1, 2, and 3 (E/E' varies, Figure 3); soils 1, 4, and 5 (G'/E' varies, Figure 4); and soils 1, 6, and 7 (ν/ν' varies, Figure 5).

In each figure the cases $kz = -0.3$ (E, E', and G' increase with depth) and $kz = 0$ (homogeneous) are shown, in the left and right panes respectively. From Figure 3, left, we see that for $x/z < 1$, the order of the induced compression stress is soil 1 > soil 2 > soil 3. However, with an increase of x/z, that order would be reversed.

In Figure 4, left, we see that the magnitudes of $z\sigma_{zz}/P_x$ obey the order soil 5 > soil 1 > soil 4, while the corresponding order for Figure 5, left is soil 6 > soil 1 > soil 7, with a slight tensile stress observed in the case of soil 7.

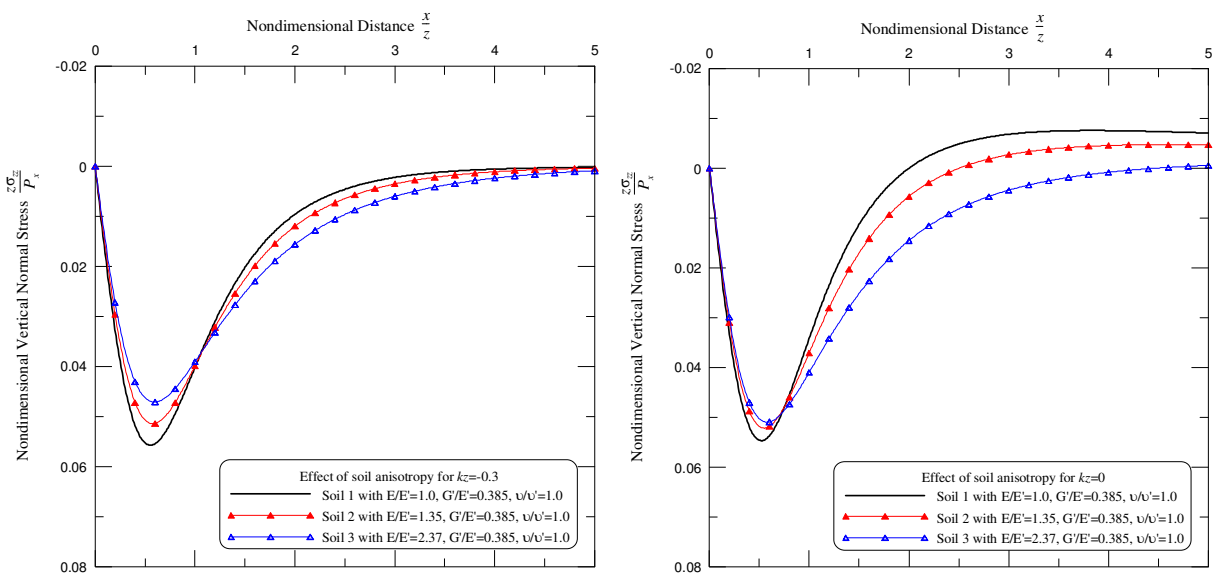

Figure 3. Effect of ratio E/E' on the vertical normal stress (σ_{zz}) induced by a horizontal line load (P_x) when $kz = -0.3$ (left) and $kz = 0$ (right). Comparison of soils 1, 2, and 3.

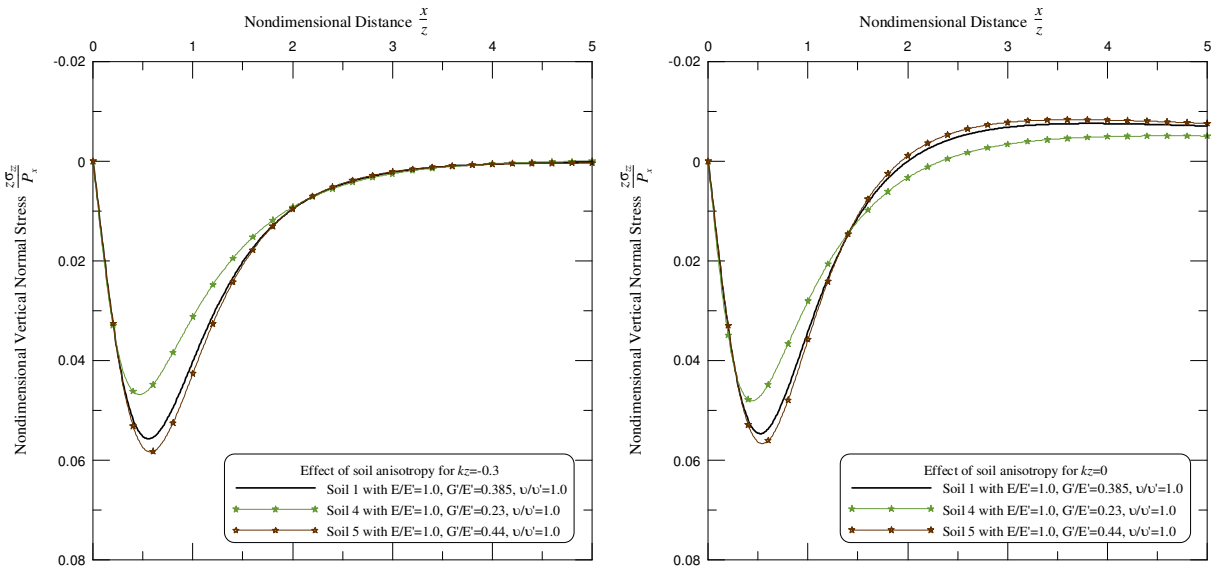

Figure 4. Effect of ratio G'/E' on the vertical normal stress (σ_{zz}) induced by a horizontal line load (P_x) when $kz = -0.3$ (left) and $kz = 0$ (right). Comparison of soils 1, 4, and 5.

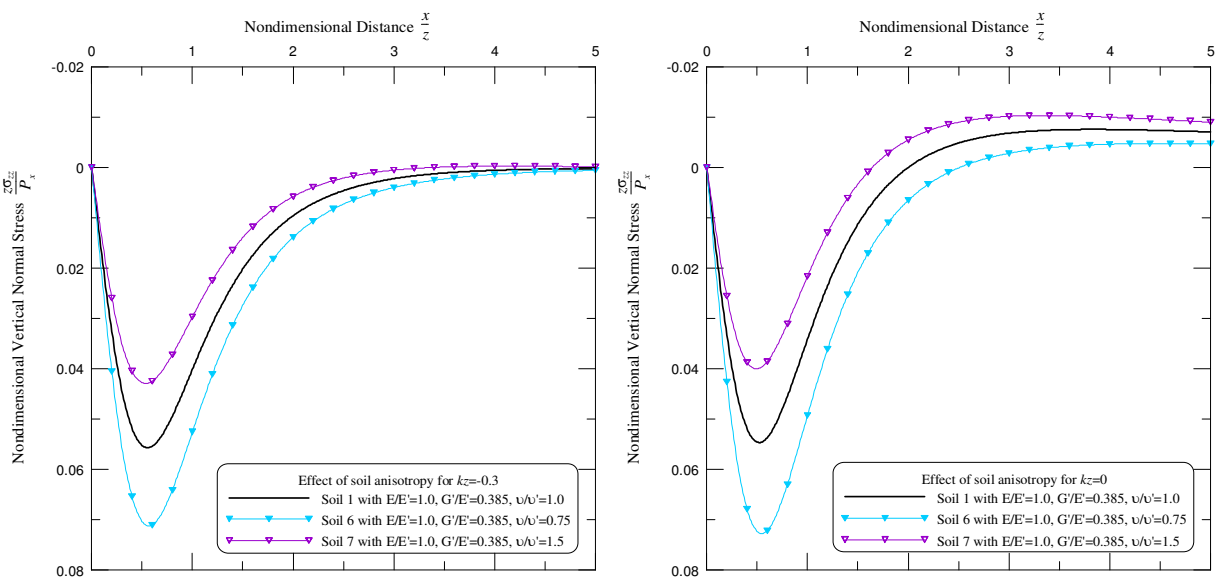

Figure 5. Effect of ratio ν/ν' on the vertical normal stress (σ_{zz}) induced by a horizontal line load (P_x) when $kz = -0.3$ (left) and $kz = 0$ (right). Comparison of soils 1, 6, and 7.

The right halves of Figures 3–5 represent the homogeneous case, $kz = 0$. The trends here are quite different from those in the case $kz = -0.3$, especially in that a great deal of tension stress is produced in the homogeneous isotropic/cross-anisotropic media.

From Figures 3–5 it is clear that the type and degree of soil anisotropy (E/E', G'/E', and ν/ν') affects profoundly the vertical normal stress due to a horizontal line load in an inhomogeneous isotropic/cross-anisotropic material.

Figure 6 shows the effect of the nondimensional inhomogeneity parameter kz (equal to -0.3, -0.2, -0.1, or 0) on the nondimensional vertical normal stress ($z\sigma_{zz}/P_z$) versus the nondimensional horizontal distance (x/z), subjected to a vertical line load (P_z) for isotropic soil 1 and cross-anisotropic soils 2–7. The figure suggests that the results of the present solutions when $kz = 0$ for soils 1–7 agree very well with those in the Appendix. Additionally, we see that the vertical normal stresses due to a vertical line

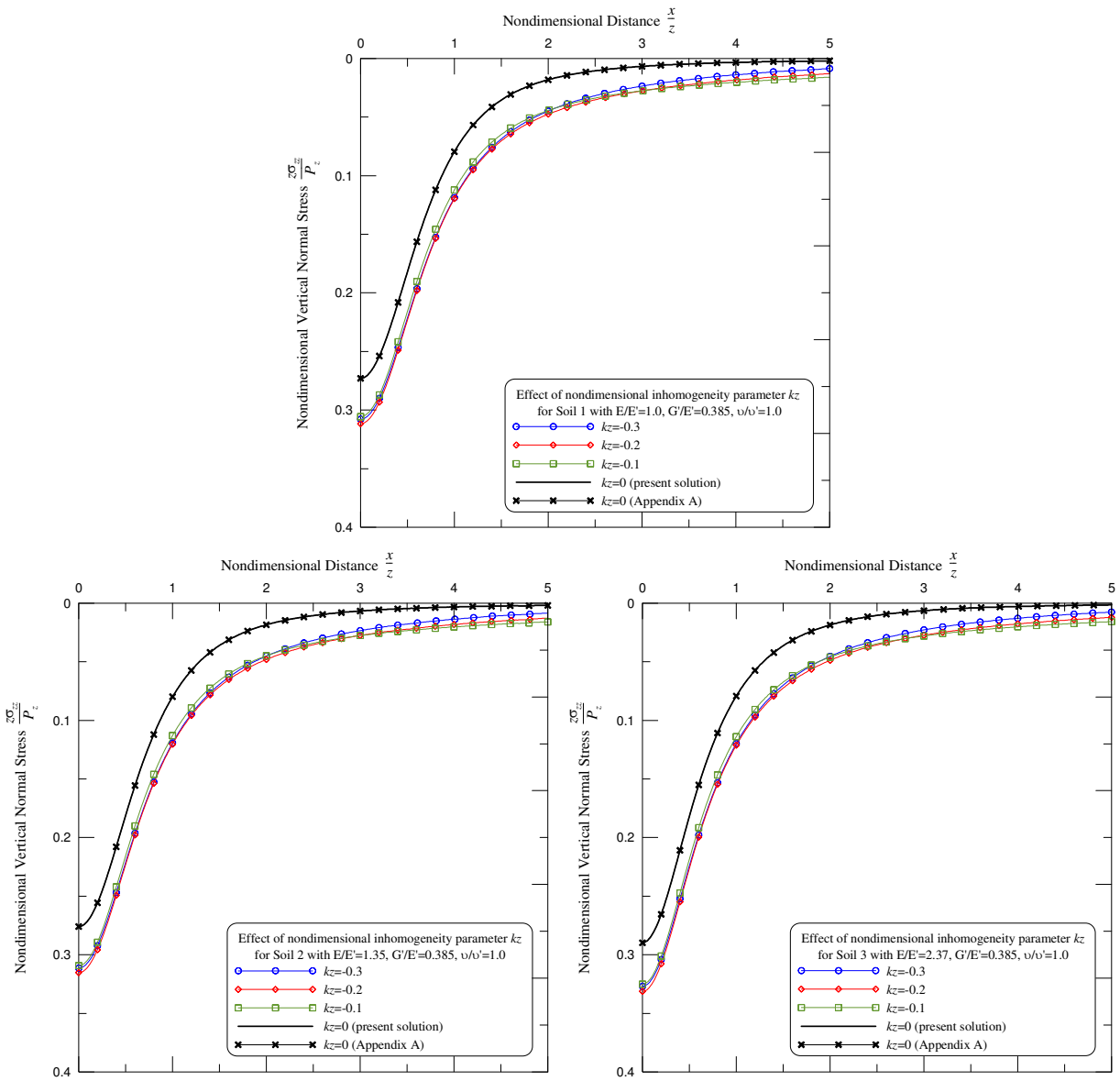

Figure 6. Effect of the inhomogeneity parameter kz on the vertical normal stress (σ_{zz}) induced by a vertical line load (P_z) for soil types 1–3. (Continued on next page.)

load are all compressive, and these phenomena are different from those in Figure 2 for the stresses owing to a horizontal line load.

It can be seen that the magnitudes of σ_{zz} induced by vertical line loading (Figure 6) are greater than those induced by horizontal line loading (Figure 2). Thus the type of loading (P_x or P_z) has a strong influence on σ_{zz}.

The plots for soils 1, 2 and 3 in Figure 6, with E/E' increasing from 1 to 1.35 and 2.37, all show the same trend, indicating that increases in E/E' (in this range) have only a minor effect on σ_{zz}.

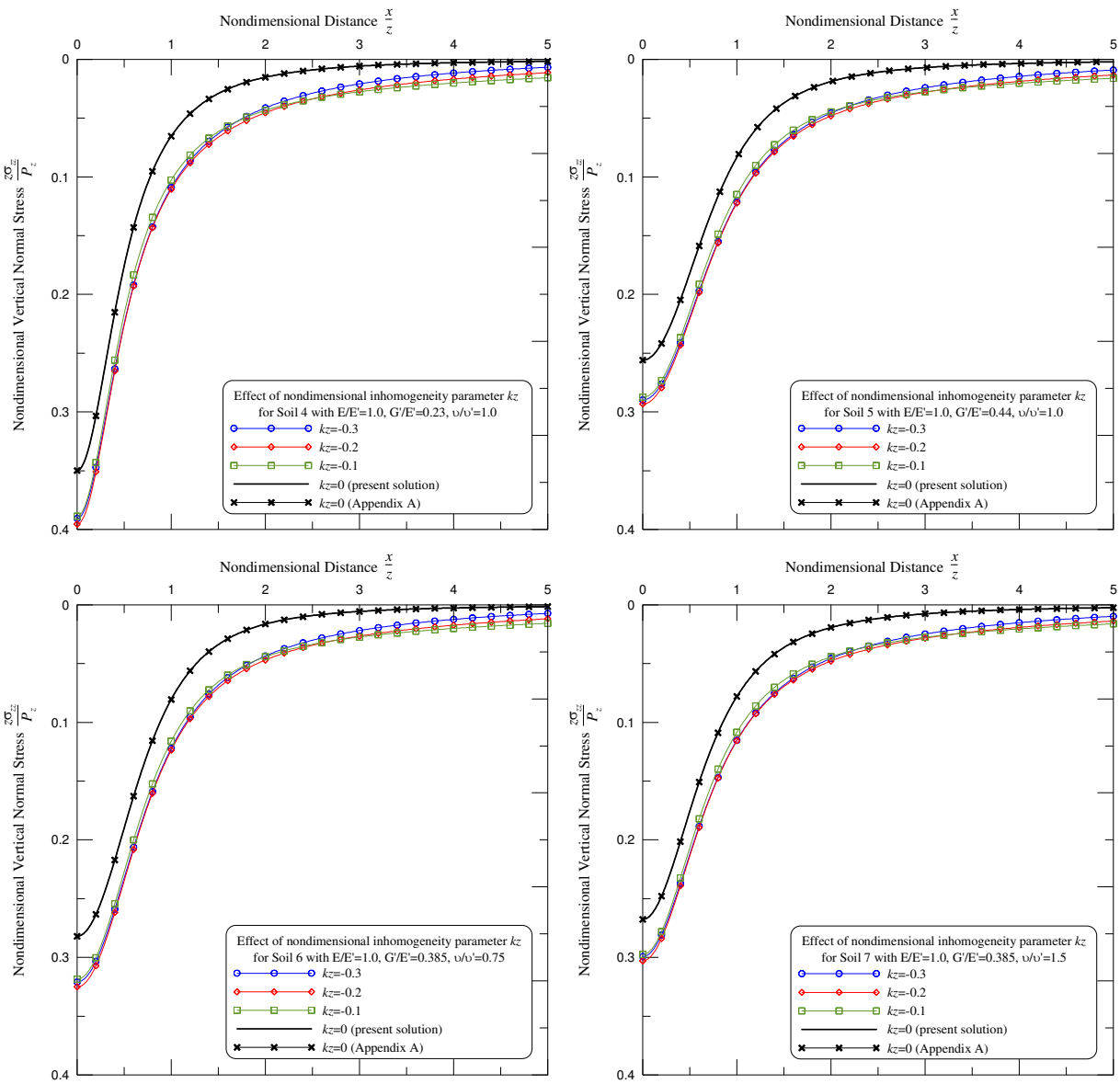

Figure 6 (continued). Effect of the inhomogeneity parameter kz on the vertical normal stress (σ_{zz}) induced by a vertical line load (P_z) for soil types 4–7.

A comparison of the plots as G'/E' decreases from 0.385 for soil 1 to 0.23 for soil 4, and again as it increases to 0.44 for soil 5, indicates that the ordering (relative to kz) of the graphs of $z\sigma_{zz}/P_z$ remains the same, but the magnitude changes significantly. The same is true for the decrease in ν/ν' from 1 for soil 1 to 0.75 for soil 6, and its increase to 1.5 for soil 7.

Figures 7–9 depict the effect of soil anisotropy (E/E', G'/E', and ν/ν') on the vertical normal stress (σ_{zz}) induced by a vertical line load (P_z) for three groups of soils: 1, 2, and 3 (E/E' varies, Figure 7); soils 1, 4, and 5 (G'/E' varies, Figure 8); and soils 1, 6, and 7 (ν/ν' varies, Figure 9).

In each figure the cases $kz = -0.3$ (E, E', and G' increase with depth) and $kz = 0$ (homogeneous) are shown, in the left and right panes respectively. It is seen that the induced vertical normal stresses are compressive for $kz = -0.3$ in all types of soil considered.

From Figure 7, left, we see that for $x/z < 0.5$, the value of $z\sigma_{zz}/P_z$ increases as E/E' grows from 1 to 1.35 to 2.37; however, with higher x/z from 0.5 to 2, $z\sigma_{zz}/P_z$ in soils 1, 2, and 3 moves toward the same values. In Figure 8, left, $z\sigma_{zz}/P_z$ increases as G'/E' drops from 0.385 to 0.23, and decreases as G'/E' grows from 0.385 to 0.44, within the range $x/z < 0.5$. It also can be found in Figure 9, left, that $z\sigma_{zz}/P_z$ increases with a drop in ν/ν' from 1 to 0.75, and decreases with an increase in ν/ν' from 1 to 1.5, at about $x/z < 1.2$.

The homogeneous case ($kz = 0$) is shown in the right-hand halves of Figures 7–9. When comparing this with the case $kz = -0.3$, we see that except for the magnitudes of $z\sigma_{zz}/P_z$ being diverse, the trends are similar. Overall, Figures 7–9 suggest that the magnitudes of vertical normal stresses are decisively influenced by soil anisotropy owing to a vertical line load in the isotropic/cross-anisotropic materials.

Moreover, it is evident from Figures 2–9 that the isotropic/cross-anisotropic materials resulting from different loading types (P_x and P_z) would affect the vertical normal stress. Therefore, we choose cross-anisotropic soil 6 ($\nu/\nu' = 0.75$) to interpret the effects of both loading types on σ_{zz}. Figure 10 shows

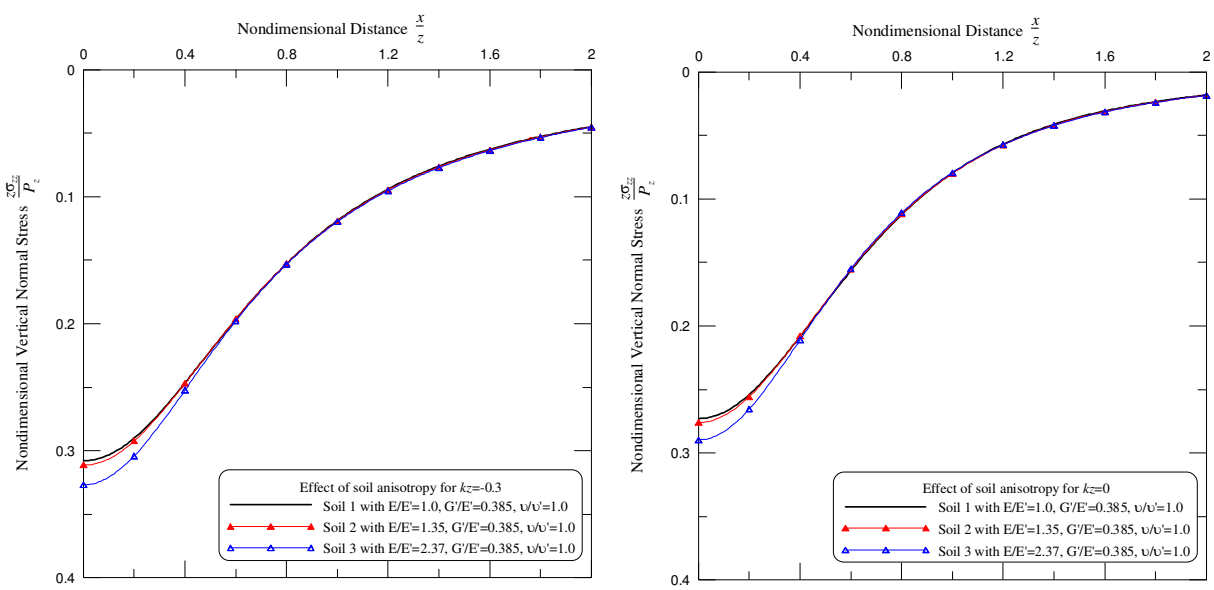

Figure 7. Effect of ratio E/E' on the vertical normal stress (σ_{zz}) induced by a vertical line load (P_z) when $kz = -0.3$ (left) and $kz = 0$ (right). Comparison of soils 1, 2, and 3.

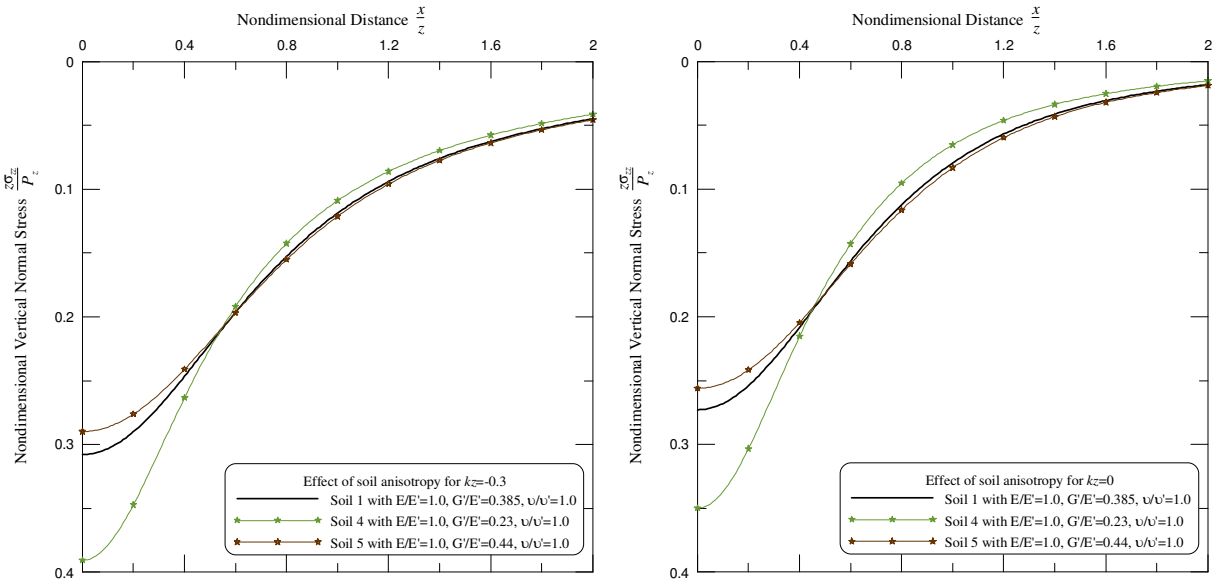

Figure 8. Effect of ratio G'/E' on the vertical normal stress (σ_{zz}) induced by a vertical line load (P_z) when $kz = -0.3$ (left) and $kz = 0$ (right). Comparison of soils 1, 4, and 5.

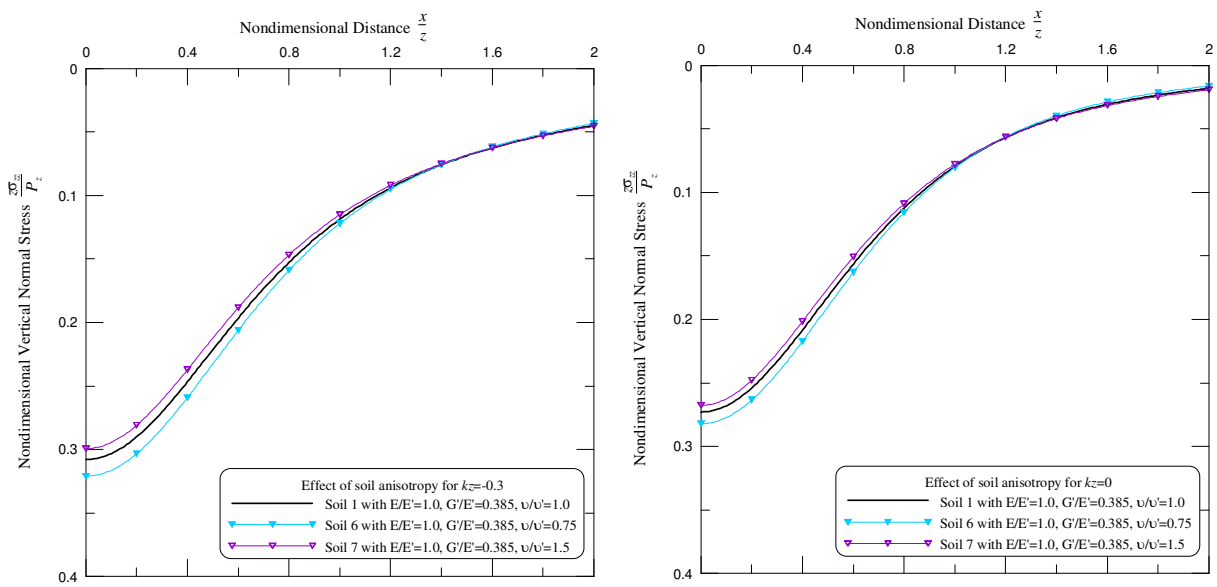

Figure 9. Effect of ratio ν/ν' on the vertical normal stress (σ_{zz}) induced by a vertical line load (P_z) when $kz = -0.3$ (left) and $kz = 0$ (right). Comparison of soils 1, 6, and 7.

the results for $kz = -0.3$, -0.2, -0.1, and 0. We see that the induced vertical normal stresses are larger from a vertical line load (P_z) than from a horizontal one (P_x) in the case of $kz \leq 0$. Thus the type of loading deeply affect the vertical normal stress in inhomogeneous cross-anisotropic soil 6.

The examples above confirm the present solutions and clarify how the nondimensional inhomogeneity parameter kz, the type and degree of soil anisotropy, and the types of loading would influence the vertical

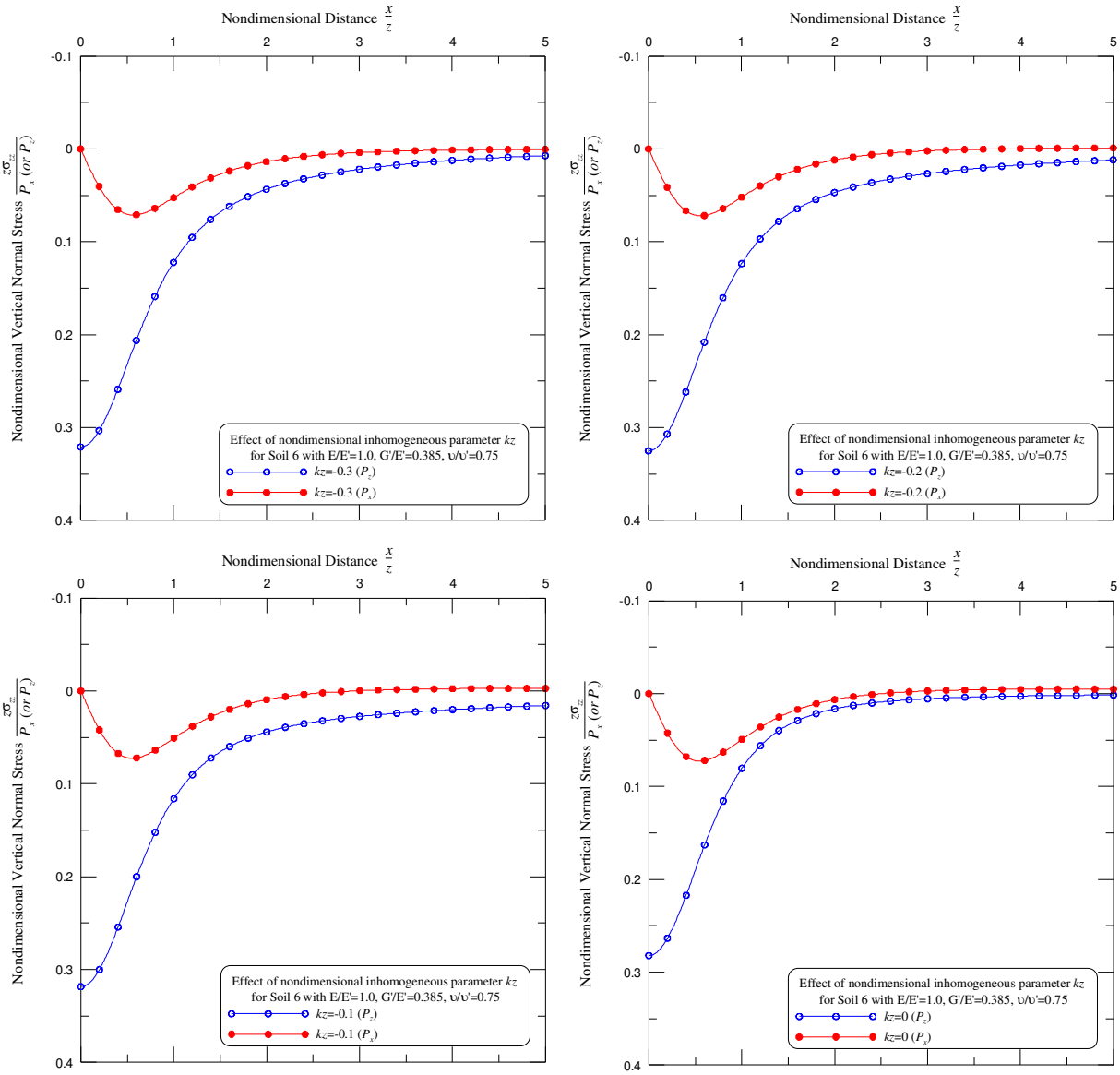

Figure 10. Effect of loading types (P_x and P_z) on the vertical normal stress (σ_{zz}) for cross-anisotropic soil 6 for $kz = -0.3$ (top left), -0.2, -0.1, and 0 (bottom right).

normal stress, σ_{zz}, in the inhomogeneous plane strain isotropic/cross-anisotropic material. Numerical results also show that the stress in the continuously inhomogeneous plane strain cross-anisotropic full space resulting from horizontal and vertical line loads can be easily calculated by the proposed solutions. The magnitudes and distributions of vertical normal stress are simply sensitive to the nondimensional inhomogeneity parameter kz (Figures 2 and 6), the anisotropic ratios specified by E/E', G'/E', ν/ν' (Figures 3–5 and 7–9), and the different loading types (Figure 10). Also, the adopted nondimensional horizontal distance x/z is another factor that could affect the present stress. Hence, the aforementioned

factors should be taken into account when estimating the displacements and stresses in an inhomogeneous plane strain cross-anisotropic medium subjected to applied line loads.

Conclusions

The fundamental solutions of displacements and stresses in a cartesian coordinate system for a continuously inhomogeneous plane strain cross-anisotropic full space with Young's and shear moduli varying exponentially with depth, due to horizontal and vertical line loads, are derived in this article. The planes of cross-anisotropy are assumed to be horizontal. Fourier transforms with respect to x are employed to find the solutions. However, inverse Fourier transforms for displacements and stresses are associated with complicated polynomial and exponential functions which cannot be given in exact closed forms; hence, numerical integration is required. The resulting integrals can be performed by the subroutine QDAGI between the limits $-\infty$ and ∞. The present solutions, setting the nondimensional inhomogeneity parameter $kz = 0$, are then compared with the extension of Wang and Liao's horizontal/vertical point load solutions to horizontal/vertical infinite line load solutions for a homogeneous cross-anisotropic full space, as shown in the Appendix. The numerical results agree very well with those obtained in the Appendix. Overall, the generated solutions indicate that the displacements and stresses are deeply affected by all the factors considered: the nondimensional inhomogeneity parameter (kz), the type and degree of material anisotropy (E/E', G'/E', and ν/ν'), the types of loading (P_x and P_z), and the nondimensional horizontal distance (x/z).

A series of parametric studies is conducted to demonstrate the present solutions, and elucidate the influence of aforementioned factors on the vertical normal stress. The results reveal that the computations of stresses (or displacements) should consider inhomogeneous characteristics in a cross-anisotropic material induced by applied line loads. In addition, these solutions could realistically imitate the actual stratum of loading problems in practical engineering. Most importantly, the proposed solutions can be used to derive the solutions of displacements and stresses resulting from the subjected line loads in an inhomogeneous plane strain cross-anisotropic half space; in particular, the actions of horizontal forces have never been provided in the literature. These matters will be addressed in forthcoming papers.

Appendix

The point load solutions of stress components for a homogeneous cross-anisotropic full space in a cartesian coordinate system can be rewritten from the solutions of [Wang and Liao 1999] as

$$\sigma_{xx}^{p} = \frac{P_x}{4\pi}\Big[(C_{11}-u_1' m_1 C_{13})g\frac{p_{11}}{m_1} - (C_{11}-u_2' m_2 C_{13})g\frac{p_{12}}{m_2} - 2C_{66}g\Big(\frac{p_{71}}{m_1}-\frac{p_{72}}{m_2}\Big) + 2u_3' p_{73}\Big] \qquad \text{(A.1)}$$
$$+\frac{P_z}{4\pi}g\big[(C_{11}-u_1' m_1 C_{13}-2C_{66})p_{31} - (C_{11}-u_2' m_2 C_{13}-2C_{66})p_{32} + 2C_{66}(p_{51}-p_{52})\big],$$

$$\sigma_{yy}^{p} = \frac{P_x}{4\pi}\Big[(C_{11}-u_1' m_1 C_{13}-2C_{66})g\frac{p_{11}}{m_1} - (C_{11}-u_2' m_2 C_{13}-2C_{66})g\frac{p_{12}}{m_2} + 2C_{66}g\Big(\frac{p_{71}}{m_1}-\frac{p_{72}}{m_2}\Big) - 2u_3' p_{73}\Big]$$
$$+\frac{P_z}{4\pi}g\big[(C_{11}-u_1' m_1 C_{13}-2C_{66})p_{31} - (C_{11}-u_2' m_2 C_{13}-2C_{66})p_{32} + 2C_{66}(p_{61}-p_{62})\big],$$

$$\sigma_{zz}^{p}=\frac{P_x}{4\pi}g\Big[(C_{13}-u_1'm_1C_{33})\frac{p_{11}}{m_1}-(C_{13}-u_2'm_2C_{33})\frac{p_{12}}{m_2}\Big] \tag{A.2}$$
$$+\frac{P_z}{4\pi}g\big[(C_{13}-u_1'm_1C_{33})p_{31}-(C_{13}-u_2'm_2C_{33})p_{32}\big],$$
$$\tau_{xy}^{p}=\frac{P_x}{4\pi}\Big[2C_{66}\Big(\frac{g}{m_1}p_{81}-\frac{g}{m_2}p_{82}\Big)-u_3'(2p_{83}-p_{23})\Big]-\frac{P_z}{2\pi}C_{66}g(p_{41}-p_{42}),$$
$$\tau_{yz}^{p}=-\frac{P_x}{4\pi}\Big[(u_1'+m_1)C_{44}\frac{g}{m_1}p_{41}-(u_2'+m_2)C_{44}\frac{g}{m_2}p_{42}-p_{43}\Big]-\frac{P_z}{4\pi}gC_{44}\big[(u_1'+m_1)p_{21}-(u_2'+m_2)p_{22}\big],$$
$$\tau_{xz}^{p}=\frac{P_x}{4\pi}\Big[(u_1'+m_1)C_{44}\frac{g}{m_1}p_{51}-(u_2'+m_2)C_{44}\frac{g}{m_2}p_{52}+p_{63}\Big]-\frac{P_z}{4\pi}gC_{44}\big[(u_1'+m_1)p_{11}-(u_2'+m_2)p_{12}\big],$$

where:

- C_{11}, C_{13}, C_{33}, and C_{44} are the elastic moduli or elasticity constants of the cross-anisotropic material, as seen in (2); however, $C_{66}=E/\big(2(1+\nu)\big)$.
- $u_3'=\sqrt{C_{66}/C_{44}}$, u_1', and u_2' are the roots of the following characteristic equation: $u'^4-su'^2+q=0$, where $s=\big(C_{11}C_{33}-C_{13}(C_{13}+2C_{44})\big)/(C_{33}C_{44})$ and $q=C_{11}/C_{33}$.

Since the strain energy is assumed to be positive definite in the material, the values of the elastic constants are restricted. Hence, there are three categories of the characteristic roots, u_1' and u_2', as follows:

Case 1: $u_{1,2}'=\pm\sqrt{\frac{1}{2}\left(s\pm\sqrt{s^2-4q}\right)}$ are two real distinct roots when $s^2-4q>0$;

Case 2: $u_{1,2}'=\pm\sqrt{\frac{s}{2}},\pm\sqrt{\frac{s}{2}}$ are double equal real roots when $s^2-4q=0$;

Case 3: $u_1'=\frac{1}{2}\sqrt{s+2\sqrt{q}}-i\frac{1}{2}\sqrt{-s+2\sqrt{q}}=\gamma-i\delta$ and $u_2'=\gamma+i\delta$ are two complex conjugate roots (where γ cannot be equal to zero) when $s^2-4q<0$.

- $m_j=\dfrac{(C_{13}+C_{44})u_j'}{C_{33}u_j'^2-C_{44}}=\dfrac{C_{11}-C_{44}u_j'^2}{(C_{13}+C_{44})u_j'}\quad(j=1,2),\qquad g=\dfrac{C_{13}+C_{44}}{C_{33}C_{44}(u_1'^2-u_2'^2)}.$
- Defining p_{1i}–p_{8i} in (A.1)–(A.2) as the elementary functions, they can be represented as

$$p_{1i}=\frac{x}{R_i^3},\qquad p_{2i}=\frac{y}{R_i^3},\qquad p_{3i}=\frac{z_i}{R_i^3},\qquad p_{4i}=\frac{xy(2R_i+z_i)}{R_i^3(R_i+z_i)^2},$$
$$p_{5i}=\frac{1}{R_i(R_i+z_i)}-\frac{x^2(2R_i+z_i)}{R_i^3(R_i+z_i)^2},\qquad p_{6i}=\frac{1}{R_i(R_i+z_i)}-\frac{y^2(2R_i+z_i)}{R_i^3(R_i+z_i)^2},$$
$$p_{7i}=\frac{x}{R_i^3}-\frac{3x}{R_i(R_i+z_i)^2}+\frac{x^3(3R_i+z_i)}{R_i^3(R_i+z_i)^3},\qquad p_{8i}=\frac{y}{R_i^3}-\frac{3y}{R_i(R_i+z_i)^2}+\frac{y^3(3R_i+z_i)}{R_i^3(R_i+z_i)^3},$$

and

$$R_i=\sqrt{x^2+y^2+z_i^2},\qquad z_i=u_i'z\quad(i=1,2,3).$$

The solutions for stresses in a homogeneous cross-anisotropic full space due to infinite horizontal and vertical line loads can be directly obtained by integrating the elementary functions of the point load solutions (p_{1i}–p_{8i}). That is, the explicit solutions for stresses caused by horizontal and vertical infinite line loads in a full space can be regrouped in the form of (A.1)–(A.2). In other words, the exact

solutions for the present case are the same as (A.1)–(A.2) except that the elementary functions, p_{1i}–p_{8i} $(i = 1, 2, 3)$, are replaced by the integral functions, L_{1i}–L_{8i} $(i = 1, 2, 3)$, respectively. Therefore, only L_{1i}–L_{8i} $(i = 1, 2, 3)$ are derived, and are given as

$$\begin{aligned}
L_{1i} &= \int_{-\infty}^{\infty} p_{1i}\,dy = \frac{2x}{x^2 + z_i^2}, & L_{2i} &= \int_{-\infty}^{\infty} p_{2i}\,dy = 0,\\
L_{3i} &= \int_{-\infty}^{\infty} p_{3i}\,dy = \frac{2z_i}{x^2 + z_i^2}, & L_{4i} &= \int_{-\infty}^{\infty} p_{4i}\,dy = 0,\\
L_{5i} &= \int_{-\infty}^{\infty} p_{5i}\,dy = \frac{2z_i}{x^2 + z_i^2}, & L_{6i} &= \int_{-\infty}^{\infty} p_{6i}\,dy = 0,\\
L_{7i} &= \int_{-\infty}^{\infty} p_{7i}\,dy = 0, & L_{8i} &= \int_{-\infty}^{\infty} p_{8i}\,dy = 0.
\end{aligned} \tag{A.3}$$

References

[Azis and Clements 2001] M. I. Azis and D. L. Clements, "A boundary element method for anisotropic inhomogeneous elasticity", *Int. J. Solids Struct.* **38**:32–33 (2001), 5747–5763.

[Barros and Mesquita 1999] P. L. A. Barros and E. de Mesquita Neto, "Elastodynamic Green's functions for orthotropic plane strain continua with inclined axes of symmetry", *Int. J. Solids Struct.* **36**:31–32 (1999), 4767–4788.

[Chen et al. 2001] L. Chen, A. J. Kassab, D. W. Nicholson, and M. B. Chopra, "Generalized boundary element method for solids exhibiting nonhomogeneities", *Eng. Anal. Boundary Elem.* **25**:6 (2001), 407–422.

[Cihan 2003] O. A. Cihan, "Contact mechanics of a graded surface with elastic gradation in lateral direction", MS Thesis, The Middle East Technical University, Ankara, 2003.

[Davis and Rabinowitz 1984] P. J. Davis and P. Rabinowitz, *Methods of numerical integration*, 2nd ed., Academic Press, New York, 1984.

[Doherty and Deeks 2002] J. P. Doherty and A. J. Deeks, "Applications of the scaled boundary finite-element method to offshore geotechnical problems", pp. 706–711 in *Twelfth International Offshore and Polar Engineering Conference*, Kyushu, 2002.

[Doherty and Deeks 2003a] J. P. Doherty and A. J. Deeks, "Elastic response of circular footings embedded in a non-homogeneous half-space", *Géotechnique* **53**:8 (2003), 703–714.

[Doherty and Deeks 2003b] J. P. Doherty and A. J. Deeks, "Scaled boundary finite-element analysis of a non-homogeneous axisymmetric domain subjected to general loading", *Int. J. Numer. Anal. Meth. Geomech.* **27**:10 (2003), 813–835.

[Doherty and Deeks 2003c] J. P. Doherty and A. J. Deeks, "Scaled boundary finite-element analysis of a non-homogeneous elastic half-space", *Int. J. Numer. Meth. Eng.* **57**:7 (2003), 955–973.

[Doherty and Deeks 2005] J. P. Doherty and A. J. Deeks, "Stiffness of flexible caisson foundations embedded in nonhomogeneous elastic soil", *J. Geotech. Geoenvironmental Eng., ASCE* **131**:12 (2005), 1498–1508.

[Doherty and Deeks 2006] J. P. Doherty and A. J. Deeks, "Stiffness of a flexible circular footing embedded in an elastic half-space", *Int. J. Geomech., ASCE* **6**:1 (2006), 46–54.

[Gazetas 1982] G. Gazetas, "Stresses and displacements in cross-anisotropic soils", *J. Geotech. Eng. Div., ASCE* **108**:4 (1982), 532–553.

[Giannakopoulos and Suresh 1997] A. E. Giannakopoulos and S. Suresh, "Indentation of solids with gradients in elastic properties: Part I. Point force", *Int. J. Solids Struct.* **34**:19 (1997), 2357–2392.

[Gibson 1974] R. E. Gibson, "The analytical method in soil mechanics", *Géotechnique* **24**:2 (1974), 115–140.

[Gray et al. 2001] L. J. Gray, J. D. Richardson, T. Kaplan, J. Berger, P. A. Martin, and G. H. Paulino, "Green's functions for exponentially graded elastic materials", pp. 327 in *Sixth U.S. National Congress on Computational Mechanics*, Dearborn, 2001.

[Hu et al. 2007] T. B. Hu, C. D. Wang, and J. J. Liao, "Elastic solutions for a transversely isotropic full space with inclined planes of symmetry subjected to a point load", *Int. J. Numer. Anal. Meth. Geomech.* **31**:12 (2007), 1401–1442.

[Lee and Rowe 1989] K. M. Lee and R. K. Rowe, "Deformation caused by surface loading and tunneling: the role of elastic anisotropy", *Géotechnique* **39**:1 (1989), 125–140.

[Longman 1956a] I. M. Longman, "Note on a method for computing infinite integrals of oscillatory functions", *Proc. Cambridge Philos. Soc.* **52** (1956), 764–768.

[Longman 1956b] I. M. Longman, "Tables for the rapid and accurate numerical evaluation of certain infinite integrals involving Bessel functions", *Proc. Cambridge Philos. Soc.* **52** (1956), 166–180.

[Martin 2004] P. A. Martin, "Fundamental solutions and functionally graded materials", in *Seventh International Conference on Integral Methods in Science and Engineering* (Saint-Étienne, 2002), edited by C. Constanda et al., Birkhäuser, Boston, 2004.

[Martin et al. 2002] P. A. Martin, J. D. Richardson, L. J. Gray, and J. R. Berger, "On Green's function for a three-dimensional exponentially graded elastic solid", *Proc. Royal Soc. London A* **458** (2002), 1931–1947.

[Piessens et al. 1983] R. Piessens, R. DeDoncker-Kapenga, C. W. Überhuber, and D. K. Kahaner, *QUADPACK: a subroutine package for automatic integration*, Springer, New York, 1983.

[Poulos and Davis 1974] G. H. Poulos and E. H. Davis, *Elastic solutions for soil and rock mechanics*, Wiley, New York, 1974.

[Tarn and Lu 1991] J. Q. Tarn and C. C. Lu, "Analysis of subsidence due to a point sink in an anisotropic porous elastic half space", *Int. J. Numer. Anal. Meth. Geomech.* **15**:4 (1991), 573–592.

[Wang and Liao 1999] C. D. Wang and J. J. Liao, "Elastic solutions for a transversely isotropic half-space subjected to buried asymmetric-loads", *Int. J. Numer. Anal. Meth. Geomech.* **23**:2 (1999), 115–139.

[Wang and Tzeng 2009] C. D. Wang and C. S. Tzeng, "Displacements and stresses induced by nonuniform circular loads in an inhomogeneous cross-anisotropic material", *Mech. Res. Commun.* **36** (2009), 921–932.

[Wang et al. 2003] C. D. Wang, C. S. Tzeng, E. Pan, and J. J. Liao, "Displacements and stresses due to a vertical point load in an inhomogeneous transversely isotropic half-space", *Int. J. Rock Mech. Mining Sci.* **40**:5 (2003), 667–685.

[Wang et al. 2006] C. D. Wang, E. Pan, C. S. Tzeng, F. Han, and J. J. Liao, "Displacements and stresses due to a uniform vertical circular load in an inhomogeneous cross-anisotropic half-space", *Int. J. Geomech., ASCE* **6**:1 (2006), 1–10.

[Wang et al. 2008] C. D. Wang, M. T. Chen, and T. C. Lee, "Surface displacements due to batter piles driven in cross-anisotropic media", *Int. J. Numer. Anal. Meth. Geomech.* **32**:2 (2008), 121–141.

[Ward et al. 1965] W. H. Ward, A. Marsland, and S. G. Samuels, "Properties of the London clay at the ashford common shaft", *Géotechnique* **15**:4 (1965), 321–344.

Received 13 Jan 2009. Revised 8 Aug 2009. Accepted 13 Aug 2009.

CHENG-DER WANG: cdwang@nuu.edu.tw
Department of Civil and Disaster Prevention Engineering, National United University, No. 1, Lien Da, Kung-Ching Li, Miao-Li, Taiwan 360, Taiwan

JIA-YAN HOU: ayanyan1982@yahoo.com.tw
Department of Civil and Disaster Prevention Engineering, National United University, No. 1, Lien Da, Kung-Ching Li, Miao-Li, Taiwan 360, Taiwan

WEI-JER WANG: wwj111@nuu.edu.tw
Department of Civil and Disaster Prevention Engineering, National United University, No. 1, Lien Da, Kung-Ching Li, Miao-Li, Taiwan 360, Taiwan

JOURNAL OF MECHANICS OF MATERIALS AND STRUCTURES
Vol. 5, No. 2, 2010

MECHANICAL AND FRACTURE ANALYSIS OF WELDED PEARLITIC RAIL STEELS

ALDINTON ALLIE, HESHMAT A. AGLAN AND MAHMOOD FATEH

Welding rail steels using gas metal arc welding shows promise for repairing railhead defects. Finite element analysis was performed on the rail before and during the welding process. It was revealed that the sizes of the heat affected zone (HAZ) and fusion zone would be approximately 15 mm and 5 mm respectively. Hardness tests showed that the parent material is harder than both the HAZ and the welded region. The parent steel has ultimate strength, yield strength, and elongation to failure of 1114 MPa, 624 MPa, and 11.1% respectively. These values are higher than those of the welded rail steel. The average K_I for the parent specimen was 70 MPa·m$^{0.5}$, while for the welded steel it was 54 MPa·m$^{0.5}$. The pearlitic steel displayed ductile fracture features immediately ahead of the crack tip but approaching the end of the fracture surface the failure mechanism became less ductile. The welded rail steel in contrast consists of ductile features throughout the entire fracture surface.

1. Introduction

Welding produces very high temperatures in the area of the weld and these temperatures decrease rapidly as the distance from the weld increases. This heating followed by cooling to ambient temperature produces stresses in the rail. When the temperature of the rail returns to ambient temperature these stresses remain and are referred to as residual stresses [Little and Kamtekar 1998]. To reduce the formation of residual stresses, the rail steel is usually heated before the welding process begins [Funderburk 1997]. This method of heating the rail is called preheating and creates a softer and tougher structure. Properly monitoring and sometimes adjusting the temperature of both the base metal and weld metal before, during, and after welding is more likely to yield a successful weld. Improper rates of heating and cooling may cause defects to be formed in the welded area or the base material [Funderburk 2000]. Examinations and audits of welding procedures on failed welds conducted by Mutton and Alvarez [2004] have shown that the most likely cause of defects is an insufficient preheat temperature. Preheating may be done by gas torches, ovens, or electrical devices depending on the size of the part being welded and the type of welding equipment being used [Funderburk 2000; WTIA 2006]. When preheating, the temperature of the base material must also be in the range of the preheat temperature within 75 mm of the welded area in all directions [Mutton and Alvarez 2004; Chandler 2008]. The temperature of the welded joint can be checked by using a thermocouple, a temperature indicating crayon, or a contact thermometer [Reis and Harness 2004]. Preheating is done for several reasons; it slows the cooling rate in the base material and weld metal, which produces a more ductile metallurgic structure. This slow cooling also

Keywords: welded rail steels, heat affected zone, welding efficiency, fracture toughness.
This work was sponsored by the Federal Railroad Administration. The authors would also like to acknowledge Mike Cannon, lab manager at Tuskegee University, for his assistance in the welding procedures.

allows hydrogen to diffuse from the weld metal, reducing the potential for forming imperfections. It also reduces shrinkage stresses that help in reducing imperfections that may be formed in the weld metal or base material [WTIA 2006; Chandler 2008].

The interpass temperature is defined as the temperature of the base metal between the first and last welding pass at the time welding is to be performed [Funderburk 1999; 2000; Mutton and Alvarez 2004; Lincoln 2005]. The interpass temperature is usually considered as more important than the preheat temperature with regards to the mechanical and microstructural properties of the weldment [Lincoln 2005]. A high interpass temperature will reduce the weld metal strength but usually improves toughness due to a finer grain structure with grain size measured in microns. However, if the interpass temperature is excessive the toughness trend is reversed. Therefore, it is important to maintain the minimum interpass temperature to prevent weld defects while at the same time the maximum interpass temperature must be controlled to provide satisfactory mechanical properties [Lincoln 2005]. The proper preheat and interpass temperatures to be used are dependent on the chemical composition and the thickness of the base material [Funderburk 1999; Tojo 2003]. For low carbon steels with a carbon content of approximately 0.3% a preheat temperature of 25–150°C is required. For medium carbon steels with carbon content of approximately 0.3%–0.45% a preheat temperature of 150–260°C is required. And for high carbon steels with carbon content exceeding 0.45% a preheat temperature of 260–425°C is required. To determine appropriate temperatures within the ranges of the different carbon content steels, use higher temperatures for higher carbon contents and for larger base materials [Funderburk 1999].

The hardness of a metal is mainly dependent on the phases that are present, with increases in martensite giving an increased hardness [El-Banna et al. 2000]. When conducting hardness testing the distributions of hardness in the weld, heat affected zone (HAZ), and rail base metal should be shown [Saarna and Laansoo 2004]. A weld containing a wide HAZ or having a low hardness in the fusion zone is predisposed to batter, which may contribute to premature failure in the weld [Mutton and Alvarez 2004]. An increase in the cooling rate of a work piece will provide higher hardness values [El-Banna et al. 2000]. However, if the cooling rate is too fast it may cause the base material to crack. Hardness testing is the simplest method for approximating the quality of a rail weld, but on its own it does not give a true assessment of the rail weld. It is therefore complemented by other test results, including tensile, fatigue, and fracture tests, et cetera [Saarna and Laansoo 2004].

Tensile tests are used to determine the weld metal quality in comparison to the parent rail. The ratio of the weld-to-parent ultimate tensile strength is known as the weld efficiency [Orange 1966]. The tensile strength of pearlitic steels has been proven to be dependent on the ferrite-cementite lamellae spacing, with a smaller spacing giving a higher strength [Aglan and Fateh 2006; 2007]. The thermal cycle associated with welding may cause the mechanical properties in the HAZ to be degraded by grain coarsening, precipitation, and by segregation of trace impurities [Kim et al. 2001]. When a sequence of several weld deposits, called a multirun, is used in welding the microstructure of the weld becomes much more complicated as the deposition of each successive layer of weld heat treats the underlying microstructure. This heat treating may apply a temperature high enough to cause the reformation of austenite, which during cooling transforms the part to a different microstructure [Sugden and Bhadeshia 1989; Bhadeshia 1997].

The purpose of fracture toughness testing is to give a measure of the resistance of the material to fracture [Crear 2001, Chapter 5, p. 5-4]. Once the critical crack length is detected in a rail, it is considered

unsafe and must therefore be removed from the track. There are four methods that may be used to calculate the fracture toughness, including the Charpy v-notch test, the crack tip opening displacement, the plain strain fracture toughness test (K_{Ic}), and the plain stress fracture toughness (K_I). The latter will be used to study the fracture resistance of the welded pearlitic rail steel. Due to the complexity of the welding process, the toughness of welds is dependent on a lot more variables than the toughness of the steel [Bhadeshia 1997]. The toughness of carbon steels has been shown to be dependent on the prior austenite grain size, with a decrease in the grain size increasing the fracture toughness [Gray et al. 1982; Lewandowski and Thompson 1986]. In most cases, an increase in the strength of a steel decreases its toughness. This occurs because as the strength increases, plastic deformation, which is the major energy absorption mechanism during fracture, becomes more difficult [Bhadeshia 1997]. The type of welding process that is used will also play a significant role in the toughness of the steel, because each welding process is different, and forms different microstructures in the process [Bhadeshia 1997]. The general expression that is used to calculate the value of K_{Ic} is shown in the following equation:

$$K_{Ic} = \sigma \sqrt{\pi a} f\left(\frac{a}{W}\right), \tag{1}$$

where σ is the residual strength for a notched specimen, a is the crack length, and $f(a/W)$ is a geometrical correctional factor, which is given by the following equation [Aglan and Fateh 2007]:

$$f\left(\frac{a}{W}\right) = 1.12 - 0.231\frac{a}{W} + 10.55\left(\frac{a}{W}\right)^2 - 21.72\left(\frac{a}{W}\right)^3 + 30.39\left(\frac{a}{W}\right)^4. \tag{2}$$

The ASTM E399, plain strain fracture toughness is generally used in determining K_{IC}. This standard requires that the thickness, t, and crack length, a, both exceed $2.5 \times (K_{1c}/\sigma_{ys})^2$ for the result to qualify as a plain strain fracture toughness, K_{1c}. K_{1c} is the calculated fracture toughness and σ_{ys} is the yield strength of the unnotched sample. For thin specimens, plain stress may be dominant and K_I can be designated as the plain stress fracture toughness.

2. Materials and experimental parameters

The materials used in the present work were pearlitic rail steels provided by the Transportation Technology Center, Inc. The composition of the material is shown in Table 1. The rail sections provided were approximately 304.8 mm long. Two grooves were milled in the railhead, each having 25.4 mm width and 19.05 mm depth. Each groove was located 63.5 mm away from an end. This was done to

	C	Mn	P	Si	Ti
Parent	0.92–1.01	0.69–1.04	~0.015	0.37–0.44	0.001–0.018
LA-100	0.05–0.06	1.55–1.70	0.005–0.007	0.40–0.50	0.02–0.04
	Cu	N	S	Cr	
Parent	~0.3	~0.0054	~0.007	~0.22	
LA-100	0.10–0.20		0.003–0.005	0.02–0.05	

Table 1. Chemical compositions of the pearlitic rail steel and of the Superarc LA-100 welding wire.

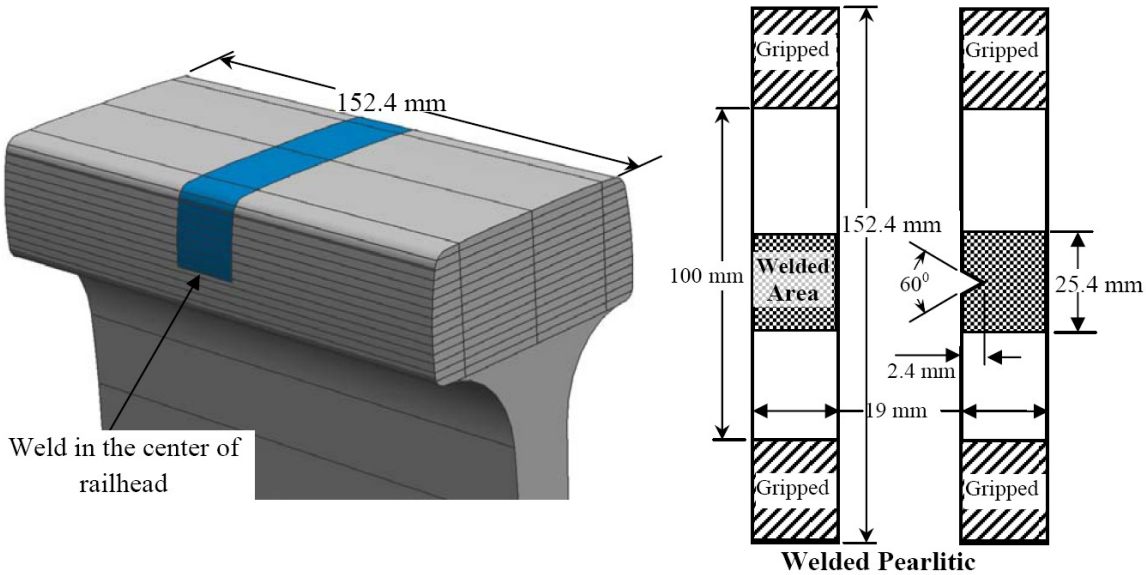

Figure 1. Schematic diagram of the railhead showing how specimens were machined (left) and the dimensions of the welded test specimens (right).

simulate the removal of materials from a railhead containing defects. A strip heater, 177.8 mm long and 38.1 mm wide, was placed on each side of the rail web in the center of the longitudinal direction. The strip heaters used had a maximum heat transfer of 250 W each. Finite element analysis (FEA) was performed to determine the temperature profile before and during welding and to determine the size of the HAZ. Before welding, the rail was preheated to 340°C, to prevent cracking or inclusions in the weld. The groove was then filled using a Millermatic350, a gas metal arc welder. A heat input of 1397.6 KJ/m and a wire feed speed of 10.41 m/min were employed. The welding wire used was the Superarc LA-100 manufactured by Lincoln Electric with chemical properties shown in Table 1. This wire was chosen because its mechanical properties were the closest match to that of the parent rail steel.

After welding, the excess weldment was removed from the rail steel by grinding. The rail was then cut into two halves with the weld in the center of both sections. Specimens were then machined from the welded pearlitic rail head along the direction of the rail using electrical discharge machining. A Unigraphics drawing of the welded rail after grinding is shown in Figure 1 along with the typical slices that were prepared for testing.

The welded pearlitic rail steel contains the weld in the center of the specimen and is 25.4 mm long. Both parent and welded rail steel had dimension of 152 mm length, 19 mm width, and 2 mm thickness. Notched specimens were also prepared with a 60° notch at one free edge in the center of the specimen. The notch depth was approximately 2.4 mm with a notch depth to width ratio (a/W) of 0.125 for both the pearlitic and welded rail steels. Static tensile tests were performed on both notched and unnotched specimens under displacement control mode using an MTS servohydraulic machine with TestStar data acquisition software. The results from the unnotched specimen were used to obtain the stress-strain relationship and the results from the notched specimen were used to obtain the residual strength and fracture properties.

3. Results and discussion

3.1. ***Finite element analysis (FEA) of heated rail sections.*** FEA was used to study the heat transfer of the rail steel, with heat strips on opposite sides of the rail web, before and during the welding process. SolidWorks 2007 was utilized to perform the FEA. The temperature that was applied to the rail by the strip heaters in this study was 340°C. This temperature was applied because the preheat temperature of high carbon steels should range from 260–425°C, with the high carbon range being above 0.45% carbon [Lincoln 2005]. This implies that a thick material with carbon content of 1% should use a higher temperature from this range. The heat flux of the heaters was calculated as Q/A, where Q is the amount of heat transferred and A is the area of the heating surface. The heat flux of each electrical strip heater was calculated and found to be 36.93 KW/m^2.

The boundary conditions that were used in the thermal analysis of the rail steel include: The web and base of the rail were considered adiabatic because fiber glass insulation was used to help prevent the loss of heat to the environment and the head of the rail was considered as undergoing convection since it was open to its surroundings. The ambient temperature used for this analysis was 26°C and the convection was calculated using the equation

$$h = \frac{\mathrm{Nu}\,K}{L}, \tag{3}$$

where h is the convective heat transfer coefficient, Nu is the Nusselt number, K is the thermal conductivity, and L is the average length of the railhead represented as a square. From this calculation, it was found that the convective heat transfer coefficient of the rail was 10.26 W/m^{2}K.

Prewelding. All the boundary conditions mentioned above were used in the prewelding analysis of the rail. The FEA heat distribution diagram was obtained for these conditions. From the plot it was noted that there is an insignificant variation in the temperature distribution in the rail, since the highest temperature was 340°C compared to the lowest, 310°C. This is a difference of 30°C. This demonstrates that the electrical strip heaters are very efficient in heating the groove to the desired temperature, even with the rail head exposed to the environment.

During welding. During welding, all the boundary conditions that were applied previously were applied again, along with one additional boundary condition. For this condition, it was assumed that the welding arc applied a heat of 4500°C and this heat was applied to a small circular location at the bottom of the groove. The assumption of 4500°C was based on an average value stated in the literature. The range given was between 3000°C to 6000°C for the temperature of the arc generated from a MIG welder [Dorzin 2003]. The plot of the heat distribution was obtained from the FEA. The distribution showed that the temperature at the arc was much higher than that of the heaters. It can be assumed from this observation that the temperature of the electrical strip heaters does not play a significant role in heating the groove during welding. However, the heat strips are still considered very important during welding because the process will be stopped at times to remove any inclusions that may be present in the weld, and the heaters will be needed to maintain the minimum interpass temperature during this period.

The temperature profile at the welding arc to the center of the rail web directly below the arc was studied to understand the temperature distribution of the arc on the rail; this distribution is shown in Figure 2a. The temperature is taken every 5 mm starting from the bottom of the groove.

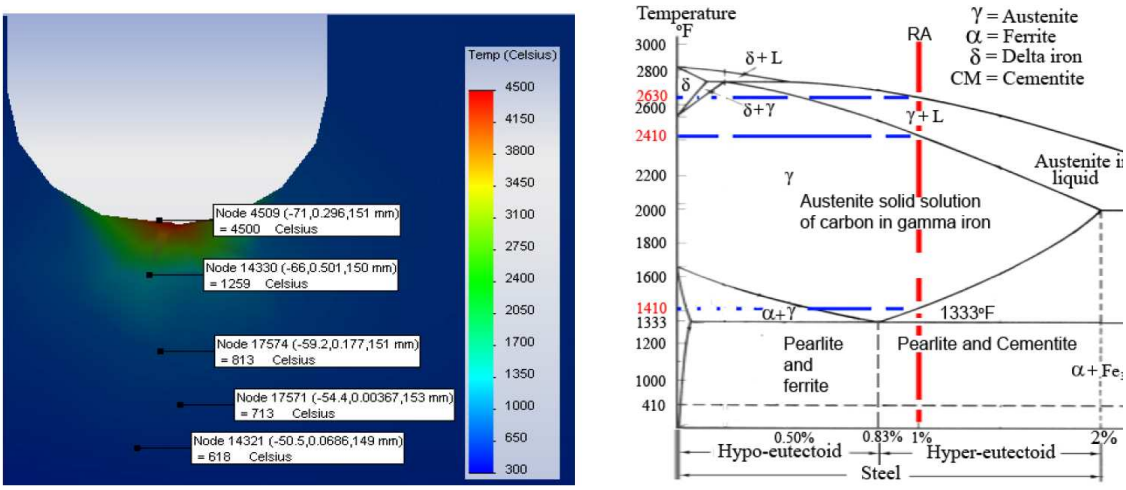

Figure 2. Left: Heat distribution during welding. Right: Iron-carbon phase diagram.

Studying this distribution in conjunction with the iron-carbon phase diagram shown in Figure 2b, taken from [Cornell and Bhadeshia 1999], will give a good indication of the sizes of the HAZ and the fusion zone. The line labeled RA shows the carbon content of the rail being studied. Following this line to the first change in the microstructure of the material would indicate the minimum temperature of the HAZ. The diagram shows that this temperature is 723°C. Figure 2a suggests that this temperature is reached approximately 15 mm from the center, so this length is indicative of the size of the HAZ. From the phase diagram it is seen that once the temperature reaches 1443°C all of the metal becomes liquid, which shows where the fusion would start. This region is at approximately 5 mm, which shows that the rail should be properly fused with the weld metal.

3.2. ***Hardness distribution of welded pearlitic rail steel.*** The hardness distribution from the center of the weld was recorded using a handheld hardness tester. The first two slices of the rail were removed to expose the middle layers for hardness testing. The hardness distribution of the rail steel from the weld's center is shown in Figure 3, with the center of the weld being at 0 mm and the weld's width extending from −12.7 mm to 12.7 mm. The hardness of the rail is taken every 12.7 mm.

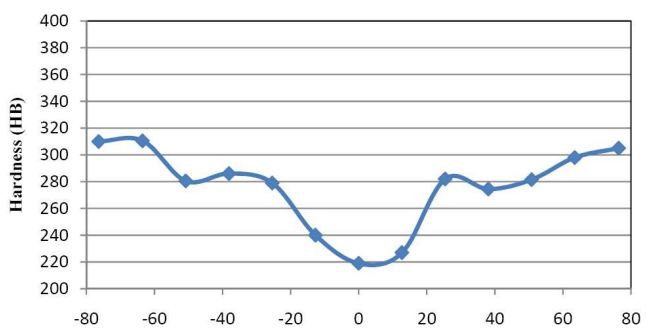

Figure 3. Hardness of rail steel versus distance to center of weld, in mm.

There is a clear trend to the right and to the left of the center of the weld, which shows that the further from the weld the harder the material. The two furthest points to the left and to the right of the weld, the parent rail, are in the range 300–315 HB. The graph shows that 20.4 mm to 50.8 mm to the right and left of the weld's center the hardness is slightly lower than the actual hardness of the rail, being in the range 279–286 HB. This decrease in hardness is associated with the HAZ, with decreased hardness due to the heat treatment produced during welding. The weld's hardness is significantly lower than the parent rail with a range of 220–240 HB. This hardness is due to the filler material used for welding and the heat treatment associated with multirun welds. The hardness of the weld and HAZ may be increased by heat treating the rail using a specific type of hardening technique, either induction or flame hardening. If this is not done the weld and HAZ will be prone to batter, leading to premature failure of the weld in service.

3.3. ***Microstructure of welded rail.*** The microstructure of the parent rail, HAZ, fusion line, and weld were studied using optical microscopy. The locations where the optical micrographs were taken are shown in Figure 4, together with sample micrographs at 100 times magnification. In the micrograph on the top left, taken in the parent rail, a typical pearlite microstructure is clearly seen. The pearlite microstructure consists of a fine lamellar aggregate of soft and ductile ferrite and very hard cementite. The micrograph on the top right shows that the microstructure of the HAZ has been altered by the welding process. This micrograph shows that the HAZ consists of a coarser pearlite structure than the parent rail.

The fusion zone of the weld shown in micrograph in Figure 4, bottom left, consists of the weld to the right and the HAZ to the left of the image. The change in the microstructure from the HAZ to the weld can be clearly seen and shows that the grain size of the weld is much smaller than that of the HAZ. The micrograph on the bottom right part of the figure reveals that the metallurgy of the weld is very different from that of the parent material. The weld material consists of a lower acicular ferrite plate structure containing small amounts of cementite. The dark regions between the ferrite consist of mainly martensite. This mixture containing mostly ferrite and small amounts of cementite and martensite explains the hardness of the weld; ferrite is soft while martensite and cementite are hard.

3.4. ***Stress-strain relationships.*** A comparative study was conducted on both the welded and parent pearlitic rail to study the effects of welding on the mechanical properties of the rail. The stress-strain relationships of the pearlitic rail steels used were previously studied [Aglan and Gan 2001; Aglan et al. 2004; 2006; 2007]. Figure 5, left, shows the average stress-strain curves for the welded and parent pearlitic rail steel. Both curves consist of linear elastic behavior followed by nonlinear plastic behavior until failure. However, the elastic modulus of the welded pearlitic rail steel is higher than that of the parent pearlitic rail steel, with that for the welded rail being 275 GPa and for the parent rail being 200 GPa [Aglan and Gan 2001]. The figure also shows that the nonlinear plastic portion of the welded rail's curve falls below that of the parent rail. This shows that the welded rail's tensile strength is not as high as the parent rail. The strain to failure of the welded rail shows a significant decrease which reveals that the welded rail is not as ductile as the parent rail.

Table 2 lists the mechanical properties for both the welded and parent pearlitic rail steels. The ultimate strength declined by 47% from 1114 MPa for the parent rail to 760 MPa for the welded rail. The weld efficiency is the ratio of the weld-to-parent ultimate tensile strength, found to be 68%. The yield strength had a negligible decline of 5% from 624 MPa for the parent rail to 595 MPa for the welded rail. This negligible decline is very positive as the yield strength is used in design rather than the ultimate tensile

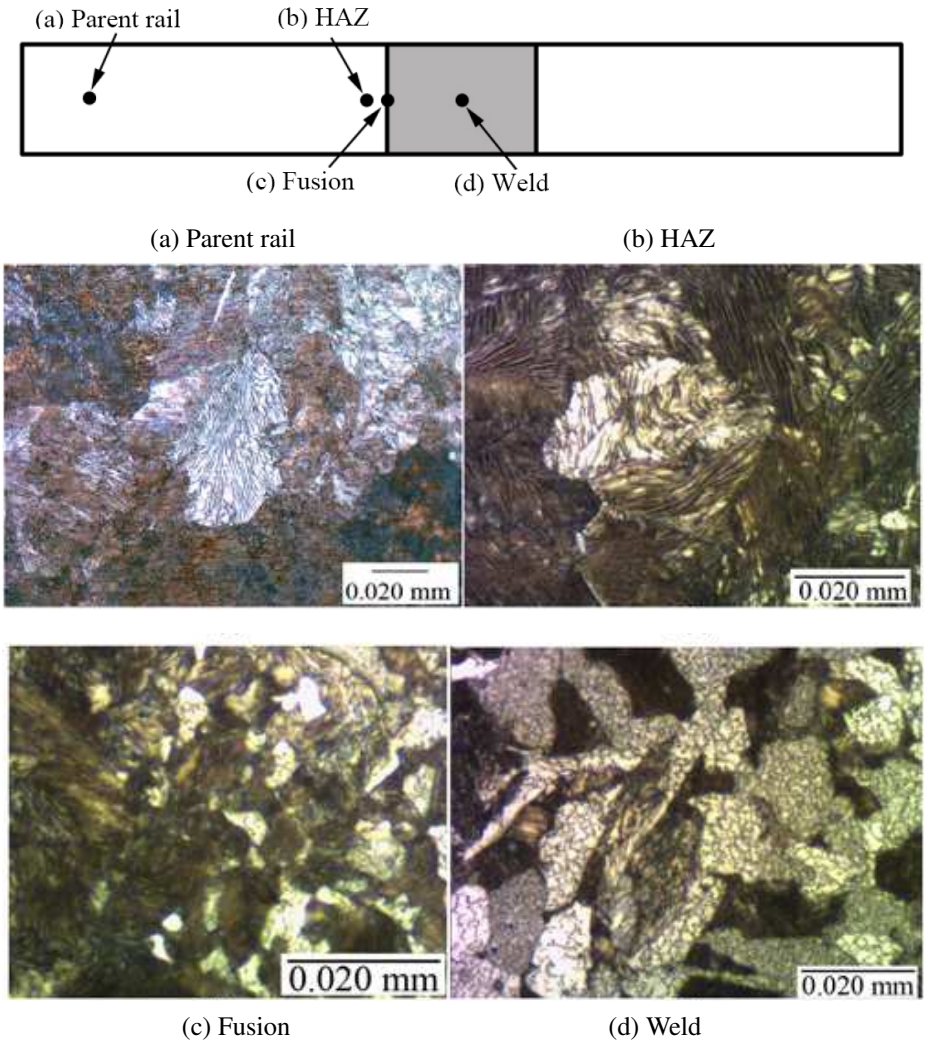

Figure 4. Micrographs at 100 times of the rail steel examined. The sections correspond to the points marked on the diagram.

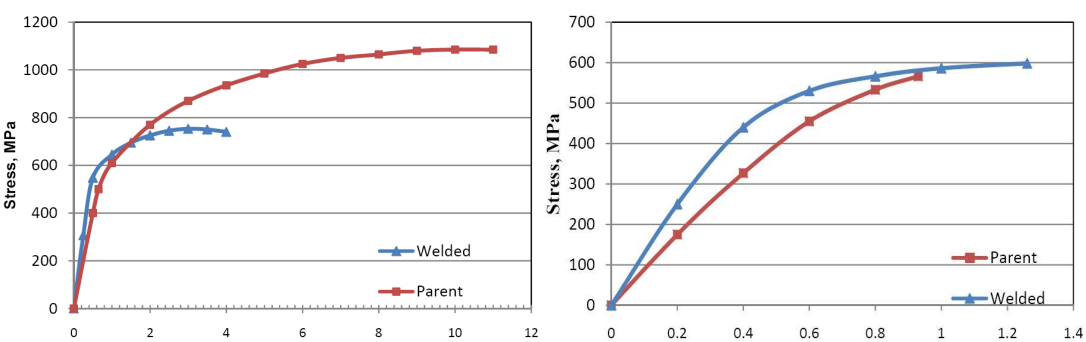

Figure 5. Stress-strain relationships of welded and unwelded pearlitic rail steels: unnotched (left) and notched (right). The horizontal axis shows the percent strain.

Condition	Specimen number	Ultimate strength	Yield strength	Failure strain (%)
Welded	1	865	650	3.34
	2	695	580	3.98
	3	726	585	3.81
	4	755	565	4.46
	Average	760	595	3.90
Parent	1	1161	667	11.3
	2	1059	548	11.8
	3	1121	657	10.2
	Average	1114	624	11.1

Table 2. Ultimate and yield strengths (in MPa) and failure strain of welded and parent pearlitic rail steel specimens.

strength. The strain to failure decreased from 11.1% for the parent rail to 3.9% for the welded rail, a two-fold decrease in ductility.

The parent and welded rail steel materials with simulated defects were tested to determine their residual strengths. A notch was created using a triangular file with a crack length to sample width ratio of 0.125. The specimens were tested and the unnotched cross sectional area was used to calculate the stress. The average stress-strain relationship for both the parent and welded rail steel is shown in Figure 5, right. This figure shows that the average residual strength of the welded rail is slightly higher than that of the parent rail. The strain to failure of the welded rail is also higher than that of the parent rail. The parent rail has a linear elastic behavior followed by a very short nonlinear plastic behavior until failure, while the welded rail has a linear elastic behavior followed by a longer nonlinear plastic behavior until failure.

The mechanical properties of the notched parent and welded pearlitic rail steel specimens are shown in Table 3. This table shows an increase of 5% in the residual strength from 566 MPa for the parent rail

Condition	Specimen number	K_1	Residual strength	Failure strain (%)	Notch sensitivity
Welded	1	53	588	1.22	0.23
	2	50	577	0.78	0.24
	3	59	631	1.77	0.17
	Average	54	598	1.26	0.21
Parent	1	84	685	1.1	0.39
	2	56	457	0.7	0.59
	3	84	683	1.1	0.39
	4	54	438	0.8	0.61
	Average	70	566	0.93	0.49

Table 3. Mechanical properties of notched welded and parent pearlitic rail steel specimens (K_1 in units of MPa·$m^{0.5}$ and residual strength in units of MPa).

to 598 MPa for the welded rail. There is a considerable increase of 26% in the ductility of the welded rail over the parent rail, with the strains to failure being 1.26% and 0.93% respectively. The notch sensitivity is defined as $(S_{ut} - S_r)/S_{ut}$ where S_r is the residual strength and S_{ut} is the ultimate tensile strength of the unnotched specimen. The notch sensitivity decreased from 0.49 for the parent rail to 0.21 for the welded rail. This shows that the parent rail is a lot more sensitive to the introduction of a notch than the welded rail.

The notched parent rail steel has an average residual strength of 566 MPa which is a 51% decrease in the ultimate tensile strength of the unnotched specimen. The average residual strength of the welded rail steel is 598 MPa which is a 27% decrease in the ultimate tensile strength of the unnotched welded rail steel. The average strain to failure, which is a measure of the ductility of the material, decreased from 11.1% for the unnotched parent specimens to 0.93% for the notched parent specimen which is almost a 12 fold decrease in ductility. This is compared to the average strain to failure of the notched welded rail steel, which was 1.26%, a mere 3 fold decrease from 3.9% for the unnotched welded rail steel. As a result of the introduction of a notch equal to 0.125 of the specimen width, the parent material lost almost half of its strength compared to the welded material, which only lost approximately a quarter of its strength. The introduction of the notch also caused the parent material to lose practically all its ductility, showing high notch sensitivity. The welded material, however, only lost a small fraction of its ductility when compared to the parent material, showing low notch sensitivity.

The test results show that the samples failed in the center of the weld. This happened in all tests. This failure reveals that the fusion between the parent rail and the weld material was very good and that there was perfect fusion, else failure would have occurred at the fusion line. The failure in the center of welded area also confirms that the weld is not as strong as the parent rail. The welded specimen also shows a significant amount of necking which demonstrates that the weld material is ductile. This shows that even if there is a defect or crack in the rail steel during service there might not be a catastrophic failure due to the high ductility of the weld.

3.5. ***Plain stress fracture toughness evaluation.*** Equations (1) and (2) were used to calculate the fracture toughnesses of the parent and welded rail steel. To qualify as a plain strain fracture toughness, as stated before, the thickness, t, and crack length, a, must both be greater than $2.5 \times (K_{1c}/\sigma_{ys})^2$. Using $\sigma_{ys} = 595$ MPa and $K_{1c} = 54\,\text{MPa}\sqrt{m}$, gives $2.5 \times (54/595)^2 = 20.6$ mm. This value is much larger than both the thickness and the crack length. Therefore, this is not considered a valid K_{IC} and is referred to as the plain stress fracture toughness K_1.

The plain stress fracture toughness of the parent material is $70\text{MPa}\sqrt{m}$ compared to $54\text{MPa}\sqrt{m}$ for the welded material. This is a 30% decrease in the fracture toughness for the parent compared with that for the welded rail material. However, the residual strength, strain to failure, and notch sensitivity of the welded rail are all better than those of the parent rail.

3.6. ***Fractography.*** A schematic representation of the fracture surface is shown in Figure 6, top. The notch is on the left side of the figure, which means the crack propagation direction is from left to right. Points A and B represent the locations at which SEM micrographs were taken. Immediately ahead of the crack tip, at point A, is referred to as the crack initiation region, while close to the end of the fracture surface, at point B, and is referred to as the fast crack propagation region. The fracture surface morphology of the parent and welded rail steel, respectively are shown in the top and bottom micrographs

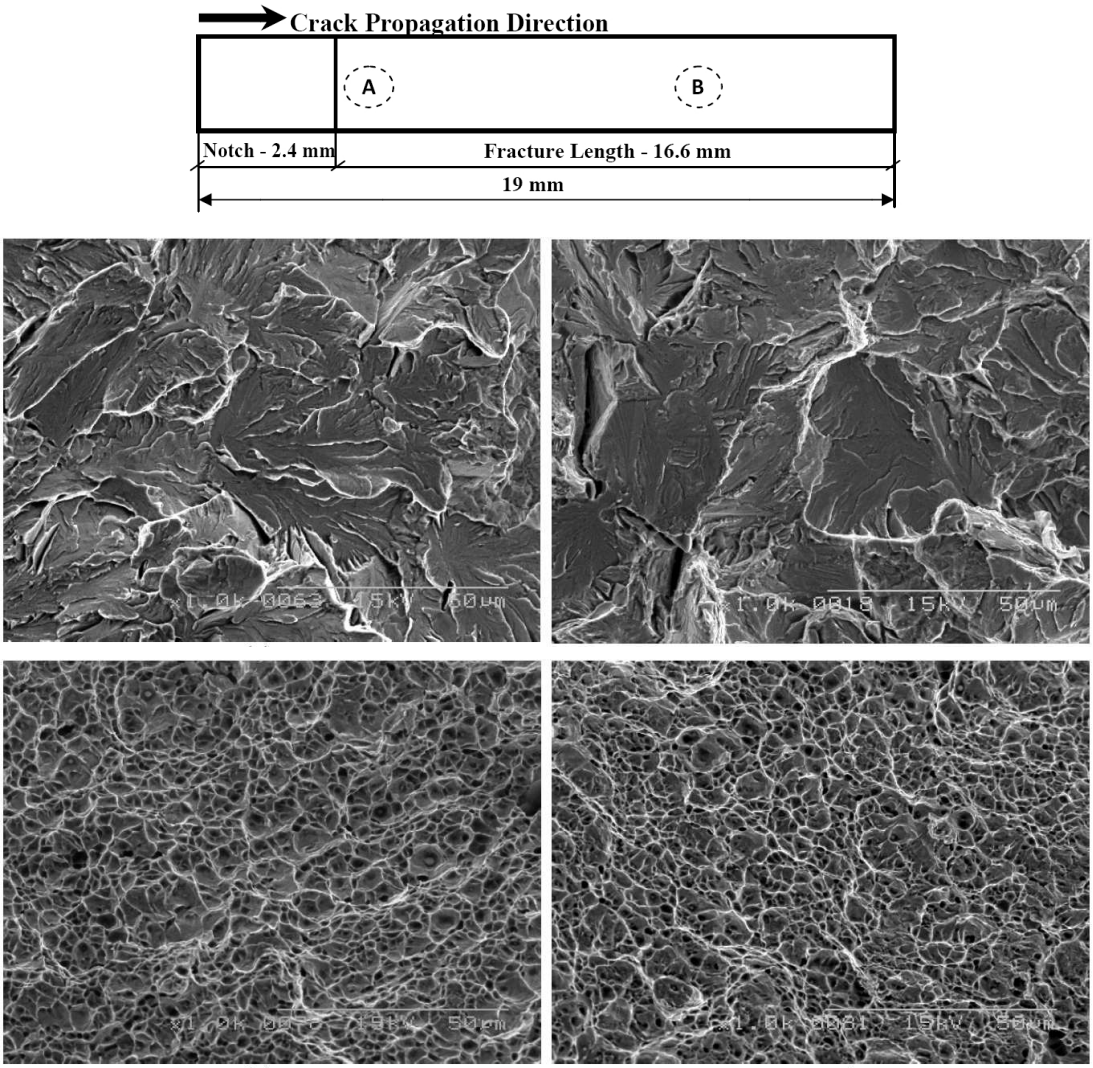

Figure 6. SEM micrograph at 1000 times of the parent rail (top row) and welded rail (bottom row) at the beginning of the notch (left column, region A in the diagram) and toward the end of the fracture surface (right column, region B in the diagram).

in Figure 6: the micrographs on the left were taken at point A, and those on the right at point B. All these micrographs were taken at 1000 times magnification.

The fracture surface morphology of the parent pearlitic rail steel specimen taken immediately ahead of the crack tip can be seen in the top left micrograph. The image displays cleavage facets and river patterns. The entire fracture surface contains well-drawn ferrite strips. Pulled up lamellae and tearing ridgelines inside the grains can also be seen [Khourshid et al. 2001]. The fracture surface of the parent rail taken from location B is shown in the top right micrograph. The fracture surface displays a mixed type of fracture mechanism with the ductile mechanism dominant. The ductile behavior is evident in the micrograph from ductile tearing features such as pulled up ferrite strips and tearing ridges. Small

amounts of cleavage facets and river patterns can also be seen, which are associated with brittle fracture. In some areas, there exist intergranular cracks along the grain boundaries as shown in the left hand section of the micrograph. It is observed that further from the fracture surface the failure mechanism becomes less ductile.

The fracture surface morphology of the welded rail steel taken from location A consists of a dimpled appearance and can be seen in the bottom left micrograph in Figure 6. Dimpled rupture is created by microvoid coalescence, which is formed as a result of particle matrix decohesion or cracking of second-phase particles [Davis 1998, pp. 1212–1216]. This type of fracture morphology is associated with ductile fracture. The fracture morphology of the welded rail steel taken at location B is shown in the bottom right micrograph, which looks very similar to the one taken at location A. This similarity shows that the entire fracture surface of the welded rail steel consists of a dimpled appearance, and also explains its relatively high ductility.

4. Concluding remarks

- Finite element analysis revealed that the sizes of the heat affected zone (HAZ) and fusion zone of the pearlitic rail steel under consideration are approximately 15 mm and 5 mm respectively at a preheat temperature of 340°C and an arc temperature of 4500°C.
- The pearlitic rail, welded rail, and HAZ had hardness ranges of 300–315 HB, 200–240 HB, and 279–286 HB respectively.
- The parent rail steel has ultimate tensile strength, yield strength, and elongation of about 1114 MPa, 624 MPa, and 11.1% respectively while the welded rail steel has 760 MPa, 595 MPa, and 3.90% respectively.
- The average residual strength of the welded rail was slightly higher than that of the parent rail and the parent rail was more sensitive to the introduction of a notch.
- The average plain stress fracture toughnesses of the parent and welded rail steels were 70 $\mathrm{MPa{\cdot}m^{0.5}}$ and 54 $\mathrm{MPa{\cdot}m^{0.5}}$ respectively.
- The fracture surface morphologies of both the parent and welded rail steel display ductile failure mechanisms. However, the failure mechanisms seen in the welded rail steel are more ductile than those in the pearlitic rail steel.

References

[Aglan and Fateh 2006] H. Aglan and M. Fateh, "Fatigue damage tolerance of bainitic and pearlitic rail steels", *Int. J. Damage Mech.* **15**:4 (2006), 393–410.

[Aglan and Fateh 2007] H. Aglan and M. Fateh, "Fracture and fatigue crack growth analysis of rail steels", *J. Mech. Mater. Struct.* **2**:2 (2007), 335–346.

[Aglan and Gan 2001] H. Aglan and Y. X. Gan, "Fatigue crack growth analysis of a premium rail steel", *J. Mater. Sci.* **36**:2 (2001), 389–397.

[Aglan et al. 2004] H. Aglan, Z. Y. Liu, M. F. Hassan, and M. Fateh, "Mechanical and fracture behavior of bainitic rail steel", *J. Mater. Process. Technol.* **151**:1–3 (2004), 268–274.

[Bhadeshia 1997] H. K. D. H. Bhadeshia, "Models for the elementary mechanical properties of steel welds", pp. 229–284 in *Mathematical modelling of weld phenomena 3* (Graz, 2005), edited by H. Cerjak, Institute of Materials, London, 1997.

[Chandler 2008] J. Chandler, *Field welding inspection guide*, Ohio Department of Transportation, Department of Materials Management, Columbus, OH, 2008, Available at http://tinyurl.com/ODOT-OMM-FWIG.

[Cornell and Bhadeshia 1999] R. Cornell and H. K. D. H. Bhadeshia, "Decarburization of steel", online material, University of Cambridge, Department of Materials Science and Metallurgy, 1999, Available at http://www.msm.cam.ac.uk/phasetrans/abstracts/M0.html.

[Crear 2001] R. Crear, *Engineering design: inspection, evaluation, and repair of hydraulic steel structures*, US Army Corps of Engineers, Washington, DC, 2001, Available at http://tinyurl.com/USACE-EM-1110-2-6054. Publication EM 1110-2-6054.

[Davis 1998] J. R. Davis (editor), *Metals handbook*, Desk ed., 2nd ed., ASM International, Materials Park, OH, 1998.

[Dorzin 2003] E. Dorzin, "Temperature of a MIG welder", 2003, Available at http://tinyurl.com/temp-MIG-welder.

[El-Banna et al. 2000] E. M. El-Banna, M. S. Nageda, and M. M. Abo El-Saadat, "Study of restoration by welding of pearlitic ductile cast iron", *Mater. Lett.* **42**:5 (2000), 311–320.

[Funderburk 1997] R. S. Funderburk, "Fundamentals of preheat", *Weld. Innov.* **14**:2 (1997), 14–15.

[Funderburk 1999] R. S. Funderburk, "How hot is hot enough? A primer on weldment preheating and interpass temperature", *Weld. Des. Fabr.* **72**:5 (1999), 40–44.

[Funderburk 2000] R. S. Funderburk, "Taking your weld's temperature", *Mod. Steel Constr.* **40**:2 (2000), 56–61.

[Gray et al. 1982] G. T. Gray, III, A. W. Thompson, J. C. Williams, and D. H. Stone, "The effect of microstructure on fatigue crack propagation in pearlitic eutectoid steels", *Can. Metall. Q.* **21** (1982), 73–78.

[Khourshid et al. 2001] A. M. Khourshid, Y. X. Gan, and H. A. Aglan, "Microstructure origin of strength and toughness of a premium rail steel", *J. Mater. Eng. Perform.* **10**:3 (2001), 331–336.

[Kim et al. 2001] J. H. Kim, Y. J. Oh, I. S. Hwang, D. J. Kim, and J. T. Kim, "Fracture behavior of heat-affected zone in low alloy steels", *J. Nucl. Mater.* **299**:2 (2001), 132–139.

[Lewandowski and Thompson 1986] J. J. Lewandowski and A. W. Thompson, "Microstructural effects on the cleavage fracture stress of fully pearlitic eutectoid steel", *Metall. Mater. Trans. A* **17**:10 (1986), 1769–1786.

[Lincoln 2005] *Hardfacing guide: product and procedure selection*, Lincoln Electric Company, Cleveland, OH, 2005, Available at http://tinyurl.com/LE-C7-710. Publication C7.710.

[Little and Kamtekar 1998] G. H. Little and A. G. Kamtekar, "The effect of thermal properties and weld efficiency on transient temperatures during welding", *Comput. Struct.* **68**:1–3 (1998), 157–165.

[Mutton and Alvarez 2004] P. J. Mutton and E. F. Alvarez, "Failure modes in aluminothermic rail welds under high axle load conditions", *Eng. Fail. Anal.* **11**:2 (2004), 151–166.

[Orange 1966] T. W. Orange, "Evaluation of special 301-type stainless steel for improved low-temperature notch toughness of cryoformed pressure vessels", Technical Note D-3445, NASA/Lewis Research Center, Washington, DC/Cleveland, OH, 1966, Available at http://tinyurl.com/NASA-TN-D-3445.

[Reis and Harness 2004] T. L. Reis and D. J. Harness, "Field welding inspection manual", Materials Instructional Memo 558 (version of April 20, 2004), 2004, Available at http://tinyurl.com/IDOT-MIM-558-2004.

[Saarna and Laansoo 2004] M. Saarna and A. Laansoo, "Rail and rail weld testing", pp. 217–219 in *Proceedings of the 4th International Conference of DAAAM: Industrial Engineering – Innovation as Competitive Edge For SME* (Tallinn, 2004), edited by J. Papstel and B. Katalinic, DAAAM Estonia, Tallinn University of Technology, Tallinn, 2004.

[Sugden and Bhadeshia 1989] A. A. B. Sugden and H. K. D. H. Bhadeshia, "Lower acicular ferrite", *Metall. Mater. Trans. A* **20**:9 (1989), 1811–1818.

[Tojo 2003] M. Tojo, "Welding of offshore structures, 2: Essential factors in welding procedure controls", *Kobelco Weld. Today* **6**:2 (2003), 3–7.

[WTIA 2006] *Repair welding of crane rails using arc welding processes*, Welding Technology Institute of Australia, Newington, NSW, 13 May 2006, Available at http://tinyurl.com/WTIA-TGN-BC-05. Technical Guidance Note TGN-BC-05.

Received 22 Jan 2009. Revised 2 Jul 2009. Accepted 7 Jul 2009.

ALDINTON ALLIE: aallie7239@mytu.tuskegee.edu
Mechanical Engineering Department, Tuskegee University, Tuskegee, AL 36088, United States

HESHMAT A. AGLAN: aglanh@tuskegee.edu
College of Engineering, Architecture and Physical Sciences, 218 Foster Hall, Tuskegee University, Tuskegee, AL 36088, United States

MAHMOOD FATEH: mahmood.fateh@dot.gov
Federal Railroad Administration, 1120 Vermont Avenue NW, Mail Stop 20, Washington, DC 20590, United States

JOURNAL OF MECHANICS OF MATERIALS AND STRUCTURES
Vol. 5, No. 2, 2010

RATE DEPENDENCE OF INDENTATION SIZE EFFECTS IN FILLED SILICONE RUBBER

RAMANJANEYULU V. S. TATIRAJU AND CHUNG-SOUK HAN

Indentation experiments at the nanometer and micrometer range reported in the literature have shown that the deformation of polymers is — similarly to metals — size-dependent. In addition its size dependence, the deformation behavior of polymers is also known to be rate-dependent. Here silicone rubber is considered. In order to characterize the relation between size and rate-dependent deformation indentation tests of silicone at indentation depths of between 30 and 300 microns and loading times of between 1 and 1000 seconds are performed. In these experiments the hardness and dissipation increased with decreasing loading time and decreasing indentation depth. These experimental results are analyzed with a recently suggested indentation model which incorporates a Frank energy-related nonlocal deformation work. It is found that the indentation model is in good agreement with the experimental data. Evaluation of the experimental data indicates that the rate effects are mostly related to the nonlocal, size-dependent deformation.

1. Introduction

The indentation size effect manifests itself in increasing hardness at decreasing indentation depths and is fairly well investigated for metals [Ma and Clarke 1995; Nix and Gao 1998; Han et al. 2007a]. Such elevated hardnesses at small indentation depths have also been observed in polymers [Briscoe et al. 1998; Chong and Lam 1999; Tjernlund et al. 2004; Lim and Chaudhri 2006; Han and Nikolov 2007] but, in comparison to metals, for polymers these effects are not well understood. An understanding of size-dependent deformation behavior is important not only for small components in MEMS/NEMS (micro/nano-electromechanical systems), but also for the development of advanced material systems and composite materials with small material phases and other applications such as sealants, gaskets [Tan et al. 2007], and adhesives [Han et al. 2007b]. As many biological materials can be viewed as polymers, the relevance of size effects in polymers extends also to these materials [Yang et al. 2002].

Rate effects in indentation testing have been studied in [Sargent and Ashby 1992; Larsson and Carlsson 1998; Ebenstein and Wahl 2006; Tweedie and Van Vliet 2006], for instance, but without considering size effects. The effects of cross-linking and adhesion on the determination of the elasticity modulus of polydimethylsiloxane elastomers have been studied in [Carrillo et al. 2005]. A phenomenological constitutive model incorporating both rate and size effects has been suggested in [Gudmundson 2006], for instance. The elasticity modulus has also been determined to vary with the indentation depth [McFarland and Colton 2005; Tweedie et al. 2007]; this may be seen as a indication that a change in the dominant forces or mechanisms may be present at small indentation depths.

Keywords: indentation, hardness, polymeric material, viscoelasticity, size dependent deformation.

In [Han and Nikolov 2007] indentation experiments in the literature have been analyzed, and it has been found that the indentation size effect strongly depends on the polymeric material and its molecular structure [Han 2010]. For instance, Teflon (polytetrafluoroethylene) [Li and Bhushan 2000] does not seem to show any indentation size effects, while epoxy and polycarbonate show significant indentation size effects at indentation depths from 100 nm up to several microns [Chong and Lam 1999].

Assuming the rate of deformation does not alter the basic characteristics, these experimental results were evaluated with a hardness model suggested in [Han and Nikolov 2007]. The model and experimental results were found to be in good agreement for indentation depths above some 200 nm. The model is based on an elastoplastic extension of the rotation gradient model suggested in [Nikolov et al. 2007], which relates the length scale component of the deformation work to the Frank energy known from liquid crystal polymers. For indentation depths smaller than 200 nm surface effects may be present which are not represented in the hardness model. In metals such surface effects may include the effect of the curvature of the indenter tip [Qu et al. 2004], different deformation mechanisms close to free surfaces [Han et al. 2006], and surface roughness effects [Zhang and Xu 2002; Zhang et al. 2004].

Among the different polymers tested for size-dependent deformation, silicone rubber appears to exhibit astonishing behavior. While at the macroscale silicone rubber is very soft, at indentation depths of under one micron it exhibits higher hardness than many macroscopically harder polymers [Zhang and Xu 2002; Xu and Zhang 2004; Han and Nikolov 2007]. Here we investigate the rate dependence of the indentation size effect in silicone rubber with indentation tests at indentation depth ranges of approximately 30–300 microns and in loading time ranges of 1–1000 seconds. The data for these experiments are analyzed and discussed using the hardness model suggested in [Han and Nikolov 2007].

2. Experimental setting

Indentation system. The indentation tests were performed with the commercially available Fischerscope HM2000S indentation system (Fischer Technology Inc., USA). It is a load controlled system for the determination of hardness and other material properties [ISO 14577-1 2002]. The applicable load of the machine ranges between 0.4 and 2000 mN and the loading time between 0.6 and 10^6 seconds. The load and penetration depth resolutions are given by the manufacturer as $\leq 40\ \mu$N and ≤ 100 pm, respectively. Also according to the manufacturer the curvature of the indenter tip is guaranteed to be less than 500 nm, approximately between 200 and 300 nm; only polymeric materials with this indenter tip have been tested.

Silicone rubber material. The ingredients for the silicone rubber sample fabrication were obtained from Gelest, Inc., Morrisville, PA, USA. The silicone materials were produced in two parts, both of them silicone blends. Part A consists of fumed silica-reinforced vinyl-terminated polydimethylsiloxane (Gelest catalog code DMS-V31S15) as a base and a precious metal catalyst for vinyl-addition silicone cure platinum-divinyltetramethyldisiloxane complex in xylene (Gelest SIP 6831.2). Part B consist of vinyl-terminated polydimethylsiloxanes (Gelest DMS-V31) as vinyl silicone, methylhydrosiloxane-dimethyl-siloxane copolymers and a trimethylsiloxy terminated (Gelest HMS-301) cross-linker.

For part A, 84.85 ml of the base was poured into a glass beaker by measuring its mass on a weighing machine; meanwhile, 3 ml of the catalyst was slowly added with a pipette. The compound was then thoroughly mixed with a stirrer for a couple of minutes. For part B, 80 ml of vinyl silicone and 20 ml of cross-linker were thoroughly mixed with a stirrer in another beaker. Parts A and B were poured in a

proportion of 3:1 into a polypropylene specimen cup. To get rid of any bubbles, the whole mixture was placed in an airtight chamber using a vacuum pump. The aggregate was then poured into a Petri dish (50 mm in diameter and 9 mm in depth, Pall Corporation, USA) to avoid damage and straining of the material due to handling. Finally the specimen was allowed to cure for several days at room temperature.

3. Indentation experiments

Figure 1 shows the indentation depth h and its projected counterpart h_c. Also shown are the elastic, W_I^e, and inelastic, W_I^p, parts of the total indentation work $W_I = W_I^e + W_I^p$ in the loading and unloading sequence of the load-displacement curve. A Berkovich indenter tip was applied with a characteristic angle of about 65°2′. The nominal contact area is $A_s = c_B h^2$ for the Berkovich tip, where $c_B = 26.440$ [ISO 14577-1 2002].

The stress and strain fields are highly inhomogeneous during indentation [Dao et al. 2001]. Because of this inhomogeneity, strain fields and strain rates vary strongly. From a classical local continuum mechanics viewpoint, where the constitutive equations are described by the stresses and strains and their rates, these stress and strain fields should be affine to each other with h under certain conditions: first, the indenter tip geometry should be self-affine, that is, the nominal penetrating shape of the indenter tip should scale with the indentation depth, and, second, the strain and strain rate fields should also be affine to the indentation depth at a certain time.

For the self-affine cone geometry of the Berkovich indenter tip used here, the maximum indentation depth h_{max} is related to the maximal applied force F_{max} by

$$h_{max}^2 = c_o F_{max}, \tag{1}$$

where the constant c_o depends on the specific indenter shape, material constants, and loading rise time t_R; see [Oyen 2006]. Following the discussion above, the relation (1) should be true irrespective of the maximum applied load if material points experience the same strain rates spatially affine to the maximum indentation depth h_{max} at all times. In other words, under these conditions the location of a material point with the same strain rate history scales with h_{max}. From a classical continuum mechanical viewpoint this should be fulfilled if the load F goes up from 0 to its maximum F_{max} linearly in time, as in [Oyen 2006]; in symbols, $F = (t/t_R)F_{max}$, where t_R is the load raising time. If the load is raised quadratically then $F = (t/t_R)^2 F_{max}$. If t_R remains the same while F_{max} changes, the stress fields and the strain and

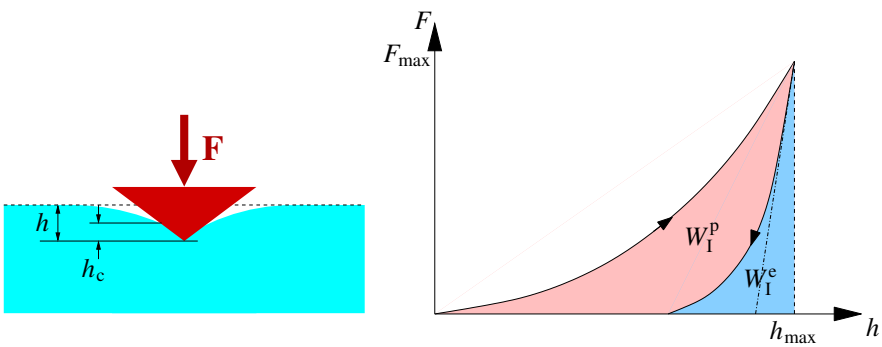

Figure 1. Indentation depths (left) and elastic W_I^e and inelastic W_I^p parts of the total indentation work W_I in a load-displacement diagram (right).

strain rate fields will be affine with respect to $h_{\max}$. As a direct consequence of (1) the universal hardness $H_{\max} = F_{\max}/(c_B h_{\max}^2)$ is not dependent on $F_{\max}$ or on $h_{\max}$, which is the expected result from a classical continuum mechanical viewpoint in terms of local stresses and strains and their rates.

In order to examine the rate dependence of the silicone rubber various loading times were applied for a given maximum load $F_{\max}$. The load rising and falling time of the load-controlled indentations were chosen to be equal and set to be t_R = 1, 10, 100, and 1000 seconds with zero holding time to minimize creep type deformation. The load increased quadratically in time till the maximum prescribed load was reached at t_R. The unloading was correspondingly decreased quadratically in the same time interval.

It has been found that the tested silicone material is highly elastic. Typical load-displacement curves with different indentation times are shown in Figure 2, left, including the load-displacement curves of the loading and unloading sequences. The lines in loading and unloading for these loading times can hardly be distinguished. Particularly for the 1000 second test, the indentation depth h at zero load was also practically zero, which indicates that there is little if any plastic deformation. However, to visualize that there is some dissipation, the load displacement curves in loading and unloading for the 1 second test have been redrawn in Figure 2, right.

Essentially no permanent indentation h was observed after the load had been removed, although at small loading times t_R (see Figure 2, right) some indentation depth h is measured at zero applied load. Because there is hardly any remaining indentation depth for the indentations for $t_R = 1000\,\mathrm{s}$ it can arguably be assumed that most of the remaining h in Figure 2, right, at the end of the unloading sequence is actually recovered in time. This motivates the use of

$$W_I = W_I^e + W_I^v \tag{2}$$

as the decomposition of the indentation work, where W_I^v is the viscous part of the indentation work which, is not recovered.

In Figure 3 the ratio between W_I^e and W_I, that is, $\eta^e = W_I^e / W_I$, is illustrated for different indentation depths and loading/unloading times. As depicted therein, with decreasing indentation time the ratio η^e

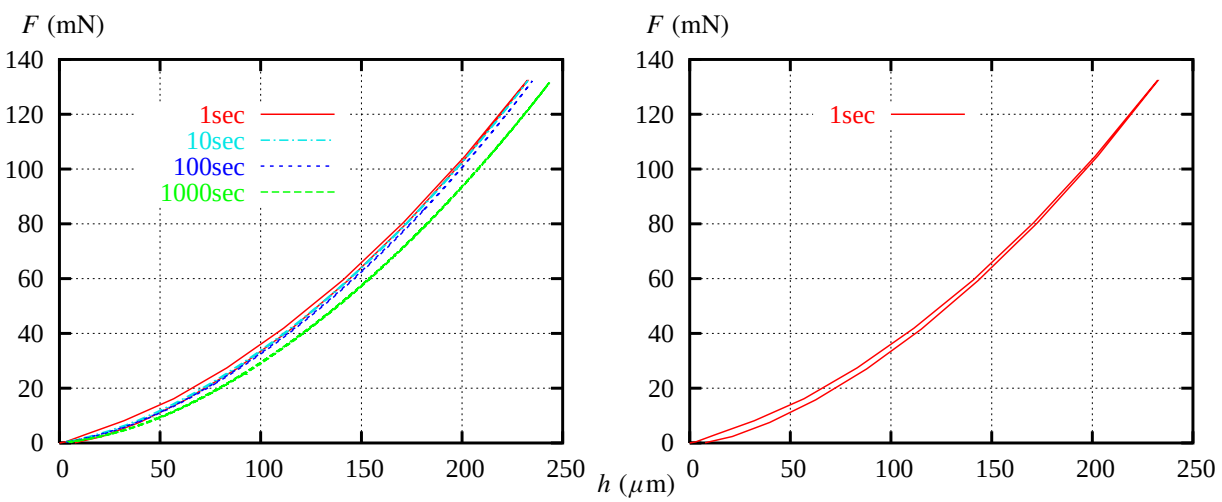

Figure 2. Indentation depth h versus load F at various loading/unloading times (left). The curves for 1 second are repeated on the right.

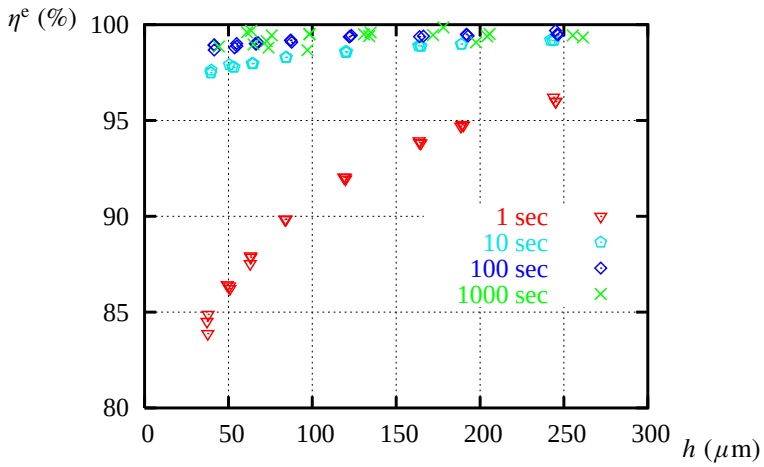

Figure 3. Ratio η^e versus indentation depth h for various loading times.

decreases, corresponding to increasing dissipation. Such behavior is well known and widely observed in other material tests such as simple tensile tests [Lemaitre and Chaboche 1990]. The values in Figure 3, however, also show a decrease of η^e with decreasing h, and therefore the dissipation of the indentation work increases with decreasing h. Similar tendencies have also been observed in other polymers [Briscoe et al. 1998; Tatiraju et al. 2008]. The magnitude with which η^e decreases is more pronounced at shorter loading times. As the majority of the deformation is elastic and hardly any plastic deformation is present the hardness values characterize elastic rather than plastic deformation.

A material model that is formulated only in local stress and strain related terms would not predict any change in η^e with the indentation depth h. The changes in η^e with h are, however, apparent in Figure 3. The indentation size effect is usually assessed by the relation between hardness and indentation depth. The values of these quantities corresponding to Figure 3 are shown in Figure 4, which plots the universal hardness,

$$H = F/A_s, \tag{3}$$

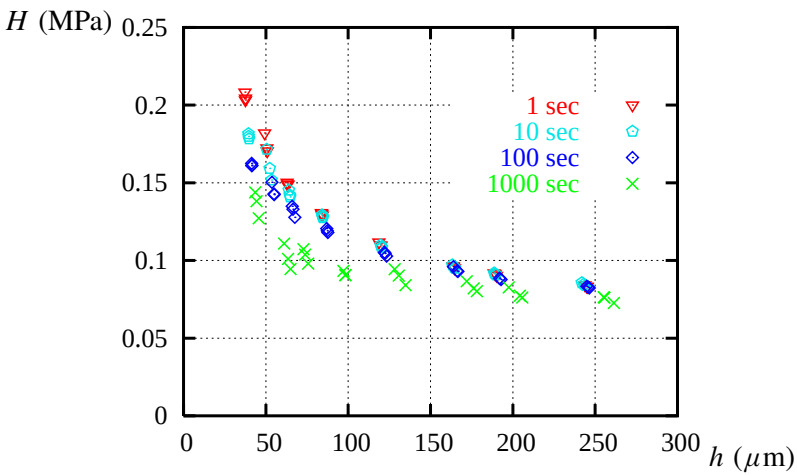

Figure 4. Universal hardness H versus indentation depth h for various loading times.

versus h for different loading times; here F denotes the force applied by the indenter and $A_s = 26.44h^2$ is the nominal contact area of the indenter penetrating beyond the zero-point of contact, h, described above [ISO 14577-1 2002].

The universal or Martens hardness was chosen because the determination of the indentation hardness has been developed for metallic materials where the elastic deformation is small compared to the inelastic deformation [Oliver and Pharr 1992], and is therefore questionable for a highly elastic material such as silicone rubber; while the universal hardness can be applied to all materials [ISO 14577-1 2002]. If size effects are not present both the universal hardness and the indentation hardness are independent of h. As can be seen in Figure 4, however, a significant increase in the universal hardness, H, has been determined for small indentation depths below about 100 microns. The figure also shows that with longer indentation times and corresponding smaller strain rates H decreases. Such increased hardness at lower loading times has also been observed by others [Shen et al. 2004], and is consistent with the increased dissipation at lower loading times shown in Figure 3. Assuming that the deformation in the considered silicone rubber is of viscoelastic nature the data in Figure 3 would indicate that the viscosity and rate dependence are increasing with decreasing h.

4. Analysis and evaluation of experimental data

In the above described experiments we observed significant indentation size effects at indentation depths between 30 and 300 microns and, with decreasing loading times, the dissipation and the indentation size effect increased. While the dissipation increases with decreasing h the elastic indentation work W_I^e is large compared to the dissipation W_I^v in all indentations performed here. For an analysis of the h-dependent universal hardness, the rate-independent hardness model suggested in [Han and Nikolov 2007] may therefore be considered as an approximation, where rate effects have been neglected.

It is well established that the deformation of liquid crystal polymers can be described by the Frank energy and the related rotational gradients [de Gennes and Prost 1993; Stewart 2004] which originate from molecular interactions. While the here-considered filled silicone rubber is not a liquid crystal polymer it is here assumed that for glassy polymers the molecular interactions related to the Frank energy still play an important role in the deformation process at small scales because the lack of nematic order is due to topological defects like cross-links and entanglements rather than to the absence of sufficiently strong molecular interactions. Following this assumption, that the Frank energy is also relevant in amorphous polymers, a Frank elasticity type rotation gradient energy was suggested by Nikolov et al. [2007] to account for the observed elastic size effects in the bending of epoxy microbeams [Lam et al. 2003; McFarland and Colton 2005]. A corresponding extension for elastoplastic materials and a related hardness model were deduced in [Han and Nikolov 2007] by including a Frank energy related indentation work term W_I^F in the total indentation work. For viscoelastic materials this extension of (2) can be given by $W_I = W_{I\varepsilon}^e + W_{I\varepsilon}^v + W_I^F$, where the subscript ε has been added to indicate the local nature of these indentation work components. The Frank energy density in its one-parameter form $W^F = \frac{1}{2}K\langle \nabla \boldsymbol{n} : \nabla \boldsymbol{n}\rangle = \frac{1}{2}K\langle n_{i,j}n_{i,j}\rangle$ is a quadratic function in the gradients of the orientations of the more rigid (nematic) parts of the polymer chain $\boldsymbol{n}$ (averaged over all directions, which is indicated by $\langle\ \rangle$) and is also directly proportional to the Frank constant K, which depends on the molecular structure and properties of the polymer [Liu and Fredrickson 1993]. The change in the Frank energy density from

the initial configuration $\boldsymbol{n}^0$ to the current configuration $\boldsymbol{n}$ can then be expressed by

$$\Delta W^{\mathrm{F}} = \frac{K}{2}\big(\langle n_{i,j} n_{i,j}\rangle - \langle n^0_{i,j} n^0_{i,j}\rangle\big). \tag{4}$$

This expression is not a practical description in deformation related terms. Assuming, firstly, a decoupling of the local work densities $W^{\mathrm{e}}_{\varepsilon}$, $W^{\mathrm{v}}_{\varepsilon}$, and the Frank energy and that, secondly, a Frank energy related deformation potential is zero in the undeformed state and increases with deformation, Nikolov et al. [2007] motivated a Frank energy type deformation potential $\Delta\tilde{W}^{\mathrm{F}}$

$$\Delta\tilde{W}^{\mathrm{F}} = \frac{\tilde{K}}{3}\chi^{\mathrm{S}}_{ij}\chi^{\mathrm{S}}_{ij}, \tag{5}$$

where $\chi^{\mathrm{S}}_{ij} = \frac{1}{2}(\chi_{ij} + \chi_{jj})$ and $\chi_{ij} = \frac{1}{2} e_{inm} u_{m,jn}$ represent gradients in the rotations. The displacement field is u_m and the permutation symbol is e_{jnm}. The tilde is introduced in (5) to differentiate it from the Frank energy, (4), due to the applied assumptions and approximations. In spite of the modifications of the Frank energy, (4), the K-related constant $\tilde{K}$ in (5) should be of the same order.

With $\Delta\tilde{W}^{\mathrm{F}}$, the total deformation work density is suggested as

$$W = W^{\mathrm{e}}_{\varepsilon} + W^{\mathrm{v}}_{\varepsilon} + \Delta\tilde{W}^{\mathrm{F}}, \tag{6}$$

where $W^{\mathrm{v}}_{\varepsilon}$ corresponds to the indentation work component $W^{\mathrm{v}}_{\mathrm{I}\varepsilon}$ and is described in local stress and strain related terms.

To a first order approximation the magnitude of the rotation gradient χ^{S} averaged over the area under the indenter increases with decreasing h as the distances are proportional to h. Consequently for large indentation depths h the nonlocal work $W^{\mathrm{F}}_{\mathrm{I}}$ should become small relative to $W^{\mathrm{e}}_{\mathrm{I}\varepsilon} + W^{\mathrm{v}}_{\mathrm{I}\varepsilon}$. With decreasing h, however, the energy $W^{\mathrm{F}}_{\mathrm{I}}$ to be exerted during indentation will increase relative to $W^{\mathrm{e}}_{\mathrm{I}\varepsilon} + W^{\mathrm{v}}_{\mathrm{I}\varepsilon}$ resulting in higher applied forces and corresponding higher hardness values (see [Han and Nikolov 2007] for more details).

Based on the additional indentation work $W^{\mathrm{F}}_{\mathrm{I}}$ associated with the deformation work density $\Delta\tilde{W}^{\mathrm{F}}$, an approximate hardness model,

$$H = H_0\Big(1 + \frac{c_\ell}{h}\Big), \tag{7}$$

was deduced in [Han and Nikolov 2007]. It involves a length scale parameter c_ℓ and a macroscopic hardness H_0, which also represents the lower limit of H. This model was developed by neglecting rate effects and assuming that the essential characteristics will not change with the loading time. A more general model discussed in the same paper is $H = H_0(1 + (c_\ell/h)^\gamma)$, with a fitting parameter accounting for the assumptions applied in its deduction. For $\gamma = 1/2$ this is identical to the model suggested in [Chong and Lam 1999]. For a short range h the differences from using (7), that is, $\gamma = 1$, and $\gamma = 1/2$ are small, but they increase with the range of h.

Equation (7) describes the h-H relation fairly well for elastoplastically deforming epoxy, polycarbonate, and polystyrene for which experimental data of up to 10 microns were reported in the literature [Chong and Lam 1999]. For small indentation depths (under 50 nm or so), effects from surface roughness, indenter tip curvature, and surface effects may be present, as discussed in the introduction. Equation (7) does not take into account these effects and consequently does not represent the size-dependent hardness below about 50 nm indentation depth.

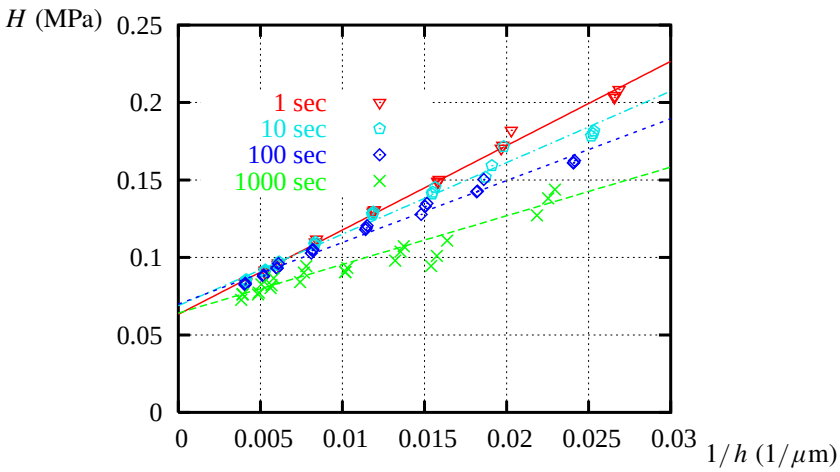

Figure 5. Universal hardness H versus inverse indentation depth $1/h$.

The dissipation is rather small in the indentation of our silicone material (see Figure 3) and therefore one could assume that the above approach should be a good approximation. In fact, (7) was also found to predict the h-H relation quite well for different loading times, as can be seen in Figure 5 where $1/h$ versus H is shown. The figure also contains linear curves in $1/h$ obtained from least square fits of the parameters of (7), that is, H_0 and c_ℓ. As can be seen from these figures the deviation of the experimental data from these linear curves in $1/h$ is rather small. As the differences in H at small loading times increase with decreasing h it can be concluded that rate effects are pronounced and thus more important at small indentations, while at large indentation depth rate effects are less important.

The numerical values of these least square fits are given in Table 1, where the macroscopic hardness H_0 varies little with the loading time, while there are quite significant increases of c_ℓ with decreasing t_R. This can also be seen in Figure 5 where the fitted lines for different t_R values more or less converge to a common H_0 at $1/h = 0$. This would imply that there is little rate dependence in the macroscopic hardness H_0 which in turn also implies that there is little rate dependence in the macroscopic deformation (that is, the deformation with or without small rotation gradients).

Loading time t_R	1 s	10 s	100 s	1000 s
H_0 (MPa)	0.0633	0.0689	0.0698	0.0633
c_ℓ (μm)	85.988	66.972	57.192	47.442

Table 1. Least square fits for H_0 and c_ℓ.

5. Discussion

Adhesion forces may be of importance at indentation depths below the micron range, as reported in [Carrillo et al. 2005] where a spherical indenter tip was used at indentation depths of about 500 nm. With a cone shaped indenter tip and in the indentation depth range considered herein, between 30 and 300 microns, the work of adhesion should, however, be less significant, or negligible compared to the

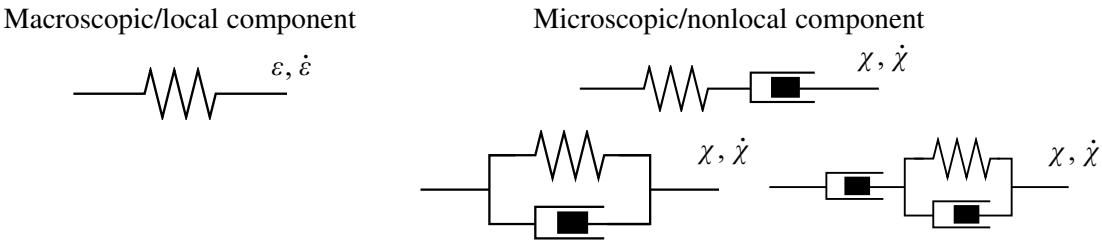

Figure 6. Rheological representation at the macro and micro levels (including the Maxwell, Kelvin–Voigt, and combined models).

indentation work components indicated in Figure 1. In this respect it is worth noting that in a numerical analysis friction effects [Mata and Alcalá 2004] could not be related to the indentation size effect. Similarly adhesion forces should also scale with the contact area and should therefore be affine with the indentation depth. These are therefore unlikely to be the cause of the indentation size effect. Using conical indenter tips the effect of the indenter tip curvature is of more relevance at submicron indentation depths [Qu et al. 2004] than the here-considered range of 30–300 microns. While rate effects were not investigated in [Lim and Chaudhri 2006] it was found that for a silicone rubber with a higher cross-link density elevated hardnesses were also observed for small indentation depths.

As opposed to [Lim and Chaudhri 2006], the silicone rubber material used in this work is not a pure polydimethylsiloxane as described in Section 2. The silicone rubber used here is more of a polymer blend, and that has not been taken into consideration in the analysis and evaluation given in Section 4. There is also a lack of clarity about the length scale of the second phases that may be present due to the fumed silica reinforced vinyl-terminated polydimethylsiloxane and the divinyltetramethyldisiloxane complex in xylene used in the fabrication process of the samples used in this work. We believe however that the issue of quantification/characterization of microscopic phases and corresponding possibly present anisotropy would be quite complicated and beyond the scope and intent of this work. Given the fact, however, that such an indentation size effect in a similar indentation depth range has also been found in [Lim and Chaudhri 2006] for highly cross-linked polydimethylsiloxane, this may indicate that the notion suggested in Section 4 is nevertheless valid for the silicone rubber used in this work as well as the highly cross-linked polydimethylsiloxane of [Lim and Chaudhri 2006]. The possible differences between the polydimethylsiloxane of [Lim and Chaudhri 2006] and the polymer blend used here fabricated with fumed silica reinforced vinyl terminated polydimethylsiloxane remains an open question which is not considered in this article.

As the depth-dependent hardness cannot be related to $W_{\mathrm{I}\varepsilon}^{\mathrm{e}}$ and $W_{\mathrm{I}\varepsilon}^{\mathrm{v}}$, the small changes in H_0 at different t_{R} values indicate that the rate effects are mostly related to the rotational gradient-dependent $W_{\mathrm{I}}^{\mathrm{F}}$. That would necessitate a reformulation of $\Delta\tilde{W}^{\mathrm{F}}$, as it should be rate-dependent and not purely elastic, as described in (5).

The viscoelastic nature of the Frank elasticity per se has already been investigated for liquid crystal polymers both in theory and experiment [Jamieson et al. 1996]. Possible combined micro-macro rheological models are suggested in Figure 6, where the macroscopic model is not rate-sensitive while the microscopic model includes damping terms dependent on $\dot{\chi}$. Note that because the macroscopic model is an elastic solid the overall local/nonlocal model would remain rheologically a (viscoelastic) solid even

if the nonlocal rheological component on its own would be a fluid. A corresponding constitutive material formulation in χ^{S} and its rate would necessitate a decomposition of χ^{S} into elastic and viscous parts. The constitutive equations and boundary conditions of such a material model would be quite complex. A phenomenological theory for elastoplastic materials with such a decomposition of a strain gradient tensor into elastic and plastic parts has been, for instance, suggested in [Chen and Wang 2002].

6. Conclusions

The rate dependence of indentation size effects in silicone rubber has been studied in the range of 30–300 microns and 1–1000 seconds. From the experimental results we can draw the following conclusions:

- The dissipation and hardness H increase with decreasing indentation depth h and with decreasing loading time.
- The rate dependence increases with decreasing indentation depth for the investigated silicone rubber. Therefore rate effects are very significant and important at small indentation depths of below 100 microns.
- The rate-independent hardness model $H = H_0\left(1 + \frac{c_\ell}{h}\right)$ describes the hardness indentation depth relation well for a constant loading time.
- In this model the length scale parameter c_ℓ decreases with loading time, while H_0 as a projected value of the macroscopic hardness is relatively unaffected by the loading time. Consequently rate effects are mostly associated with nonlocal deformation.

Acknowledgments. The support of this work by the North Dakota EPSCoR Program (EPS-0447679) and the National Science Foundation through the CAREER program (Grant CMMI 0846692) is appreciated. The authors would also like to acknowledge the assistance of Eon-Chul Song in producing the silicone samples and the valuable comments and discussions with Dr. Hosup Jung.

References

[Briscoe et al. 1998] B. J. Briscoe, L. Fiori, and E. Pelillo, "Nano-indentation of polymeric surfaces", *J. Phys. D Appl. Phys.* **31**:19 (1998), 2395–2405.

[Carrillo et al. 2005] F. Carrillo, S. Gupta, M. Balooch, S. J. Marshall, G. W. Marshall, L. Pruitt, and C. M. Puttlitz, "Nanoindentation of polydimethylsiloxane elastomers: effect of crosslinking, work of adhesion, and fluid environment on elastic modulus", *J. Mater. Res.* **20**:10 (2005), 2820–2830.

[Chen and Wang 2002] S. H. Chen and T. C. Wang, "A new deformation theory with strain gradient effects", *Int. J. Plast.* **18**:8 (2002), 971–995.

[Chong and Lam 1999] A. C. M. Chong and D. C. C. Lam, "Strain gradient plasticity effect in indentation hardness of polymers", *J. Mater. Res.* **14**:10 (1999), 4103–4110.

[Dao et al. 2001] M. Dao, N. Chollacoop, K. J. Van Vliet, T. A. Venkatesh, and S. Suresh, "Computational modeling of the forward and reverse problems in instrumented sharp indentation", *Acta Mater.* **49**:19 (2001), 3899–3918.

[Ebenstein and Wahl 2006] D. M. Ebenstein and K. J. Wahl, "A comparison of JKR-based methods to analyze quasi-static and dynamic indentation force curves", *J. Colloid Interface Sci.* **298**:2 (2006), 652–662.

[de Gennes and Prost 1993] P. G. de Gennes and J. Prost, *The physics of liquid crystals*, 2nd ed., International Series of Monographs on Physics **83**, Oxford University Press, New York, 1993.

[Gudmundson 2006] P. Gudmundson, "Modelling of length scale effects in viscoelastic materials", *Eur. J. Mech. A Solids* **25**:3 (2006), 379–388.

[Han 2010] C.-S. Han, "Influence of the molecular structure on indentation size effect in polymers", *Mater. Sci. Eng. A* **527**:3 (2010), 619–624.

[Han and Nikolov 2007] C.-S. Han and S. Nikolov, "Indentation size effects of polymers and related rotation gradients", *J. Mater. Res.* **22**:6 (2007), 1662–1672.

[Han et al. 2006] C.-S. Han, A. Hartmaier, H. Gao, and Y. Huang, "Discrete dislocation dynamics simulations of surface induced size effects in plasticity", *Mater. Sci. Eng. A* **415**:1–2 (2006), 225–233.

[Han et al. 2007a] C.-S. Han, A. Ma, F. Roters, and D. Raabe, "A finite element approach with patch projection for strain gradient plasticity formulations", *Int. J. Plast.* **23**:4 (2007), 690–710.

[Han et al. 2007b] C.-S. Han, C. Zhang, J. Wang, J. Kim, and S.-B. Choi, "Finite element analysis of thickness dependent debonding forces of elastomer coatings", *J. Adhesion* **83**:6 (2007), 535–551.

[ISO 14577-1 2002] ISO 14577-1, "Metallic materials – instrumented indentation test for hardness and materials parameters, 1: Test method", 2002, Available at http://tinyurl.com/ISO-14577-1-2002.

[Jamieson et al. 1996] A. M. Jamieson, D. Gu, F. L. Chen, and S. Smith, "Viscoelastic behavior of nematic monodomains containing liquid crystal polymers", *Prog. Polym. Sci.* **21**:5 (1996), 981–1033.

[Lam et al. 2003] D. C. C. Lam, F. Yang, A. C. M. Chong, J. Wang, and P. Tong, "Experiments and theory in strain gradient elasticity", *J. Mech. Phys. Solids* **51**:8 (2003), 1477–1508.

[Larsson and Carlsson 1998] P.-L. Larsson and S. Carlsson, "On microindentation of viscoelastic polymers", *Polym. Test.* **17**:1 (1998), 49–75.

[Lemaitre and Chaboche 1990] J. Lemaitre and J.-L. Chaboche, *Mechanics of solid materials*, Cambridge University Press, Cambridge, 1990.

[Li and Bhushan 2000] X. Li and B. Bhushan, "Continuous stiffness measurement and creep behavior of composite magnetic tapes", *Thin Solid Films* **377-378** (2000), 401–406.

[Lim and Chaudhri 2006] Y. Y. Lim and M. M. Chaudhri, "Indentation of elastic solids with a rigid Vickers pyramidal indenter", *Mech. Mater.* **38**:12 (2006), 1213–1228.

[Liu and Fredrickson 1993] A. J. Liu and G. H. Fredrickson, "Free energy functionals for semiflexible polymer solutions and blends", *Macromolecules* **26**:11 (1993), 2817–2824.

[Ma and Clarke 1995] Q. Ma and D. R. Clarke, "Size dependent hardness of silver single crystals", *J. Mater. Res.* **10**:4 (1995), 853–863.

[Mata and Alcalá 2004] M. Mata and J. Alcalá, "The role of friction on sharp indentation", *J. Mech. Phys. Solids* **52**:1 (2004), 145–165.

[McFarland and Colton 2005] A. W. McFarland and J. S. Colton, "Role of material microstructure in plate stiffness with relevance to microcantilever sensors", *J. Micromech. Microeng.* **15**:5 (2005), 1060–1067.

[Nikolov et al. 2007] S. Nikolov, C.-S. Han, and D. Raabe, "On the origin of size effects in small-strain elasticity of solid polymers", *Int. J. Solids Struct.* **44**:5 (2007), 1582–1592. Corrigendum: *Int. J. Solids Struct.* **44**:22–23 (2007), 7713.

[Nix and Gao 1998] W. D. Nix and H. Gao, "Indentation size effects in crystalline materials: a law for strain gradient plasticity", *J. Mech. Phys. Solids* **46**:3 (1998), 411–425.

[Oliver and Pharr 1992] W. C. Oliver and G. M. Pharr, "An improved technique for determining hardness and elastic modulus using load and displacement sensing indentation experiments", *J. Mater. Res.* **7**:6 (1992), 1564–1583.

[Oyen 2006] M. L. Oyen, "Analytical techniques for indentation of viscoelastic materials", *Philos. Mag.* **86**:33–35 (2006), 5625–5641.

[Qu et al. 2004] S. Qu, Y. Huang, W. D. Nix, H. Jiang, F. Zhang, and K. C. Hwang, "Indenter tip radius effect on the Nix–Gao relation in micro- and nanoindentation hardness experiments", *J. Mater. Res.* **19**:11 (2004), 3423–3434.

[Sargent and Ashby 1992] P. M. Sargent and M. F. Ashby, "Indentation creep", *Mater. Sci. Technol.* **8**:7 (1992), 594–601.

[Shen et al. 2004] L. Shen, I. Y. Phang, T. Liu, and K. Zeng, "Nanoindentation and morphological studies on nylon 66/organoclay nanocomposites, II: Effect on strain rate", *Polymer* **45**:24 (2004), 8221–8229.

[Stewart 2004] I. W. Stewart, *The static and dynamic continuum theory of liquid crystals*, Taylor and Francis, London, 2004.

[Tan et al. 2007] J. Tan, Y. J. Chao, X. Li, and J. W. Van Zee, "Degradation of silicone rubber under compression in a simulated PEM fuel cell environment", *J. Power Sources* **172**:2 (2007), 782–789.

[Tatiraju et al. 2008] R. V. S. Tatiraju, C.-S. Han, and S. Nikolov, "Size dependent hardness of polyamide/imide", *Open Mech. J.* **2** (2008), 89–92.

[Tjernlund et al. 2004] J. A. Tjernlund, E. K. Gamstedt, and Z.-H. Xu, "Influence of molecular weight on strain-gradient yielding in polystyrene", *Polym. Eng. Sci.* **44**:10 (2004), 1987–1997.

[Tweedie and Van Vliet 2006] C. A. Tweedie and K. J. Van Vliet, "On the indentation recovery and fleeting hardness of polymers", *J. Mater. Res.* **21**:12 (2006), 3029–3036.

[Tweedie et al. 2007] C. A. Tweedie, G. Constantinides, K. E. Lehman, D. J. Brill, G. S. Blackman, and K. J. Van Vliet, "Enhanced stiffness of amorphous polymer surfaces under confinement of localized contact loads", *Adv. Mater.* **19**:18 (2007), 2540–2546.

[Xu and Zhang 2004] W.-H. Xu and T.-Y. Zhang, "Surface effect for different types of materials in nanoindentation", *Key Eng. Mat.* **261-263** (2004), 1587–1592.

[Yang et al. 2002] F. Yang, A. C. M. Chong, D. C. C. Lam, and P. Tong, "Couple stress based strain gradient theory for elasticity", *Int. J. Solids Struct.* **39**:10 (2002), 2731–2743.

[Zhang and Xu 2002] T.-Y. Zhang and W.-H. Xu, "Surface effects on nanoindentation", *J. Mater. Res.* **17**:7 (2002), 1715–1720.

[Zhang et al. 2004] T.-Y. Zhang, W.-H. Xu, and M.-H. Zhao, "The role of plastic deformation of rough surfaces in the size-dependent hardness", *Acta Mater.* **52**:1 (2004), 57–68.

Received 24 Jan 2009. Revised 13 Aug 2009. Accepted 19 Aug 2009.

RAMANJANEYULU V. S. TATIRAJU: ramanjaneyulu.tatiraju@ndsu.edu
North Dakota State University, Department of Civil Engineering, PO Box 6050, Fargo, ND 58108, United States

CHUNG-SOUK HAN: chung-souk.han@ndsu.edu
North Dakota State University, Department of Civil Engineering, PO Box 6050, Fargo, ND 58108, United States

and

University of Wyoming, Department of Mechanical Engineering (Dept. #3295), 1000 E. University Avenue, Laramie, WY 82071, United States

JOURNAL OF MECHANICS OF MATERIALS AND STRUCTURES
Vol. 5, No. 2, 2010

A NOVEL APPLICATION OF A LASER DOPPLER VIBROMETER IN A HEALTH MONITORING SYSTEM

DAVOOD REZAEI AND FARID TAHERI

This paper presents the results of an experimental study of the applicability of the laser Doppler vibrometer (LDV) as a potential measurement tool for structural health monitoring in pipelines. In this case, use of the LDV has been integrated into a novel damage detection method referred to as the empirical mode decomposition (EMD) energy damage index. This method involves monitoring the free vibrations of a pipe through sensors, followed by decomposition of the sensor generated signals using EMD, and subsequently comparing an energy term of the pipe in its healthy state to that of the same pipe in a damaged state. In the experiment, a single beam LDV was utilized to acquire the vibration of a cantilever steel pipe impacted by an impulse hammer. Three cases were studied: pipes with a single half-circumferential damage, a single full-circumferential damage, and with multiple circumferential damages. The integrity of the LDV results was verified by comparison with those obtained from piezoceramic sensors bonded to the pipe surface. The results confirmed the effectiveness of the LDV and its integration into the proposed EMD damage index for identifying and locating single and multiple damages. Compared to piezoceramic sensors, the LDV, as a remote and accurate optical measurement system, provided more satisfactory identification of single and multiple damages and can therefore be successfully utilized in structural health monitoring.

Introduction

Despite the development of new sources of energy, the world economy is still heavily dependent upon petroleum, which is distributed in the form of oil and natural gas to numerous industries through widespread pipeline networks. Consequently, pipelines should always be maintained in a healthy condition to ensure the safe, reliable, and effective transportation of petroleum and other chemicals. Cracking and corrosion are the most common sources of damage in an operative pipeline, and may interrupt energy supplies and result in severe property damages and/or industry shut downs. These damages ultimately result in large repair, environmental clean-up, and legal costs. To avoid such misfortunes, the use of different structural health monitoring (SHM) methodologies is becoming increasingly common. The main purpose of SHM is to increase operational reliability and effectiveness via pipeline monitoring by detecting damage at its earliest stage and thereby reducing the risk of interruption of the energy supply.

In addition to common nondestructive damage detection methods in pipelines (visual inspection, X-ray, magnetic particle, and ultrasonic), modal based damage identification methods have been considered by many researchers. In these methods, deviations in specific dynamic characteristics of the structure before

Keywords: structural health monitoring, vibration-based damage detection, laser Doppler vibrometer, pipeline damage detection, piezoceramic sensors, empirical mode decomposition.

The financial support of the Natural Sciences and Engineering Council of Canada (NSERC) in support of this work is gratefully acknowledged.

and after damage are treated as the measures for damage identification. Every modal based SHM requires two key elements: sensors, which monitor the structural vibrations, and a method of data interpretation for extraction of the damage sensitive features.

Accelerometers and piezoelectric sensors (PZTs) are two well-known sensors used for capturing vibration in various applications such as mechanical systems, buildings, bridges, and aircrafts. Accelerometers have been commonly used to measure real-time acceleration of structures caused by vibration [Peeters et al. 2001; Hong et al. 2002; Kim and Melhem 2004; Lin et al. 2005]. There is also extensive work in the literature which considers the use of PZTs to monitor vibration [Banks et al. 1996; Jian et al. 1997; Soh et al. 2000; Winston et al. 2001; Fukunaga et al. 2002; Giurgiutiu et al. 2002]. Among conventional sensors in SHM, PZTs have the advantages of being small, light, inexpensive, and self-excited with the further benefits of having a high signal to noise ratios and being easily integrated into structures.

Despite the advantages of conventional contact sensors, such as accelerometers and PZTs, they still must be attached to the monitored structure. The necessity of direct contact with the structure introduces several drawbacks: added mass in the system (especially in the case of accelerometers on lightweight components), sensor slippage, sensor damage, failure in harsh environments, and the considerable difficulty of setting a large number of sensors on a structure and wiring them to a data acquisition system. Furthermore, most conventional sensors cannot cover the high frequency domain because of low measurement accuracy and inadequate sensitivity.

Greater sensitivity is required to pick up the minuscule amplitudes usually observed in structures undergoing vibration [Kaito et al. 2005]. There are also cases where access to the components is difficult. In order to overcome these shortcomings, important innovations have been achieved in the field of noncontact sensors by introducing laser-based measurements. Among the different laser-based methods, the laser Doppler vibrometer (LDV) is one of the most common techniques. For more information on laser Doppler vibrometry, the reader is referred to [Polytec 2009]. As a replacement for traditional sensors, LDVs are widely used for vibration measurements in fields such as biomedicine and field measurements such as quality control testing, material characterization, casting systems, structural testing, and damage detection in aerospace as well as civil and mechanical engineering. LDVs are able to monitor vibrations with a high degree of accuracy, sensitivity, and resolution. An LDV monitors the velocity and displacement of a vibrating object through the frequency shift between the laser beam projecting to the object and the reflected beam.

Kaito et al. [2005] employed an LDV scanning system to measure the vibration of real-scale structures such as steel girders and reinforced concrete decks of actual bridges. For the steel members, this study verified that the LDV and the accelerometer results matched with a high degree of accuracy in the time and frequency domains. It was reported that the accuracy of the LDV was reduced due to low laser reflection when the specimen was a concrete or dirt-adhering steel member. To overcome this problem, Kaito et al. [2005] suggested that a surface treatment, such as reflective tape, should be applied prior to measuring.

A comparative study performed by Nassif et al. [2005] showed that an LDV, as a noncontact and nondestructive measuring system, could provide accurate results for monitoring bridge vibration and deflection. Moreover, the LDV's results compared well with results from contact sensors such as linear variable differential transformers (LVDTs) mounted on the structure. This study also proved the capabilities of an LDV in interpreting accurate velocity measurements compared with mounted geophone

sensors. Therefore, an LDV can replace two systems (LVDT and geophone) for measuring vibration deflection and velocity while maintaining sufficient accuracy.

Khan et al. [2000] performed a set of experiments to detect cracks in structures with a scanning laser Doppler vibrometer (SLDV). Their study focused on detecting cracks in a cantilever beam, a concrete beam, and plates. They found that if the defects are such that they produce localized mode-shape discontinuities, the SLDV can successfully detect and locate damages. Khan et al. [2000] also reported that speckle noise could affect the results which led them to recommend using a low-pass filter to improve measurement quality.

As mentioned previously, the analysis and interpretation of a structure's dynamic response is a key factor in an effective and successful damage identification technique. There is a vast amount of work in the published literature utilizing different modal properties as damage sensitive features such as natural frequencies and mode shapes [Peeters et al. 1996; Hassiotis 2000; Wang et al. 2001; Kim et al. 2003; Kim and Chun 2004], modal strain energy [Shi et al. 2000], and stiffness matrices [Ren and De Roeck 2002; Hwang and Kim 2004]. Other researchers have focused on vibration signal processing and have introduced methods based on frequency domain techniques, such as the Fourier transform, or based on time-frequency domain decompositions, such as the wavelet transform method [Douka et al. 2004; Kim and Melhem 2004; Ovanesova and Suarez 2004; Cheraghi et al. 2005b]. An emerging signal time-frequency processing technique called the Hilbert–Huang transform (HHT) has recently been investigated in the field of SHM and has proven its potential in damage detection [Xu and Chen 2004; Cheraghi et al. 2005a; Lin et al. 2005; Liu et al. 2006; Cheraghi and Taheri 2007; 2008]. This method employs a decomposition technique called empirical mode decomposition (EMD), which is used to decompose the signal into basic oscillatory modes that contain crucial information about the structure's dynamic characteristics and from which damage sensitive features can be deduced. These oscillatory modes are referred to as intrinsic mode functions (IMFs).

Xu and Chen [2004] experimentally investigated the applicability of EMD for identifying the damage resulting from stiffness changes in a three-story shear building model. The structure was monitored continuously under free vibration, random vibration, and earthquake simulation. Xu and Chen [2004] were successful in identifying the damage time instant and damage location through spikes in the IMF derived from the EMD.

Lin et al. [2005] employed the HHT technique to identify damage in an IASC-ASCE benchmark four-story building under ambient vibration. In this study, the damage was identified by a comparison of the structural stiffness and damping, obtained by the HHT technique, between the intact and damaged structure.

Liu et al. [2006] experimentally investigated the applicability of the HHT technique for damage detection in the benchmark problem (a four-story building), developed by the University of British Columbia. They could identify the damage and instant of occurrence of damage, based on a comparison of the first three IMFs and their time-frequencies between the undamaged and damaged structure. The damaged structure was simulated by removing bracings and loosening bolts.

In [Cheraghi et al. 2005a; Cheraghi and Taheri 2007; 2008] an SHM methodology was introduced based on the HHT and developed a novel damage index, called the EMD energy damage index (DI), which uses the energy of the first IMF of a structure's response signals in the healthy and damaged states. This method was theoretically applied to a 6-DOF mechanical system [Cheraghi and Taheri 2008] and

successfully detected the damage. The integrity of the proposed DI was also verified experimentally [Cheraghi et al. 2005a] to detect the unbounded region in an adhesively bonded join in PVC pipes. For further verification of the EMD energy DI, Cheraghi and Taheri [2007] carried out a numerical study to detect damage in a cantilever aluminum pipe having various forms of defects simulated by removing material from the pipe surface at different locations. They applied the Fourier transform, Wavelet transform, and EMD energy DI methods; it was concluded that the EMD and wavelet approaches were the most successful methods in detecting the locations and the EMD was the best method for identifying damage severity.

In the present work, a set of experiments was completed to further investigate the applicability of the EMD energy DI introduced in [Cheraghi and Taheri 2008]. The experiments included a cantilever steel pipe having different damage cases in terms of defect location, number, and severity. The damages were created to simulate corrosion; they were created by manually grinding the pipe to remove material from its surface. The pipe was excited using an impulse hammer and the free vibrations generated were captured via an LDV. MATLAB code was written to perform the signal processing including data filtration and cleansing, decomposition of the signals via EMD, and calculation of the EMD energy. To verify the performance of the LDV, its results were compared with those obtained from piezoceramic sensors bonded to the pipe surface. The capability of both the LDV and PZTs for the extraction of the pipe's natural frequencies has been investigated. The results of the proposed damage detection methodology with the integrated LDV are presented, discussed and compared with those obtained from the PZTs.

EMD energy damage index

Huang et al. [1998] introduced the Hilbert–Huang transform (HHT) signal processing method, which almost satisfied all the requirements for processing linear, nonlinear, stationary, and nonstationary signals. The HHT consists of two main parts: the EMD and the Hilbert transform. The EMD method decomposes a real signal into a collection of simpler modes or intrinsic mode functions (IMFs) which are basically associated with energy at different time scales and contain important data characteristics [Huang et al. 1998]. The Hilbert transform, once applied to IMFs, produces an energy-frequency-time distribution of the data known as a Hilbert spectrum. In general, the decomposition resulting from an HHT is well localized in the time-frequency domain and reveals important information within its data.

The procedure of sifting is schematically illustrated in Figure 1. To extract the IMFs for a given time signal $x(t)$, two cubic splines are fitted through the local maxima and minima to produce the upper and lower envelopes of the original signal, respectively (note that the upper and lower envelopes should contain all the data). Then the mean, $m_1(t)$, of these two splines is calculated and subtracted from the original signal. The difference between the signal and mean, $h_1(t)$, is called the first component, defined as $h_1(t) = x(t) - m_1(t)$.

Now h_1 is treated as the original time signal and the sifting process is repeated to get the next component (that is, $h_{11}(t) = h_1(t) - m_{11}(t)$). Each step of the sifting process produces a more symmetric signal with respect to the zero mean. To achieve the desired symmetry, more siftings have to be performed, mathematically represented by $h_{1k}(t) = h_{1(k-1)}(t) - m_{1k}(t)$.

If the sifting process continues to the extreme, it will remove the physically meaningful amplitudes and fluctuations. In response, Huang et al. [1998] proposed a criterion for limiting the size of the standard

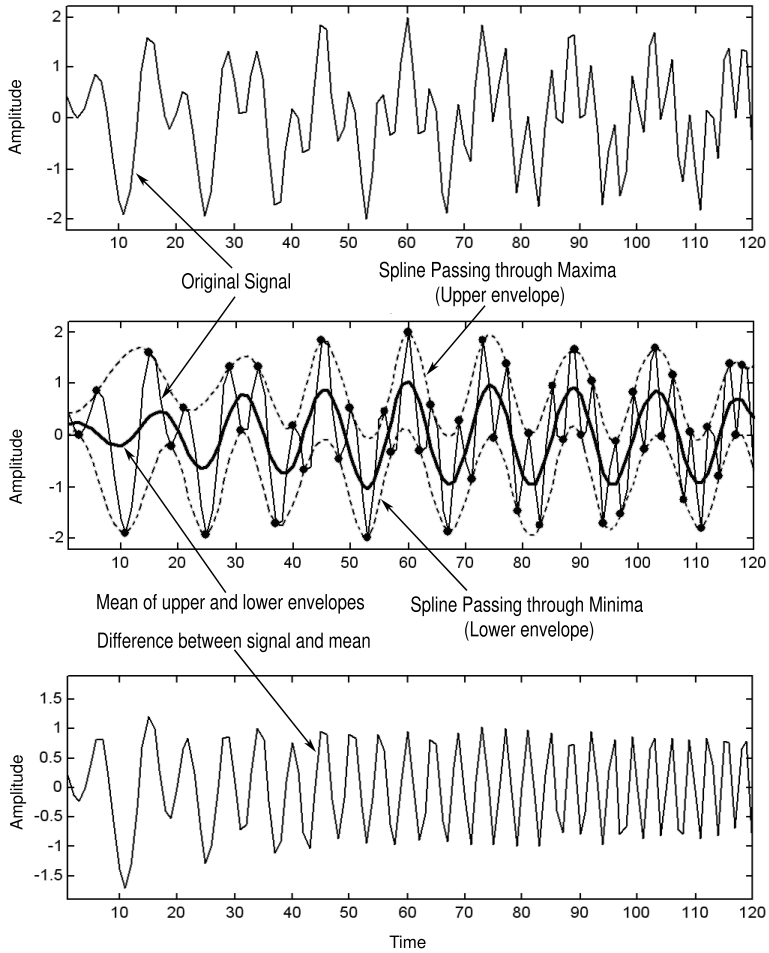

Figure 1. Schematic of the EMD sifting process.

deviation (SD) computed from two successive sifting results. This stoppage criterion is expressed as

$$\mathrm{SD} = \sum_{t=0}^{T} \left[\frac{|h_{1(k-1)}(t) - h_{1k}(t)|^2}{h_{1(k-1)}^2(t)} \right]. \tag{1}$$

If the SD is smaller than a predetermined value (usually between 0.2 and 0.3), the sifting process is stopped and $h_{1k}(t)$ is called the first IMF component ($c_1(t)$) of the signal; that is $c_1(t) = h_{1k}(t)$.

The first IMF component $c_1(t)$ contains the finest scale or the shortest period component of the signal. Each IMF satisfies two conditions. Firstly, the numbers of extrema and zero crossings either are equal or differ by one. Secondly, the average of the envelopes, defined by the local maxima and local minima, is zero. To derive the other IMFs, $c_1(t)$ is removed from the signal: $r_1(t) = x(t) - c_1(t)$.

The residue $r_1(t)$ contains the larger scales or longer period components. Then $r_1(t)$ is considered as the new signal and the sifting process is performed on it to obtain the second IMF component. This procedure is repeated for all subsequent $r_i(t)$ to derive the longer period components. At each repetition, the signal is modified with respect to the obtained IMF: $r_n(t) = r_{n-1}(t) - c_n(t)$.

After extracting all the IMFs, the original signal is decomposed into n empirical modes and a residue $r_n(t)$, which can be either the mean trend or a constant. Hence,

$$x(t) = \sum_{i=1}^{n} c_i(t) + r_n(t). \tag{2}$$

In the present work, the damage index (DI) introduced by Cheraghi and Taheri [2008] was used to identify and locate damage in a cantilever steel pipe. This DI is based on the energy of the vibration signal's first IMF. According to this method, the dynamic characteristics of the healthy structure during free vibration are collected through sensors; the acquired signals are then passed through a band-pass filter to ensure the existence of the first natural frequency within the data. This is followed by extraction of the first IMF through EMD as described in the previous paragraphs. Finally, the energy of the first IMF for each sensor is established by:

$$E = \int_0^{t_0} (c_1(t))^2 \, dt, \tag{3}$$

where $c_1(t)$ is the first IMF, t_0 is the duration of the signal, and E is a scalar value representing the energy of the first IMF. As mentioned earlier, the first IMF contains the highest frequency component within the signal. Furthermore, structural damage is associated with higher frequencies and therefore only the first IMF is considered in the proposed DI.

The above procedure is repeated for the same structure in its damaged state to determine the energy of each sensor's first IMF. The last step is the application of the EMD energy DI to each sensor:

$$\mathrm{DI} = \left| \frac{E_{\mathrm{Healthy}} - E_{\mathrm{Damaged}}}{E_{\mathrm{Healthy}}} \right| \times 100. \tag{4}$$

Once the DI is calculated for each sensor (for each measurement location when using a single LDV), the existence and locations of damages may be determined by associating high index values with the existence of damage close to the respective sensors.

Experimental setup

The test specimen used in this study was an API compliant [API 2000] standard steel pipe commonly used in oil and gas pipelines. The pipe was size $6^{5/8}$, grade A; its specifications are listed in Table 1. Figure 2 is an image of the experimental setup showing the pipe as a cantilever supported by two clamps at one end. The clamps are bolted to a massive structure in order to provide a rigid support and to reduce vibration dissipation through support flexibility.

A VibroMet 500 single beam LDV, manufactured by MetroLaser, Inc., is used in this study. The VibroMet 500 consists of a laser head and an electronic controller box. The laser head contains a diode

Pipe size $6^{5/8}$, Grade A, API Standard			
Outside diameter	168.3 mm	E	200 GPa
Wall thickness	6.4 mm	n	0.30
Length	2.0 m	r	7850 kg/m^3

Table 1. Dimensions and properties of the pipe.

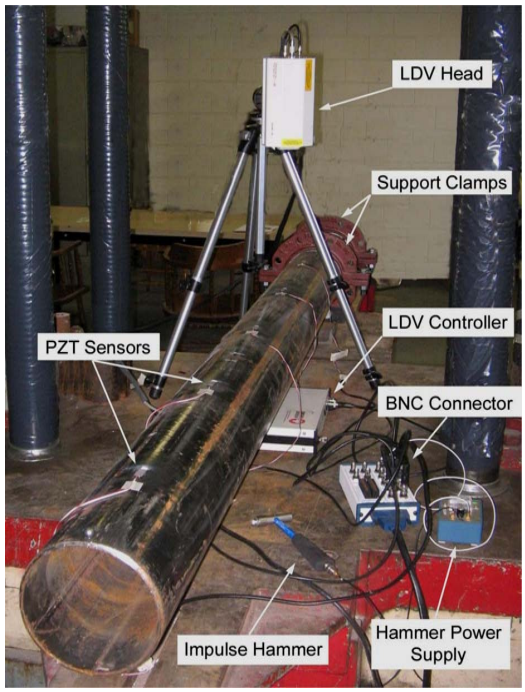

Figure 2. Experimental setup of the cantilever steel pipe and data acquisition equipment.

laser, a Bragg cell, a photodetector, and front-end electronics. The electronic controller contains the power supply, RF power for the Bragg cell, and an analog demodulator, which processes the laser head output and provides an analog velocity signal of the vibrations in real time. The electronic controller also contains a signal strength indicator, two selectable velocity ranges, and five selectable low pass filters (1, 2, 5, 10, and 20 kHz) which may be used to improve the signal to noise ratio of certain spectral bands.

As mentioned before, in order to compare and verify the results obtained from the LDV, the dynamic response of the pipe was monitored by PZTs bonded to the upper surface of the pipe (see Figure 2). The sensors were of type PZT-5H available in 72.4 × 72.4 mm sheets from Piezo Systems, Inc. The PZT sensors were cut into small pieces (24 × 10 mm) and then bonded to the pipe surface using Araldite 2011 two part epoxy, distributed by Huntsman Advanced Materials Americas, Inc. These sensors are polarized through the thickness, so two electrodes were soldered to the top and bottom surfaces of each sensor.

In order to attain a good description of pipe vibration, five locations along the pipe were selected for LDV measurement. Because of the dark surface of the pipe, which is a poor reflector for the laser beam, a white spot was created using correction liquid at each measurement location to provide a proper reflector. Adjacent to each spot, a PZT sensor was bonded to the surface of the pipe (see Figure 3). Figure 3 also depicts the arrangement of the measurement locations. The locations are numbered from 1, at the clamped end, to 5, at the free end. The same numbering was used for the PZTs.

To observe the free vibration of pipe, the pipe was excited with a piezoelectric impulse hammer (model 5800B5) manufactured by Dytran Instruments, Inc. The sensitivity of the hammer is 5 mV/lb and is able to apply a force up to 1000 lb. This hammer produces a constant force over the frequency range of interest. The output of the hammer is an analog voltage which is the representative of the input impulse.

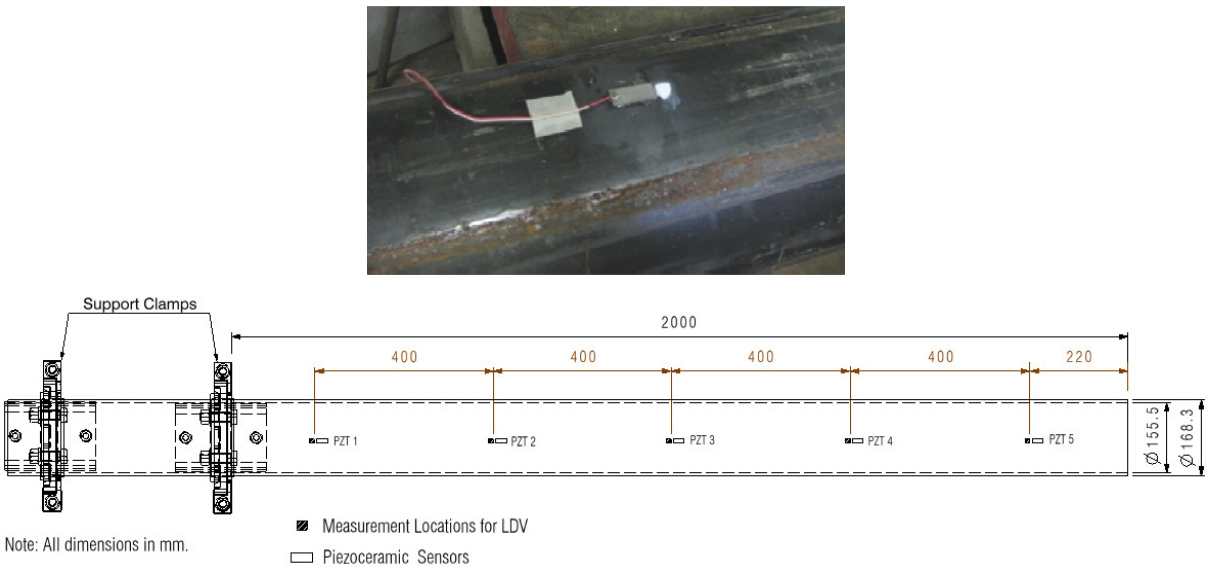

Figure 3. A typical reflective (white) spot and its adjacent PZT sensor on the pipe (top) and arrangement of measurement locations (bottom).

The impulse hammer can be equipped with either an aluminum tip or a hard plastic tip. The difference between the two tips is that the aluminum tip can excite frequencies up to 5 kHz while the hard plastic tip is only capable of exciting frequencies below 2 kHz. In the present study the aluminum tip was employed.

The responses of the LDV, impulse hammer, and PZT sensors were collected through a multifunction PCI-6220 data acquisition card manufactured by National Instruments, Inc. During all experiments the sampling frequency was kept at 20 kHz. The collected data was stored in an ASCII file which was then read by a MATLAB program, developed in-house, for processing. The code was constructed so that it could remove unwanted data before impact, compensate for any offset, normalize the signals, apply a band-pass filter, decompose the signals based on the EMD method, and finally calculate the energy of first IMF for each sensor. In order to remove the influence of the impact hammer on the pipe vibration, the acquired signals from sensors were normalized with respect to the hammer signal.

During the experiment, it was necessary to impact the free end of the pipe using the impulse hammer. It was observed that a slight change in the location of impact could affect the results. This change in location happened easily when the hammer was manually carried and guided to the impact location. To resolve this problem, a small steel ball (of diameter 12 mm) was glued to the free end of the pipe using Araldite 2011. This ball acted as a target for the impulse hammer thus ensuring impact at the same location on the pipe for each test. This method resulted in reasonable consistency for different impacts.

Procedure of EMD damage detection

In order to employ the EMD damage detection methodology, the first step was to investigate the vibration of the pipe in its healthy state by using the LDV. Afterward, damage was introduced to the pipe and the vibration of the damaged pipe was monitored. The LDV responses from before and after the creation of

damage were processed by EMD, the energies of the first IMF for both the healthy and damaged states were calculated accordingly, and finally the EMD energy damage index (DI) was evaluated based on Equation (4). Once evaluated at each measurement location, the distribution of indices identified the location of damage on the pipe. The same procedure was employed for the PZT sensors and their results were compared with those of the LDV.

As stated earlier, the healthy pipe was restrained at one end by two clamps (see Figures 2 and 3). Clamp bolts were tightened to a torque of 145.0 Nm and the LDV beam was positioned to capture the vibration of the pipe at the measurement locations (the white spots in Figures 2 and 3). The LDV was set to a high velocity measurement setting with a low-pass filter of 5 kHz. After the pipe was impacted at the free end with the impulse hammer, the voltages of the impulse hammer and the LDV were acquired simultaneously by the data acquisition system. Following the collection of data for the first measurement location, the LDV was moved to the next location after which the pipe was again impacted and the LDV and hammer outputs were monitored. This procedure was repeated for all measurement locations to acquire the pipe vibration at all specified locations. After measurements were taken using the LDV, the pipe's vibrations were also monitored using the PZT sensors.

In order to achieve consistent results, the pipe was impacted three times for each measurement and the acquired signals were normalized based on the input force (the hammer signal). The difference between the signals after normalization was deemed to be a good measure of the repeatability of the impact procedure. To normalize the signals, the fast Fourier transform of each sensor response was divided by the fast Fourier transform of the hammer signal. The result was then transferred to time domain by the inverse fast Fourier transform. As mentioned above, the test was repeated three times for each case to ensure consistency of the results; their average was chosen as the EMD energy used in further calculations of the DI. Note that all these calculations were done by MATLAB code developed in-house.

The healthy pipe was then removed from the setup and damage was created by manually grinding the outer surface of the pipe. The damage was intended to simulate typical partial corrosion in a pipeline. Three damage cases were studied on the pipe. The first damage applied was material removal in the form of a half circumference with dimensions of 100 mm length and 3 mm depth, located halfway between measurement locations 3 and 4 (see Figure 4a). The second damage case extended the first damage to a full circumference with the same dimensions. In the third case, in addition to the first damage, another half-circumferential damage was created halfway between measurement locations 2 and 3 to represent multiple damages in the system (see Figure 4b). This damage had the same length and depth as in the first case. After creating the damage for each case, the pipe was placed in the setup and clamp bolts were tightened to the same torque as was used for the intact pipe. Subsequently the pipe was impacted and its free vibration was recorded by the data acquisition system. After collecting the response of the LDV at all measurement locations as well as the PZTs responses for the healthy and damaged pipe states, the developed MATLAB code was employed.

According to [Cheraghi and Taheri 2008], the acquired signal should be filtered through a band-pass so that the data will only contain the first natural frequency of the system. It was concluded that the suggested method works well for cases where the first frequency is the dominant vibrating frequency of the structure; otherwise, more frequency components should be included in the data to increase the accuracy of the proposed method. In the conducted experiment, the amplitude of the first frequency was of the same (or even lower) order as the other components (see Figure 5). Consequently, to improve

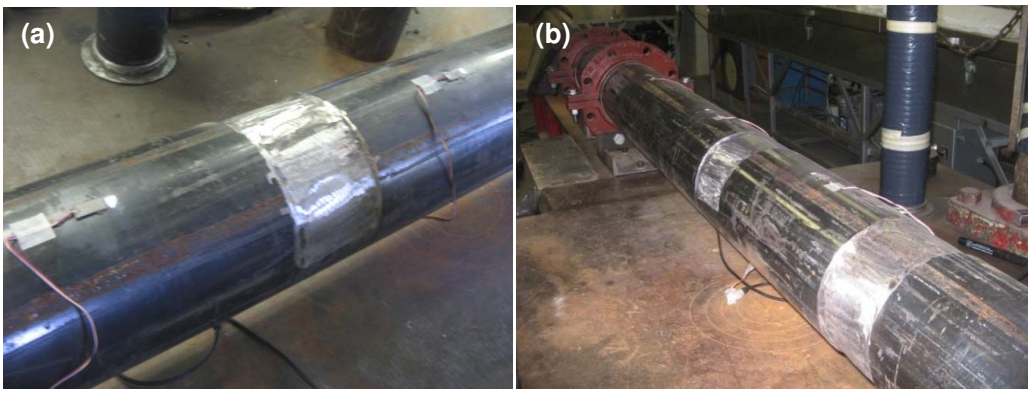

Figure 4. (a) Damage case 1: Half-circumferential damage between PZTs 3 and 4. (b) Damage case 3: Multiple damages — full-circumferential damage between PZTs 3 and 4 and half-circumferential damage between PZTs 2 and 3.

accuracy, a pass-band filter was designed in the MATLAB code to filter out all frequencies except the first six components. This filter was of the Butterworth type and passed frequencies in the range 10 Hz to 700 Hz.

The acquired signals from both the LDV and the PZT sensors lasted up to 3 s before decaying to zero. Considering the high sampling frequency used in the experiments, the acquired signal consisted of a huge amount of data, requiring lengthy processing time. Fortunately, the EMD energy DI is based on the comparison of special features in the PZT signals before and after the existence of damage; therefore, there are no limitations on the duration of the signals so long as the same duration is used for processing the pipe vibrations in the healthy and damaged states. Consequently, in the present work only the first 0.5 s of the signals were considered for evaluating the EMD energy.

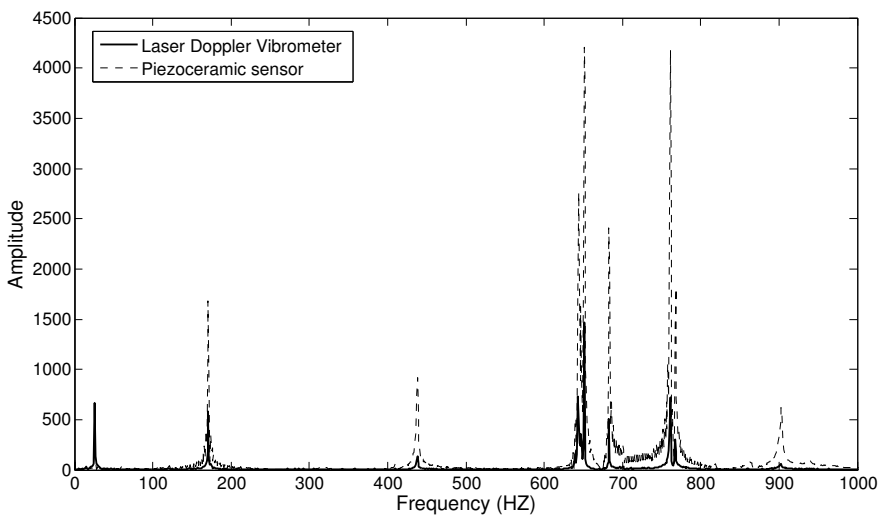

Figure 5. Frequency spectrum of response of the LDV at location 3 and its adjacent PZT.

Results and discussion

Figure 5 illustrates the frequency spectrum obtained from the LDV at measurement location 3 and its adjacent PZT sensor. This figure shows a good agreement of the natural frequency extraction results between the LDV and the piezoceramic sensors. However, the LDV was not as successful as the PZT sensors in capturing all the frequencies. This can be explained by noting that the LDV is located on top of the pipe and can therefore only measure the flexural vibration modes in the vertical direction; it is unable to monitor in-plane vibrations. Consequently, those modes are missing in the frequency spectrum of the LDV.

Figure 6 illustrates a typical LDV response and its full decomposition via the EMD sifting process. The decomposition consists of seven IMF and a residue. As mentioned previously, the first IMF contains the highest frequency component within the data. Table 2 shows the energy of the first IMF of the LDV signals for the intact pipe at the five measurement locations. Table 3 lists the EMD energy for the first damage case. The EMD energy DI calculated from Equation (1) for the first damage case is illustrated using a bar chart in Figure 7. Figure 7 also shows a bar chart representing the EMD damage energy indices obtained from the piezoceramic sensors. Ignoring the DI at location 5 (PZT 5) it can be observed in both bar charts that the indices in the vicinity of the damage (locations 3 and 4, PZTs 3 and 4) are higher compared to those for locations 1 and 2. This clearly shows the capability of the proposed DI as well as the efficacy of the LDV in identifying and localizing the damage.

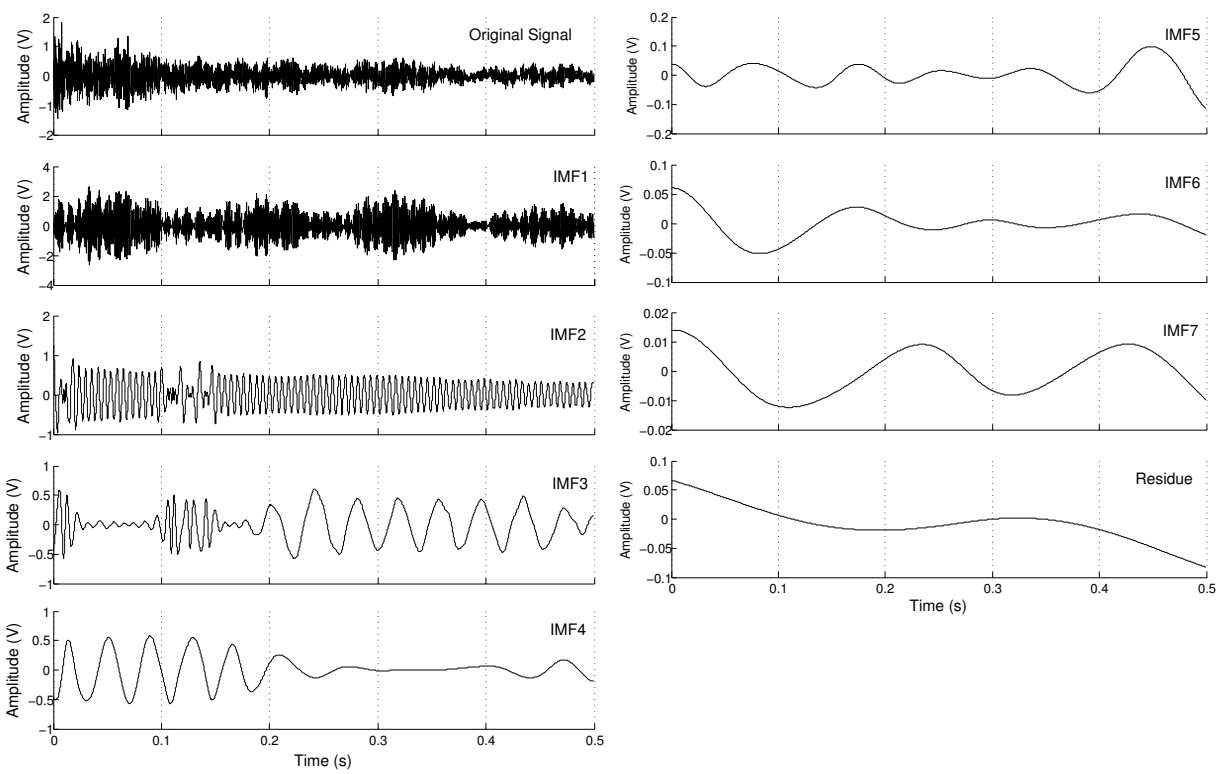

Figure 6. Typical PZT signal and its first five IMFs after decomposition.

	Test 1	Test 2	Test 3	Average
LDV signal at location 1	0.169797	0.165133	0.181408	0.172112
LDV signal at location 2	0.396397	0.454278	0.461394	0.437357
LDV signal at location 3	0.345839	0.343561	0.371000	0.353467
LDV signal at location 4	0.539827	0.484020	0.448339	0.490728
LDV signal at location 5	0.560725	0.511886	0.546993	0.539868

Table 2. EMD energy of the first IMF of the pipe in its healthy state.

	Test 1	Test 2	Test 3	Average
LDV signal at location 1	0.155000041	0.143422832	0.139656454	0.146026
LDV signal at location 2	0.415372962	0.36785452	0.346687328	0.376638
LDV signal at location 3	0.181852193	0.186811528	0.214943954	0.194536
LDV signal at location 4	0.135520932	0.135375133	0.139095011	0.136664
LDV signal at location 5	0.957739222	0.8970118	0.971491258	0.942081

Table 3. EMD energy of the first IMF of the pipe in its damaged state (case 1: half-circumferential damage between locations 3 and 4).

The high value of the DI at location 5 (PZT 5) in Figure 7, is due to the fact that this location is very close to the free end at which the pipe is impacted. Impact at that location produces considerable perturbations in the vibration in that vicinity and therefore the results from this sensor do not provide reliable results.

In Figure 7, PZT 1 also has a relatively high DI value although there is no damage in the vicinity of this sensor. It is believed that this error was caused by the changes in the pipe's support conditions due to the removal of the pipe from its original setup state to create the damage, and then its replacement (which was unavoidable). It was practically impossible to reach the same boundary conditions as before the pipe removal even if the same torque was applied on the clamp bolts. Fortunately, this would not be encountered in real pipelines, since pipes are installed once and corrosion occurs gradually, and thus the support conditions remain the same. Interestingly, the LDV had smaller values at locations 1 and 5 (as

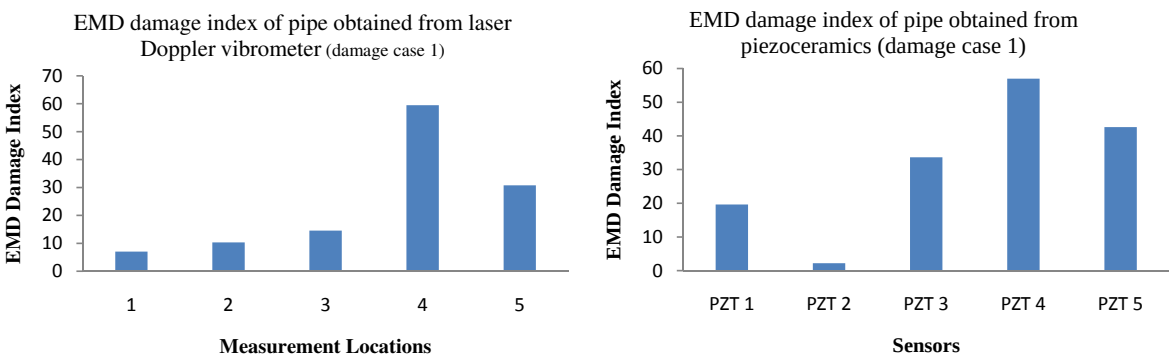

Figure 7. EMD damage index for the first damage case: a half circumference between locations 3 and 4.

opposed to PZTs 1 and 5). This shows that an advantage of the LDV over PZT sensors is less sensitivity to support conditions or impact location. A reason for this sensitivity reduction may be that the PZT sensors' output is related to the longitudinal pipe while the LDV measures the pipe's vertical vibrational velocity. Knowing this, it may be proposed that the boundary conditions and the impact location do not affect the velocity as much as the strain in the pipe. From Figure 7, it can be observed that the damage indices calculated from the LDV at locations 1 and 5 (where there was no damage) are lower than those obtained by the PZTs. The DI obtained from the LDV at location 4 (which is in the vicinity of the damage) is higher than that of PZT 4. However, the LDV predicted a lower DI at location 3 (which is in the vicinity of the damage) compared to the one calculated from PZT 3. Thus, in general it can be concluded that using the data obtained through LDV produced better damage identification compared to that taken through the piezoceramics.

Figure 8 depicts the EMD damage indices predicted by the LDV and the piezoceramics for the second damage case. The material removal for the second damage case was extended from the first case to a full circumference in order to examine more severe damage. Ignoring the signals from location 5, it can be seen that indices in the vicinity of the damage show higher values, which further demonstrates the applicability of the proposed damage methodology to locate damage. Comparing Figures 7 and 8, the following observations can be made:

- The damage indices computed from the LDV and PZTs at locations 3 and 4 for the second damage case are greater than those in the first case. This verifies the capability of the EMD DI in identifying the severity of damage.
- The LDV indices at locations 3 and 4 have higher values than those from the PZTs while at locations 1 and 5 the LDV indices are lower than those of the PZTs. This emphasizes the advantages of the LDV in terms of better damage location identification and less sensitivity to the boundary conditions and impact location.
- The damage indices obtained from the LDV show a greater difference between damage cases 1 and 2 compared to the PZT sensor results. This highlights the suitability of the LDV for damage severity assessment.

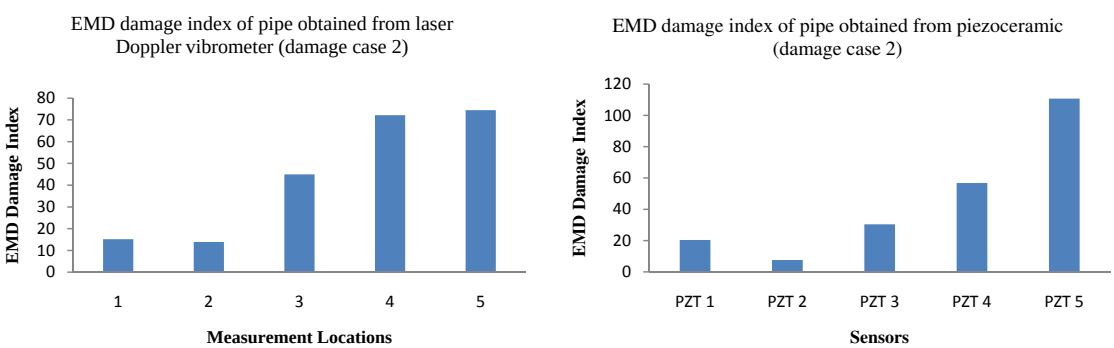

Figure 8. EMD damage index for the second damage case: a full circumference between locations 3 and 4.

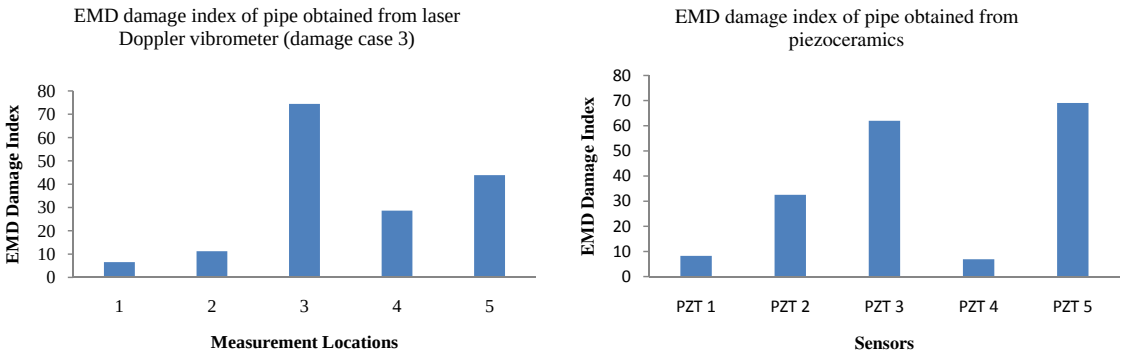

Figure 9. EMD damage index for the third damage case: a full circumference between locations 3 and 4 and a half circumference between locations 2 and 3.

Based on these observations, use of the LDV provides a clearer damage identification method compared with use of the piezoceramic sensors.

The effectiveness of the EMD DI in detection of multiple damages is further illustrated in Figure 9 by considering the results of the LDV and piezoceramic sensors for the third damage case. In this case, a full-circumferential damage was created between locations 3 and 4 and a half-circumferential damage was created between locations 2 and 3. Neglecting the DI at location 5 (PZT 5), the bars in Figure 9 show higher indices at locations 2, 3, and 4, which are all in the vicinity of damages. This verifies the validity of the proposed methodology in identifying multiple damages. Moreover, the LDV has been shown to be an effective remote sensor that can be successfully utilized with an SHM methodology.

Conclusion

In the present study, the applicability of the laser Doppler vibrometer (LDV) as a vibration measurement tool for structural health monitoring (SHM) was experimentally investigated through the application of a novel damage index (DI). This index is referred to as the EMD energy DI and is based on the Hilbert–Huang transform. For the experiment, a cantilever steel pipe was excited with an impulse hammer and its free vibrational velocity was acquired by the LDV at specified measurement locations. The vibration signals were then processed and decomposed via EMD and the energy of the first IMF for each signal was calculated for both the healthy and damaged pipe states. Three cases were analyzed to simulate various degrees of corrosion on the pipe surface: a single damage case (a partial circumference), a more severe single damage case (a full circumference), and a multiple damage case. In order to verify the LDV's results, they were compared with the results from PZT sensors bonded to the pipe's surface close to the LDV measurement locations.

The experimental results verified the capability of the LDV and the EMD energy DI to successfully detect and localize single and multiple damages in addition to qualifying damage severity. It was also observed that signal pass-band filtering should be carefully applied to avoid filtering out meaningful frequency components required for the proposed damage detection method. The frequency spectrum obtained from the LDV was in good agreement with the PZT results. However, a few frequency components were missing in the LDV results; these components corresponded to the in-plane vibration modes which the LDV was not able to capture. Compared to piezoceramic sensors, the LDV provided higher

damage indices at damage locations as well as a better assessment of damage severity. Furthermore, the LDV was less sensitive to boundary conditions and impact locations.

In general, use of the LDV as a remote and accurate high resolution optical measurement system provided satisfactory identification of single and multiple damages and can therefore be successfully utilized in SHM.

References

[API 2000] *API spec 5L: specification for line pipe*, 42nd ed., American Petroleum Institute, Washington, DC, 2000. Replaced by 44th edition.

[Banks et al. 1996] H. T. Banks, D. J. Inman, D. J. Leo, and Y. Wang, "An experimentally validated damage detection theory in smart structures", *J. Sound Vib.* **191**:5 (1996), 859–880.

[Cheraghi and Taheri 2007] N. Cheraghi and F. Taheri, "A damage index for structural health monitoring based on the empirical mode decomposition", *J. Mech. Mater. Struct.* **2**:1 (2007), 43–62.

[Cheraghi and Taheri 2008] N. Cheraghi and F. Taheri, "Application of the empirical mode decomposition for system identification and structural health monitoring", *Int. J. Appl. Math. Eng. Sci.* **2**:1 (2008), 61–72.

[Cheraghi et al. 2005a] N. Cheraghi, M. J. Riley, and F. Taheri, "A novel approach for detection of damage in adhesively bonded joints in plastic pipes based on vibration method using piezoelectric sensors", pp. 3472–3478 in *Proceedings of the International Conference on Systems, Man, and Cybernetics* (Waikoloa, HI, 2005), vol. 4, IEEE, Piscataway, NJ, 2005.

[Cheraghi et al. 2005b] N. Cheraghi, G. P. Zou, and F. Taheri, "Piezoelectric-based degradation assessment of a pipe using Fourier and wavelet analyses", *Comput.-Aided Civ. Infrastruct. Eng.* **20**:5 (2005), 369–382.

[Douka et al. 2004] E. Douka, S. Loutridis, and A. Trochidis, "Crack identification in plates using wavelet analysis", *J. Sound Vib.* **270**:1–2 (2004), 279–295.

[Fukunaga et al. 2002] H. Fukunaga, N. Hu, and F.-K. Chang, "Structural damage identification using piezoelectric sensors", *Int. J. Solids Struct.* **39**:2 (2002), 393–418.

[Giurgiutiu et al. 2002] V. Giurgiutiu, A. Zagrai, and J. J. Bao, "Piezoelectric wafer embedded active sensors for aging aircraft structural health monitoring", *Struct. Health Monit.* **1**:1 (2002), 41–61.

[Hassiotis 2000] S. Hassiotis, "Identification of damage using natural frequencies and Markov parameters", *Comput. Struct.* **74**:3 (2000), 365–373.

[Hong et al. 2002] J.-C. Hong, Y. Y. Kim, H. C. Lee, and Y. W. Lee, "Damage detection using the Lipschitz exponent estimated by the wavelet transform: applications to vibration modes of a beam", *Int. J. Solids Struct.* **39**:7 (2002), 1803–1816.

[Huang et al. 1998] N. E. Huang, Z. Shen, S. R. Long, M. C. Wu, H. H. Shih, Q. Zheng, N.-C. Yen, C. C. Tung, and H. H. Liu, "The empirical mode decomposition and the Hilbert spectrum for nonlinear and non-stationary time series analysis", *Proc. R. Soc. Lond. A* **454**:1971 (1998), 903–995.

[Hwang and Kim 2004] H. Y. Hwang and C. Kim, "Damage detection in structures using a few frequency response measurements", *J. Sound Vib.* **270**:1–2 (2004), 1–14.

[Jian et al. 1997] X. H. Jian, H. S. Tzou, C. J. Lissenden, and L. S. Penn, "Damage detection by piezoelectric patches in a free vibration method", *J. Compos. Mater.* **31**:4 (1997), 345–359.

[Kaito et al. 2005] K. Kaito, M. Abe, and Y. Fujino, "Development of non-contact scanning vibration measurement system for real-scale structures", *Struct. Infrastruct. Eng.* **1**:3 (2005), 189–205.

[Khan et al. 2000] A. Z. Khan, A. B. Stanbridge, and D. J. Ewins, "Detecting damage in vibrating structures with a scanning LDV", *Opt. Lasers Eng.* **32**:6 (2000), 583–592.

[Kim and Chun 2004] H.-S. Kim and Y.-S. Chun, "Structural damage assessment of building structures using dynamic experimental data", *Struct. Des. Tall Spec. Build.* **13**:1 (2004), 1–8.

[Kim and Melhem 2004] H. Kim and H. Melhem, "Damage detection of structures by wavelet analysis", *Eng. Struct.* **26**:3 (2004), 347–362.

[Kim et al. 2003] J.-T. Kim, Y.-S. Ryu, H.-M. Cho, and N. Stubbs, "Damage identification in beam-type structures: frequency-based method vs. mode-shape-based method", *Eng. Struct.* **25**:1 (2003), 57–67.

[Lin et al. 2005] S. Lin, J. N. Yang, and L. Zhou, "Damage identification of a benchmark building for structural health monitoring", *Smart Mater. Struct.* **14**:3 (2005), 162–169.

[Liu et al. 2006] J. Liu, X. Wang, S. Yuan, and G. Li, "On Hilbert–Huang transform approach for structural health monitoring", *J. Intell. Mater. Syst. Struct.* **17**:8–9 (2006), 721–728.

[Nassif et al. 2005] H. H. Nassif, M. Gindy, and J. Davis, "Comparison of laser Doppler vibrometer with contact sensors for monitoring bridge deflection and vibration", *NDT & E Int.* **38**:3 (2005), 213–218.

[Ovanesova and Suarez 2004] A. V. Ovanesova and L. E. Suarez, "Applications of wavelet transforms to damage detection in frame structures", *Eng. Struct.* **26**:1 (2004), 39–49.

[Peeters et al. 1996] B. Peeters, M. Abdel Wahab, G. De Roeck, J. De Visscher, W. P. De Wilde, J.-M. Ndambi, and J. Vantomme, "Evaluation of structural damage by dynamic system identification", pp. 1349–1361 in *Proceedings of ISMA21: 1996 International Conference on Noise and Vibration Engineering* (Leuven, 1996), edited by P. Sas, Katholieke Universiteit Leuven, Leuven, 1996.

[Peeters et al. 2001] B. Peeters, J. Maeck, and G. De Roeck, "Vibration-based damage detection in civil engineering: excitation source and temperature effects", *Smart Mater. Struct.* **10**:3 (2001), 518–527.

[Polytec 2009] Polytec, "Single-point vibrometers", 2009, Available at http://www.polytec.com/usa/158_421.asp.

[Ren and De Roeck 2002] W.-X. Ren and G. De Roeck, "Structural damage identification using modal data, II: Test verification", *J. Struct. Eng.* (*ASCE*) **128**:1 (2002), 96–104.

[Shi et al. 2000] Z. Y. Shi, S. S. Law, and L. M. Zhang, "Structural damage detection from modal strain energy change", *J. Eng. Mech.* (*ASCE*) **126**:12 (2000), 1216–1223.

[Soh et al. 2000] C. K. Soh, K. K.-H. Tseng, S. Bhalla, and A. Gupta, "Performance of smart piezoceramic patches in health monitoring of a RC bridge", *Smart Mater. Struct.* **9**:4 (2000), 533–542.

[Wang et al. 2001] X. Wang, N. Hu, H. Fukunaga, and Z. H. Yao, "Structural damage identification using static test data and changes in frequencies", *Eng. Struct.* **23**:6 (2001), 610–621.

[Winston et al. 2001] H. A. Winston, F. Sun, and B. S. Annigeri, "Structural health monitoring with piezoelectric active sensors", *J. Eng. Gas Turb. Power* (*ASME*) **123**:2 (2001), 353–358.

[Xu and Chen 2004] Y. L. Xu and J. Chen, "Structural damage detection using empirical mode decomposition: experimental investigation", *J. Eng. Mech.* (*ASCE*) **130**:11 (2004), 1279–1288.

Received 27 Jan 2009. Revised 9 Jul 2009. Accepted 5 Aug 2009.

DAVOOD REZAEI: drezaei@dal.ca
Department of Civil and Resource Engineering, Dalhousie University, 1360 Barrington St., Halifax, NS B3J 1Z1, Canada

FARID TAHERI: farid.taheri@dal.ca
Department of Civil and Resource Engineering, Dalhousie University, 1360 Barrington St., Halifax, NS B3J 1Z1, Canada
http://myweb.dal.ca/farid/

JOURNAL OF MECHANICS OF MATERIALS AND STRUCTURES
Vol. 5, No. 2, 2010

ENERGY ABSORPTION OF A HELICOIDAL BISTABLE STRUCTURE

SEUBPONG LEELAVANICHKUL, ANDREJ CHERKAEV,
DANIEL O. ADAMS AND FLORIAN SOLZBACHER

The concept of a bistable structure as an energy absorbing structure is presented. A bistable structure is capable of distributing damage throughout the whole body, thus increasing the amount of energy dissipation. Using this concept, a helicoidal bistable structure is developed. We investigate a structure in which a helicoidal orthotropic shell envelops a solid cylinder. The center core of the structure is treated as a linear-elastic isotropic material. Numerical simulations of damage (breakages) are performed under static loads, and the force-displacement relation is obtained as a result. As an energy absorbing structure, the helicoidal bistable structure can absorb more energy than a conventional structure before it fails. The helicoidal bistable structure can be designed to sustain a small elongation while still being able to release energy effectively. The additional twisting degrees of freedom correspond to the additional energy released in the process of elongation.

1. Introduction

The total fracture energy is an important consideration when determining the ability of a structure to withstand dynamic loading. In most structures, however, localized yielding occurs at a particular location such that the total energy associated with a fracture in the structure is relatively small.

Bistable structures allow an increase in the total fracture energy. In a bistable structure there are redundant localized load paths, so that when one load path yields and subsequently fails, the remaining load paths can carry the load, preserving structural integrity. A bistable structure can be developed by forming a chain of bistable structural elements such that multiple regions of the structure may exhibit yielding behavior prior to ultimate structural failure. In other words, yielding is delocalized, occurring in a larger fraction of the structure.

The analytical solution to the dynamic loading of a chain of bistable structural elements was first proposed by Slepyan and Troyankina [1984; 1988]. This dynamic yielding model was later extended by Balk et al. [2001a; 2001b] to the case of reversible two-phase chains of bistable structural elements. The dynamic response of elastic-brittle bistable structures was also studied by Cherkaev et al. [2005; 2005]. The response of chains of bistable structural elements under quasistatic and dynamic loading was investigated by Cherkaev and Zhornitskaya [2003]. The numerical results obtained showed that a chain of bistable links can withstand impact energy levels that are several times larger than for a conventional chain without bistable behavior.

A special structural design using a "waiting element" [Cherkaev and Slepyan 1995] has been used to increase stability. Waiting elements are parts of the structure that are initially not active and which remain nonactive until the strain becomes sufficiently large. Each link in the chain transitions from the lower

Keywords: bistable structure, helicoidal composites, energy absorption, damage.

strain state to the higher strain state, which produces a transition wave that propagates along the chain. Unlike conventional structures, in which the strain is concentrated near the impact zone, a structure with waiting elements distributes the strain over a larger area. Cherkaev et al. [2006] showed that by using an elastic-plastic material in the redundant load path, or waiting element, the cross sectional area of this portion could be made significantly smaller than the main load path, or main element, because an elastic-plastic material can sustain larger deformations beyond the material yield strength. An elastic-brittle material, on the other hand, fails once the yield strength is reached. This concept was also explored experimentally by Whitman and La Saponara [2007a; 2007b].

The bistable structure presented in our previous work [Cherkaev et al. 2006] (see Figure 1) requires that the waiting element (waiting link) be sufficiently long to remain inactive upon initial loading. However, more space is needed as the waiting element becomes longer and more curved. In this paper, we investigate another configuration, a helicoid, which remedies the spacing issue faced in our previous work. A bistable response under extension can be achieved similar to that of the matrix fracturing in the composite described by Slepyan et al. [2000].

Note on terminology. In this work, we will use the term *strip* (rather than the earlier "link" or "element") to mean each of the two components of a *bistable link*: the main strip and the waiting strip. A *bistable structure* is a chain of bistable links.

Consider a helicoidal bistable link consisting of a main strip and a waiting strip, as in Figure 2. The center core, a solid cylinder, is treated as the main strip, and is made of an isotropic material. The outer layer serves as the waiting strip, and consists of an orthotropic material having its primary direction of orthotropy spiraling about the main strip (central core). By enveloping the inner cylinder in a helicoidal anisotropic shell, the structure maintains symmetry about its cylindrical axis.

Under an axial tensile load, both components of the helicoidal bistable link elongate until the main strip yields. As yielding continues, an increasing portion of the applied load is transferred to the outer helicoidal waiting strip. This paper investigates the energy absorption concept of a bistable structure using a simplified model where the central main strip exhibits linear elastic material behavior to failure (brittle failure). The outer helicoidal waiting strip is assumed to remain nonactive (unloaded) until the

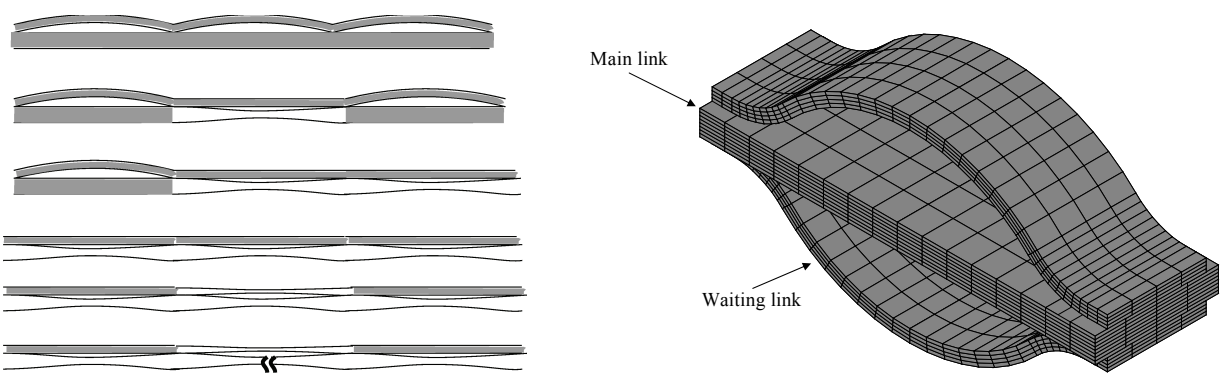

Figure 1. Left: A chain of bistable structures and their damage process. Gray regions represent the undamaged main strips. The broken main strips are shown in white. Right: A bistable structure with a symmetric waiting element.

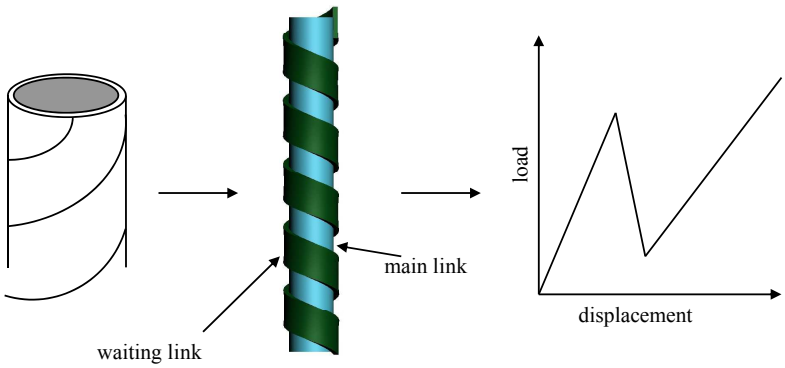

Figure 2. Representative model of a helicoidal bistable structure.

inner main strip fails in a brittle manner. Thus, for a chain of bistable links, each link transitions from a lower strain state to a higher strain state as the main strip (inner cylinder) fails. The main strip produces a transition wave that propagates along the chain. Unlike conventional structures, in which the strain is concentrated near the impact zone, a structure with a waiting strip distributes the strain over a large area.

The outline of this paper is as follows. First, the analytical solutions to the displacements and stresses are computed using the theory of elasticity. The process by which the main strip breaks and the waiting strip becomes active to maintain the structural stability is demonstrated using finite elements. The analytical solutions to the displacements and stresses are used to develop an equivalent one-dimensional discrete model. Three case studies are considered: a single bistable link, a chain of bistable links with sequential breakages of the main strip in each link, and a chain of bistable links with random breakages of the main strip in each link.

2. Modeling of a helicoidal bistable structure

To investigate the force-displacement relationship of an individual helicoidal bistable link, a displacement field corresponding to a given applied load is determined from a generalized theory of linear anisotropic elasticity as described in [Lekhnitskii 1981; Leelavanichkul and Cherkaev 2009]. The main strip is made of an isotropic material, while the waiting strip is made of an orthotropic material with its main axis of orthotropy oriented at an angle ϕ, as shown in Figure 3.

2A. ***Linear elasticity solution.*** The structure shown in Figure 3 possesses cylindrical anisotropy; hence, it is more desirable to determine the solution in cylindrical coordinates. The detailed formulation of the solution is given in [Leelavanichkul and Cherkaev 2009]. In three-dimensional stress analysis, stresses and strains are related via Hooke's law in cylindrical coordinates as

$$\begin{Bmatrix} \sigma_{rr} \\ \sigma_{\theta\theta} \\ \sigma_{zz} \\ \sigma_{\theta z} \\ \sigma_{rz} \\ \sigma_{r\theta} \end{Bmatrix} = \begin{bmatrix} c_{11} & c_{12} & c_{13} & c_{14} & 0 & 0 \\ c_{21} & c_{22} & c_{23} & c_{24} & 0 & 0 \\ c_{31} & c_{32} & c_{33} & c_{34} & 0 & 0 \\ c_{41} & c_{42} & c_{43} & c_{44} & 0 & 0 \\ 0 & 0 & 0 & 0 & c_{55} & c_{56} \\ 0 & 0 & 0 & 0 & c_{65} & c_{66} \end{bmatrix} \begin{Bmatrix} \epsilon_{rr} \\ \epsilon_{\theta\theta} \\ \epsilon_{zz} \\ \epsilon_{\theta z} \\ \epsilon_{rz} \\ \epsilon_{r\theta} \end{Bmatrix}. \tag{2-1}$$

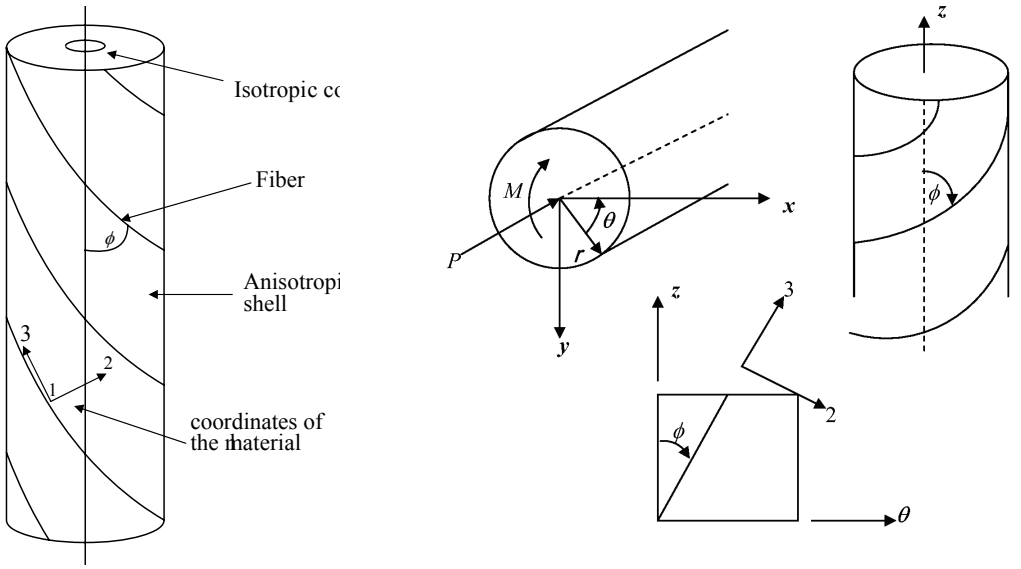

Figure 3. Helicoidal structure and its coordinate system.

Replacing the strains in (2-1) using the strain-displacement relationship

$$\varepsilon_{rr}=\frac{\partial u_r}{\partial r},\qquad \varepsilon_{\theta\theta}=\frac{1}{r}\frac{\partial u_\theta}{\partial\theta}+\frac{u_r}{r},\qquad \varepsilon_{zz}=\frac{\partial u_z}{\partial z},\qquad \varepsilon_{\theta z}=\frac{1}{2}\Big(\frac{\partial u_\theta}{\partial z}+\frac{1}{r}\frac{\partial u_z}{\partial\theta}\Big),$$
$$\varepsilon_{zr}=\frac{1}{2}\Big(\frac{\partial u_z}{\partial r}+\frac{\partial u_r}{\partial z}\Big),\qquad \varepsilon_{r\theta}=\frac{1}{2}\Big(\frac{1}{r}\frac{\partial u_r}{\partial\theta}+\frac{\partial u_\theta}{\partial r}-\frac{u_\theta}{r}\Big), \tag{2-2}$$

and substituting into the equilibrium equations

$$0=\frac{1}{r}\frac{\partial}{\partial r}(r\sigma_{rr})+\frac{1}{r}\frac{\partial}{\partial\theta}\sigma_{r\theta}+\frac{\partial}{\partial z}\sigma_{rz}-\frac{\sigma_{\theta\theta}}{r},$$
$$0=\frac{1}{r^2}\frac{\partial}{\partial r}(r^2\sigma_{\theta r})+\frac{1}{r}\frac{\partial}{\partial\theta}\sigma_{\theta\theta}+\frac{\partial}{\partial z}\sigma_{\theta z}, \tag{2-3}$$
$$0=\frac{1}{r}\frac{\partial}{\partial r}(r\sigma_{zr})+\frac{1}{r}\frac{\partial}{\partial\theta}\sigma_{z\theta}+\frac{\partial}{\partial z}\sigma_{zz},$$

we obtain the solution to the main strip as

$$u=C_1 r,\qquad v=\Theta r z,\qquad w=Cz, \tag{2-4}$$

and the solution to the waiting strip as

$$U(r,\theta)=C_1 r^k+C_2^{-k}-c_{11}m_1 r^2-4c_{11}m_2 r+m_1 c_{22}r^2+m_2 c_{22}r,\quad V(r,\theta)=\Theta r z,\quad W(r,\theta)=zC, \tag{2-5}$$

where

$$k=\sqrt{\frac{c_{22}}{c_{11}}},\qquad m_1=\frac{2\Theta\big(c_{14}-\frac{1}{2}c_{24}\big)}{(c_{22}-c_{11})(c_{22}-4c_{11})},\qquad m_2=\frac{C(c_{13}-c_{23})}{(c_{22}-c_{11})(c_{22}-4c_{11})}.$$

The unknown constants C, Θ, C_1, and C_2 can be found using the boundary conditions

$$\begin{aligned} &\sigma_r\big|_{r_1} = \sigma_r\big|_{r_2}, \quad \tau_{\theta z}\big|_{r_1} = \tau_{\theta z}\big|_{r_2}, \quad \tau_{rz}\big|_{r_1} = \tau_{rz}\big|_{r_2}, \quad \tau_{r\theta}\big|_{r_1} = \tau_{r\theta}\big|_{r_2}, \\ &u(r,\theta)\big|_{r_1} = u(r,\theta)\big|_{r_2}, \quad v(r,\theta)\big|_{r_1} = v(r,\theta)\big|_{r_2}, \quad w(r,\theta)\big|_{r_1} = w(r,\theta)\big|_{r_2}, \end{aligned} \tag{2-6}$$

and the end conditions

$$\int_0^{r_2}\int_0^{2\pi} \sigma_{zz_{\text{iso}}} r\,dr + \int_{r_1}^{r_2}\int_0^{2\pi} \sigma_{zz_{\text{aniso}}} r\,dr = P, \tag{2-7}$$

$$\int_0^{r_2}\int_0^{2\pi} \sigma_{\theta z_{\text{iso}}} r^2\,dr + \int_{r_1}^{r_2}\int_0^{2\pi} \sigma_{\theta z_{\text{aniso}}} r^2\,dr = 0, \tag{2-8}$$

where r_1 is the radius of the main strip and r_2 is the outer radius of the waiting strip. Once all the unknown constants are determined, Equations (2-4) and (2-5) can be substituted into (2-2) to obtain the strains, after which the stresses can be computed using (2-1).

2B. ***Simulation of breakages using the finite element method.*** While analytical solutions to the displacements and stresses of the undamaged link are obtained from the theory of anisotropic elasticity, we investigate the breakages of the main strip using the finite element method. Our analytical solution gives stresses based on the assumption that the strains do not vary along the structure's generator. Hence, the solution obtained cannot describe how stresses are distributed along the longitudinal direction of the structure when the length of the structure is finite or when there is a boundary effect from a discontinuity. A single breakage in a bistable link is simulated to show the effect that the spiraling angle ϕ (see Figure 3) has on the force-displacement relationship. Then, a simulation where multiple breakages occur is performed to determine the minimum length of each link such that stress interactions due to breakages of the main strips are minimal. Notice that for simplicity we do not consider stress interactions in neighboring breakage points, and we assume that the failure occurs only in the main strips.

To simulate the failure of the main strip, two load steps are used. The first load step is applied to the point where failure of the main strip occurs. The second load step begins following the localized failure of the main strip. Each of these two load steps consists of several substeps that discretely update the stiffness matrix.

Example 2.1: *Numerical simulation of a breakage in the main strip.* A three-dimensional finite element model of the structure is used and its undamaged model is verified with an analytical solution as shown in Figure 4. For demonstration purposes, we consider a bistable structure made from materials with the following properties:

- The main strip's isotropic material has a shear modulus of 25.51 GPa and a Poisson's ratio of 0.35.
- The waiting strip is modeled using an anisotropic material having a helicoidal fiber orientation and the following material properties:

Parameter	$E_{11} = E_{22}$	E_{33}	$G_{23} = G_{13}$	G_{12}	$\nu_{23} = \nu_{13}$	ν_{12}
Value	7.591 GPa	139.348 GPa	3.789 GPa	2.782 GPa	0.0178	0.364

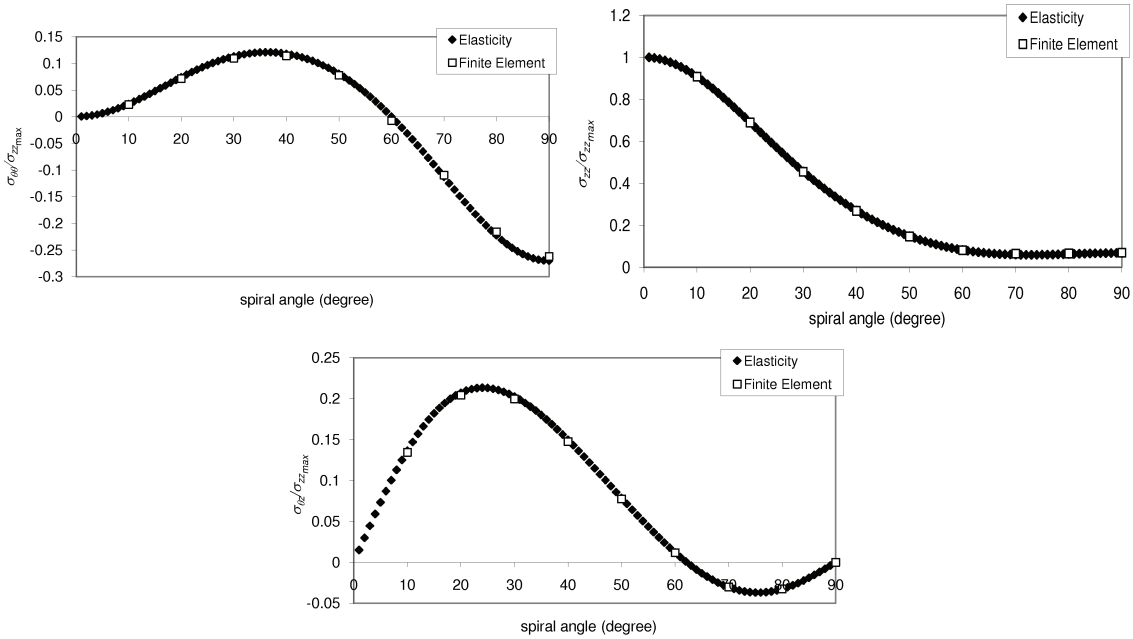

Figure 4. Verification of the finite element model.

- The radius of the inner cylinder is 6.35 mm and the thickness of the outer shell is 1.59 mm. Only axial tensile loading is considered.

The force versus displacement response for a range of fiber angles in the helicoidal waiting strip is shown in Figure 5. The effect of the main strip breakage (produced at an applied displacement of 0.127 mm) increases as the fiber angle increases. As the fiber angle increases, the axial stiffness of the waiting strip decreases as evidenced by the decreasing slope in Figure 5. This behavior is desirable in order to achieve the desired bistable response.

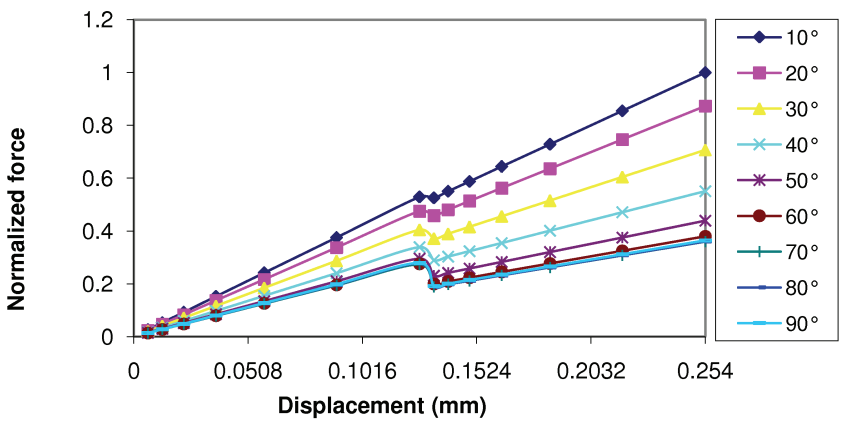

Figure 5. Force-displacement of the bistable model with a single damage. The force is normalized by the maximum force when the displacement is 0.254 mm.

Ideally, the waiting strip should have no effect on the structural response until the main strip fails. At lower fiber angles, the waiting strip becomes stiffer and requires a higher applied load to achieve the same axial displacement. The dips in the curves shown in Figure 5 represent the amount of energy dissipated as a result of the main strip breakage. Hence, less energy is dissipated when the spiraling angle is small.

Example 2.2: *Stress distribution around the broken area of the main strip.* The stress field near the broken area in the main strip is investigated in this example to determine the stress distribution when three-dimensional effects are considered. When more than one damage point is expected, the distance between each damage point must be determined such that the stresses in the neighborhoods of these points do not interact with each other. The objective of this part is to determine the most basic condition which simplifies the analysis of the breakage; namely, to avoid any complication of the stress riser due to the finite region. We investigate the distribution of the stresses near the broken area in the main strip. Using the model discussed in the previous section, the von Mises stresses of each variation of the angle of orthotropy and applied loads are computed for the main strip material and shown in Figure 6.

The stresses shown in these figures are normalized to their corresponding maximum stress values. Roughly, three groups of stress results can be seen in these figures. They represent when the fiber angles are 10°, 30°, and $\geq 50°$. Each line within each group represents the result for a different magnitude of the applied load. These figures illustrate that the interval of the high stress concentration x_0 does not depend on the magnitude of the applied load nor the spiraling angle. For the structural configuration in Example 2.1, x_0 is approximately 12.7 mm.

When there are multiple locations of the damage, as shown in Figures 7 and 8, the interactions of the concentrated stresses are still minimal as long as the broken locations take place 25.4 mm from each other. Here, breakages are introduced to seven locations simultaneously, 50.8 mm apart from each other. One can see that the distribution of stresses around the breakages has the same characteristics, and they do not interact with one another.

Next, the effect due to the change of the radius r_i of the main strip is investigated, with the total cross-sectional area of the structure held constant.

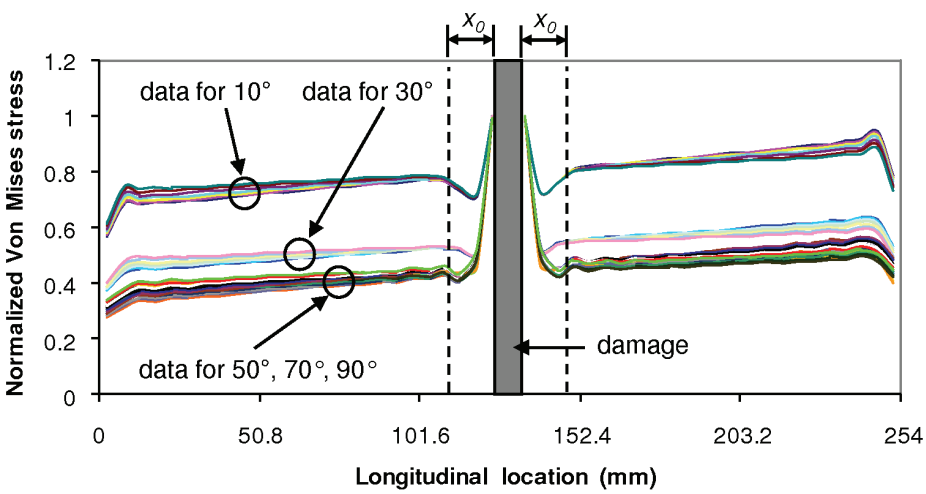

Figure 6. Normalized von Mises stress around the breakage.

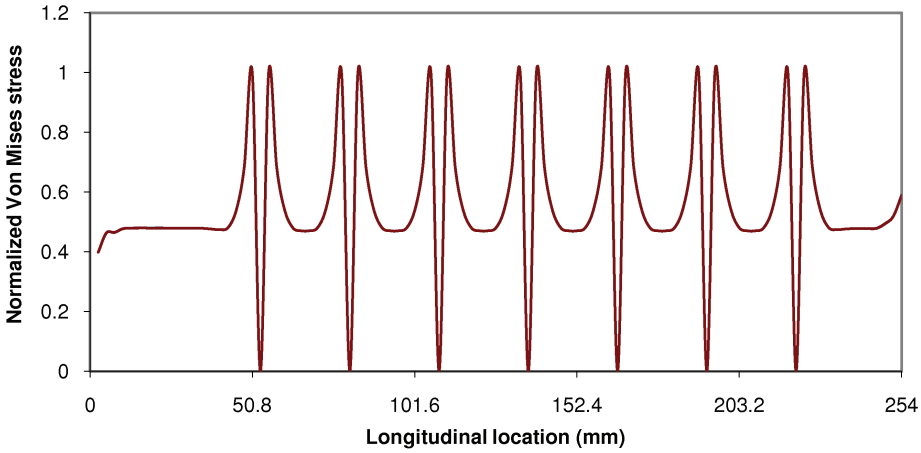

Figure 7. Stress distribution when the breakage locations are 50.8 mm apart (60°).

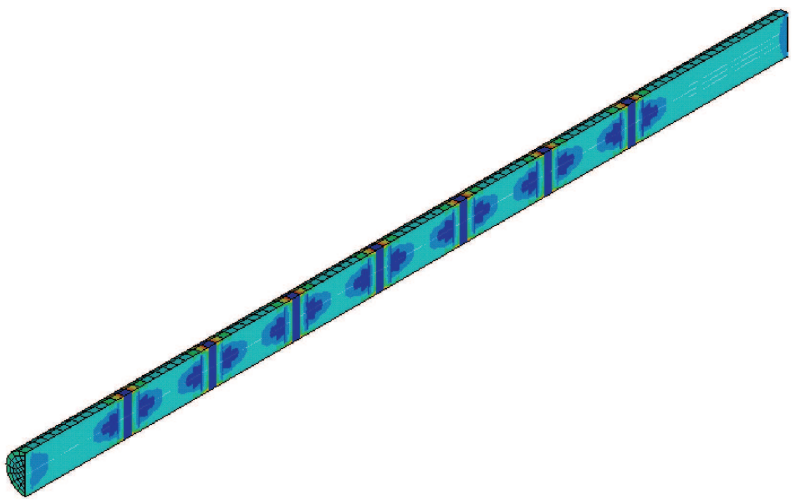

Figure 8. Contour plot of normalized von Mises stress in the main link when the breakage locations are 50.8 mm apart. Darker (blue) areas correspond to values near 0 and lighter areas to values near 0.3.

Example 2.3: *Effect of changes in the radii of the main strip and waiting strip.* The normalized von Mises stress in the center core is shown in Figure 9, top. The legends there represent the ratio between the radii of the waiting strip and the main strip, r_o/r_i. The pattern of stress distributions cannot be obtained from these plots due to the fluctuation of the stresses. The fluctuation of the von Mises stress becomes more visible at lower r_o/r_i ratios. These oscillations are the result of the approximation of the element stress. However, the differences in the magnitudes between peaks are reduced, but remain, as the number of elements is increased while the results converge. Each period of the oscillation corresponds to the length of the element, which 5.08 mm.

To further investigate the distribution of the stresses, two more scenarios are investigated. The first occurs when the main strip's radius remains fixed 6.35 mm and the radius of the waiting strip is varied.

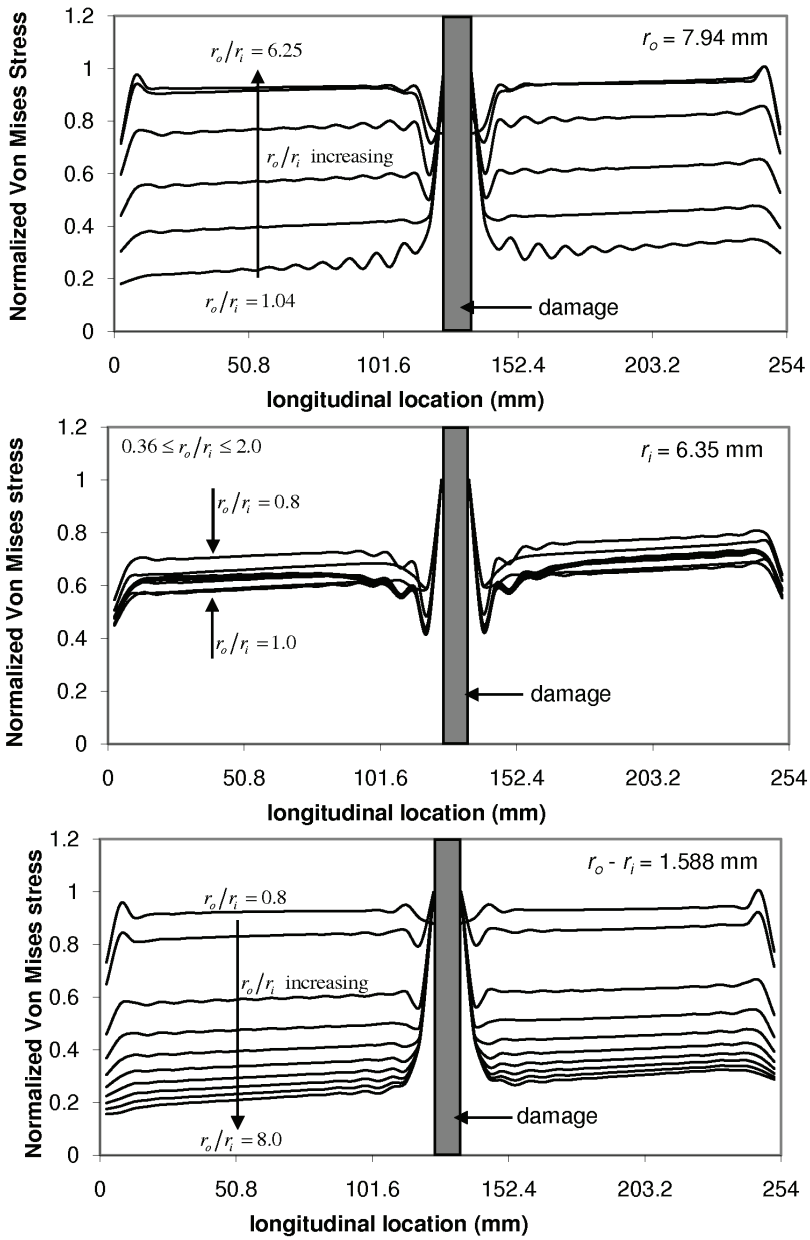

Figure 9. Stress distribution around the breakage in the main link. Top: r_i is varied while r_o remains at 7.94 mm. Middle: r_o is varied while r_i remains at 6.35 mm. Bottom: r_i and r_o are varied while the thickness of the waiting link is held at 1.59 mm.

The second case occurs when the thickness of the waiting strip is fixed at 1.59 mm and the radius of the main strip is varied. Results for these two cases are shown in the last two parts of Figure 9.

These results show that the stress distribution depends greatly on the ratio of the inner and outer radii of the spiraling layer, r_o/r_i. For the specific model having the properties as given in Example 2.1, the

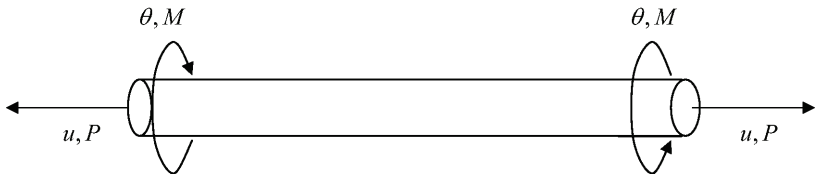

Figure 10. One-dimensional structural model.

range of x_0 values from three-dimensional analysis is 25.4 mm. This value, however, may change as the geometry of the structure varies. To maintain our focus on the bistable structure and its energy absorption capabilities, we did not analyze further the three-dimensional stress effect.

3. One-dimensional models

Since the deformations of the structure considered in this paper are symmetric about a cylindrical axis, this structure can be represented by a one-dimensional model. It is convenient to replace the three-dimensional cylinder with a link. The helicoidal symmetry results in a coupling between a rotation about the axis and the elongation as shown in Figure 10.

3A. ***One-dimensional structural model.*** A one-dimensional structural element is developed based on the formulation given in [Leelavanichkul and Cherkaev 2009], where an elongation is coupled to a rotation. Linkages are useful in describing the physics of a larger structure assembled from multiple links where the displacement and reactions at their ends are of major interest. We obtain the stiffness matrix $\boldsymbol{k}$ relating the force P and moment M at the element ends to the elongation and the rotation about the θ-axis:

$$\boldsymbol{f} = \boldsymbol{k}\boldsymbol{u} \qquad \text{or} \qquad \begin{Bmatrix} P \\ M \end{Bmatrix} = \begin{bmatrix} k_1 & k_2 \\ k_4 & k_3 \end{bmatrix} \begin{Bmatrix} u \\ \theta \end{Bmatrix}. \tag{3-1}$$

The quantities of interest are the stiffness constants k_1, k_2, k_3, and k_4. Without losing generality, one can assume that $k_4 = k_2$. Using the displacements, which are given by (2-4) and (2-5), at two measures of the loads P and M, the stiffness k constants can be determined [Leelavanichkul and Cherkaev 2009].

Example 3.1: *Illustration of the varying stiffnesses as function of angle ϕ.* The stiffness values of the equivalent one-dimensional model of the structure given in Example 2.1 are illustrated in Figure 11. These plots demonstrate how the stiffness values vary with the spiral angle. The values of the stiffness also vary linearly with the load P and the length L of the three-dimensional model. Despite having only an axial load applied, the stiffness constants k_2 and k_3 generate rotation as the structure is stretched. We realize that the effect of the coupling increases the energy release capability while the elongation remains the same. The additional twisting degrees of freedom correspond to additional energy released in the process of elongation.

3B. ***Finite element model: formulation of the stiffness matrix.*** A single element, as shown in Figure 12, used in the finite element model can be constructed based on the one-dimensional structural model given in the previous section including both elongation and rotational degrees of freedom. When the structure is subjected to an axial load, the force-displacement relation is governed by

$$\boldsymbol{F} = \boldsymbol{K}(\boldsymbol{u})\boldsymbol{u},$$

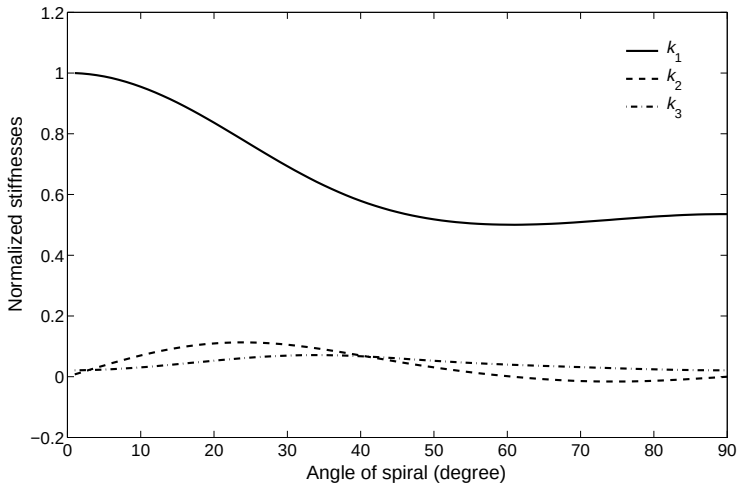

Figure 11. Stiffnesses of the one-dimensional model (normalized by the maximum value of k_1).

where

$$\boldsymbol{K}(\boldsymbol{u}) = \begin{cases} \boldsymbol{K}_1 & \text{if } \sigma_e \le \sigma_Y, \\ \boldsymbol{K}_2 & \text{otherwise,} \end{cases}$$

and σ_e and σ_Y represent the stress in the element and the main strip yield stress, respectively. The stiffness matrix $\boldsymbol{K}_1$ is the total stiffness of the bistable structure and the stiffness matrix $\boldsymbol{K}_2$ is the stiffness of the waiting strip only. The axial deformation is coupled with the rotation about the generator; see Figure 12.

Thus, the deformations are represented by

$$\delta = \hat{d}_{2x} - \hat{d}_{1x}, \qquad \gamma = \hat{\phi}_{2x} - \hat{\phi}_{1x}, \tag{3-2}$$

where δ and γ are the elongation and rotation, respectively. The local axial displacement is represented by $\hat{d}$ while the nodal rotation is represented by $\hat{\phi}$. The force-displacement relationship is expressed as

$$P = k_1\delta + k_2\gamma, \qquad M = k_2\delta + k_3\gamma, \tag{3-3}$$

where P and M are the axial and torsional loads, respectively. The quantities k_1, k_2, and k_3 are the stiffness constants. Substituting (3-2) into (3-3), we have

$$P = k_1(\hat{d}_{2x} - \hat{d}_{1x}) + k_2(\hat{\phi}_{2x} - \hat{\phi}_{1x}), \qquad M = k_2(\hat{d}_{2x} - \hat{d}_{1x}) + k_3(\hat{\phi}_{2x} - \hat{\phi}_{1x}). \tag{3-4}$$

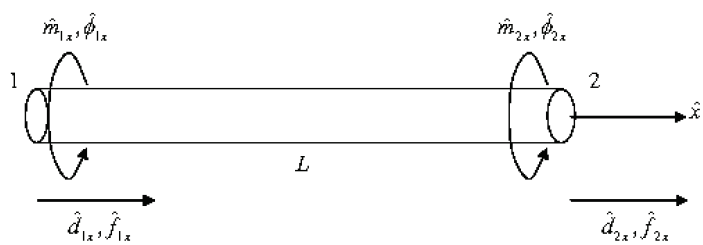

Figure 12. One-dimensional structural element.

By the sign convention for the nodal forces and equilibrium,

$$\hat{f}_{1x} = -P, \qquad \hat{f}_{2x} = P, \qquad \hat{m}_{1x} = M, \qquad \hat{m}_{2x} = -M. \tag{3-5}$$

Substituting (3-4) into (3-5), the following system is constructed:

$$\begin{Bmatrix} \hat{f}_{1x} \\ \hat{m}_{1x} \\ \hat{f}_{2x} \\ \hat{m}_{2x} \end{Bmatrix} = \begin{bmatrix} k_1 & k_2 & -k_1 & -k_2 \\ k_2 & k_3 & -k_2 & -k_3 \\ -k_1 & -k_2 & k_1 & k_2 \\ -k_2 & -k_3 & k_2 & k_3 \end{bmatrix} \begin{Bmatrix} \hat{d}_{1x} \\ \hat{\phi}_{1x} \\ \hat{d}_{2x} \\ \hat{\phi}_{2x} \end{Bmatrix}. \tag{3-6}$$

Hence, the element stiffness matrix is defined as

$$\hat{\boldsymbol{K}} = \begin{bmatrix} k_1 & k_2 & -k_1 & -k_2 \\ k_2 & k_3 & -k_2 & -k_3 \\ -k_1 & -k_2 & k_1 & k_2 \\ -k_2 & -k_3 & k_2 & k_3 \end{bmatrix}, \tag{3-7}$$

where k_1, k_2, and k_3 are the values calculated from the one-dimensional structural model as discussed in Section 3.

Two breakage scenarios are investigated: a sequential breakage and a random breakage. Both scenarios are demonstrated in this paper using numerical examples based on the formulation discussed above. Considering the structure given in Example 2.1, breakages of the main strip are assumed to occur at 50.8 mm intervals for this particular example to avoid interaction of concentrated stresses [Leelavanichkul 2007].

Example 3.2: *Sequential breakages.* For the case of sequential breakage of the main strip (central core), each new breakage occurs adjacent to the previous one. The location of the new core breakage is assumed to be 50.8 mm from the preceding core breakage as shown in Figure 13 ($2x_0 = 50.8$). The objective of this analysis is to determine the total energy absorption during the sequence of core breakages.

The material of the main strip is assumed to return to its unloaded state after a breakage occurs. The stiffness $\boldsymbol{K}(u)$ of the damaged link is updated with the new values $\boldsymbol{K}_2$ obtained from the computation of the one-dimensional structural model. We treat the main strip as an elastic-brittle material, therefore, the von Mises failure criterion is chosen to determine when the failure of the main strip occurred. Axial

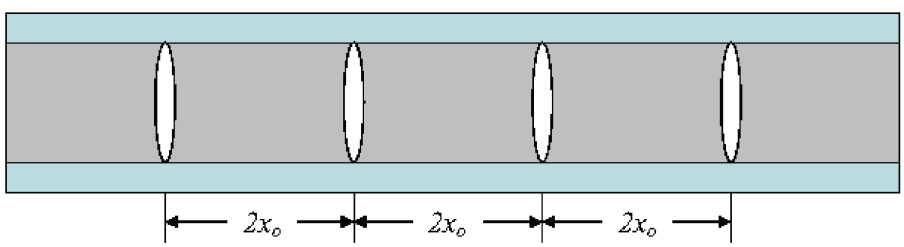

Figure 13. Representative model of sequential breakages.

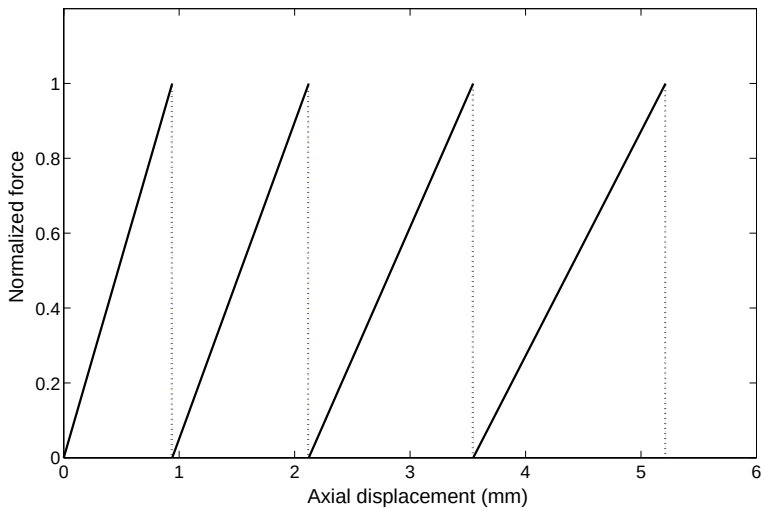

Figure 14. Force-displacement diagram for three sequential core breakages of a 254 mm axially loaded chain consisting of twenty links.

and shear stresses are determined separately using the nodal displacements,

$$\sigma_x = E\varepsilon_x = E\frac{du}{dx} = \frac{E}{L}(\hat{d}_{2x} - \hat{d}_{2x}), \qquad \tau_{xy} = G\gamma_{xy} = \frac{Gr}{L}(\hat{\phi}_{2x} - \hat{\phi}_{2x}). \tag{3-8}$$

The applied load is increased until the material yield strength is met:

$$\sigma_e = \sqrt{\sigma_1^2 - \sigma_1\sigma_2 + \sigma_2^2} \le \sigma_Y, \tag{3-9}$$

where σ_e is the element von Mises stress and σ_Y is the material yield stress. The principal stresses σ_1 and σ_2 are expressed as

$$\sigma_{1,2} = \frac{\sigma_x}{2} \pm \sqrt{\left(\frac{\sigma_x}{2}\right)^2 + \tau_{xy}^2}. \tag{3-10}$$

The force versus displacement response for the sequential breakage of a chain composed of four helicoidal bistable structures, each with a waiting strip having a fiber angle of 60°, is illustrated in Figure 14. Three main strip breakages take place in the chain (represented by vertical lines in the figure). Each time a breakage occurs, the overall stiffness of the structure is reduced and an increase in displacement is required for the next breakage to occur. The total strain energy of 31 J is required to produce three breakages for the chosen materials and specimen geometry.

Due to the anisotropy of the waiting strips, the conventional maximum strength criterion for isotropic materials gives a poor prediction of the failure. We use the Tsai–Hill failure criterion to determine whether the outer helicoidal layer fails:

$$\left(\frac{\sigma_1}{\sigma_{1u}}\right)^2 + \left(\frac{\sigma_2}{\sigma_{2u}}\right)^2 - \frac{\sigma_1\sigma_2}{\sigma_{1u}^2} + \left(\frac{\tau_{12}}{\tau_{12u}}\right)^2 < 1. \tag{3-11}$$

When the left side is reaches or exceeds 1, failure is predicted. For an angle of 60°, the predicted values are approximately 0.2 and 0.45 at the outer and inner surfaces, respectively, of the helicoidal layer.

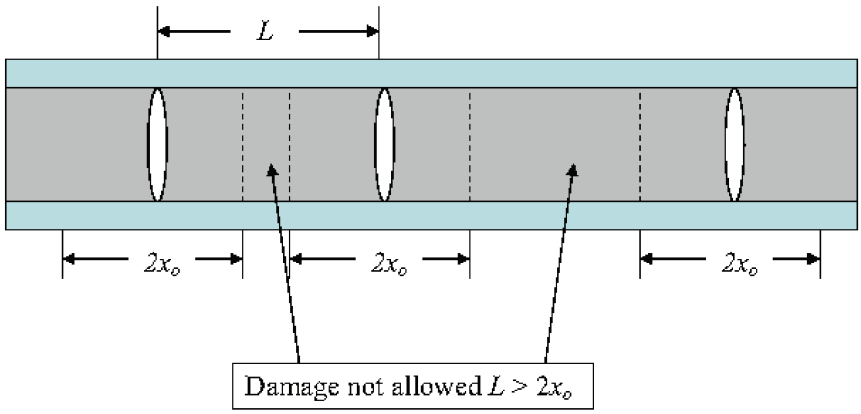

Figure 15. Representative model of random breakages.

The Tsai–Hill failure criterion does not distinguish between tensile and compressive failures, but is sufficient for our goal. The waiting strip becomes active only after the main strip fails. The nature of the main strip failure is not considered here. Axial and shear stresses computed in the element are used in the Tsai–Hill failure criterion.

Example 3.3: *Random breakages.* The breakages of the main strip may not necessarily occur sequentially. For nonsequential breakages, the same requirement for the spacing (50.8 mm) between the main strip breakages as in the sequential analysis is imposed. As shown in Figure 15, the spacing x_0 can become as large as 101.6 mm for the same structure used in the previous section.

Consider a vector $\boldsymbol{A}$ containing elements 1 to n, $[e_1, e_2, e_3, \ldots, e_n]$, as shown in Figure 16. The random breakages are assumed to be uniformly distributed over the interval $[1, n]$. Each time an element is selected, the load is incrementally applied and the von Mises stress is computed. Once the yield strength of the selected element is reached, that element is presumed to have failed. The elements within the range 25.4 mm to the left and to the right of the broken element are then removed from the vector $\boldsymbol{A}$. The next randomly selected element is taken from the new updated $\boldsymbol{A}$. The process is repeated until no elements are left in the updated vector $\boldsymbol{A}$.

Using the stiffness matrix formulated in Section 3, the resulting force versus displacement response is presented in Figure 17 for the case when three breakages occur before the chain of consisting of four bistable structures completely fails. The main strip (inner core) breakages occur at the following positions from the fixed end: 145 mm, 66 mm, and finally 201 mm. Despite the random sequence of main strip breakages, the same force-displacement diagram is produced as for the case of sequential breakages.

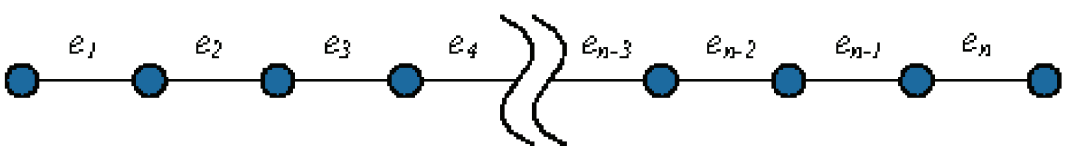

$$\mathbf{A} = [e_1, e_2, e_3, e_4, \ldots, e_{n-3}, e_{n-2}, e_{n-1}, e_n]$$

Figure 16. Elements as components of vector $\boldsymbol{A}$.

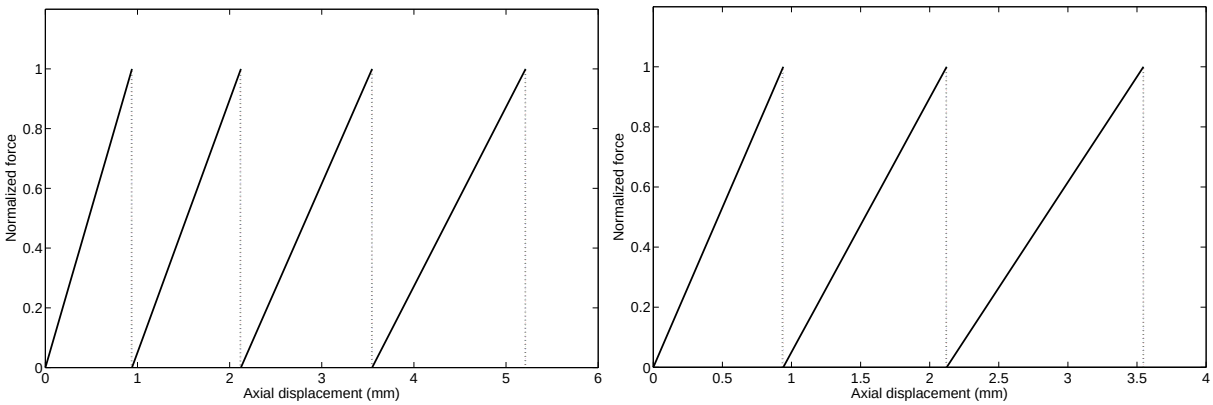

Figure 17. Force-displacement diagram for random breakages: three breakages (left) and two breakages (right).

The total strain energy required to produce three random breakages, 31.0 J, is also the same as for the case of sequential breakages.

The results presented in Figures 14 and 17 show that the order in which the core breakages occur does not affect the force versus displacement response of the structure. Thus, the amount of energy absorbed depends only on the number of the breakages — since the same amount of strain energy per unit volume is required to break the helicoidal main strip.

A comparison of the energy absorbed by the structure in this investigation to a conventional structure of the same size and geometry made of only isotropic material is presented here:

Conventional structure	7.74 J
Bistable structure (sequential)	31.0 J
Bistable structure (random)	24.0–31.0 J

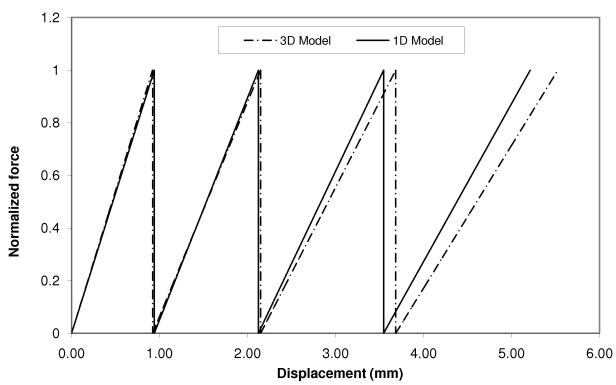

Figure 18. Comparison of force-displacement relation between one- and three-dimensional models. The results show good agreement for small deformations.

A comparison of the force-displacement relation between the two models is shown in Figure 18. This comparison illustrates that the simplified one-dimensional model gives an approximation of the force-displacement relation close to that of the three-dimensional model only when the deformation is sufficiently small. The advantage of the one-dimensional finite element model is the relatively low number of elements required in comparison to the three-dimensional model. Hence, the computational time is reduced significantly, which is extremely beneficial to the design, optimization, and concept development process.

4. Conclusion

A helicoidal bistable structure is proposed and its energy absorption behavior studied. In comparison with the earlier bistable structure studied in [Cherkaev et al. 2006], the helicoidal bistable structure allows for a longer waiting inactive time relative to the additional spacing required, It can also be designed to sustain a smaller elongation for the same energy release. The additional twisting degrees of freedom correspond to the additional energy released in the process of elongation.

A one-dimensional model is formulated for numerical simulations of a linear chain of helicoidal bistable links. The location where the breakages occur does not affect the amount of the energy absorbed. Comparison of the force-displacement relations shows that the one-dimensional model gives a good approximation of the three-dimensional model when the deformation is sufficiently small. The helicoidal bistable structure can absorb more energy, in comparison to the conventional structure, by distributing the damage along its length.

Acknowledgements

Support of this work by the Army Research Office (ARO) is gratefully acknowledged. Helpful insights from the reviewers and the editor have significantly improved the exposition of the paper.

References

[Balk et al. 2001a] A. M. Balk, A. V. Cherkaev, and L. I. Slepyan, "Dynamics of chains with non-monotone stress-strain relations, I: model and numerical experiments", *J. Mech. Phys. Solids* **49**:1 (2001), 131–148.

[Balk et al. 2001b] A. M. Balk, A. V. Cherkaev, and L. I. Slepyan, "Dynamics of chains with non-monotone stress-strain relations, II: nonlinear waves and waves of phase transition", *J. Mech. Phys. Solids* **49**:1 (2001), 149–171.

[Cherkaev and Slepyan 1995] A. Cherkaev and L. Slepyan, "Waiting element structures and stability under extension", *Int. J. Damage Mech.* **4**:1 (1995), 58–82.

[Cherkaev and Zhornitskaya 2003] A. Cherkaev and L. Zhornitskaya, "Dynamics of damage in two-dimensional structures with waiting links", pp. 273–284 in *IUTAM symposium on Asymptotics, Singularities and Homogenisation in Problems of Mechanics* (Liverpool, United Kingdom, 2002), edited by A. B. Movchan, Solid mechanics and its applications, Kluwer, Dordrecht, 2003.

[Cherkaev et al. 2005] A. Cherkaev, E. Cherkaev, and L. Slepyan, "Transition waves in bistable structures, I: delocalization of damage", *J. Mech. Phys. Solids* **53**:2 (2005), 383–405.

[Cherkaev et al. 2006] A. Cherkaev, V. Vinogradov, and S. Leelavanichkul, "The waves of damage in elastic-plastic lattices with waiting links: design and simulation", *Mech. Mater.* **38**:8-10 (2006), 748–756.

[Leelavanichkul 2007] S. Leelavanichkul, *Helicoidal morphology in engineering structures*, Ph.D. thesis, University of Utah, Salt Lake City, 2007.

[Leelavanichkul and Cherkaev 2009] S. Leelavanichkul and A. Cherkaev, "Elastic cylinder with helicoidal orthotropy: theory and applications", *Int. J. Eng. Sci.* **47**:1 (2009), 1–20.

[Lekhnitskii 1981] S. G. Lekhnitskii, *Theory of elasticity of an anisotropic body*, Mir Publishers, Moscow, 1981.

[Slepyan and Tronyankina 1988] L. I. Slepyan and L. V. Tronyankina, "Impact waves in a nonlinear chain", *Strength and Visco-plasticity* (1988), 301–305. in Russian.

[Slepyan and Troyankina 1984] L. I. Slepyan and L. V. Troyankina, "Fracture wave in a chain structure", *J. Appl. Mech. Tech. Phys.* **25**:6 (1984), 921–927.

[Slepyan et al. 2000] L. I. Slepyan, V. Krylov, and R. Parnes, "Helical inclusion in an elastic matrix", *J. Mech. Phys. Solids* **48**:4 (2000), 827 – 865.

[Slepyan et al. 2005] L. Slepyan, A. Cherkaev, and E. Cherkaev, "Transition waves in bistable structures, II: analytical solution: Wave speed and energy dissipation", *J. Mech. Phys. Solids* **53**:2 (2005), 407–436.

[Whitman and La Saponara 2007a] Z. Whitman and V. La Saponara, "Bistable structures for energy absorption, I: metallic structures under tension", *J. Mech. Mater. Struct.* **2**:2 (2007), 347–358.

[Whitman and La Saponara 2007b] Z. Whitman and V. La Saponara, "Bistable structures for energy absorption, II: composite structures under tension", *J. Mech. Mater. Struct.* **2**:2 (2007), 359–376.

Received 6 Feb 2009. Revised 23 Jun 2009. Accepted 20 Aug 2009.

SEUBPONG LEELAVANICHKUL: sleelava@eng.utah.edu
Department of Mechanical Engineering, University of Utah, Salt Lake City, UT 84112, United States

ANDREJ CHERKAEV: cherk@math.utah.edu
Department of Mathematics, University of Utah, 155 S. 1400 E., Room 233, Salt Lake City, UT 84112, United States

DANIEL O. ADAMS: adams@mech.utah.edu
Department of Mechanical Engineering, University of Utah, Salt Lake City, UT 84112, United States

FLORIAN SOLZBACHER: solzbach@ece.utah.edu
Department of Electrical & Computer Engineering, University of Utah, Salt Lake City, UT 84112, United States

JOURNAL OF MECHANICS OF MATERIALS AND STRUCTURES
Vol. 5, No. 2, 2010

DECAY PROPERTIES OF SOLUTIONS OF A MINDLIN-TYPE PLATE MODEL FOR RHOMBIC SYSTEMS

FRANCESCA PASSARELLA, VINCENZO TIBULLO AND VITTORIO ZAMPOLI

In the present paper, we investigate the spatial behavior of transient and steady-state solutions for the problem of bending applied to a linear Mindlin-type plate model; the plate is supposed to be made of a material characterized by rhombic isotropy, with the elasticity tensor satisfying the strong ellipticity condition. First, using an appropriate family of measures, we show that the transient solution vanishes at distances greater than cT from the support of the given data on the time interval $[0, T]$, where c is a characteristic material constant. For distances from the support less than cT, we obtain a spatial decay estimate of Saint-Venant type. Then, for a plate whose middle section is modelled as a (bounded or semiinfinite) strip, a family of measures is used to obtain an estimate describing the spatial behavior of the amplitude of harmonic vibrations, provided that the frequency is lower than a critical value.

A list of symbols can be found on page 337.

1. Introduction

Mechanical structures involving elastic plates are useful in a wide range of technical applications and have been the subject of many studies, such as [Green and Naghdi 1967; Naghdi 1971; Lagnese and Lions 1988]. Initially, authors considered the plate model based on Kirchhoff's elastic strain-displacement relations, completely neglecting the effects of transverse shear forces [Nowinski 1978; Lagnese and Lions 1988]. Then, increasingly refined models were introduced, taking into account not only the deflection of the middle section, but also transverse shear deformations. The theory of elastic plates based on the Mindlin model has been developed by Constanda [1990] for the elastostatic bending of a thin slab, including the effects of transverse shear deformation. Furthermore, a dynamic model for small deformations of a thin thermoelastic plate was developed by Schiavone and Tait [1993].

The Reissner–Mindlin and Kirchhoff–Love models are the two most common models of a thin linear elastic plate. It is often remarked in the engineering literature that the Reissner–Mindlin model is more accurate, particularly for thin plates and when transverse shear strain plays a significant role [Hughes 1987]; in fact, both Mindlin [1951] and Reissner [1945; 1947] independently proposed theories which also include the effects of transverse shear deformation. Arnold et al. [2002] showed that the Reissner–Mindlin plate bending model has a wider range of applicability than the Kirchhoff–Love model. Under the assumption of constant body force density in the transverse direction, they proved that the Reissner–Mindlin model solution converges to the three-dimensional linearly elastic solution in the relative energy norm for the full range of surface loads. Fabrizio and Chiriță [2004] studied the deformations of a linear viscoelastic plate, including transverse shear deformations.

Keywords: plates, rhombic systems, strong ellipticity, transient and steady-state solutions.
The work in this paper was performed under the auspices of the GNFM of the Italian INdAM..

The state of bending for a transversely isotropic plate of Mindlin-type has been analyzed by Passarella and Zampoli [2009a; 2009b]. The first of these papers contains a uniqueness result and a Galerkin representation of the solution, without positive definiteness assumptions on the elasticity tensor. Furthermore, under the hypotheses of positive definiteness of the elasticity tensor, the authors prove a Gurtin type variational theorem and a minimum principle. In [Passarella and Zampoli 2009b], previous hypotheses are relaxed and, assuming strong ellipticity of the elasticity tensor, results about the spatial behavior of transient and steady-state solutions are established.

With regard to the spatial behavior of solutions, Saint-Venant's principle plays a central role in the theory and applications of elasticity. A comprehensive review of research on the spatial behavior of solutions is given by [Toupin 1965; Knowles 1966; Flavin 1974; Horgan and Knowles 1983; Gregory and Wan 1985; Horgan 1989; 1996; Mielke 1988].

For genuine dynamic problems of elasticity, useful information on the spatial behavior of solutions can be furnished by the well-known domain of influence theorem as presented by Gurtin [1972] and ascribed to Wheeler and Sternberg [1968]. According to Gurtin the domain of influence of the given external data at time T consists of the set D_T of all points in the body that can be reached by signals propagating from the support $\widehat{D}_T$, on the time interval $[0, T]$, with speeds equal to or less than the maximum speed of propagation c. Then the domain of influence theorem shows that on $[0, T]$ the externally given data have no effect on points outside of D_T.

In the present paper we study a bending state of a rhombic system modelled as a (either bounded or unbounded) Mindlin-type plate, under a strong ellipticity condition on the elasticity tensor. In this context, we use the properties of rhombic systems widely investigated by Gurtin [1972] and Chiriță et al. [2007]. Such systems, together with transversely isotropic materials, show a good applicability to mathematical models of plates that take into account transverse shear deformations (see [Paroni et al. 2006] for details). In particular, in the context of the linear theory, we investigate the spatial behavior of transient and steady-state solutions. This investigation is concerned with some properties of the solutions of the evolution equations ruling the displacement and rotation fields, supposing the plate to be initially at rest. Moreover, time-dependent displacements and rotation fields are imposed on its boundary. These fields on the boundary induce disturbances that propagate in the interior of the plate.

Outline of paper. In Section 2, we derive the evolution equations for the two-dimensional theory and state assumptions concerning the strong ellipticity of the elasticity tensor.

In Section 3, considering the spatial support of data contained in a bounded domain D_T^*, we define a set of appropriate line-integral measures $\mathcal{I}_\kappa$ and establish some estimates in order to obtain the domain of influence and the spatial decay of transient solutions away from D_T^*. Using these estimates and following the time-weighted power function method [Chiriță and Ciarletta 1999; 2003; Ciarletta et al. 2005], we determine the speed of propagation of mechanical disturbances from D_T^*, as well as the spatial decay of solutions.

In Section 4, we treat a more specific mechanical problem, concerning the steady-state vibrations of a (either bounded or semiinfinite) strip. Starting from an idea of Ciarletta et al. [2005] and Chiriță [1995], we introduce a set of appropriate line-integral measures $\mathcal{J}_\kappa$ associated with the amplitude of time-harmonic vibrations. We obtain a differential inequality describing the behavior of steady-state solutions under the hypothesis that the frequency of harmonic vibrations is lower than a certain critical value.

2. Formulation of the problem

In this paper, we study the behavior of a homogeneous body filled by a material that occupies at time $t = 0$ a right cylinder $\bar{B}$ of height $2h$ with (bounded or unbounded) cross-section $\bar{\Sigma}$ and smooth lateral boundary Π. We call B and Σ the interiors of $\bar{B}$ and $\bar{\Sigma}$; we choose the rectangular Cartesian coordinate frame in such a way that Ox_1x_2 is the middle plane of the cylinder and thus its faces are located at $x_3 = \pm h$. We also suppose that Σ is a simply connected region, $\partial\Sigma$ is the boundary of Σ, and $h \ll \operatorname{diam}\Sigma$. Latin subscripts (unless otherwise specified) range over the integers $\{1, 2, 3\}$, whereas Greek subscripts are confined to the range $\{1, 2\}$; summation over repeated subscripts is implied. Superposed dots, or subscripts preceded by a comma, mean a partial derivative with respect to time or to the corresponding Cartesian variables. When needed, vector fields are represented by bold-type letters. We will disregard regularity questions, simply assuming a degree of smoothness sufficient to ensure analysis is valid.

For each point $(x_1, x_2, x_3) \in \bar{B}$ and $t \in [0, \infty)$, a bending state for such an elastic cylinder is characterized by

$$u_\alpha(x_1, x_2, x_3, t) = -u_\alpha(x_1, x_2, -x_3, t) \qquad \text{and} \qquad u_3(x_1, x_2, x_3, t) = u_3(x_1, x_2, -x_3, t),$$

where u_i are the components of the displacement vector that vary smoothly with respect to x_3. Nevertheless, as with the study carried out in [Passarella and Zampoli 2009a; 2009b], we restrict our attention to the bending state characterized by

$$u_\alpha(x_1, x_2, x_3, t) = x_3 v_\alpha(x_1, x_2, t) \qquad \text{and} \qquad u_3(x_1, x_2, x_3, t) = w(x_1, x_2, t),$$

and we assume that the components f_i of the body force vector obey the relations

$$f_\alpha(x_1, x_2, x_3, t) = -f_\alpha(x_1, x_2, -x_3, t), \qquad f_3(x_1, x_2, x_3, t) = f_3(x_1, x_2, -x_3, t).$$

The behavior of thin plates of uniform thickness is described by the equations of motion

$$\tfrac{1}{3}h^2 M_{\beta\alpha,\beta} - \tau_{\alpha 3} + H_\alpha = \tfrac{1}{3}h^2 \varrho \ddot{v}_\alpha, \qquad \tau_{\beta 3,\beta} + F = \varrho \ddot{w}, \qquad \text{on } \bar{\Sigma} \times (0, \infty) \tag{2-1}$$

and the constitutive equations

$$\begin{aligned} M_{ij}(x_1, x_2, t) &= \frac{3}{2h^3} \int_{-h}^{h} x_3 C_{ijkl} u_{k,l}(x_1, x_2, x_3, t)\, dx_3, \\ \tau_{ij}(x_1, x_2, t) &= \frac{1}{2h} \int_{-h}^{h} C_{ijkl} u_{k,l}(x_1, x_2, x_3, t)\, dx_3, \end{aligned} \tag{2-2}$$

where ϱ is the reference mass density, C_{ijkl} are the components of the elasticity tensor obeying the usual symmetry relations, and

$$\begin{aligned} F(x_1, x_2, t) &= \frac{1}{2h} \int_{-h}^{h} f_3(x_1, x_2, x_3, t)\, dx_3 + \frac{1}{h} C_{33kl} u_{k,l}(x_1, x_2, h, t), \\ H_\alpha(x_1, x_2, t) &= \frac{1}{2h} \int_{-h}^{h} x_3 f_\alpha(x_1, x_2, x_3, t)\, dx_3 + C_{3\alpha kl} u_{k,l}(x_1, x_2, h, t). \end{aligned}$$

Suppose that

$$H_\alpha = 0, \qquad F = 0, \qquad \text{on } \bar{\Sigma} \times [0, \infty). \tag{2-3}$$

In what follows, we consider a homogeneous rhombic elastic material, with the group $\mathscr{C}_3$ generated[1] by $\boldsymbol{R}^{\pi}_{\boldsymbol{e}_3}$ and $\boldsymbol{R}^{\pi}_{\boldsymbol{e}_2}$ characterized by (see, for example, [Gurtin 1972])

$$\begin{aligned} C_{1123} = C_{1131} = C_{1112} = C_{2223} = C_{2231} = C_{2212} = 0,\\ C_{3323} = C_{3331} = C_{3312} = C_{2331} = C_{2312} = C_{3112} = 0. \end{aligned} \tag{2-4}$$

Using these equations and defining as usual

$$\begin{aligned} &c_{11} = C_{1111}, \quad c_{22} = C_{2222}, \quad c_{33} = C_{3333}, \quad c_{44} = C_{2323}, \quad c_{55} = C_{1313},\\ &c_{66} = C_{1212}, \quad c_{12} = C_{1122}, \quad c_{23} = C_{2233}, \quad c_{31} = C_{3311}, \end{aligned}$$

the constitutive equations (2-2) for rhombic materials become

$$M_{11} = c_{11}v_{1,1} + c_{12}v_{2,2}, \quad M_{22} = c_{12}v_{1,1} + c_{22}v_{2,2}, \quad M_{12} = M_{21} = c_{66}(v_{1,2} + v_{2,1}), \tag{2-5}$$

$$\tau_{13} = \tau_{31} = c_{55}(w_{,1} + v_1), \quad \tau_{23} = \tau_{32} = c_{44}(w_{,2} + v_2). \tag{2-6}$$

Now, we restrict our attention to the class of rhombic materials having a strongly elliptic elasticity tensor, that is,

$$C_{ijkl}m_i m_k n_j n_l > 0 \tag{2-7}$$

for all nonzero vectors (m_1, m_2, m_3) and (n_1, n_2, n_3). As it is possible to see in [Gurtin 1972], this hypothesis on the elasticity tensor is weaker than positive definiteness. Chiriță et al. [2007] prove that for rhombic systems the strong ellipticity condition (2-7) is equivalent to

$$\begin{aligned} &c_{11}n_1^2m_1^2 + c_{22}n_2^2m_2^2 + c_{33}n_3^2m_3^2 + c_{66}(n_1m_2 + n_2m_1)^2 + c_{44}(n_3m_2 + n_2m_3)^2\\ &\quad + c_{55}(n_1m_3 + n_3m_1)^2 + 2c_{12}n_1m_1n_2m_2 + 2c_{23}n_2m_2n_3m_3 + 2c_{31}n_3m_3n_1m_1 > 0, \end{aligned} \tag{2-8}$$

and this relation implies the conditions

$$\begin{aligned} &c_{11} > 0, \quad c_{22} > 0, \quad c_{33} > 0, \quad c_{44} > 0, \quad c_{55} > 0, \quad c_{66} > 0,\\ &|c_{12} + c_{66}| < c_{66} + \sqrt{c_{11}c_{22}}, \quad |c_{13} + c_{55}| < c_{55} + \sqrt{c_{11}c_{33}}, \quad |c_{23} + c_{44}| < c_{44} + \sqrt{c_{22}c_{33}}. \end{aligned}$$

3. Transient solutions: decay estimate of Saint-Venant type

In this section, we establish results describing the spatial behavior of solutions of the given data on the interval $[0, T]$ under the strong ellipticity condition on the elasticity tensor. To this end, we can rewrite the system of (2-1), (2-3), (2-5), and (2-6) in terms of (v_α, w) as

$$\begin{aligned} \tfrac{1}{3}h^2[c_{11}v_{1,11} + c_{66}v_{1,22} + (c_{12} + c_{66})v_{2,12}] - c_{55}(w_{,1} + v_1) &= \tfrac{1}{3}h^2\varrho\ddot{v}_1,\\ \tfrac{1}{3}h^2[c_{66}v_{2,11} + c_{22}v_{2,22} + (c_{12} + c_{66})v_{1,12}] - c_{44}(w_{,2} + v_2) &= \tfrac{1}{3}h^2\varrho\ddot{v}_2,\\ c_{55}(w_{,11} + v_{1,1}) + c_{44}(w_{,22} + v_{2,2}) &= \varrho\ddot{w}, \end{aligned} \tag{3-1}$$

or, equivalently, as

$$\tfrac{1}{3}h^2\widetilde{M}_{\beta\alpha,\beta} - \tau_{\alpha 3} = \tfrac{1}{3}\varrho h^2\ddot{v}_\alpha, \qquad \tau_{\beta 3,\beta} = \varrho\ddot{w}, \tag{3-2}$$

[1] $\boldsymbol{R}^{\theta}_{\boldsymbol{u}}$ is the orthogonal tensor corresponding to a right-handed rotation through the angle θ about an axis of unit vector $\boldsymbol{u}$.

where $\widetilde{M}_{\beta\alpha}$ represents the family of tensors depending on the parameter κ through

$$\begin{aligned} \widetilde{M}_{11} &= c_{11}v_{1,1} + (c_{66}-\kappa)v_{2,2}, & \widetilde{M}_{12} &= (c_{12}+\kappa)v_{1,2} + c_{66}v_{2,1}, \\ \widetilde{M}_{21} &= c_{66}v_{1,2} + (c_{12}+\kappa)v_{2,1}, & \widetilde{M}_{22} &= (c_{66}-\kappa)v_{1,1} + c_{22}v_{2,2}, \end{aligned} \tag{3-3}$$

and $\tau_{\beta 3}$ is defined by Equation (2-6). The family of tensors $\widetilde{M}_{\beta\alpha}$ has a nonvanishing skew-symmetric part, depending on the skew-symmetric part of $v_{\alpha,\beta}$.

Let $\mathcal{P}$ be the problem defined by (2-6), (3-2), (3-3) and the initial-boundary conditions

$$\begin{aligned} v_\alpha(x_1,x_2,0) &= 0, & w(x_1,x_2,0) &= 0 && \text{on } \Sigma, \\ \dot{v}_\alpha(x_1,x_2,0) &= 0, & \dot{w}(x_1,x_2,0) &= 0 && \text{on } \Sigma, \\ v_\alpha &= \breve{v}_\alpha, & w &= \breve{w} && \text{on } L\times[0,+\infty), \\ v_\alpha &= 0, & w &= 0 && \text{on } L_C\times[0,+\infty), \end{aligned}$$

where L and L_C are disjoint and complementary nonempty subsets of $\partial\Sigma$ and $\mathcal{D} = (\breve{v}_\alpha, \breve{w})$ is the set of assigned fields representing the external data of the problem in question.

We define the support $\widehat{D}_T$ of external data $\mathcal{D}$ on the time interval $[0,T]$ as the set of points

$$\boldsymbol{x} = (x_1, x_2) \in L$$

for which there exists $\tau \in [0,T]$ such that $\breve{v}_\alpha(\boldsymbol{x},\tau) \neq 0$ or $\breve{w}(\boldsymbol{x},\tau) \neq 0$. In other words, for $\boldsymbol{x} \in \partial\Sigma\setminus\widehat{D}_T$, we have

$$\breve{v}_\alpha(\boldsymbol{x},t) = 0 \quad \text{and} \quad \breve{w}(\boldsymbol{x},t) = 0 \qquad \text{for all } t \in [0,T]. \tag{3-4}$$

For convenience, we assume that $\widehat{D}_T$ is a nonempty bounded set and that D_T^* is the smallest regular subcurve of L including $\widehat{D}_T$. We consider the sets

$$D_r = \{\boldsymbol{x} \in \overline{\Sigma} : D_T^* \cap S(\boldsymbol{x},r) \neq \varnothing\}, \qquad \Sigma_r = \overline{\Sigma}\setminus D_r, \qquad \Sigma(r_1,r_2) = \Sigma_{r_2}\setminus\Sigma_{r_1},$$

where $r > 0$, $r_2 \le r_1$, and $S(\boldsymbol{x},r)$ is the closed ball with radius r and center at $\boldsymbol{x}$, that is,

$$S(\boldsymbol{x},r) = \{\boldsymbol{y} \in \mathbb{R}^2 : |\boldsymbol{y}-\boldsymbol{x}| \le r\}.$$

Then, $L_r = \partial\Sigma_r \cap \Sigma$ is the subcurve of $\partial\Sigma_r$ that lies inside the inner part of $\overline{\Sigma}$, and whose unit normal vector $\boldsymbol{n}$ is directed towards the interior of Σ_r (or, equivalently, towards the exterior of D_r).

We also agree that, for $r = 0$, D_0 and L_0 coincide with D_T^*, and the normal vector $\boldsymbol{n}$ to L_0 is directed towards the interior of Σ.

For any positive parameter λ, we introduce the function

$$\mathcal{I}_\kappa(r,t) = -\int_0^t \int_{L_r} e^{-\lambda s}\big[\tau_{\beta 3}(s)\dot{w}(s) + \tfrac{1}{3}h^2\widetilde{M}_{\beta\alpha}(s)\dot{v}_\alpha(s)\big]n_\beta\, dl\, ds, \quad r \ge 0, \quad t \in [0,T]; \tag{3-5}$$

for what follows, it is useful to remark that

$$\mathcal{I}_\kappa(r,0) = 0 \quad \text{for all } r \ge 0. \tag{3-6}$$

From direct differentiation of (3-5) with respect to the variable t, we get

$$\frac{\partial \mathcal{J}_\kappa}{\partial t}(r,t) = -\int_{L_r} e^{-\lambda t}\big[\tau_{\beta 3}(t)\dot{w}(t) + \tfrac{1}{3}h^2\widetilde{M}_{\beta\alpha}(t)\dot{v}_\alpha(t)\big]n_\beta\, dl. \tag{3-7}$$

On the other hand, from the definition of Σ_r, from (3-4), and from the divergence theorem, we have

$$\mathcal{J}_\kappa(r_1,t) - \mathcal{J}_\kappa(r_2,t) = -\int_0^t \int_{\Sigma(r_1,r_2)} e^{-\lambda s}\big[\tau_{\beta 3}(s)\dot{w}(s) + \tfrac{1}{3}h^2\widetilde{M}_{\beta\alpha}(s)\dot{v}_\alpha(s)\big]_{,\beta}\, d\sigma\, ds.$$

Using (2-6) and (3-2)–(3-5), we obtain, for $r_2 < r_1$,

$$\begin{aligned}
&\mathcal{J}_\kappa(r_1,t) - \mathcal{J}_\kappa(r_2,t)\\
&\quad = -\frac{1}{2}\int_0^t \int_{\Sigma(r_1,r_2)} e^{-\lambda s}\frac{\partial}{\partial s}\Big\{\varrho\big[\dot{w}^2(s) + \tfrac{1}{3}h^2\dot{v}_\alpha(s)\dot{v}_\alpha(s)\big] + c_{55}\big(w_{,1}(s) + v_1(s)\big)^2 + c_{44}\big(w_{,2}(s) + v_2(s)\big)^2\\
&\qquad\qquad + \tfrac{1}{3}h^2\big[c_{11}v_{1,1}^2(s) + c_{22}v_{2,2}^2(s) + 2(c_{66}-\kappa)v_{1,1}(s)v_{2,2}(s)\\
&\qquad\qquad\quad + c_{66}\big(v_{2,1}^2(s) + v_{1,2}^2(s)\big) + 2(c_{12}+\kappa)v_{2,1}(s)v_{1,2}(s)\big]\Big\}\, d\sigma\, ds.
\end{aligned} \tag{3-8}$$

Introducing

$$\mathcal{T} = \tfrac{1}{2}\varrho\big(\dot{w}^2 + \tfrac{1}{3}h^2\dot{v}_\alpha\dot{v}_\alpha\big), \qquad \mathcal{W} = \tfrac{1}{2}\big(\mathcal{W}_0 + \tfrac{1}{3}h^2\mathcal{W}_1 + \tfrac{1}{3}h^2\mathcal{W}_2\big), \tag{3-9}$$

and

$$\begin{aligned}
&\mathcal{W}_0 = c_{55}(w_{,1}+v_1)^2 + c_{44}(w_{,2}+v_2)^2, \qquad \mathcal{W}_1 = c_{11}v_{1,1}^2 + c_{22}v_{2,2}^2 + 2(c_{66}-\kappa)v_{1,1}v_{2,2},\\
&\mathcal{W}_2 = c_{66}(v_{2,1}^2 + v_{1,2}^2) + 2(c_{12}+\kappa)v_{2,1}v_{1,2},
\end{aligned} \tag{3-10}$$

it follows from (3-8) that

$$\mathcal{J}_\kappa(r_1,t) - \mathcal{J}_\kappa(r_2,t) = -\int_0^t \int_{\Sigma(r_1,r_2)} e^{-\lambda s}\frac{\partial}{\partial s}[\mathcal{T}(s) + \mathcal{W}(s)]\, d\sigma\, ds \qquad \text{if } r_2 < r_1. \tag{3-11}$$

Now, it is possible to show that $\mathcal{J}_\kappa$ is continuously differentiable with respect to r; in fact, considering

$$\begin{aligned}
\lim_{r_1\to r_2}\frac{\mathcal{J}_\kappa(r_1,t) - \mathcal{J}_\kappa(r_2,t)}{r_1 - r_2} &= -\lim_{r_1\to r_2}\frac{1}{r_1 - r_2}\int_0^t \int_{\Sigma(r_1,r_2)} e^{-\lambda s}\frac{\partial}{\partial s}[\mathcal{T}(s) + \mathcal{W}(s)]\, d\sigma\, ds\\
&= -\int_0^t \int_{L_r} e^{-\lambda s}\frac{\partial}{\partial s}[\mathcal{T}(s) + \mathcal{W}(s)]\, d\sigma\, ds,
\end{aligned}$$

and integrating by parts with respect to the time variable s, we arrive at

$$\frac{\partial \mathcal{J}_\kappa}{\partial r}(r,t) = -\int_{L_r} e^{-\lambda t}[\mathcal{T}(t) + \mathcal{W}(t)]\, dl - \lambda\int_0^t \int_{L_r} e^{-\lambda s}[\mathcal{T}(s) + \mathcal{W}(s)]\, dl\, ds. \tag{3-12}$$

Let $\mathcal{A}_0$, $\mathcal{A}_1$, and $\mathcal{A}_2$ be the matrices associated with the quadratic forms $\mathcal{W}_0$, $\mathcal{W}_1$, and $\mathcal{W}_2$, respectively. When the strong ellipticity condition (2-8) is valid and κ satisfies the relation

$$\max\big\{-c_{66} - c_{12},\, c_{66} - \sqrt{c_{11}c_{22}}\big\} < \kappa < \min\big\{c_{66} - c_{12},\, c_{66} + \sqrt{c_{11}c_{22}}\big\}, \tag{3-13}$$

the eigenvalues of $\mathcal{A}_0$, $\mathcal{A}_1$, and $\mathcal{A}_2$, which are

$$c_{55}, \quad c_{44}, \quad \tfrac{1}{2}\big[c_{11} + c_{22} \pm \sqrt{(c_{11} - c_{22})^2 + 4(c_{66} - \kappa)^2}\,\big], \quad c_{66} \pm |c_{12} + \kappa|,$$

are all strictly positive. In what follows, we denote with μ_κ and η_κ the smallest and largest eigenvalues of $\mathscr{A}_0$, $\mathscr{A}_1$, and $\mathscr{A}_2$, respectively. These are

$$\mu_\kappa = \min\Big\{c_{44}, c_{55}, \tfrac{1}{2}\big[c_{11}+c_{22}-\sqrt{(c_{11}-c_{22})^2+4(c_{66}-\kappa)^2}\big], c_{66}-|c_{12}+\kappa|\Big\},$$
$$\eta_\kappa = \max\Big\{c_{44}, c_{55}, \tfrac{1}{2}\big[c_{11}+c_{22}+\sqrt{(c_{11}-c_{22})^2+4(c_{66}-\kappa)^2}\big], c_{66}+|c_{12}+\kappa|\Big\}.$$

If $\varrho > 0$ and (2-8) and (3-13) hold, then $\mathcal{T}$ and $\mathcal{W}$ are positive definite; thus, we show through (3-12) that $\mathcal{I}_\kappa(r,t)$ is a nonincreasing function with respect to r, that is,

$$\mathcal{I}_\kappa(r_1,t) \le \mathcal{I}_\kappa(r_2,t) \qquad \text{if } r_2 < r_1. \tag{3-14}$$

If the plate is bounded and $\ell = \max_{\boldsymbol{x}\in\bar{\Sigma}}\{\min_{\boldsymbol{y}\in D_T^*}\sqrt{(x_1-y_1)^2+(x_2-y_2)^2}\}$, we obtain from the definition of L_r that $L_\ell = \varnothing$ and, consequently,

$$\mathcal{I}_\kappa(\ell,t) = 0, \qquad t\in[0,T]; \tag{3-15}$$

moreover, (3-11), (3-14), and (3-15) imply that

$$0 \le \mathcal{I}_\kappa(r,t) = \int_0^t \int_{\Sigma(\ell,r)} e^{-\lambda s}\frac{\partial}{\partial s}[\mathcal{T}(s)+\mathcal{W}(s)]\,d\sigma\,ds \quad \text{for } r\le\ell. \tag{3-16}$$

In this case, it is obvious that $\Sigma(\ell,r) = \Sigma_r$. It is possible to obtain a relation similar to (3-16) for an unbounded plate. To this end, we estimate $\mathcal{I}_\kappa(r,t)$ and $\partial\mathcal{I}_\kappa(r,t)/\partial t$ in terms of $\partial\mathcal{I}_\kappa(r,t)/\partial r$.

Theorem 3.1. *Let $\varrho > 0$ and suppose the hypotheses (2-8) and (3-13) hold. Let (v_α, w) be a solution of the initial-boundary value problem $\mathcal{P}$ and $\widehat{D}_T$ the bounded support of external data $\mathcal{D}$ on the time interval $[0,T]$, then the function $\mathcal{I}_\kappa$ satisfies the first-order differential inequalities*

$$|\mathcal{I}_\kappa(r,t)| + \frac{c_\kappa}{\lambda}\frac{\partial\mathcal{I}_\kappa}{\partial r}(r,t) \le 0, \qquad \Big|\frac{\partial\mathcal{I}_\kappa}{\partial t}(r,t)\Big| + c_\kappa\frac{\partial\mathcal{I}_\kappa}{\partial r}(r,t) \le 0, \qquad \text{with } c_\kappa = \sqrt{\frac{\eta_\kappa}{\varrho}}. \tag{3-17}$$

Proof. Under the hypotheses (2-8) and (3-13), we can observe that

$$0 \le k_m^{(\alpha)}(\gamma_1^2+\gamma_2^2) \le \mathcal{F}[\mathscr{A}_\alpha;\boldsymbol{\gamma},\boldsymbol{\gamma}] \le k_M^{(\alpha)}(\gamma_1^2+\gamma_2^2), \tag{3-18}$$

where $k_m^{(\alpha)}$ and $k_M^{(\alpha)}$ are the smallest and largest eigenvalues of $\mathcal{W}_\alpha$, the functional $\mathcal{F}$ is given by

$$\mathcal{F}[\mathscr{A}_\alpha;\boldsymbol{\varphi},\boldsymbol{\gamma}] := \boldsymbol{\varphi}\cdot\mathscr{A}_\alpha\boldsymbol{\gamma},$$

with the variables $\boldsymbol{\varphi} = (\varphi_1,\varphi_2)$ and $\boldsymbol{\gamma} = (\gamma_1,\gamma_2)$. In particular,

$$k_m^{(1)} = \tfrac{1}{2}\big[c_{11}+c_{22}-\sqrt{(c_{11}-c_{22})^2+4(c_{66}-\kappa)^2}\,\big], \quad k_m^{(2)} = c_{66}-|c_{12}+\kappa|,$$
$$k_M^{(1)} = \tfrac{1}{2}\big[c_{11}+c_{22}+\sqrt{(c_{11}-c_{22})^2+4(c_{66}-\kappa)^2}\,\big], \quad k_M^{(2)} = c_{66}+|c_{12}+\kappa|.$$

Through the Schwarz inequality and Equations (3-3) and (3-10), we get

$$\mathcal{F}[\mathscr{A}_q;\boldsymbol{\varphi},\boldsymbol{\gamma}] \le \big[\mathcal{F}[\mathscr{A}_q;\boldsymbol{\varphi},\boldsymbol{\varphi}]\big]^{1/2}\big[\mathcal{F}[\mathscr{A}_q;\boldsymbol{\gamma},\boldsymbol{\gamma}]\big]^{1/2} \tag{3-19}$$

and

$$\begin{aligned} &\mathcal{F}\big[\mathcal{A}_1;\hat{\boldsymbol{\gamma}}^{(1)},\hat{\boldsymbol{\gamma}}^{(1)}\big]=\mathcal{W}_1, \qquad &&\mathcal{F}\big[\mathcal{A}_1;\widetilde{\boldsymbol{M}}^{(1)},\hat{\boldsymbol{\gamma}}^{(1)}\big]=\widetilde{M}_{11}^2+\widetilde{M}_{22}^2,\\ &\mathcal{F}\big[\mathcal{A}_2;\hat{\boldsymbol{\gamma}}^{(2)},\hat{\boldsymbol{\gamma}}^{(2)}\big]=\mathcal{W}_2, \qquad &&\mathcal{F}\big[\mathcal{A}_2;\widetilde{\boldsymbol{M}}^{(2)},\hat{\boldsymbol{\gamma}}^{(2)}\big]=\widetilde{M}_{21}^2+\widetilde{M}_{12}^2, \end{aligned} \tag{3-20}$$

where

$$\hat{\boldsymbol{\gamma}}^{(1)}=(v_{1,1},v_{2,2}),\quad \widetilde{\boldsymbol{M}}^{(1)}=(\widetilde{M}_{11},\widetilde{M}_{22}),\quad \hat{\boldsymbol{\gamma}}^{(2)}=(v_{1,2},v_{2,1}),\quad \widetilde{\boldsymbol{M}}^{(2)}=(\widetilde{M}_{21},\widetilde{M}_{12}).$$

Now, collecting (3-10) and (3-18)–(3-20), we deduce that

$$\begin{aligned} \widetilde{M}_{11}^2+\widetilde{M}_{22}^2&\le\mathcal{F}^{1/2}\big[\mathcal{A}_1;\widetilde{\boldsymbol{M}}^{(1)},\widetilde{\boldsymbol{M}}^{(1)}\big]\mathcal{W}_1^{1/2}\le\big[k_M^{(1)}(\widetilde{M}_{11}^2+\widetilde{M}_{22}^2)\big]^{1/2}\mathcal{W}_1^{1/2},\\ \widetilde{M}_{21}^2+\widetilde{M}_{12}^2&\le\mathcal{F}^{1/2}\big[\mathcal{A}_2;\widetilde{\boldsymbol{M}}^{(2)},\widetilde{\boldsymbol{M}}^{(2)}\big]\mathcal{W}_2^{1/2}\le\big[k_M^{(2)}(\widetilde{M}_{21}^2+\widetilde{M}_{12}^2)\big]^{1/2}\mathcal{W}_2^{1/2}. \end{aligned} \tag{3-21}$$

On the other hand, from (2-6) and (3-10) it follows that

$$0\le k_m^{(0)}\mathcal{W}_0\le\tau_{\beta3}\tau_{\beta3}\le k_M^{(0)}\mathcal{W}_0, \tag{3-22}$$

where $k_m^{(0)}=\min\{c_{44},c_{55}\}$ and $k_M^{(0)}=\max\{c_{44},c_{55}\}$. Equations (3-9), (3-21), and (3-22) allow us to show easily that

$$\tau_{\beta3}\tau_{\beta3}+\tfrac{1}{3}h^2\widetilde{M}_{\beta\alpha}\widetilde{M}_{\beta\alpha}\le k_M^{(0)}\mathcal{W}_0+\tfrac{1}{3}h^2k_M^{(1)}\mathcal{W}_1+\tfrac{1}{3}h^2k_M^{(2)}\mathcal{W}_2\le 2\eta_\kappa\mathcal{W}. \tag{3-23}$$

Next, the Cauchy–Schwarz and arithmetic-geometric mean inequalities lead to

$$\Big|\big(\tau_{\beta3}\dot{w}+\tfrac{1}{3}h^2\widetilde{M}_{\beta\alpha}\dot{v}_\alpha\big)n_\beta\Big|\le\frac{\varepsilon\varrho}{2}\big(\dot{w}^2+\tfrac{1}{3}h^2\dot{v}_\alpha\dot{v}_\alpha\big)+\frac{1}{2\varepsilon\varrho}\big(\tau_{\beta3}\tau_{\beta3}+\tfrac{1}{3}h^2\widetilde{M}_{\beta\alpha}\widetilde{M}_{\beta\alpha}\big). \tag{3-24}$$

Finally, we use the estimates (3-23) and (3-24) in (3-5) and (3-7) in order to obtain

$$|\mathcal{I}_\kappa(r,t)|\le\varepsilon\int_0^t\int_{L_r}e^{-\lambda s}\Big[\mathcal{T}(s)+\frac{\eta_\kappa}{\varepsilon^2\varrho}\mathcal{W}(s)\Big]dl\,ds, \tag{3-25}$$

$$\left|\frac{\partial\mathcal{I}_\kappa}{\partial t}(r,t)\right|\le\varepsilon\int_{L_r}e^{-\lambda t}\Big[\mathcal{T}(t)+\frac{\eta_\kappa}{\varepsilon^2\varrho}\mathcal{W}(t)\Big]dl. \tag{3-26}$$

Recalling (3-12) and setting $\varepsilon=c_\kappa$ in (3-25) and (3-26), we derive the differential inequalities (3-17). □

Using Theorem 3.1, a result similar to (3-16) may be shown for an unbounded plate. In this case, the variable r ranges in $[0,\infty)$. Thanks to $(3\text{-}17)_2$ and for any pair (r_0,t_0) such that $t_0\in[0,T]$ and $r_0\ge c_\kappa t_0$, we can see that the functions $\mathcal{I}_\kappa(r,\,t_0+(r-r_0)/c_\kappa)$ and $\mathcal{I}_\kappa(r,\,t_0-(r-r_0)/c_\kappa)$ are nonincreasing with respect to r. This feature, together with (3-6), implies

$$\begin{aligned} &\mathcal{I}_\kappa(r_0,t_0)\le\mathcal{I}_\kappa(r_0-c_\kappa t_0,0)=0, \qquad &&r_0\ge r_0-c_\kappa t_0,\\ &\mathcal{I}_\kappa(r_0,t_0)\ge\mathcal{I}_\kappa(r_0+c_\kappa t_0,0)=0, \qquad &&r_0+c_\kappa t_0\ge r_0, \end{aligned} \quad\Longrightarrow\quad \lim_{r_0\to\infty}\mathcal{I}_\kappa(r_0,t_0)=0. \tag{3-27}$$

Taking into account (3-11), (3-14), and (3-27), it follows that

$$0\le\mathcal{I}_\kappa(r,t)=\lim_{r_0\to\infty}\int_0^t\int_{\Sigma(r_0,r)}e^{-\lambda s}\frac{\partial}{\partial s}[\mathcal{T}(s)+\mathcal{W}(s)]d\sigma\,ds, \tag{3-28}$$

and it is obvious that $\lim_{r_0\to\infty}\Sigma(r_0,r)=\Sigma_r$.

With the help of (3-16) and (3-28), and integrating by parts with respect to s, it is possible to prove, for bounded or unbounded plates, the following theorem.

Theorem 3.2. *Let the hypotheses of Theorem 3.1 be still valid. The function $\mathcal{I}_\kappa(r,t)$ is nonnegative and*

$$0 \le \mathcal{I}_\kappa(r,t) = \int_{\Sigma_r} e^{-\lambda t}[\mathcal{T}(t)+\mathcal{W}(t)]\,d\sigma + \lambda \int_0^t \int_{\Sigma_r} e^{-\lambda s}[\mathcal{T}(s)+\mathcal{W}(s)]\,d\sigma\,ds. \tag{3-29}$$

Now, since $\mathcal{I}_\kappa(r,t)$ is a nonnegative function, we can write from (3-17)$_1$

$$\frac{\partial}{\partial r}\Big[\exp\Big(\frac{\lambda}{c_\kappa}r\Big)\mathcal{I}_\kappa(r,t)\Big] \le 0 \quad \Longrightarrow \quad \mathcal{I}_\kappa(r,t) \le \exp\Big(-\frac{\lambda}{c_\kappa}r\Big)\mathcal{I}_\kappa(0,t).$$

On the other hand, (3-17)$_2$ implies that the function $\mathcal{I}_\kappa(c_\kappa t,t)$ is nonincreasing with respect to t. This characteristic, together with (3-6), implies

$$\mathcal{I}_\kappa(c_\kappa t,t) \le \mathcal{I}_\kappa(0,0) = 0, \qquad t \ge 0. \tag{3-30}$$

We deduce from (3-14) and (3-29) that

$$0 \le \mathcal{I}_\kappa(r,t) \le \mathcal{I}_\kappa(c_\kappa t,t), \qquad r \ge c_\kappa t. \tag{3-31}$$

Thus, (3-29)–(3-31) imply

$$\int_{\Sigma_r} e^{-\lambda t}[\mathcal{T}(t)+\mathcal{W}(t)]\,d\sigma + \lambda \int_0^t \int_{\Sigma_r} e^{-\lambda s}[\mathcal{T}(s)+\mathcal{W}(s)]\,d\sigma\,ds = 0 \quad \text{for} \quad r \ge c_\kappa t. \tag{3-32}$$

When $\mathcal{T}$ and $\mathcal{W}$ are positive definite, (3-32) is valid if and only if $\mathcal{T}$ and $\mathcal{W}$ are null in Σ_r for any $r \ge c_\kappa t$.

The results obtained up to now lead us to formulate the following theorem about the spatial decay.

Theorem 3.3. *Let the hypotheses of Theorem 3.1 be still valid; for each fixed $t \in [0,T]$, we have*

$$\mathcal{I}_\kappa(r,t) \le \exp\Big(-\frac{\lambda}{c_\kappa}r\Big)\mathcal{I}_\kappa(0,t) \quad \text{for} \quad 0 \le r < c_\kappa t, \qquad \mathcal{I}_\kappa(r,t) = 0 \quad \text{for} \quad r \ge c_\kappa t. \tag{3-33}$$

It is easy to observe that, for $t \in [0,T]$ and for each $r \ge c_\kappa t$, (3-29) and (3-33)$_2$ lead to

$$\int_{\Sigma_r} e^{-\lambda t}[\mathcal{T}(t)+\mathcal{W}(t)]\,d\sigma + \lambda \int_0^t \int_{\Sigma_r} e^{-\lambda s}[\mathcal{T}(s)+\mathcal{W}(s)]\,d\sigma\,ds = 0.$$

Consequently, when $\varrho > 0$ and $\mathcal{W}$ is positive definite, we obtain $\dot{v}_\alpha = \dot{w} = 0$ on $\Sigma_r \times [0,T]$, and through homogeneous initial conditions, we get

$$v_\alpha = w = 0 \qquad \text{on } \Sigma_r \times [0,T]. \tag{3-34}$$

Following [Gurtin 1972], we depict the domain of influence of the externally given data at time T as the set of the points of $\bar{\Sigma}$ that can be reached by signals propagating from the support $\hat{D}_T$ on the time interval $[0,T]$, with speeds equal to or less than the maximum speed of propagation

$$c = \sqrt{\frac{\eta}{\varrho}} \qquad \text{with} \qquad \eta = \inf_\kappa \eta_\kappa,$$

where κ satisfies the relation (3-13). In fact, for a bounded or unbounded plate, we can show by means of (3-34) that on $[0,T]$ the externally given data have no effect on points outside of D_{cT}.

Lemma 3.4 (domain of influence). *Let the hypotheses of Theorem 3.1 be still valid and let (v_α, w) be a solution of initial-boundary value problem $\mathcal{P}$. Then, $v_\alpha = w = 0$, on $\Sigma_{cT} \times [0,T]$.*

We can easily prove the following uniqueness result, valid for a bounded or unbounded plate.

Lemma 3.5 (uniqueness). *Let the hypotheses of Theorem 3.1 hold. There exists at most one solution for the initial-boundary value problem $\mathcal{P}$.*

Proof. Thanks to the linearity of the problem, we have only to show that the null data imply a null solution. Let $(\tilde{v}_\alpha, \tilde{w})$ be a solution corresponding to the null data. If we choose $T_1 > 0$, since the set $\hat{D}_T = \varnothing$ for each $T \in (0, T_1)$ and the function $\mathcal{F}_\kappa(r,t) = 0$, we can conclude that: $v_\alpha = w = 0$, on $\bar{\Sigma} \times [0, T_1]$. □

4. Steady-state solutions: decay estimate of Saint-Venant type

Throughout this section, the cross-section $\bar{\Sigma}$ is a rectangular strip, and the problem of steady-state vibrations is studied assuming that (v_α, w) are separable with respect to space and time variables and that the time dependence is periodic, that is $v_\alpha = \mathrm{Re}[\zeta_\alpha(x_1,x_2)e^{i\omega t}]$, $w = \mathrm{Re}[\psi(x_1,x_2)e^{i\omega t}]$, where $\mathrm{Re}[f]$ represents the real part of f, $\omega \in \mathbb{R}^+$ is the prescribed frequency of oscillations, and ζ_α and ψ are complex functions. We choose a Cartesian frame of reference such that the middle section of the plate is defined by $\bar{\Sigma} = [0, \ell_1] \times [0, \ell_2] \subset \mathbb{R}^2$, where ℓ_1 and ℓ_2 are some positive constants and ℓ_1 can also tend to infinity. Moreover, we impose prescribed harmonic vibrations on the end of the strip located at $x_1 = 0$.

Using the equations of motion (3-1), we conclude that the amplitude (ζ_α, ψ) satisfies

$$\begin{aligned}
\tfrac{1}{3}h^2[c_{11}\zeta_{1,11} + c_{66}\zeta_{1,22} + (c_{12}+c_{66})\zeta_{2,12}] - c_{55}(\psi_{,1} + \zeta_1) + \varrho\tfrac{1}{3}h^2\omega^2\zeta_1 = 0,\\
\tfrac{1}{3}h^2[c_{66}\zeta_{2,11} + c_{22}\zeta_{2,22} + (c_{12}+c_{66})\zeta_{1,12}] - c_{44}(\psi_{,2} + v_2) + \varrho\tfrac{1}{3}h^2\omega^2\zeta_2 = 0,\\
c_{55}(\psi_{,11} + \zeta_{1,1}) + c_{44}(\psi_{,22} + \zeta_{2,2}) + \varrho\omega^2\psi = 0,
\end{aligned}$$

or, equivalently, it satisfies the system

$$\tfrac{1}{3}h^2\Gamma_{\beta\alpha,\beta} - \chi_\alpha + \varrho\tfrac{1}{3}h^2\omega^2\zeta_\alpha = 0, \qquad \chi_{\beta,\beta} + \varrho\omega^2\psi = 0, \tag{4-1}$$

with

$$\begin{aligned}
\Gamma_{11} &= c_{11}\zeta_{1,1} + (c_{66} - \kappa)\zeta_{2,2}, & \Gamma_{12} &= (c_{12} + \kappa)\zeta_{1,2} + c_{66}\zeta_{2,1},\\
\Gamma_{21} &= c_{66}\zeta_{1,2} + (c_{12} + \kappa)\zeta_{2,1}, & \Gamma_{22} &= (c_{66} - \kappa)\zeta_{1,1} + c_{22}\zeta_{2,2},
\end{aligned} \tag{4-2}$$

and

$$\chi_1 = c_{55}(\psi_{,1} + \zeta_1), \qquad \chi_2 = c_{44}(\psi_{,2} + \zeta_2). \tag{4-3}$$

In particular, using (4-1) we can easily show that

$$\tfrac{1}{3}h^2\Gamma_{1\alpha,1} = -\tfrac{1}{3}h^2\Gamma_{2\alpha,2} + \chi_\alpha - \varrho\tfrac{1}{3}h^2\omega^2\zeta_\alpha, \qquad \chi_{1,1} = -\chi_{2,2} - \varrho\omega^2\psi. \tag{4-4}$$

Let $\mathcal{P}_0$ be the problem defined by (4-1)–(4-3) and by the boundary conditions

$$\begin{aligned}
&\zeta_\alpha(x_1,0) = 0, \quad \psi(x_1,0) = 0, \quad \zeta_\alpha(x_1,\ell_2) = 0, \quad \psi(x_1,\ell_2) = 0, \quad x_1 \in [0,\ell_1],\\
&\zeta_\alpha(\ell_1,x_2) = 0, \quad \psi(\ell_1,x_2) = 0, \quad \zeta_\alpha(0,x_2) = \breve{\zeta}_\alpha(x_2), \quad \psi(0,x_2) = \breve{\psi}(x_2), \quad x_2 \in [0,\ell_2],
\end{aligned} \tag{4-5}$$

where $\breve{\zeta}_\alpha$ and $\breve{\psi}$ are prescribed continuous functions such that

$$\breve{\zeta}_\alpha(0) = 0, \qquad \breve{\psi}(0) = 0, \qquad \breve{\zeta}_\alpha(\ell_2) = 0, \qquad \breve{\psi}(\ell_2) = 0.$$

Using a superposed bar for complex conjugation and defining the segment $L_{x_1}=\{(x_1,x_2): x_2\in[0,\ell_2]\}$, we introduce the function

$$\mathcal{J}_\kappa(x_1)=\int_{L_{x_1}} 2\,\mathrm{Re}\big[\overline{\chi}_1\psi+\tfrac{1}{3}h^2\overline{\Gamma}_{1\alpha}\zeta_\alpha\big]dx_2,\qquad x_1\in[0,\ell_1]. \tag{4-6}$$

Differentiating $\mathcal{J}_\kappa$, we obtain

$$\mathcal{J}'_\kappa(x_1)=\int_{L_{x_1}} 2\,\mathrm{Re}\big[\overline{\chi}_{1,1}\psi+\overline{\chi}_1\psi_{,1}+\tfrac{1}{3}h^2(\overline{\Gamma}_{1\alpha,1}\zeta_\alpha+\overline{\Gamma}_{1\alpha}\zeta_{\alpha,1})\big]dx_2. \tag{4-7}$$

Using integration by parts, boundary conditions (4-5), and Equations (4-3), (4-4), and (4-7), we arrive at

$$\mathcal{J}'_\kappa(x_1)=\int_{L_{x_1}} 2\big[\widehat{W}-\varrho\omega^2\big(\bar{\psi}\psi+\tfrac{1}{3}h^2\bar{\zeta}_\alpha\zeta_\alpha\big)\big]dx_2, \tag{4-8}$$

where

$$\begin{aligned}
\widehat{W}&=\widehat{W}_0+\tfrac{1}{3}h^2\widehat{W}_1+\tfrac{1}{3}h^2\widehat{W}_2,\\
\widehat{W}_0&=c_{55}(\bar{\zeta}_1+\bar{\psi}_{,1})(\zeta_1+\psi_{,1})+c_{44}(\bar{\zeta}_2+\bar{\psi}_{,2})(\zeta_2+\psi_{,2}),\\
\widehat{W}_1&=c_{11}\bar{\zeta}_{1,1}\zeta_{1,1}+c_{22}\bar{\zeta}_{2,2}\zeta_{2,2}+(c_{66}-\kappa)(\bar{\zeta}_{1,1}\zeta_{2,2}+\zeta_{1,1}\bar{\zeta}_{2,2}),\\
\widehat{W}_2&=c_{66}(\zeta_{2,1}\bar{\zeta}_{2,1}+\zeta_{1,2}\bar{\zeta}_{1,2})+(c_{12}+\kappa)(\bar{\zeta}_{2,1}\zeta_{1,2}+\zeta_{2,1}\bar{\zeta}_{1,2}).
\end{aligned}$$

Again, as in the previous section, the matrices associated with $\widehat{W}_0$, $\widehat{W}_1$, and $\widehat{W}_2$ are $\mathcal{A}_0$, $\mathcal{A}_1$, and $\mathcal{A}_2$, respectively. When the relations (2-8) and (3-13) are satisfied, we have

$$\widehat{W}\ge\mu_\kappa\big[(\bar{\zeta}_\alpha+\bar{\psi}_{,\alpha})(\zeta_\alpha+\psi_{,\alpha})+\tfrac{1}{3}h^2\bar{\zeta}_{\alpha,\beta}\zeta_{\alpha,\beta}\big]>0. \tag{4-9}$$

Taking into account the well-known membrane problem, we can write

$$\frac{\pi^2}{\ell_2^2}\int_{L_{x_1}}\bar{\zeta}_\alpha\zeta_\alpha\,dx_2\le\int_{L_{x_1}}\bar{\zeta}_{\alpha,2}\zeta_{\alpha,2}\,dx_2,\qquad \frac{\pi^2}{\ell_2^2}\int_{L_{x_1}}\bar{\psi}\psi\,dx_2\le\int_{L_{x_1}}\bar{\psi}_{,2}\psi_{,2}\,dx_2, \tag{4-10}$$

and considering (4-8) and (4-9) we arrive at

$$\mathcal{J}'_\kappa(x_1)\ge\int_{L_{x_1}}2\mu_\kappa\Big[(\bar{\zeta}_\alpha+\bar{\psi}_{,\alpha})(\zeta_\alpha+\psi_{,\alpha})+\tfrac{1}{3}h^2\bar{\zeta}_{\alpha,\beta}\zeta_{\alpha,\beta}-\frac{\varrho\omega^2\ell_2^2}{\mu_\kappa\pi^2}\big(\bar{\psi}_{,2}\psi_{,2}+\tfrac{1}{3}h^2\bar{\zeta}_{\alpha,2}\zeta_{\alpha,2}\big)\Big]dx_2. \tag{4-11}$$

Using relations (4-10), we can observe that

$$\frac{6\ell_2^2}{\pi^2h^2}\int_{L_{x_1}}\big[(\bar{\zeta}_2+\bar{\psi}_{,2})(\zeta_2+\psi_{,2})+\tfrac{1}{6}h^2\bar{\zeta}_{2,2}\zeta_{2,2}\big]dx_2\ge\frac{\ell_2^2}{\pi^2}\int_{L_{x_1}}\zeta_{2,2}\bar{\zeta}_{2,2}\,dx_2\ge\int_{L_{x_1}}\zeta_2\bar{\zeta}_2\,dx_2. \tag{4-12}$$

On the other side, Schwarz and arithmetic-geometric mean inequalities imply

$$(\bar{\zeta}_2+\bar{\psi}_{,2})(\zeta_2+\psi_{,2})\ge(1-\varepsilon)\zeta_2\bar{\zeta}_2+\Big(1-\frac{1}{\varepsilon}\Big)\psi_{,2}\bar{\psi}_{,2}\qquad\text{for every }\varepsilon>0,$$

and in particular, for $\varepsilon = 2$, $(\bar{\zeta}_2 + \bar{\psi}_{,2})(\zeta_2 + \psi_{,2}) \geq -\zeta_2\bar{\zeta}_2 + \frac{1}{2}\psi_{,2}\bar{\psi}_{,2}$; thus,

$$\int_{L_{x_1}} \left[(\bar{\zeta}_2 + \bar{\psi}_{,2})(\zeta_2 + \psi_{,2}) + \tfrac{1}{6}h^2\bar{\zeta}_{2,2}\zeta_{2,2}\right] dx_2 \geq \int_{L_{x_1}} (\bar{\zeta}_2 + \bar{\psi}_{,2})(\zeta_2 + \psi_{,2})\, dx_2$$
$$\geq \int_{L_{x_1}} \left(-\bar{\zeta}_2\zeta_2 + \tfrac{1}{2}\bar{\psi}_{,2}\psi_{,2}\right) dx_2. \tag{4-13}$$

Combining (4-12) and (4-13) we obtain

$$\int_{L_{x_1}} \left[(\bar{\zeta}_2 + \bar{\psi}_{,2})(\zeta_2 + \psi_{,2}) + \tfrac{1}{6}h^2\bar{\zeta}_{2,2}\zeta_{2,2}\right] dx_2 \geq \frac{h^2\pi^2}{2(6\ell_2^2 + \pi^2h^2)} \int_{L_{x_1}} \bar{\psi}_{,2}\psi_{,2}\, dx_2. \tag{4-14}$$

Moreover, (4-11) and (4-14) imply

$$\mathcal{J}'_\kappa(x_1) \geq \int_{L_{x_1}} \mu_\kappa \left\{ 2(\bar{\zeta}_1 + \bar{\psi}_{,1})(\zeta_1 + \psi_{,1}) + \frac{h^2\pi^2}{6\ell_2^2 + \pi^2h^2}\left[1 - \frac{2\varrho\ell_2^2\omega^2}{\pi^2\mu_\kappa}\left(1 + \frac{6\ell_2^2}{\pi^2h^2}\right)\right]\bar{\psi}_{,2}\psi_{,2} \right.$$
$$\left. + \tfrac{1}{3}h^2\left[2\bar{\zeta}_{1,1}\zeta_{1,1} + 2\bar{\zeta}_{2,1}\zeta_{2,1} + 2\left(1 - \frac{\varrho\ell_2^2\omega^2}{\pi^2\mu_\kappa}\right)\bar{\zeta}_{1,2}\zeta_{1,2} + \left(1 - \frac{2\varrho\ell_2^2\omega^2}{\pi^2\mu_\kappa}\right)\bar{\zeta}_{2,2}\zeta_{2,2}\right]\right\} dx_2. \tag{4-15}$$

If $\varrho > 0$, (2-8) and (3-13) hold and

$$\omega < \omega_m \qquad \text{with} \qquad \omega_m = \left[\frac{2\varrho\ell_2^2}{\pi^2\mu_\kappa}\left(1 + \frac{6\ell_2^2}{\pi^2h^2}\right)\right]^{-1/2}. \tag{4-16}$$

The frequency ω_m depends on the geometrical properties of the plate, namely h and ℓ_2. We can see that μ_κ is strictly positive and the critical frequency ω_m is such that

$$0 < 1 - \frac{\omega^2}{\omega_m^2} = \min\left\{1 - \frac{2\varrho\ell_2^2\omega^2}{\pi^2\mu_\kappa}\left(1 + \frac{6\ell_2^2}{\pi^2h^2}\right), 1 - \frac{\varrho\ell_2^2\omega^2}{\pi^2\mu_\kappa}, 1 - \frac{2\varrho\ell_2^2\omega^2}{\pi^2\mu_\kappa}\right\}. \tag{4-17}$$

Then, (4-15) and (4-17) lead to

$$\mathcal{J}'_\kappa(x_1) \geq \int_{L_{x_1}} \mu_\kappa\left[p_1(\bar{\zeta}_1 + \bar{\psi}_{,1})(\zeta_1 + \psi_{,1}) + p_2\bar{\psi}_{,2}\psi_{,2}\right.$$
$$\left. + \tfrac{1}{3}h^2(p_3\bar{\zeta}_{1,1}\zeta_{1,1} + p_4\bar{\zeta}_{2,1}\zeta_{2,1} + p_5\bar{\zeta}_{1,2}\zeta_{1,2} + p_6\bar{\zeta}_{2,2}\zeta_{2,2})\right] dx_2, \tag{4-18}$$

where $p_1, \ldots, p_6$ represent the following strictly positive coefficients:

$$p_1 = p_3 = p_4 = 2, \qquad p_2 = \frac{h^2\pi^2}{6\ell_2^2 + h^2\pi^2}\left(1 - \frac{\omega^2}{\omega_m^2}\right), \qquad p_5 = 2p_6 = 2\left(1 - \frac{\omega^2}{\omega_m^2}\right).$$

Under the above hypotheses, $\mathcal{J}_\kappa$ is a nondecreasing function and we can prove the following theorem.

Theorem 4.1. *Let the hypotheses of Theorem 3.1 be still valid and let the frequency of harmonic vibrations ω be lower than the critical value ω_m, as in (4-16). The function $\mathcal{J}_\kappa$ is such that*

$$\left|\mathcal{J}_\kappa(x_1)\right| \leq \int_{L_{x_1}} \frac{\ell_2}{\pi}\left[P_1(\bar{\zeta}_1 + \bar{\psi}_{,1})(\zeta_1 + \psi_{,1}) + P_2\bar{\psi}_{,2}\psi_{,2}\right.$$
$$\left. + \tfrac{1}{3}h^2(P_3\bar{\zeta}_{1,1}\zeta_{1,1} + P_4\bar{\zeta}_{2,1}\zeta_{2,1} + P_5\bar{\zeta}_{1,2}\zeta_{1,2} + P_6\bar{\zeta}_{2,2}\zeta_{2,2})\right] dx_2, \tag{4-19}$$

where

$$P_1 = c_{55}, \quad P_2 = c_{55}, \quad P_3 = c_{11}, \quad P_4 = c_{66}, \quad P_5 = (c_{11} + c_{66} + c_{12}), \quad P_6 = (2c_{66} + c_{12}). \tag{4-20}$$

Furthermore, $\mathcal{J}_\kappa$ satisfies the inequality

$$\mu_\kappa \big|\mathcal{J}_k(x_1)\big| \le \nu \mathcal{J}_k'(x_1) \qquad \textit{with} \quad \nu = \max_{i=1,\dots,6} \frac{\ell_2 P_i}{\pi p_i}. \tag{4-21}$$

We underline that, as with ω_m, ν also depends on the geometrical properties of the plate.

Proof. Considering (4-2)–(4-6), we arrive at

$$\mathcal{J}_\kappa(x_1) = \int_{L_{x_1}} 2\,\mathrm{Re}\big\{c_{55}(\bar\zeta_1 + \bar\psi_{,1})\psi + \tfrac{1}{3}h^2\big[c_{11}\bar\zeta_{1,1}\zeta_1 + (c_{66}-\kappa)\bar\zeta_{2,2}\zeta_1 + (c_{12}+\kappa)\bar\zeta_{1,2}\zeta_2 + c_{66}\bar\zeta_{2,1}\zeta_2\big]\big\}\,dx_2. \tag{4-22}$$

Using the arithmetic-geometric and Schwarz inequalities and taking into account (4-10), we can show that

$$\begin{aligned}
\int_{L_{x_1}} \mathrm{Re}[(\bar\zeta_1 + \bar\psi_{,1})\psi]\,dx_2 &\le \frac{\ell_2}{\pi}\Big(\int_{L_{x_1}}(\bar\zeta_1 + \bar\psi_{,1})(\zeta_1 + \psi_{,1})\,dx_2\Big)^{1/2}\Big(\int_{L_{x_1}}\bar\psi_{,2}\psi_{,2}\,dx_2\Big)^{1/2} \\
&\le \frac{\ell_2}{2\pi}\Big[\int_{L_{x_1}}(\bar\zeta_1 + \bar\psi_{,1})(\zeta_1 + \psi_{,1})\,dx_2 + \int_{L_{x_1}}\psi_{,2}\bar\psi_{,2}\,dx_2\Big], \\
\int_{L_{x_1}} \mathrm{Re}[\bar\zeta_{1,1}\zeta_1]\,dx_2 &\le \frac{\ell_2}{\pi}\Big(\int_{L_{x_1}}\bar\zeta_{1,1}\zeta_{1,1}\,dx_2\Big)^{1/2}\Big(\int_{L_{x_1}}\bar\zeta_{1,2}\zeta_{1,2}\,dx_2\Big)^{1/2} \le \frac{\ell_2}{2\pi}\int_{L_{x_1}}\bar\zeta_{1,\alpha}\zeta_{1,\alpha}\,dx_2, \\
\int_{L_{x_1}} \mathrm{Re}[\bar\zeta_{2,2}\zeta_1]\,dx_2 &\le \frac{\ell_2}{\pi}\Big(\int_{L_{x_1}}\bar\zeta_{2,2}\zeta_{2,2}\,dx_2\Big)^{1/2}\Big(\int_{L_{x_1}}\bar\zeta_{1,2}\zeta_{1,2}\,dx_2\Big)^{1/2} \le \frac{\ell_2}{2\pi}\int_{L_{x_1}}\bar\zeta_{\alpha,2}\zeta_{\alpha,2}\,dx_2, \\
\int_{L_{x_1}} \mathrm{Re}[\bar\zeta_{1,2}\zeta_2]\,dx_2 &\le \frac{\ell_2}{\pi}\Big(\int_{L_{x_1}}\bar\zeta_{1,2}\zeta_{1,2}\,dx_2\Big)^{1/2}\Big(\int_{L_{x_1}}\bar\zeta_{2,2}\zeta_{2,2}\,dx_2\Big)^{1/2} \le \frac{\ell_2}{2\pi}\int_{L_{x_1}}\bar\zeta_{\alpha,2}\zeta_{\alpha,2}\,dx_2, \\
\int_{L_{x_1}} \mathrm{Re}[\bar\zeta_{2,1}\zeta_2]\,dx_2 &\le \frac{\ell_2}{\pi}\Big(\int_{L_{x_1}}\bar\zeta_{2,1}\zeta_{2,1}\,dx_2\Big)^{1/2}\Big(\int_{L_{x_1}}\bar\zeta_{2,2}\zeta_{2,2}\,dx_2\Big)^{1/2} \le \frac{\ell_2}{2\pi}\int_{L_{x_1}}\bar\zeta_{2,\alpha}\zeta_{2,\alpha}\,dx_2.
\end{aligned} \tag{4-23}$$

By means of (4-22) and (4-23), we obtain the inequality

$$\begin{aligned}
\big|\mathcal{J}_\kappa(x_1)\big| \le \int_{L_{x_1}} \frac{\ell_2}{\pi}\Big\{&c_{55}(\bar\zeta_1 + \bar\psi_{,1})(\zeta_1 + \psi_{,1}) + c_{55}\bar\psi_{,2}\psi_{,2} \\
&+ \tfrac{1}{3}h^2\big[c_{11}\bar\zeta_{1,\alpha}\zeta_{1,\alpha} + (c_{66}-\kappa)\bar\zeta_{\alpha,2}\zeta_{\alpha,2} + (c_{12}+\kappa)\bar\zeta_{\alpha,2}\zeta_{\alpha,2} + c_{66}\bar\zeta_{2,\alpha}\zeta_{2,\alpha}\big]\Big\}\,dx_2,
\end{aligned}$$

which, through (4-20), leads to (4-19).

Since μ_κ and $p_1, \dots, p_6$ are strictly positive, the definition of ν_κ and (4-19) allow us to write

$$\begin{aligned}
\big|\mathcal{J}_\kappa(x_1)\big| \le \int_{L_{x_1}} \nu\big[&p_1(\bar\zeta_1 + \bar\psi_{,1})(\zeta_1 + \psi_{,1}) + p_2\bar\psi_{,2}\psi_{,2} \\
&+ \tfrac{1}{3}h^2(p_3\bar\zeta_{1,1}\zeta_{1,1} + p_4\bar\zeta_{2,1}\zeta_{2,1} + p_5\bar\zeta_{1,2}\zeta_{1,2} + p_6\bar\zeta_{2,2}\zeta_{2,2})\big]\,dx_2.
\end{aligned} \tag{4-24}$$

Finally, (4-18) and (4-24) prove that (4-21) is satisfied. □

For what follows, it is useful to introduce the class of steady-state vibrations (ζ_α, ψ) for which

$$\mathscr{E}(x_1) = \int_{S_{x_1}} \frac{\ell_2}{\pi}\big[P_1(\bar{\zeta}_1 + \bar{\psi}_{,1})(\zeta_1 + \psi_{,1}) + P_2\psi_{,2}\bar{\psi}_{,2} + \tfrac{1}{3}h^2(P_3\zeta_{1,1}\bar{\zeta}_{1,1} + P_4\bar{\zeta}_{2,1}\zeta_{2,1} + P_5\bar{\zeta}_{1,2}\zeta_{1,2} + P_6\bar{\zeta}_{2,2}\zeta_{2,2})\big]da < \infty, \quad (4\text{-}25)$$

where $S_{x_1} = \overline{\Sigma} \cap [x_1, \infty) \times [0, \ell_2]$. From a direct differentiation of $\mathscr{E}(x_1)$, we get

$$-\mathscr{E}'(x_1) = \int_{L_{x_1}} \frac{\ell_2}{\pi}\big[P_1(\bar{\zeta}_1 + \bar{\psi}_{,1})(\zeta_1 + \psi_{,1}) + P_2\psi_{,2}\bar{\psi}_{,2} + \tfrac{1}{3}h^2(P_3\zeta_{1,1}\bar{\zeta}_{1,1} + P_4\zeta_{2,1}\bar{\zeta}_{2,1} + P_5\zeta_{1,2}\bar{\zeta}_{1,2} + P_6\zeta_{2,2}\bar{\zeta}_{2,2})\big]dx_2. \quad (4\text{-}26)$$

As a consequence of (4-19) and (4-26), it follows that

$$\big|\mathscr{J}_\kappa(x_1)\big| \le -\mathscr{E}'(x_1), \quad (4\text{-}27)$$

so $\mathscr{E}(x_1)$ is a nonincreasing function.

When the strip $\overline{\Sigma}$ is bounded, the hypothesis (4-25) is trivially satisfied; Equations (4-5) and (4-27) imply

$$\mathscr{E}'(\ell_1) = 0 \quad \Rightarrow \quad \mathscr{J}_\kappa(\ell_1) = 0. \quad (4\text{-}28)$$

On the other side, if the strip $\overline{\Sigma}$ is semiinfinite and the hypothesis (4-25) is satisfied, then (4-26) and (4-27) lead to

$$\lim_{x_1\to\infty} \mathscr{E}'(x_1) = 0 \quad \Rightarrow \quad \lim_{x_1\to\infty} \mathscr{J}_\kappa(x_1) = 0. \quad (4\text{-}29)$$

Now, provided that the frequency of harmonic vibrations is lower than the critical value ω_m, we can establish the following theorem.

Theorem 4.2. *Let the hypotheses of Theorem 4.1 be still valid and let $\{\zeta_\alpha, \psi\}$ be the steady-state vibrations for which (4-25) holds. Then, the function $\mathscr{J}_\kappa$ satisfies a decay estimate of Saint-Venant type*:

$$0 \le -\mathscr{J}_\kappa(x_1) \le -\mathscr{J}_\kappa(0)\exp\Big(-\frac{\mu_\kappa}{\nu}x_1\Big). \quad (4\text{-}30)$$

Proof. Whether the considered strip is bounded or not, from hypothesis (4-16) on the frequency ω and from the nondecreasing property of $\mathscr{J}_\kappa$, (4-28) and (4-29) imply

$$\mathscr{J}_\kappa(x_1) \le 0. \quad (4\text{-}31)$$

We can also remark, from the definitions of coefficients $P_1, \dots, P_6$ and ν, that ν is strictly positive. Then, (4-21) and (4-31) allow us to write

$$\mathscr{J}'_\kappa(x_1) + \frac{\mu_\kappa}{\nu}\mathscr{J}_\kappa(x_1) \ge 0 \quad \Rightarrow \quad \frac{d}{dx_1}\Big[\mathscr{J}_\kappa(x_1)\exp\Big(\frac{\mu_\kappa}{\nu}x_1\Big)\Big] \ge 0. \quad (4\text{-}32)$$

It is easy to observe that (4-32) leads to the estimate (4-30) with exponential decay factor μ_κ/ν. □

Remark. The investigation performed is based on an assumption concerning the strong ellipticity of the elasticity tensor. The results obtained under such an hypothesis are thus valid also for classes of particular materials characterized by special properties, like negative Poisson's ratio and negative stiffness (auxetic or antirubber materials). These particular structures (see, for example, [Park and Lakes 2007]) expand laterally when stretched, in contrast to ordinary materials.

List of symbols

	Symbol	Page
Right cylinder of height $2h$	$\bar{B}$	325
Interiors of $\bar{B}$ and $\bar{\Sigma}$	B, Σ	325
Rectangular Cartesian coordinate frame	Ox_1x_2	325
Variable functions characterizing a bending state	v_α, w	325
Constitutive equations	M_{ij}, τ_{ij}	325
Family of tensors depending on a parameter κ	$\tilde{M}_{ij}$	327
Definition of initial-boundary value problem	$\mathcal{P}$	327
External data	$\mathcal{D}$	327
Support of external data	$\hat{D}_T$	327
Set defined on the plate	D_r, Σ_r, L_r	327
Integral function	$\mathcal{J}_\kappa$	327
Quadratic forms	$\mathcal{T}$, $\mathcal{W}$, $\mathcal{W}_0$, $\mathcal{W}_1$, $\mathcal{W}_2$	328
Matrices associated with the quadratic forms $\mathcal{W}_0$, $\mathcal{W}_1$, $\mathcal{W}_2$	$\mathcal{A}_0$, $\mathcal{A}_1$, $\mathcal{A}_2$	328
Smallest and largest eigenvalues of $\mathcal{A}_0$, $\mathcal{A}_1$, $\mathcal{A}_2$	μ_κ, η_κ	329
Smallest and largest eigenvalues of $\mathcal{W}_\alpha$	$k_m^{(\alpha)}$, $k_M^{(\alpha)}$	329
Constant characteristic of the material	c_κ	329
Variable functions characterizing steady-state vibrations	ζ_α, ψ	332
Frequency of oscillations	ω	332
Dimensions of the middle section of the plate	ℓ_1, ℓ_2	332
Constitutive equations for problem of steady-state vibrations	Γ_{ij}, χ_i	332
Set defined on the plate for steady-state vibrations	L_{x_1}	333
Integral function for steady-state vibrations	$\mathcal{J}_\kappa$	333
Complex quadratic forms	$\widehat{\mathcal{W}}$, $\widehat{\mathcal{W}}_0$, $\widehat{\mathcal{W}}_1$, $\widehat{\mathcal{W}}_2$	333
Estimate coefficients	$p_1, \ldots, p_6$	334
Estimate coefficients	$P_1, \ldots, P_6$	335
Constant characteristic of the material	ν	335
Integral function	$\mathcal{E}$	336
Set defined on the plate for steady-state vibrations	S_{x_1}	336

References

[Arnold et al. 2002] D. N. Arnold, A. L. Madureira, and S. Zhang, "On the range of applicability of the Reissner–Mindlin and Kirchhoff–Love plate bending models", *J. Elasticity* **67**:3 (2002), 171–185.

[Chiriţă 1995] S. Chiriţă, "Spatial decay estimates for solutions describing harmonic vibrations in a thermoelastic cylinder", *J. Therm. Stresses* **18**:4 (1995), 421–436.

[Chiriţă and Ciarletta 1999] S. Chiriţă and M. Ciarletta, "Time-weighted surface power function method for the study of spatial behaviour in dynamics of continua", *Eur. J. Mech. A Solids* **18**:5 (1999), 915–933.

[Chiriţă and Ciarletta 2003] S. Chiriţă and M. Ciarletta, "Some further growth and decay results in linear thermoelastodynamics", *J. Therm. Stresses* **26**:9 (2003), 889–903.

[Chiriţă et al. 2007] S. Chiriţă, A. Danescu, and M. Ciarletta, "On the strong ellipticity of the anisotropic linearly elastic materials", *J. Elasticity* **87**:1 (2007), 1–27.

[Ciarletta et al. 2005] M. Ciarletta, S. Chiriţă, and F. Passarella, "Some results on the spatial behaviour in linear porous elasticity", *Arch. Mech.* **57**:1 (2005), 43–65.

[Constanda 1990] C. Constanda, *A mathematical analysis of bending of thin plates with transverse shear deformation*, Longman, Essex, 1990.

[Fabrizio and Chiriţă 2004] M. Fabrizio and S. Chiriţă, "Some qualitative results on the dynamic viscoelasticity of the Reissner–Mindlin plate model", *Q. J. Mech. Appl. Math.* **57**:1 (2004), 59–78.

[Flavin 1974] J. N. Flavin, "On Knowles' version of Saint-Venant's principle in two-dimensional elastostatics", *Arch. Ration. Mech. An.* **53**:4 (1974), 366–375.

[Green and Naghdi 1967] A. E. Green and P. M. Naghdi, "The linear theory of an elastic Cosserat plate", *Math. Proc. Cambridge Philos. Soc.* **63** (1967), 537–550.

[Gregory and Wan 1985] R. D. Gregory and F. Y. M. Wan, "On plate theories and Saint-Venant's principle", *Int. J. Solids Struct.* **21**:10 (1985), 1005–1024.

[Gurtin 1972] M. E. Gurtin, *Linear theory of elasticity*, edited by S. Flügge, Handbuch der Physik **VIa/2**, Springer, Berlin, 1972.

[Horgan 1989] C. O. Horgan, "Recent developments concerning Saint-Venant's principle: an update", *Appl. Mech. Rev.* (*ASME*) **42**:11 (1989), 295–303.

[Horgan 1996] C. O. Horgan, "Recent developments concerning Saint-Venant's principle: a second update", *Appl. Mech. Rev.* (*ASME*) **49**:10S (1996), S101–S111.

[Horgan and Knowles 1983] C. O. Horgan and J. K. Knowles, "Recent developments concerning Saint-Venant's principle", *Adv. Appl. Mech.* **23** (1983), 179–269.

[Hughes 1987] T. J. R. Hughes, *The finite element method: linear static and dynamic finite element analysis*, Prentice-Hall, Englewood Cliffs, NJ, 1987.

[Knowles 1966] J. K. Knowles, "On Saint-Venant's principle in the two-dimensional linear theory of elasticity", *Arch. Ration. Mech. An.* **21**:1 (1966), 1–22.

[Lagnese and Lions 1988] J. E. Lagnese and J. L. Lions, *Modelling, analysis and control of thin plates*, Collection RMA **6**, Masson, Paris, 1988.

[Mielke 1988] A. Mielke, "On Saint-Venant's problem for an elastic strip", *Proc. R. Soc. Edinburgh A Math.* **110**:3 (1988), 161–181.

[Mindlin 1951] R. D. Mindlin, "Influence of rotatory inertia and shear on flexural motions of isotropic, elastic plates", *J. Appl. Mech.* (*ASME*) **18**:1 (1951), 31–38.

[Naghdi 1971] P. M. Naghdi, *The theory of shells and plates*, edited by C. Truesdell, Handbuch der Physik **VIa/2**, Springer, Berlin, 1971.

[Nowinski 1978] J. L. Nowinski, *Theory of thermoelasticity with applications*, Sijthoff & Noordoff, Alphen aan den Rijn, 1978.

[Park and Lakes 2007] J. B. Park and R. S. Lakes, *Biomaterials*, 3rd ed., Springer, Berlin, 2007.

[Paroni et al. 2006] R. Paroni, P. Podio-Guidugli, and G. Tomassetti, "The Reissner–Mindlin plate theory via Γ-convergence", *C. R. Acad. Sci. Paris Sér. I Math.* **343**:6 (2006), 437–440.

[Passarella and Zampoli 2009a] F. Passarella and V. Zampoli, "Some results concerning the state of bending for transversely isotropic plates", *Math. Methods Appl. Sci.* **32**:14 (2009), 1828–1843.

[Passarella and Zampoli 2009b] F. Passarella and V. Zampoli, "Spatial estimates for transient and steady-state solutions in transversely isotropic plates of Mindlin-type", *Eur. J. Mech. A Solids* **28**:4 (2009), 868–876.

[Reissner 1945] E. Reissner, "The effect of transverse shear deformation on the bending of elastic plates", *J. Appl. Mech.* (*ASME*) **12**:2 (1945), 68–77.

[Reissner 1947] E. Reissner, "On bending of elastic plates", *Quart. Appl. Math.* **5**:1 (1947), 55–68.

[Schiavone and Tait 1993] P. Schiavone and R. J. Tait, "Thermal effects in Mindlin-type plates", *Q. J. Mech. Appl. Math.* **46**:1 (1993), 27–39.

[Toupin 1965] R. A. Toupin, "Saint-Venant's principle", *Arch. Ration. Mech. An.* **18**:2 (1965), 83–96.

[Wheeler and Sternberg 1968] L. T. Wheeler and E. Sternberg, "Some theorems in classical elastodynamics", *Arch. Ration. Mech. An.* **31**:1 (1968), 51–90.

Received 2 Mar 2009. Revised 25 Sep 2009. Accepted 30 Sep 2009.

FRANCESCA PASSARELLA: passarella@diima.unisa.it
Department of Information Engineering and Applied Mathematics, University of Salerno, via Ponte Don Melillo, 84084 Fisciano (SA), Italy

VINCENZO TIBULLO: vtibullo@unisa.it
Department of Information Engineering and Applied Mathematics, University of Salerno, via Ponte Don Melillo, 84084 Fisciano (SA), Italy

VITTORIO ZAMPOLI: vzampoli@unisa.it
Department of Information Engineering and Applied Mathematics, University of Salerno, via Ponte Don Melillo, 84084 Fisciano (SA), Italy

JOURNAL OF MECHANICS OF MATERIALS AND STRUCTURES
Vol. 5, No. 2, 2010

A CONSISTENT REFINEMENT OF FIRST-ORDER SHEAR DEFORMATION THEORY FOR LAMINATED COMPOSITE AND SANDWICH PLATES USING IMPROVED ZIGZAG KINEMATICS

ALEXANDER TESSLER, MARCO DI SCIUVA AND MARCO GHERLONE

A refined zigzag theory is presented for laminated-composite and sandwich plates that includes the kinematics of first-order shear deformation theory as its baseline. The theory is variationally consistent and is derived from the virtual work principle. Novel piecewise-linear zigzag functions are used, providing a more realistic representation of the deformation states of transverse shear-flexible plates than other similar theories. The formulation does not enforce full continuity of the transverse shear stresses across the plate's thickness, yet it is robust. Transverse shear correction factors are not required to yield accurate results. The theory avoids the shortcomings of earlier zigzag theories (such as shear-force inconsistency and difficulties in simulating clamped boundary conditions) which have limited their accuracy. This new theory requires only C^0-continuous kinematic approximations and is perfectly suited for developing computationally efficient finite elements. It should be useful for obtaining relatively efficient, accurate estimates of structural response, needed in designing high-performance load-bearing aerospace structures.

A list of symbols can be found on page 363.

1. Introduction

The high-performance and lightweight characteristics of advanced composite materials have spurred numerous applications of these materials in military and civilian aircraft, aerospace vehicles, and naval and civil structures. To realize the full potential of composite structures, further advances in structural design and analysis methods are necessary. In particular, development of cost-effective and reliable laminated-composite structures as the primary load-bearing components of a vehicle requires further advances in stress analysis and failure prediction methodologies.

A wide variety of modern civilian and military aircraft employ relatively thick laminated composites, with one hundred or more layers, in the primary load-bearing structures. Such structures can exhibit pronounced transverse shear deformation and, under certain conditions, design-critical thickness-stretch deformations. Fail-safe design of these structures requires accurate stress-analysis methods, particularly for regions of stress concentration. Computationally efficient analytical models based on beam, plate, and shell assumptions that account for transverse shear and thickness-stretch deformations have recently been addressed in [Tessler 1993; Cook and Tessler 1998; Barut et al. 2002]. To achieve accurate computational models, three-dimensional finite element analyses are often preferred over beam, plate, and shell models based on first-order shear deformation theories (FSDT). This preference is due to the

Keywords: first-order shear deformation plate theory, zigzag kinematics, laminated composite plates, sandwich plates, virtual work principle.

latter having the tendency to underestimate the normal stresses, particularly in highly heterogeneous and thick composite and sandwich laminates [Reissner 1985; Librescu et al. 1987; Noor and Burton 1989; Liu and Li 1996]. For composite laminates with hundreds of layers, however, 3D modeling becomes prohibitively expensive, especially for nonlinear and progressive failure analyses. To realize improved response predictions based on beam, plate, and shell assumptions, numerous refined theories have been developed [Ambartsumyan 1961; Sun and Whitney 1973; Lo et al. 1977a; 1977b; Reddy 1997]. Many of these theories have significant flaws in their theoretical foundation and predictive capabilities and, for these reasons, have not found general acceptance in practical applications.

One class of refined theories that has emerged as practical for engineering applications is known as *zigzag* theories [Di Sciuva 1984a; 1984b; 1985a; 1985b; 1986; 1987; 1990; 1992; Murakami 1986; Toledano and Murakami 1987; Cho and Parmerter 1992; 1993; Di Sciuva et al. 2002]. This class of theories employs a zigzag-like distribution for the in-plane displacements through the laminate thickness, while ensuring a fixed number of kinematic variables regardless of the number of material layers (or laminae). Using through-the-thickness linear in-plane kinematics with displacements and transverse shearing angles as primary variables, [Di Sciuva 1984a; 1984b; 1985a; 1985b; 1986; 1987] added a piecewise linear distribution known as the zigzag displacement. By explicitly enforcing a set of equilibrium conditions along lamina interfaces, constant transverse shear stresses are developed across the laminate thickness. These theories are often referred to as linear zigzag theories (or models) to delineate through-the-thickness linear distributions of their baseline in-plane displacements. Di Sciuva [1990; 1992] and Cho and Parmerter [1992; 1993] provided further enhancements to the zigzag theory by adding quadratic and cubic power-series terms to the in-plane displacements. As in the previous efforts, the procedure relies on the transverse shear stress equilibrium constraints. The resulting transverse shear stresses are continuous across the laminate thickness, and vanish along the top and bottom laminate surfaces (see also [Di Sciuva et al. 2002]). Murakami and coworkers developed another linear zigzag theory [Murakami 1986] and a higher-order zigzag theory [Toledano and Murakami 1987] that also includes transverse normal deformations. The governing equations are derived using Reissner's mixed variational theorem [Reissner 1984], and they include transverse shear and transverse normal stresses [Toledano and Murakami 1987] as their primary unknowns.

Zigzag theories provide sufficiently accurate response predictions for relatively thick laminated-composite and sandwich structures including those for normal strains and stresses [Di Sciuva 1984a; 1984b; 1985a; 1985b; 1986; 1987; 1990; 1992; Murakami 1986; Toledano and Murakami 1987; Cho and Parmerter 1992; 1993; Di Sciuva et al. 2002]. Furthermore, these theories often yield response predictions comparable to those of layer-wise and higher-order theories that are more computationally intensive. To make a zigzag theory practical for large-scale analyses and engineering design, its analytic framework must be well suited for an efficient finite element approximation. While pursuing a computationally desirable zigzag beam theory, Averill [1994; Averill and Yip 1996] recognized two significant drawbacks that plague many previously mentioned zigzag theories, in particular those having displacements as primary unknowns [Di Sciuva 1984a; 1984b; 1985a; 1985b; 1986; 1987; 1990; 1992; Cho and Parmerter 1992; 1993]: Firstly, because the curvature is expressed as a second spatial derivative of the deflection variable, C^1 continuous functions are required to approximate the deflection within the finite element framework. Due to their complexity and overly stiff response properties, such approximations are especially undesirable for plate and shell finite elements. Secondly, transverse shear

stresses calculated from constitutive equations vanish erroneously along the clamped boundaries, this being a "physical inconsistency that plagues many popular shear deformation theories" [Averill 1994]. Averill resolved the first issue by adopting the kinematics of Timoshenko's shear deformation theory as a baseline; however, to resolve the second issue he proposed a boundary-condition compromise at the expense of the variational consistency of the theory, in which a kinematic variable representing the amplitude of the zigzag displacement is omitted from the variationally required set of boundary conditions.

Tessler et al. [2007] presented a clearer insight into the existing flaws of the linear zigzag models [Di Sciuva 1984a; 1984b; 1985a; 1985b; 1986; 1987]. In these earlier theories, the kinematic field is constructed by way of enforcing equilibrium of the transverse shear stresses along lamina interfaces, which results in constant (uniform) transverse shear stresses across the laminate thickness. The consequence of the transverse shear equilibrium constraints within a displacement-based theory is that they tend to overconstrain the kinematic field. As delineated in [Tessler et al. 2007], the overconstraint is manifested by a physical inconsistency (or anomaly) in the definition of the transverse shear forces. Consequently, the cross-sectional integral of the transverse shear stress does not correspond to the transverse shear force obtained from the bending equilibrium equation of the theory. A further byproduct of this anomaly is the *erroneous* vanishing of the transverse shear strains, stresses, and forces along the clamped boundaries. Averill [1994] pointed out the latter aspect; however, as previously discussed, he proposed only a variationally inconsistent strategy to circumvent the issue. It is also worth mentioning that the same transverse shear stress anomaly exists in many other theories, for example, the cubic zigzag theories by Di Sciuva [1990; 1992] and Cho and Parmerter [1992; 1993], and the smeared cubic theory by Reddy [1984; 1997; 2004]. Also note that almost exclusively, and this pertains to all of the aforementioned articles, the proposed theories are assessed by solving example problems with simply supported boundaries, where the solutions inherently do not exhibit transverse shear anomalies. Regrettably, the few contributions that considered clamped boundary conditions, for example [Averill 1994; Umasree and Bhaskar 2006], do not discuss shear stress distributions along the clamped boundary.

Yu [2005] proposed a variational asymptotic plate and shell analysis (VAPAS), and Kim and Cho [2005; 2006] presented an enhanced first-order shear deformation theory (EFSDT). Both of these modeling strategies use a three-step procedure [Yu et al. 2008]: (1) obtain a 2D Reissner–Mindlin type constitutive model, (2) carry out the global plate analysis using the constitutive model from step (1), and (3) recover through-the-thickness distributions of displacements and stresses from step (1). In the framework of EFSDT, the recovery of through-the-thickness distributions is performed by means of the cubic zigzag theory by Cho and Parmerter [1992; 1993]. A critical review and comparison of the two approaches in [Yu et al. 2008] reveal that VAPAS requires high-order displacement derivatives to achieve adequate predictions for the in-plane and transverse normal stresses, whereas EFSDT is somewhat inaccurate in terms of the in-plane normal stresses and its extension to nonlinear problems may not be straightforward. Furthermore, since the recovery of the 3D distributions is performed by means of the cubic zigzag theory by Cho and Parmerter [1992; 1993], it is argued that EFSDT should be affected by the aforementioned transverse shear stress anomaly. Unfortunately, Kim and Cho [2005; 2006] discuss numerical results only for plates with simply supported boundary conditions.

To construct a computationally attractive theory suitable for FEM without the flaws of the previous zigzag models, Tessler et al. [2007] proposed a *refined* zigzag theory for laminated composite and

sandwich beams. They derived a novel zigzag function without enforcing a full transverse shear stress equilibrium along the lamina interfaces. The shear force definitions are fully consistent with respect to the physical and variational requirements. The resulting theory is without the aforementioned flaws of the previous zigzag theories and has been shown to demonstrate consistently superior results.

A successful extension of this new zigzag methodology to plate theory was advanced in [Tessler et al. 2009]; in the present we detail the theoretical foundation of the refined zigzag plate theory introduced there. The theory's applicability to laminated composite and sandwich plates is demonstrated by presenting example problems with simply supported and clamped boundaries and which include relatively thick laminates with a high degree of transverse shear flexibility, anisotropy, and heterogeneity. This new formulation augments FSDT with an improved zigzag kinematic field that involves a novel C^0-continuous (across lamina interfaces) representation of the in-plane displacements. The kinematic field is independent of the number of material layers and does not require enforcement of transverse shear stress continuity to yield accurate results. Unlike other similar theories [Di Sciuva 1984a; Averill 1994], the zigzag contribution to the in-plane displacement field is physically realistic, is zero-valued at the top and bottom plate surfaces, and accounts for the shear deformation of every lamina in a consistent way. As a result, transverse shear correction factors are not needed. Additionally, the plate equilibrium equations, constitutive equations, boundary conditions, and strain-displacement relations are consistently derived from the virtual work principle. Moreover, the analytical form of this new theory is ideally suited for developing computationally efficient finite elements requiring only C^0-continuity. This benefit will enable an efficient use of accurate zigzag approximations in large-scale analyses to facilitate the development of robust designs of high-performance aerospace vehicles.

In the remainder of the paper, the theoretical foundation of the new theory and its quantitative assessment are detailed. The zigzag kinematic assumptions, strain-displacement equations, and constitutive lamina relations are presented in Section 2. A set of unique zigzag functions is then introduced and their mathematical structure is described in Section 3. The plate equilibrium equations and their associated boundary conditions, derived from the virtual work principle, are presented in Section 4. In Section 5, an extensive quantitative assessment of the theory is carried out, using closed-form solutions for simply supported and cantilevered plates made of laminated-composite and sandwich material systems. Some of the example problems represent significant challenges for any approximate theory. It is demonstrated that this new zigzag theory eliminates a major flaw of other similar theories; that is, the theory enables accurate modeling of the clamped boundary condition while adhering strictly to the variationally required boundary conditions. Finally, in Section 6, several concluding remarks emphasizing the merits of the new theory are highlighted.

2. Kinematics and formulation

Consider a laminated plate of uniform thickness $2h$ with N perfectly bonded orthotropic layers (or laminae) as shown in Figure 1. Points of the plate are located by the orthogonal Cartesian coordinates (x_1, x_2, z). The ordered pair $(x_1, x_2) \in S_m$ denotes the in-plane coordinates, where S_m represents the set of points given by the intersection of the plate with the plane $z = 0$, referred to herein as the middle reference plane (or mid-plane). The symbol $z \in [-h, h]$ denotes the through-the-thickness coordinate, with $z = 0$ identifying the plate's mid-plane. The plate is subjected to a normal-pressure loading, $q(x_1, x_2)$,

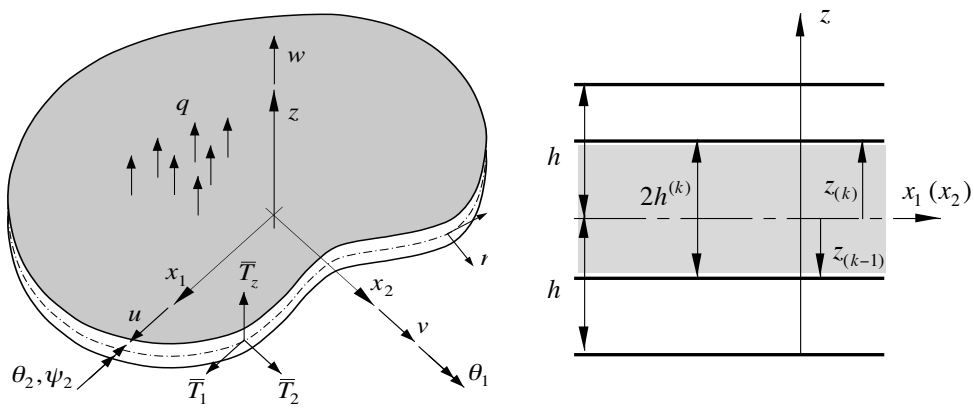

Figure 1. General plate notation (left), and lamination notation (right).

attributed to the mid-plane, S_m, that is defined as positive in the positive z direction. In addition, a traction vector, $(\bar{T}_1, \bar{T}_2, \bar{T}_z)$, is prescribed on $S_\sigma \subset S$, where S denotes the total cylindrical-edge surface. On the remaining part of the edge surface, $S_u \subset S$, displacement restraints are imposed (or prescribed). The sections of the plate edge are related by $S_\sigma \cup S_u = S$ and $S_\sigma \cap S_u = \varnothing$. Moreover, the curves $C_\sigma = S_\sigma \cap S_m$ and $C_u = S_u \cap S_m$ define the two parts of the total perimeter $C = C_\sigma \cup C_u$ surrounding the mid-plane region, S_m. Finally, it is presumed that the constitutive properties may differ appreciably from lamina to lamina, the plate deformations result in small strains, and that body and inertial forces are negligible.

The orthogonal components of the displacement vector, corresponding to material points of the plate (or laminate), are expressed as

$$\begin{aligned} u_1^{(k)}(x_1, x_2, z) &\equiv u(x_1, x_2) + z\theta_1(x_1, x_2) + \phi_1^{(k)}(z)\psi_1(x_1, x_2), \\ u_2^{(k)}(x_1, x_2, z) &\equiv v(x_1, x_2) + z\theta_2(x_1, x_2) + \phi_2^{(k)}(z)\psi_2(x_1, x_2), \\ u_z(x_1, x_2, z) &\equiv w(x_1, x_2), \end{aligned} \tag{1}$$

where the in-plane displacement components $u_1^{(k)}$ and $u_2^{(k)}$ are comprised of constant, linear, and zigzag variations through the thickness. The zigzag variations are C_0-continuous functions with discontinuous thickness-direction derivatives along the lamina interfaces. The superscript (k) is used to indicate quantities corresponding to the k-th lamina, whereas the subscript (k) defines quantities corresponding to the interface between the k-th and $(k+1)$-th laminae. Thus, the k-th lamina thickness is defined in the range $z \in [z_{(k-1)}, z_{(k)}]$ $(k = 1, \ldots, N)$; see Figure 1. The transverse displacement u_z is assumed to be constant through the thickness and is independent of constitutive properties of the k-th lamina; hence the superscript (k) does not appear in its definition.

The kinematic variables in (1) can be interpreted as follows. For homogeneous plates, the zigzag functions $\phi_\alpha^{(k)}$ $(\alpha = 1, 2)$ vanish identically and (1) yield the kinematics of FSDT. For this degenerate case, u and v represent the mid-plane displacements along the coordinate directions x_1 and x_2, respectively; θ_1 and θ_2 represent average bending rotations of the transverse normal about the positive x_2 and the negative x_1 directions, respectively; and w is the transverse deflection. For more precise definitions of the kinematic variables within FSDT refer, for example, to [Tessler 1993]. The symbols $\phi_\alpha^{(k)}$ $(\alpha = 1, 2)$

denote through-the-thickness piecewise-linear zigzag functions associated with heterogeneous plates, yet to be defined. The $\psi_\alpha = \psi_\alpha(x_1, x_2)$ $(\alpha = 1, 2)$ functions represent the spatial amplitudes of the zigzag displacements and, together with the other five kinematic variables, are the unknowns in the analysis. The zigzag displacements $\phi_\alpha^{(k)}\psi_\alpha$ $(\alpha = 1, 2)$ may be regarded as corrections to the in-plane displacements associated with laminate heterogeneity.

Consistent with the kinematic assumptions in (1), the theory accounts for transverse shear deformation. (Transverse normal deformations are neglected in the kinematics; however, their inclusion may be possible following, for example, [Tessler 1993]). Correspondingly, the in-plane and transverse shear strains are

$$\varepsilon_{11}^{(k)} = u_{,1} + z\theta_{1,1} + \phi_1^{(k)}\psi_{1,1}, \tag{2a}$$

$$\varepsilon_{22}^{(k)} = v_{,2} + z\theta_{2,2} + \phi_2^{(k)}\psi_{2,2}, \tag{2b}$$

$$\gamma_{12}^{(k)} = u_{,2} + v_{,1} + z(\theta_{1,2} + \theta_{2,1}) + \phi_1^{(k)}\psi_{1,2} + \phi_2^{(k)}\psi_{2,1}, \tag{2c}$$

$$\gamma_{\alpha z}^{(k)} = \gamma_\alpha + \beta_\alpha^{(k)}\psi_\alpha \quad (\alpha = 1, 2), \tag{2d}$$

where, henceforward, $(\bullet)_{,\alpha} \equiv \frac{\partial(\bullet)}{\partial x_\alpha}$ denotes a partial derivative with respect to the mid-plane coordinate, x_α $(\alpha = 1, 2)$. Also, the following notation is introduced

$$\gamma_\alpha \equiv w_{,\alpha} + \theta_\alpha \qquad (\alpha = 1, 2), \tag{2e}$$

$$\beta_\alpha^{(k)} \equiv \frac{\partial}{\partial z}(\phi_\alpha^{(k)}) \qquad (\alpha = 1, 2), \tag{2f}$$

where the *shear angles* γ_α are uniform through the total laminate thickness, and $\beta_\alpha^{(k)}$ are piecewise constant functions that are uniform through the thickness of each individual lamina.

The generalized Hooke's law for the k-th orthotropic lamina, whose principal material directions are arbitrary with respect to the mid-plane reference coordinates, $(x_1, x_2) \in S_m$, is written as

$$\begin{Bmatrix} \sigma_{11} \\ \sigma_{22} \\ \tau_{12} \\ \tau_{2z} \\ \tau_{1z} \end{Bmatrix}^{(k)} = \begin{bmatrix} C_{11} & C_{12} & C_{16} & 0 & 0 \\ C_{12} & C_{22} & C_{26} & 0 & 0 \\ C_{16} & C_{26} & C_{66} & 0 & 0 \\ 0 & 0 & 0 & Q_{22} & Q_{12} \\ 0 & 0 & 0 & Q_{12} & Q_{11} \end{bmatrix}^{(k)} \begin{Bmatrix} \varepsilon_{11} \\ \varepsilon_{22} \\ \gamma_{12} \\ \gamma_{2z} \\ \gamma_{1z} \end{Bmatrix}^{(k)}, \tag{3}$$

where $C_{ij}^{(k)}$ $(i, j = 1, 2, 6)$ and $Q_{pq}^{(k)}$ $(p, q = 1, 2)$ are the transformed elastic stiffness coefficients referred to the (x_1, x_2, z) coordinate system and relative to the plane-stress condition that ignores the transverse-normal stress. The expressions for these coefficients in terms of the elastic moduli corresponding to the material coordinates can be found, for example, in [Reddy 1997].

3. Refined zigzag functions and transverse shear constitutive relations

The refined zigzag functions (or zigzag displacements) of the present theory are defined by piecewise linear, C^0-continuous functions through the laminate thickness. For convenience, the zigzag functions $\phi_1^{(k)}$ and $\phi_2^{(k)}$, which have units of length, are defined in terms of their respective lamina-interface values $u_{(i)}$ and $v_{(i)}$ $(i = 0, 1, \ldots, N)$ (see Figure 2 depicting the notation for a three-layered laminate).

Thus, for the k-th lamina located in the range $[z_{(k-1)}, z_{(k)}]$, $\phi_1^{(k)}$ and $\phi_2^{(k)}$ are given as

$$\phi_1^{(k)} \equiv \tfrac{1}{2}(1-\xi^{(k)})u_{(k-1)} + \tfrac{1}{2}(1+\xi^{(k)})u_{(k)}, \qquad \phi_2^{(k)} \equiv \tfrac{1}{2}(1-\xi^{(k)})v_{(k-1)} + \tfrac{1}{2}(1+\xi^{(k)})v_{(k)}, \tag{4}$$

where

$$\xi^{(k)} = \left[\frac{z - z_{(k-1)}}{h^{(k)}} - 1\right] \in [-1, 1] \qquad (k = 1, \ldots, N), \tag{5}$$

with the first lamina beginning at $z_{(0)} = -h$, the last (N-th) lamina ending at $z_{(N)} = h$, and the k-th lamina ending at $z_{(k)} = z_{(k-1)} + 2h^{(k)}$, where $2h^{(k)}$ denotes the k-th lamina thickness.

Evaluating (4) at the laminae interfaces gives rise to the definitions of the interfacial displacements

$$\begin{aligned} u_{(k-1)} &= \phi_1^{(k)}(\xi^{(k)} = -1), & u_{(k)} &= \phi_1^{(k)}(\xi^{(k)} = 1), \\ v_{(k-1)} &= \phi_2^{(k)}(\xi^{(k)} = -1), & v_{(k)} &= \phi_2^{(k)}(\xi^{(k)} = 1) \quad (k = 1, \ldots, N), \end{aligned} \tag{6a}$$

where the interfacial displacements at the bottom and top plate surfaces are set herein to vanish identically, that is,

$$u_{(0)} = u_{(N)} = v_{(0)} = v_{(N)} = 0. \tag{6b}$$

Substituting (4) into (2f) results in the piecewise constant functions $\beta_\alpha^{(k)}$ given by

$$\begin{Bmatrix} \beta_1^{(k)} \\ \beta_2^{(k)} \end{Bmatrix} = \frac{1}{2h^{(k)}} \begin{Bmatrix} u_{(k)} - u_{(k-1)} \\ v_{(k)} - v_{(k-1)} \end{Bmatrix}. \tag{7}$$

Because the zigzag functions are zero-valued on the top and bottom surfaces, as defined by Equations (6a) and (6b), through-the-thickness integrals of the slope functions $\beta_\alpha^{(k)}$ ($\alpha = 1, 2$) vanish identically, that is,

$$\int_{-h}^{h} \begin{Bmatrix} \beta_1^{(k)} \\ \beta_2^{(k)} \end{Bmatrix} dz = \begin{Bmatrix} \sum_{k=1}^{N} 2h^{(k)}\beta_1^{(k)} \\ \sum_{k=1}^{N} 2h^{(k)}\beta_2^{(k)} \end{Bmatrix} = \begin{Bmatrix} 0 \\ 0 \end{Bmatrix}. \tag{8}$$

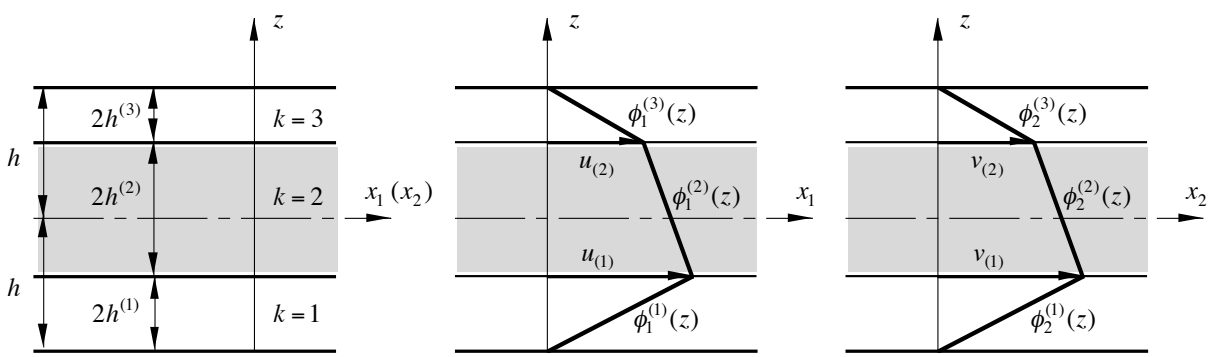

Figure 2. Notation for a three-layered laminate and $\phi_1^{(k)}$ and $\phi_2^{(k)}$ zigzag functions defined in terms of interfacial values (displacements), $u_{(i)}$ and $v_{(i)}$ ($i = 0, 1, \ldots, N$).

Integrating (2d) across the laminate thickness and normalizing the result by the total laminate thickness reveals that

$$\begin{Bmatrix}\gamma_1\\ \gamma_2\end{Bmatrix} = \frac{1}{2h}\int_{-h}^{h}\begin{Bmatrix}\gamma_{1z}^{(k)}\\ \gamma_{2z}^{(k)}\end{Bmatrix} dz. \tag{9}$$

Thus, γ_α ($\alpha = 1, 2$) represent the average transverse shear strains, coinciding with the common representation of the transverse shear strains used in FSDT. Also, (9) indicates that the zigzag amplitude variables, ψ_α ($\alpha = 1, 2$), do not contribute to the average transverse shear strains.

The $u_{(k)}$ and $v_{(k)}$ interfacial values of the zigzag functions are obtained from (7) in terms of $\beta_\alpha^{(k)}$ ($\alpha = 1, 2$; $k = 1, \ldots, N$), that is,

$$\begin{Bmatrix}u_{(k)}\\ v_{(k)}\end{Bmatrix} = 2h^{(k)}\begin{Bmatrix}\beta_1^{(k)}\\ \beta_2^{(k)}\end{Bmatrix} + \begin{Bmatrix}u_{(k-1)}\\ v_{(k-1)}\end{Bmatrix} \qquad (k = 1, \ldots, N), \tag{10a}$$

or, alternatively,

$$\begin{Bmatrix}u_{(k)}\\ v_{(k)}\end{Bmatrix} = \begin{Bmatrix}\sum_{i=1}^{k} 2h^{(i)}\beta_1^{(i)}\\ \sum_{i=1}^{k} 2h^{(i)}\beta_2^{(i)}\end{Bmatrix} \qquad (k = 1, \ldots, N). \tag{10b}$$

Following the approach in [Tessler et al. 2007], the $\beta_\alpha^{(k)}$ functions are determined by first casting the transverse shear strains, (2d), in terms of the transverse shear strain measures, $\eta_\alpha \equiv \gamma_\alpha - \psi_\alpha$ ($\alpha = 1, 2$), and the zigzag amplitude functions, ψ_α ($\alpha = 1, 2$), as

$$\begin{Bmatrix}\gamma_{1z}\\ \gamma_{2z}\end{Bmatrix}^{(k)} \equiv \begin{Bmatrix}\eta_1\\ \eta_2\end{Bmatrix} + \begin{bmatrix}1+\beta_1^{(k)} & 0\\ 0 & 1+\beta_2^{(k)}\end{bmatrix}\begin{Bmatrix}\psi_1\\ \psi_2\end{Bmatrix}. \tag{11}$$

The η_α strain measures are set to vanish explicitly in the theory of Di Sciuva [1984a] and enforced to vanish by way of penalty constraints in the theory of Averill [1994], thus equating γ_α to ψ_α. Presently, no such constraints are imposed on these strain measures.

The transverse shear stresses using Equations (3) and (11) are given as

$$\begin{Bmatrix}\tau_{1z}\\ \tau_{2z}\end{Bmatrix}^{(k)} \equiv \begin{bmatrix}Q_{11} & Q_{12}\\ Q_{21} & Q_{22}\end{bmatrix}^{(k)}\left(\begin{Bmatrix}\eta_1\\ \eta_2\end{Bmatrix} + \begin{bmatrix}1+\beta_1^{(k)} & 0\\ 0 & 1+\beta_2^{(k)}\end{bmatrix}\begin{Bmatrix}\psi_1\\ \psi_2\end{Bmatrix}\right), \tag{12a}$$

or, alternatively, they can be expressed as

$$\begin{Bmatrix}\tau_{1z}\\ \tau_{2z}\end{Bmatrix}^{(k)} \equiv \begin{bmatrix}Q_{11} & Q_{12}\\ Q_{21} & Q_{22}\end{bmatrix}^{(k)}\begin{Bmatrix}\eta_1\\ \eta_2\end{Bmatrix} + Q_{11}^{(k)}(1+\beta_1^{(k)})\begin{Bmatrix}1\\ Q_{12}^{(k)}/Q_{11}^{(k)}\end{Bmatrix}\psi_1 + Q_{22}^{(k)}(1+\beta_2^{(k)})\begin{Bmatrix}Q_{12}^{(k)}/Q_{22}^{(k)}\\ 1\end{Bmatrix}\psi_2.$$

In this form of the transverse shear constitutive relations, the stress vector associated with the η_α strain measures is independent of the zigzag functions. The second and third stress vectors include, as their normalization factors, the coefficients $Q_{\alpha\alpha}^{(k)}(1+\beta_\alpha^{(k)})$ ($\alpha = 1, 2$) that are dependent on the zigzag functions through $\beta_\alpha^{(k)}$. Herein, these normalization factors are set to be constant quantities, denoted as G_α ($\alpha = 1, 2$), thus imposing constraint conditions on the distribution of the zigzag functions.

These constraints give rise to the expressions

$$\begin{Bmatrix} \beta_1^{(k)} \\ \beta_2^{(k)} \end{Bmatrix} = \begin{Bmatrix} G_1/Q_{11}^{(k)} - 1 \\ G_2/Q_{22}^{(k)} - 1 \end{Bmatrix}. \tag{12b}$$

The G_1 and G_2 constants are obtained by integrating (12b) through the laminate thickness while making use of (8), resulting in

$$\begin{Bmatrix} G_1 \\ G_2 \end{Bmatrix} \equiv \begin{Bmatrix} \left(\frac{1}{2h}\int_{-h}^{h} \frac{dz}{Q_{11}^{(k)}}\right)^{-1} \\ \left(\frac{1}{2h}\int_{-h}^{h} \frac{dz}{Q_{22}^{(k)}}\right)^{-1} \end{Bmatrix} = \begin{Bmatrix} \left(\frac{1}{h}\sum_{k=1}^{N} \frac{h^{(k)}}{Q_{11}^{(k)}}\right)^{-1} \\ \left(\frac{1}{h}\sum_{k=1}^{N} \frac{h^{(k)}}{Q_{22}^{(k)}}\right)^{-1} \end{Bmatrix}, \tag{12c}$$

where it is seen that G_1 and G_2 are weighted-average transverse shear stiffness coefficients of their respective lamina-level coefficients, $Q_{11}^{(k)}$ and $Q_{22}^{(k)}$.

Substituting (12b) into (12a) results in the transverse shear constitutive relations of the form

$$\begin{Bmatrix} \tau_{1z} \\ \tau_{2z} \end{Bmatrix}^{(k)} \equiv \begin{bmatrix} Q_{11} & Q_{12} \\ Q_{21} & Q_{22} \end{bmatrix}^{(k)} \begin{Bmatrix} \gamma_1 + \psi_1\left(G_1/Q_{11}^{(k)} - 1\right) \\ \gamma_2 + \psi_2\left(G_2/Q_{22}^{(k)} - 1\right) \end{Bmatrix}, \tag{13a}$$

where, with the use of (12c), the dimensionless stiffness ratios are given as

$$\frac{G_\alpha}{G_{\alpha\alpha}^{(k)}} = \left(\frac{Q_{\alpha\alpha}^{(k)}}{2h}\int_{-h}^{h} \frac{dz}{Q_{\alpha\alpha}^{(k)}}\right)^{-1} \qquad (\alpha = 1, 2). \tag{13b}$$

These ratios are, in general, piecewise constant through the laminate thickness; however, for homogeneous plates, they are unit-valued. Thus, for homogeneous plates, the zigzag transverse shear contributions vanish, in which case (13a) becomes identical to the corresponding relations of FSDT.

The $\phi_\alpha^{(k)}$ ($\alpha = 1, 2$) zigzag functions are determined by substituting (10b) and (12b) into (4), while making use of (5), resulting in

$$\begin{aligned} \phi_\alpha^{(1)} &= (z+h)\left(\frac{G_\alpha}{Q_{\alpha\alpha}^{(1)}} - 1\right) && (k = 1), \\ \phi_\alpha^{(k)} &= (z+h)\left(\frac{G_\alpha}{Q_{\alpha\alpha}^{(k)}} - 1\right) + \sum_{i=2}^{k} 2h^{(i-1)}\left(\frac{G_\alpha}{Q_{\alpha\alpha}^{(i-1)}} - \frac{G_\alpha}{Q_{\alpha\alpha}^{(k)}}\right) && (k = 2, \ldots, N), \\ z \in [z_{(k-1)}, z_{(k)}], \qquad & z_{(0)} = -h, \qquad z_{(k)} = z_{(k-1)} + 2h^{(k)} && (k = 1, \ldots, N;\ \alpha = 1, 2). \end{aligned} \tag{13c}$$

It is seen that the zigzag functions are independent of the state of deformation and are represented by C^0-continuous, piecewise linear functions of the thickness coordinate. The zigzag amplitudes, ψ_α ($\alpha = 1, 2$), are vector functions of the actual response due to the applied loading, and they provide the proper scaling of the zigzag functions, thus controlling the total zigzag contribution to the in-plane displacements. The two zigzag amplitude functions and the remaining five kinematic variables constitute a set of seven kinematic variables associated with this refined zigzag plate theory.

4. Equilibrium equations, boundary conditions, and constitutive relations

The plate equilibrium equations and boundary conditions are derived from the virtual work principle which, neglecting body forces and assuming zero shear tractions on the top and bottom bounding plate surfaces, may be written as

$$\int_{S_m}\int_{-h}^{h}\left(\sigma_{11}^{(k)}\delta\varepsilon_{11}^{(k)}+\sigma_{22}^{(k)}\delta\varepsilon_{22}^{(k)}+\tau_{12}^{(k)}\delta\gamma_{12}^{(k)}+\tau_{1z}^{(k)}\delta\gamma_{1z}^{(k)}+\tau_{2z}^{(k)}\delta\gamma_{2z}^{(k)}\right)dzdS - \int_{S_m}(q\delta w)dS-\int_{c_\sigma}\int_{-h}^{h}[\bar{T}_1\delta u_1^{(k)}+\bar{T}_2\delta u_2^{(k)}+\bar{T}_z\delta u_z^{(k)}]dsdz=0, \quad (14)$$

where δ is the variational operator; all other symbols have been defined in Section 2.

Substituting (1) and (2) into (14) and integrating across the plate thickness yields the 2D statement of virtual work

$$\int_{S_m}\Big(N_1\delta u_{,1}+N_2\delta v_{,2}+N_{12}(\delta u_{,2}+\delta v_{,1})+M_1\delta\theta_{1,1}+M_2\delta\theta_{2,2}+M_{12}(\delta\theta_{1,2}+\delta\theta_{2,1}) + Q_1(\delta w_{,1}+\delta\theta_1)+Q_2(\delta w_{,2}+\delta\theta_2)-q\delta w\Big)dS-\int_{C_\sigma}(\bar{N}_{1n}\delta u+\bar{N}_{2n}\delta v+\bar{Q}_{zn}\delta w+\bar{M}_{1n}\delta\theta_y+\bar{M}_{2n}\delta\theta_x)ds + \underline{\int_{S_m}(M_1^\phi\delta\psi_{1,1}+M_2^\phi\delta\psi_{2,2}+M_{12}^\phi\delta\psi_{1,2}+M_{21}^\phi\delta\psi_{2,1}+Q_1^\phi\delta\psi_1+Q_2^\phi\delta\psi_2)dS} - \underline{\int_{C_\sigma}(\bar{M}_{1n}^\phi\delta\psi_1+\bar{M}_{2n}^\phi\delta\psi_2)ds}=0, \quad (15)$$

where the underlined terms correspond to the zigzag kinematics contributions. In Equation (15), the membrane stress resultants and conjugate strain measures are

$$\boldsymbol{N}_m^T\equiv\{N_1,N_2,N_{12}\}=\int_{-h}^{h}\{\sigma_{11}^{(k)},\sigma_{22}^{(k)},\tau_{12}^{(k)}\}dz, \qquad \boldsymbol{e}_m^T\equiv\{u_{,1},v_{,2},u_{,2}+v_{,1}\}. \quad (16)$$

Likewise, the bending stress resultants and conjugate strain measures are

$$\boldsymbol{M}_b^T\equiv\{M_1,M_1^\phi,M_2,M_2^\phi,M_{12},M_{12}^\phi,M_{21}^\phi\} =\int_{-h}^{h}\{z\sigma_{11}^{(k)},\phi_1^{(k)}\sigma_{11}^{(k)},z\sigma_{22}^{(k)},\phi_2^{(k)}\sigma_{22}^{(k)},z\tau_{12}^{(k)},\phi_1^{(k)}\tau_{12}^{(k)},\phi_2^{(k)}\tau_{12}^{(k)}\}dz, \quad (17a)$$

$$\boldsymbol{e}_b^T\equiv\{\theta_{1,1},\psi_{1,1},\theta_{2,2},\psi_{2,2},\theta_{1,2}+\theta_{2,1},\psi_{1,2},\psi_{2,1}\}, \quad (17b)$$

and the transverse shear stress resultants and conjugate strain measures are

$$\boldsymbol{Q}_s^T\equiv\{Q_2,Q_2^\phi,Q_1,Q_1^\phi\}=\int_{-h}^{h}\{\tau_{2z}^{(k)},\beta_2^{(k)}\tau_{2z}^{(k)},\tau_{1z}^{(k)},\beta_1^{(k)}\tau_{1z}^{(k)}\}dz,\ \boldsymbol{e}_s^T\equiv\{w_{,2}+\theta_2,\psi_2,w_{,1}+\theta_1,\psi_1\}. \quad (18)$$

The force and moment resultants due to the prescribed tractions have the form

$$\{\bar{N}_{1n},\bar{N}_{2n},\bar{Q}_{zn},\bar{M}_{1n},\bar{M}_{2n},\bar{M}_{1n}^\phi,\bar{M}_{2n}^\phi\}=\int_{-h}^{h}\{\bar{T}_1,\bar{T}_2,\bar{T}_z,z\bar{T}_1,z\bar{T}_2,\phi_1^{(k)}\bar{T}_1,\phi_2^{(k)}\bar{T}_2\}dz. \quad (19)$$

Integrating (15) by parts results in seven equilibrium equations and associated boundary conditions.

The equilibrium equations are

$$\begin{aligned}
&\delta u: && N_{1,1}+N_{12,2}=0, && \delta v: && N_{12,1}+N_{2,2}=0, && \delta w: Q_{1,1}+Q_{2,2}+q=0,\\
&\delta\theta_1: && M_{1,1}+M_{12,2}-Q_1=0, && \delta\theta_2: && M_{12,1}+M_{2,2}-Q_2=0, &&\\
&\delta\psi_1: && M^{\phi}_{1,1}+M^{\phi}_{12,2}-Q^{\phi}_1=0, && \delta\psi_2: && M^{\phi}_{21,1}+M^{\phi}_{2,2}-Q^{\phi}_2=0. &&
\end{aligned} \tag{20}$$

The kinematic and force boundary conditions are given by

$$\begin{aligned}
u=\bar{u} \quad &\text{on } C_u \quad \text{or} \quad N_1n_1+N_{12}n_2=\bar{N}_{1n} \quad \text{on } C_\sigma,\\
v=\bar{v} \quad &\text{on } C_u \quad \text{or} \quad N_{12}n_1+N_2n_2=\bar{N}_{2n} \quad \text{on } C_\sigma,\\
w=\bar{w} \quad &\text{on } C_u \quad \text{or} \quad Q_1n_1+Q_2n_2=\bar{Q}_{zn} \quad \text{on } C_\sigma,\\
\theta_1=\bar{\theta}_1 \quad &\text{on } C_u \quad \text{or} \quad M_1n_1+M_{12}n_2=\bar{M}_{1n} \quad \text{on } C_\sigma,\\
\theta_2=\bar{\theta}_2 \quad &\text{on } C_u \quad \text{or} \quad M_{12}n_1+M_2n_2=\bar{M}_{2n} \quad \text{on } C_\sigma,\\
\psi_1=\bar{\psi}_1 \quad &\text{on } C_u \quad \text{or} \quad M^{\phi}_1n_1+M^{\phi}_{12}n_2=\bar{M}^{\phi}_{1n} \quad \text{on } C_\sigma,\\
\psi_2=\bar{\psi}_2 \quad &\text{on } C_u \quad \text{or} \quad M^{\phi}_{21}n_1+M^{\phi}_2n_2=\bar{M}^{\phi}_{2n} \quad \text{on } C_\sigma,
\end{aligned} \tag{21}$$

where $n_1=\cos(x_1,n)$ and $n_2=\cos(x_2,n)$ are the components (direction cosines) of the unit outward normal vector to the cylindrical plate edges.

The plate constitutive relations are derived by using Equations (2) and (3) with (16)–(18), and integrating over the laminate thickness. The resulting constitutive relations of the new zigzag plate theory are expressed in matrix form as

$$\begin{Bmatrix} \boldsymbol{N}_m \\ \boldsymbol{M}_b \\ \boldsymbol{Q}_s \end{Bmatrix} = \begin{bmatrix} \boldsymbol{A} & \boldsymbol{B} & \boldsymbol{0} \\ \boldsymbol{B}^T & \boldsymbol{D} & \boldsymbol{0} \\ \boldsymbol{0} & \boldsymbol{0} & \boldsymbol{G} \end{bmatrix} \begin{Bmatrix} \boldsymbol{e}_m \\ \boldsymbol{e}_b \\ \boldsymbol{e}_s \end{Bmatrix}. \tag{22}$$

The expressions for the components of the stiffness matrices $\boldsymbol{A}\equiv[A_{ij}]$ $(i,j=1,\ldots,3)$, $\boldsymbol{B}\equiv[B_{ij}]$ $(i=1,\ldots,3,\ j=1,\ldots,7)$, $\boldsymbol{D}\equiv[D_{ij}]$ $(i,j=1,\ldots,7)$, and $\boldsymbol{G}\equiv[G_{ij}]$ $(i,j=1,\ldots,4)$ are given in the Appendix.

Introducing (22) into (20) results in seven second-order partial differential equilibrium equations in terms of seven kinematic variables, giving rise to a 14^{th}-order theory. The equilibrium equations can be solved exactly or approximately depending on the complexity of the material lay-up, boundary conditions, and loading. In addition, because the highest partial derivative appearing in the strain measures in (15) are first-order, computationally efficient C^0-continuous plate finite elements can be developed, thus enabling application of this refined zigzag theory in large-scale analyses of complex aerospace structures.

5. Example problems and results

To determine the accuracy of the present zigzag plate theory, analytic solutions for simply supported and cantilevered rectangular laminates are derived and detailed distributions of the displacements and stresses are examined. The rectangular laminates are defined on the domain $x_1\in[0,a]$, $x_2\in[0,b]$, $z\in[-h,h]$.

Example 1. A simply supported rectangular plate is subjected to the sinusoidal transverse pressure $q(x_1, x_2) = q_0 \sin(\pi x_1/a) \sin(\pi x_2/b)$. The simply supported boundary conditions are obtained from (21). For cross-ply and uniaxial laminates, the kinematic and force boundary conditions along $x_1 \in [0, a]$ are

$$v = w = \theta_2 = \psi_2 = 0, \qquad N_1 = M_1 = M_1^{\phi} = 0, \tag{23a}$$

and along $x_2 \in [0, b]$,

$$u = w = \theta_1 = \psi_1 = 0, \qquad N_2 = M_2 = M_2^{\phi} = 0. \tag{23b}$$

For this set of boundary conditions, the exact solutions are obtained by the trigonometric expansions

$$w = W \sin\frac{\pi x_1}{a} \sin\frac{\pi x_2}{b}, \quad \begin{Bmatrix} u \\ \theta_1 \\ \psi_1 \end{Bmatrix} = \begin{Bmatrix} U \\ \Theta_1 \\ \Psi_1 \end{Bmatrix} \cos\frac{\pi x_1}{a} \sin\frac{\pi x_2}{b}, \quad \begin{Bmatrix} v \\ \theta_2 \\ \psi_2 \end{Bmatrix} = \begin{Bmatrix} V \\ \Theta_2 \\ \Psi_2 \end{Bmatrix} \sin\frac{\pi x_1}{a} \cos\frac{\pi x_2}{b}, \tag{24}$$

where $\{U, V, W, \Theta_1, \Theta_2, \Psi_1, \Psi_2\}$ are the unknown amplitudes of the kinematic variables that are determined from satisfaction of the equilibrium equations.

For antisymmetric angle-ply laminates, the kinematic and force boundary conditions along $x_1 \in [0, a]$ are

$$u = w = \theta_2 = \psi_2 = 0, \qquad N_{12} = M_1 = M_1^{\phi} = 0, \tag{25a}$$

and along $x_2 \in [0, b]$

$$v = w = \theta_1 = \psi_1 = 0, \qquad N_{12} = M_2 = M_2^{\phi} = 0. \tag{25b}$$

Thus, the trigonometric expansions that satisfy (25a) and (25b) exactly differ from those in (24) only for the u and v variables, and they are given by

$$u = U \sin\frac{\pi x_1}{a} \cos\frac{\pi x_2}{b}, \qquad v = V \cos\frac{\pi x_1}{a} \sin\frac{\pi x_2}{b}. \tag{26}$$

Example 2. A cantilevered rectangular plate is clamped along a single edge ($x_1 = 0$), free along the other edges, and subjected to the uniform transverse pressure $q(x_1, x_2) = q_0$. The clamped boundary conditions along $x_1 = 0$ are

$$u = v = w = \theta_1 = \theta_2 = \psi_1 = \psi_2 = 0. \tag{27a}$$

Unlike the previous zigzag theories where the clamped boundary conditions result in erroneous solutions for transverse shear stresses and forces that vanish along the clamped edges, the solutions of the present theory do not possess such anomalies. For instance, along the clamped boundary at $x_1 = 0$, the kinematic constraints in (27a), with the use of (2e), (13b), and (18), give rise to the following transverse shear stresses, $\tau_{1z}^{(k)}(0, x_2, z)$, and force, $Q_1(0, x_2)$:

$$\begin{Bmatrix} \tau_{1z}^{(k)} \\ Q_1 \end{Bmatrix}_{(x_1=0)} = \begin{Bmatrix} Q_{11}^{(k)} \\ \int_{-h}^{h} Q_{11}^{(k)} dz \end{Bmatrix} w_{,1}(0, x_2), \tag{27b}$$

where, in general, $w_{,1}(0, x_2) \neq 0$.

The traction-free boundary conditions along the edge $x_1 = a$ are

$$N_1 = N_{12} = M_1 = M_{12} = Q_1 = M_1^{\phi} = M_{12}^{\phi} = 0, \tag{28a}$$

	Lamina material	$E_1^{(k)}, E_2^{(k)}, E_3^{(k)}$	$\nu_{12}^{(k)}, \nu_{13}^{(k)}, \nu_{23}^{(k)}$	$G_{12}^{(k)}, G_{13}^{(k)}, G_{23}^{(k)}$
C	Carbon-epoxy unidirectional composite	1.579×10^{2} 9.584 9.584	0.32 0.32 0.49	5.930 5.930 3.227
H	Titanium honeycomb core	1.915×10^{-1} 1.915×10^{-1} 1.915	0.658×10^{-2} 0.643×10^{-6} 0.643×10^{-6}	4.227×10^{-8} 3.651×10^{-1} 1.248
P	PVC core	$E^{(k)} = 1.040\times10^{-1}$	$\nu^{(k)} = 0.3$	
T	Titanium	$E^{(k)} = 1.041\times10^{2}$	$\nu^{(k)} = 0.31$	

Table 1. Mechanical properties of orthotropic materials (C and H) and isotropic material (P and T). The Young's modulus E and shear modulus G are expressed in GPa.

Laminate		Normalized lamina thickness, $h^{(k)}/h$	Lamina materials	Lamina orientation [°]
A	Cross-ply composite	(0.5/0.5)	(C/C)	(0/90)
B	Uniaxial sandwich	(0.1/0.8/0.1)	(C/P/C)	(0/0/0)
F	Uniaxial sandwich	(0.1/0.8/0.1)	(T/H/T)	(0/0/0)
G	Angle-ply sandwich	(0.05/0.05/0.8/0.05/0.05)	(C/C/P/C/C)	(30/−45/0/45/−30)

Table 2. Laminate stacking sequences (lamina sequence is in the positive z direction).

and along the edge $x_1 \in [0, b]$

$$N_{12} = N_2 = M_{12} = M_2 = Q_2 = M_{12}^{\phi} = M_2^{\phi} = 0. \tag{28b}$$

For both example problems, various laminates are considered with the emphasis on relatively thick laminated composite and sandwich plates having span-to-thickness ratio $a/2h = b/2h = 5$. The mechanical material properties are listed in Table 1, and Table 2 summarizes the stacking sequences of the laminates.

The example problems include: a two-layer, cross-ply carbon-epoxy laminate, labeled laminate A; a three-layer sandwich laminate, laminate B, having uniaxial carbon-epoxy face sheets and a thick, closed-cell polyvinyl chloride (PVC) core, where PVC is represented as an isotropic material; a sandwich laminate with two-layered titanium face sheets and a thick titanium honeycomb core, laminate F; and a five-layer, angle-ply sandwich laminate with carbon-epoxy face sheets and a thick PVC core, laminate G. Additional sandwich laminates that involve very thin face sheets have been studied in [Tessler et al. 2009].

For comparison purposes, several analytic and finite element solutions were also obtained for the corresponding boundary-value problems using 3D elasticity theory [Pagano 1969; Noor and Burton 1990], FSDT, the theory of Di Sciuva [1984a], and MSC/MD-NASTRAN finite element code [MSC 2006]. Note that application of FSDT generally requires the use of shear correction factors. For laminated composites,

lamination-dependent shear correction factors have been shown to provide relatively accurate deflection predictions (for examples, refer to [Vlachoutsis 1992; Reddy and Vijayakumar 1995]). Yet, such shear corrections fail to furnish substantial improvements for the normal strain and stress predictions. Presently, to establish a common framework reference for FSDT, a shear correction factor $k^2 = \frac{5}{6}$, appropriate for homogeneous plates, was used throughout.

For the simply supported cross-ply and uniaxial laminates, the exact solutions for the FSDT and Di Sciuva zigzag theory were obtained using the trigonometric functions in (24) (excluding those functions for ψ_α ($\alpha = 1, 2$) which do not appear in FSDT). For the angle-ply antisymmetric laminates, Di Sciuva theory permits only approximate solutions to be determined. Presently, the Rayleigh–Ritz method was employed, where the kinematic variables were approximated with suitable Gram–Schmidt polynomials [Arfken 1985] that satisfy the kinematic boundary conditions, (26), exactly (refer to [Tessler et al. 2009] for the particular expressions of the Gram–Schmidt polynomials used). Furthermore, for the simply supported cross-ply and angle-ply antisymmetric laminates, exact 3D elasticity solutions were obtained using the solution procedures developed by Pagano [1969] and Noor and Burton [1990].

For the cantilevered laminates, approximate solutions corresponding to Di Sciuva and refined (present) zigzag theories were developed using the Rayleigh–Ritz method. Here the displacement approximations are based on the Gram–Schmidt polynomials, using seven functions along the x_1 axis and five along the x_2 axis (for details, refer to [Tessler et al. 2009]). Furthermore, for the cantilevered plate (laminate B), a high-fidelity 3D finite element solution was obtained by using MSC/MD-NASTRAN. The model is regularly discretized and is comprised of three elements through the thickness for each face sheet, six elements through the core thickness, and sixty subdivisions along each span direction, with a total of 43,200 HEXA20, linear-strain elements.

The numerical and graphical results that follow are labeled as:

- 3D Elasticity (3D elasticity solutions using procedures developed by Pagano [1969] for cross-ply laminates and by Noor and Burton [1990] for angle-ply antisymmetric laminates).
- FSDT (first-order shear deformation theory, $k^2 = \frac{5}{6}$).
- Zigzag (D) [Di Sciuva 1984a].
- Zigzag (R) (present, refined zigzag theory).
- 3D FEM (3D FEM solution using MSC/MD-NASTRAN [MSC 2006]).
- Zigzag (R-E) (transverse shear stresses obtained by way of integrating 3D elasticity equilibrium equations, using the normal and in-plane shear stresses derived from the refined zigzag theory).

Comparisons of the maximum deflection and maximum top-surface displacement are presented for the simply supported square laminates ($a/1h = b/2h = 5$) in Tables 3 and 4. These results demonstrate that both zigzag theories predict accurate plate displacements as compared to the 3D elasticity solution, with the refined theory achieving slightly more accurate predictions. The laminate G case is somewhat pathological for Zigzag (D), because the solution in this case is only approximate and has not converged. The deflections predicted by FSDT are generally overly stiff; however, they are expected to improve substantially with the use of lamination-dependent shear correction factors. In Table 5, the range of applicability of the various theories is examined by comparing the maximum (central) plate deflection for a simply supported sandwich laminate B, where the solutions correspond to a span-to-thickness

Laminate	Normalization factor $(10^2 D_{11} q_0 a^4)$	3D elasticity	FSDT	Zigzag (D)	Zigzag (R)
A	8.147×10^{-2}	1.228	1.278	1.170	1.219
B	7.502×10^{-2}	29.761	2.731	29.769	29.785
F	5.444×10^{-2}	1.331	0.389	1.332	1.333
G	3.551×10^{-2}	14.124	1.055	12.734	14.105

Table 3. Normalized maximum (central) deflection, $\bar{w} = (10^2 D_{11}/q_0 a^4) w(a/2, b/2)$, for simply supported laminates subjected to sinusoidal transverse pressure loading.

Laminate	Normalization factor $(10^3 D_{11}/q_o a^4)$	3D Elasticity	FSDT	Zigzag (D)	Zigzag (R)
A	8.147×10^{-1}	4.233	4.152	3.855	4.251
B	7.502×10^{-1}	9.977	2.156	9.945	9.897
F	5.444×10^{-1}	0.643	0.796	0.646	0.649
G	3.551×10^{-1}	3.908	0.704	1.295	3.845

Table 4. Normalized maximum (top surface) displacement along the x_1 axis $\bar{u}_1 = (10^3 D_{11}/q_o a^4) \times u_1^{(N)}(a, b/2, h)$ of simply supported laminates subjected to sinusoidal transverse pressure loading.

Span-to-thickness ratio	Normalization factor $(10^2 D_{11}/q_0 a^4)$	3D Elasticity	FSDT	Zigzag (D)	Zigzag (R)
4	1.832×10^{-1}	42.420	3.739	42.124	42.189
10	4.668×10^{-3}	9.734	1.321	9.738	9.739
20	2.931×10^{-4}	3.487	0.948	3.489	3.490
50	7.502×10^{-6}	1.305	0.841	1.305	1.305
100	4.688×10^{-7}	0.945	0.826	0.945	0.945
200	2.931×10^{-8}	0.852	0.822	0.852	0.852

Table 5. Normalized maximum (central) deflection, $\bar{w} = (10^2 D_{11}/q_0 a^4) w(a/2, b/2)$, for simply supported laminate B subjected to sinusoidal transverse pressure loading and corresponding to various span-to-thickness ratios.

ratio in the range 4–200. These results are also plotted in Figure 3. It is observed that both zigzag theories predict accurate deflections for all span-to-thickness ratios examined, whereas FSDT is overly stiff, especially in the thick regime, as expected. Even for a relatively thin laminate B ($a/2h = 50$), FSDT underestimates the maximum deflection by about 36%, which means that a much more significant shear correction factor would be required for FSDT for this type of laminate.

For the simply supported laminates, normalized through-the-thickness distributions for the in-plane displacement, $\bar{u}_1 = (10^4 D_{11}/q_0 a^4) u_1^{(k)}(0, a/2, z)$, the normal stress, $\bar{\sigma}_{11} \equiv (4h^2/q_0 a^2) \times \sigma_{11}^{(k)}(a/2, a/2, z)$, and the transverse shear stress, $\bar{\tau}_{1z} \equiv (2h/q_0 a) \tau_{1z}^{(k)}(0, a/2, z)$, are depicted in Figures 4–11.

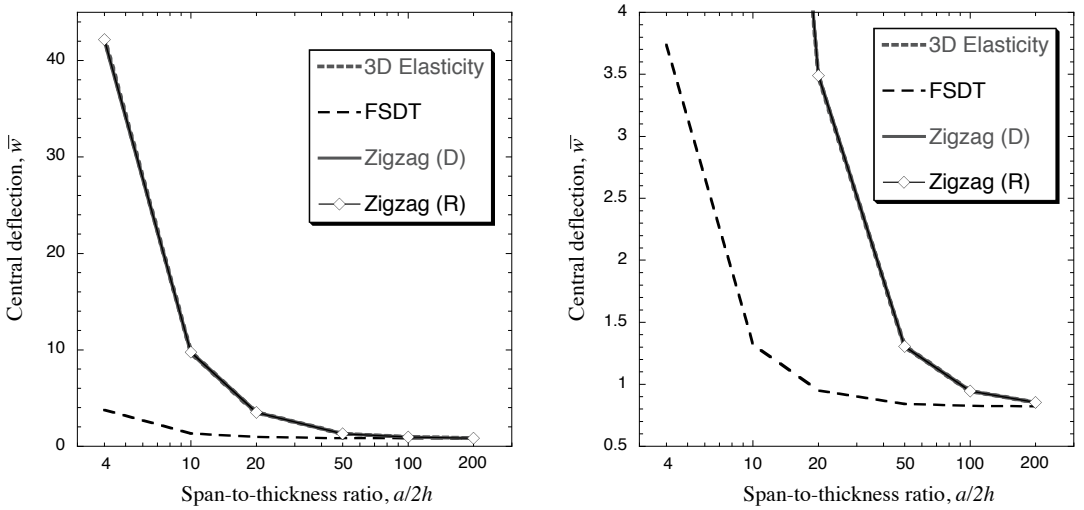

Figure 3. Normalized central deflection versus span-to-thickness ratio for simply supported laminate B subjected to sinusoidal transverse pressure (left); zoomed view (right).

For laminate A — an asymmetric cross-ply carbon-epoxy composite — the values of $\bar{u}_1$ and $\bar{\sigma}_{11}$ are accurately modeled by FSDT and the two zigzag theories (Figures 4 and 5), with Zigzag (D) producing slightly underestimated displacement near the top surface. The major differences in results for this laminate correspond to the $\bar{\tau}_{1z}$ distribution (Figure 5), where both FSDT and Zigzag (R) produce piecewise constant stresses, whereas Zigzag (D) gives a uniform distribution for $\bar{\tau}_{1z}$ significantly less accurate than the predictions of the other two theories. In addition, Zigzag (R) theory provides a more accurate evaluation of the average transverse shear stress within each lamina than does FSDT. Also, the $\bar{\tau}_{1z}$ stress, obtained by an equilibrium-based method, Zigzag (R-E), is best correlated with the 3D elasticity solution.

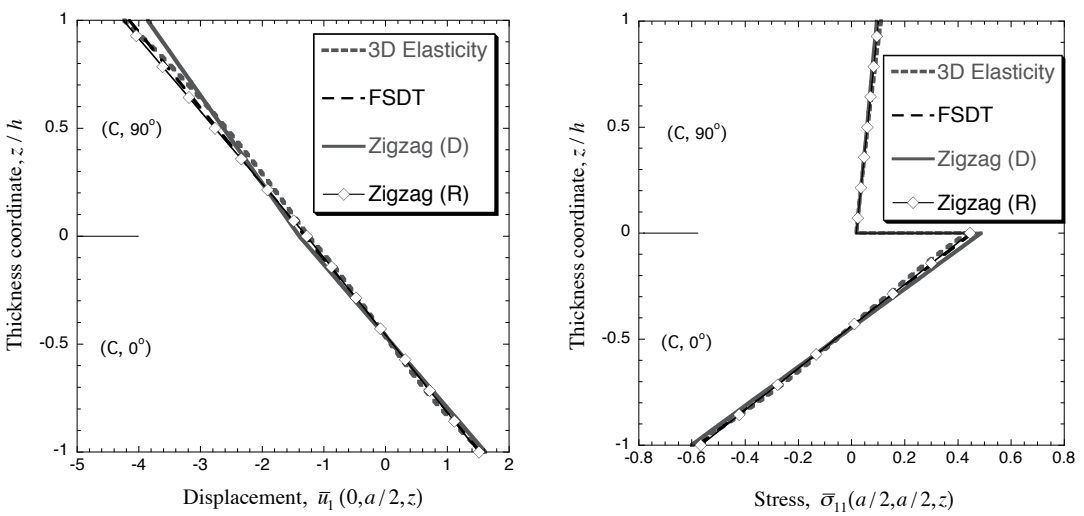

Figure 4. Normalized in-plane displacement (left) and normal stress (right) for simply supported laminate A subjected to sinusoidal transverse pressure.

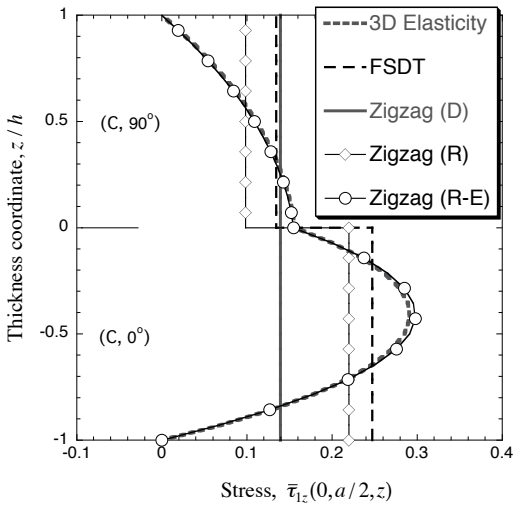

Figure 5. Normalized transverse shear stress for simply supported laminate A subjected to sinusoidal transverse pressure.

The $\bar{u}_1$, $\bar{\sigma}_{11}$, and $\bar{\tau}_{1z}$ results for sandwich panel B, which has constant-thickness carbon-epoxy face sheets and a PVC core, are provided in Figures 6 and 7. For laminate B, the top and bottom-surface values of the $\bar{u}_1$ displacement are significantly underestimated by FSDT which is only capable of a linear (average) distribution. Also, as shown in Figure 7, left, FSDT grossly underestimates the normal stress $\bar{\sigma}_{11}$ on the bounding surfaces where the greatest compression and tension occur. By contrast, Zigzag (R) yields accurate solutions of all response quantities examined. When the transverse shear stresses are evaluated from the constitutive relations, the theory provides the correct average values in the face sheets and in the core. Moreover, the equilibrium-based method, Zigzag (R-E), furnishes superior transverse shear stresses that are virtually indistinguishable from those of 3D elasticity. An

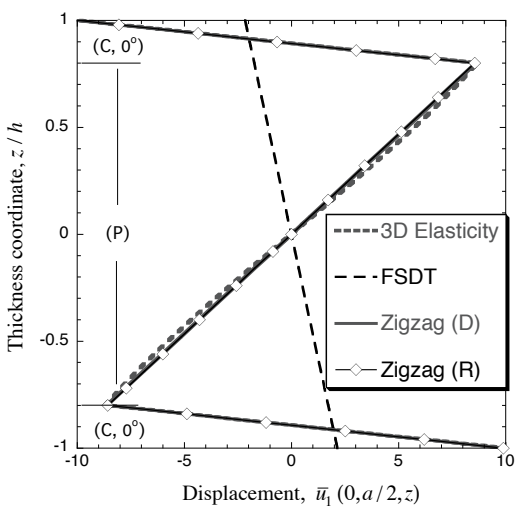

Figure 6. Normalized in-plane displacement for simply supported laminate B subjected to sinusoidal transverse pressure.

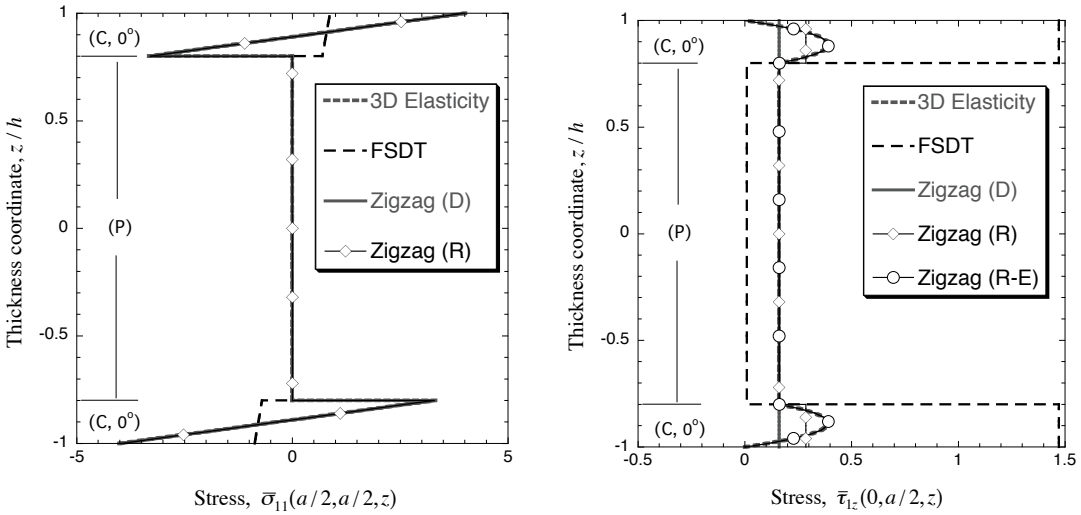

Figure 7. Normalized normal stress (left) and transverse shear stress (right) for simply supported laminate B subjected to sinusoidal transverse pressure.

additional study evaluating the effect of face-sheet thinness in sandwich laminates on the distribution of displacements and stresses through the thickness can be found in [Tessler et al. 2009].

The displacement and stress results for laminate F — a cross-ply sandwich with a lower degree of anisotropy than laminate B — are depicted in Figures 8 and 9. For this laminate, the zigzag effect of the in-plane displacement is somewhat less pronounced than for laminate B. As in the previous example, Zigzag (R) yields highly accurate predictions of all response quantities. It is seen that FSDT provides overestimated values for the in-plane displacement on the bounding surfaces. Also, it is evident from Figure 9, left, that the integral of the shear stress over the thickness computed using the Zigzag (D) transverse shear stress would result in a significantly greater value than the exact shear force.

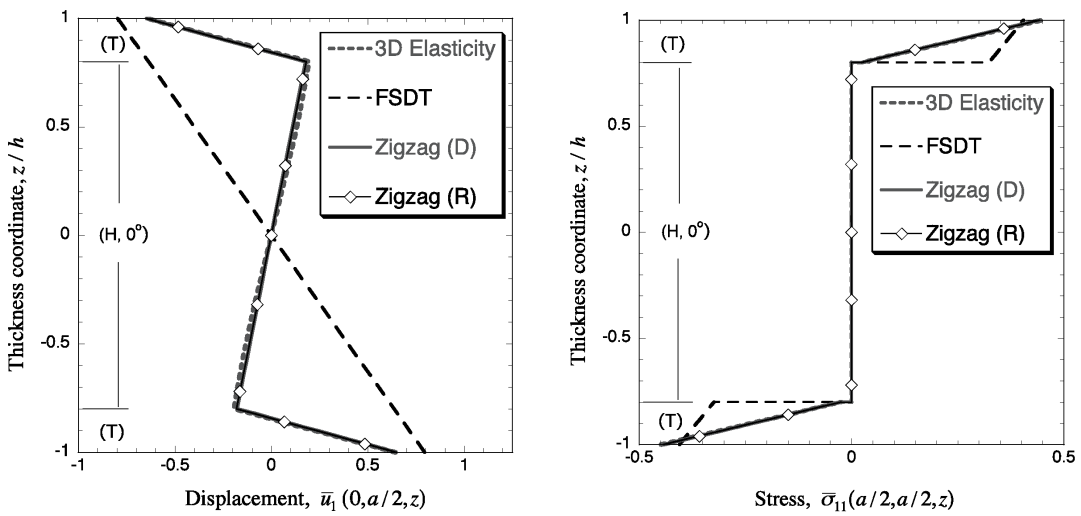

Figure 8. Normalized in-plane displacement (left) and normal stress (right) for simply supported laminate F subjected to sinusoidal transverse pressure.

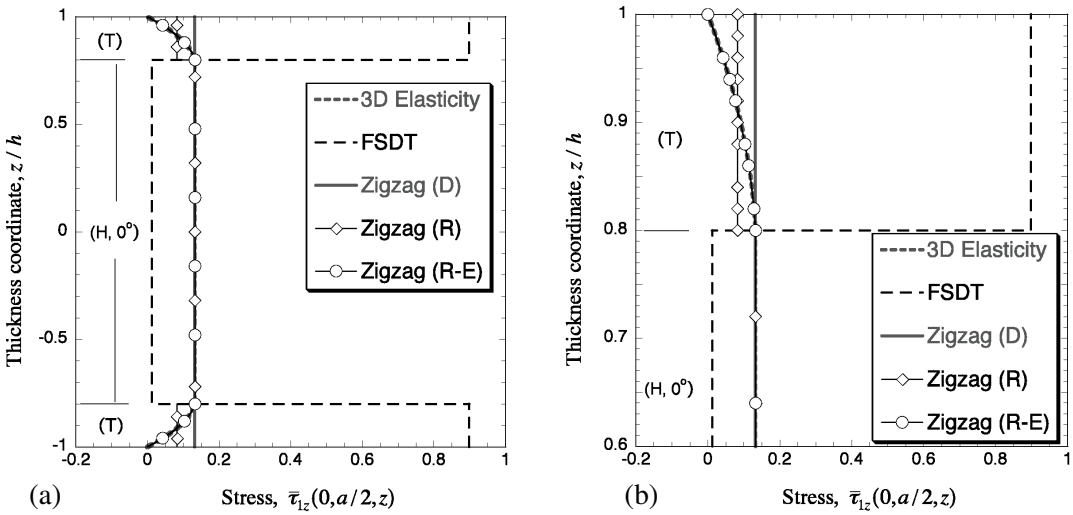

Figure 9. Left: Normalized transverse shear stress for simply supported laminate F subjected to sinusoidal transverse pressure. Right: detail near the top layer.

Figures 10 and 11 demonstrate the results for laminate G — an angle-ply antisymmetric sandwich plate with multilayered face sheets. This is a highly challenging test case for any lamination theory. For this lamination, only an approximate solution can be obtained for Zigzag (D), requiring a large number of suitable shape functions to achieve a converged solution. Using the Rayleigh–Ritz method with the Gram–Schmidt polynomials approximating the kinematic variables (see the details in [Tessler et al. 2009]), a relatively inaccurate solution was obtained. Consequently, the Zigzag (D) results for the in-plane displacement and normal stress (Figure 10) are somewhat erroneous. On the other hand, Zigzag (R) enables an exact solution to be obtained for this problem, once again yielding highly accurate predictions of the

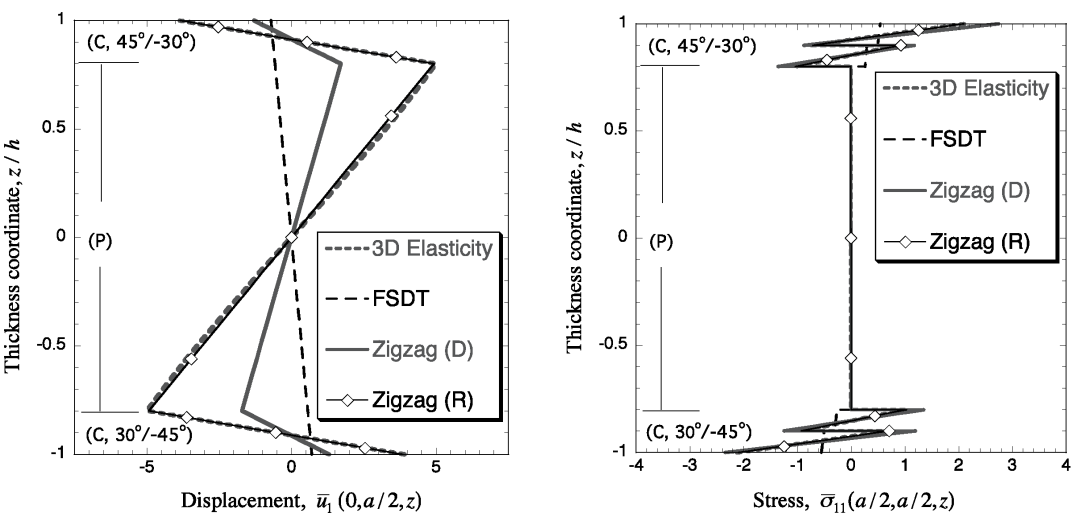

Figure 10. Normalized in-plane displacement (left) and normal stress (right) for simply supported laminate G subjected to sinusoidal transverse pressure.

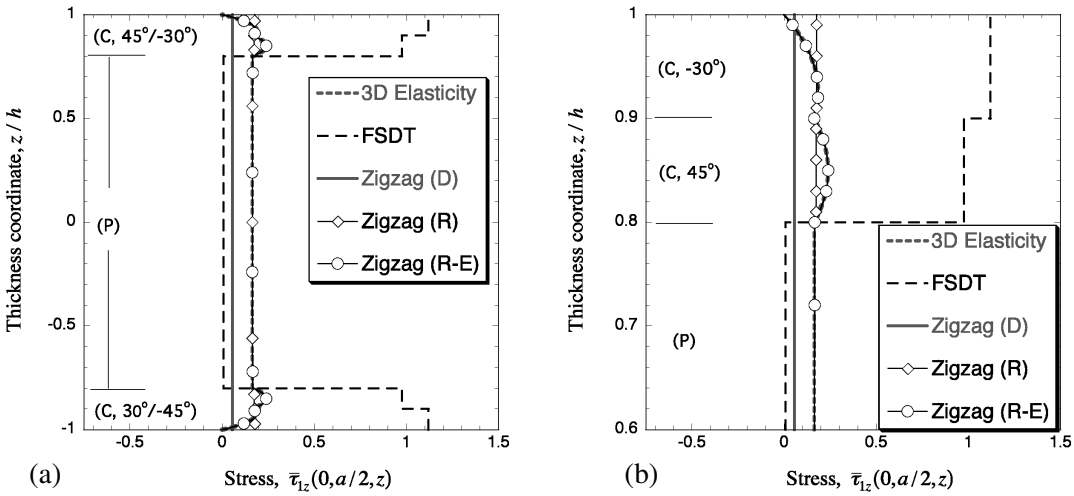

Figure 11. (a) Normalized transverse shear stress for simply supported laminate G subjected to sinusoidal transverse pressure; (b) near the top layer.

response quantities. As in the previous examples, FSDT models the in-plane displacement response only in an average sense (a linear distribution through the thickness), leading to a significant underestimation (a nonconservative prediction) of the normal stress in the face sheets. Figure 11 demonstrates the highly accurate transverse shear stress obtained by the present theory, Zigzag (R), as compared to the other plate-theory solutions.

To examine the effect of clamped boundary conditions, a square cantilevered laminate B under a uniform transverse pressure was examined. Table 6 summarizes the maximum deflection calculated using the three different theories and a 3D finite element solution that serves as a reference. The FSDT deflection is underestimated by an order of magnitude. The two zigzag theories give accurate results, with Zigzag (R) producing a somewhat superior deflection prediction.

For the cantilevered sandwich laminate B, normalized through-the-thickness distributions of the in-plane displacement, $\bar{u}_1 = (10^4 D_{11}/q_o a^4) u_1^{(k)}(a, a/2, z)$, the normal stress,

$$\bar{\sigma}_{11} = ((2h)^2/q_0 a^2) \times \sigma_{11}^{(k)}(a/5, a/2, z),$$

and the transverse shear stress, $\bar{\tau}_{1z} = (2h/q_0 a) \times \tau_{1z}^{(k)}(a/5, a/2, z)$, are provided in Figures 12 and 13. The stresses were computed near the clamped edge ($x_1 = a/5$, $x_2 = a/2$) to allow for proper comparisons with the accurate stresses obtained from the 3D FEM analysis. For this problem, both zigzag theories produce accurate results; however, application of Zigzag (R) resulted in superior predictions of transverse

Normalization factor $(10^2 D_{11}/q_0 a^4)$	3D FEM	FSDT	Zigzag (D)	Zigzag (R)
7.502×10^{-2}	246.778	25.351	244.077	245.615

Table 6. Normalized maximum (free-edge) deflection, $\bar{w} = (10^2 D_{11}/q_0 a^4) w(a/2, b/2)$, for cantilevered laminate B subjected to uniform transverse pressure loading.

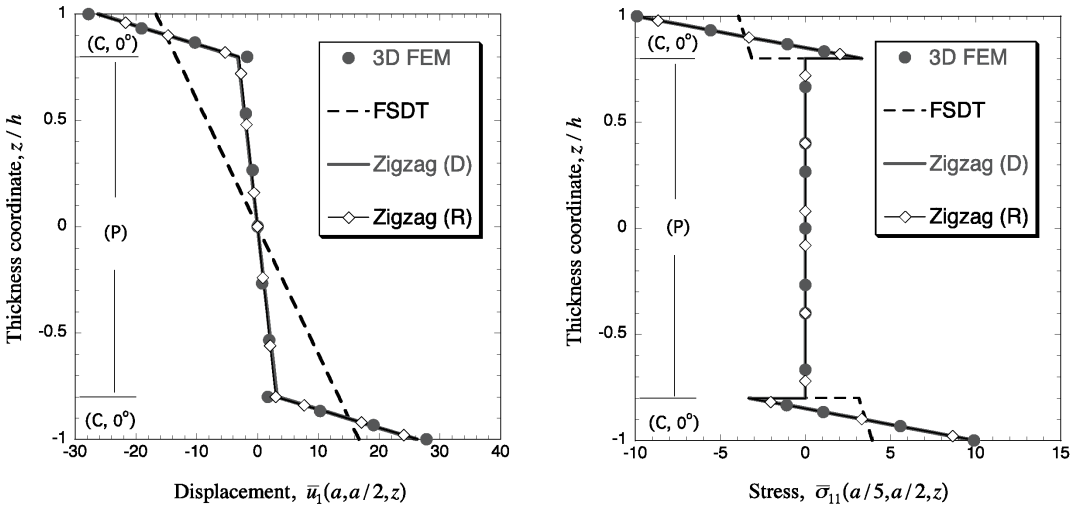

Figure 12. Normalized in-plane displacement (left) and normal stress (right) for cantilevered laminate B subjected to uniform transverse pressure.

shear stresses. Finally, the normalized transverse shear force,

$$\bar{Q}_1 = \frac{1}{q_0 a}\int_{-h}^{h} \tau_{1z}^{(k)} dz,$$

evaluated at $x_2 = a/2$, is plotted versus the normalized axial coordinate, x_1/a, as shown in Figure 14. For this problem, both FSDT and Zigzag (R) predict the correct linear distribution, yielding a maximum value at the clamped edge and vanishing at the free edge. This contrasts with an erroneous Zigzag (D) solution that varies in a nonlinear manner across the span and which vanishes at the clamped edge.

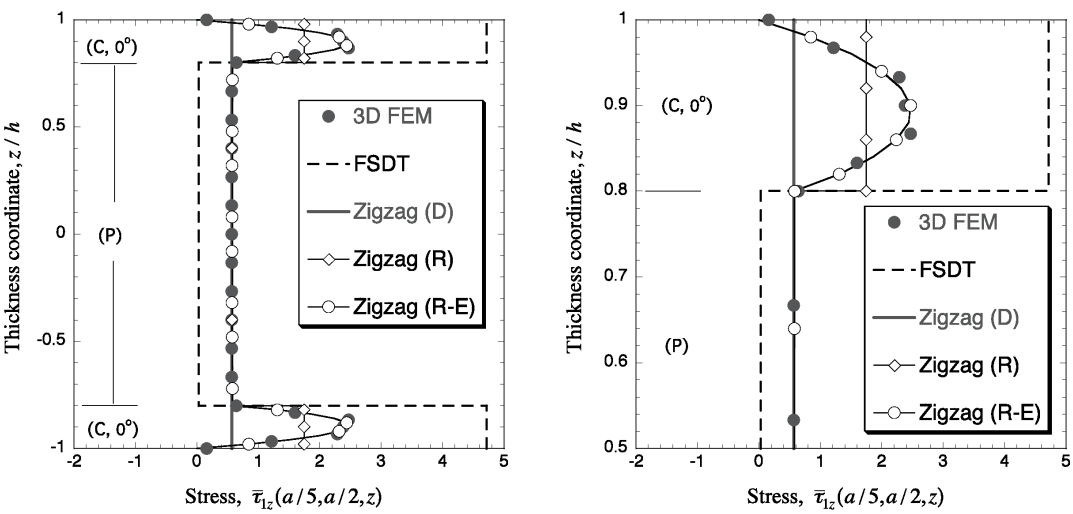

Figure 13. Normalized transverse shear stress for cantilevered laminate B subjected to uniform transverse pressure.

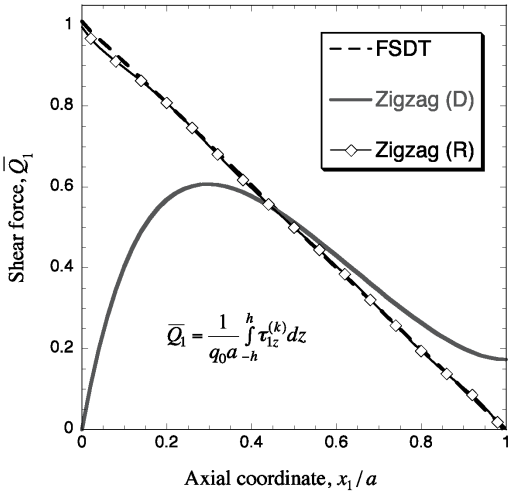

Figure 14. Normalized transverse shear force along centerline of cantilevered laminate B subjected to uniform transverse pressure.

6. Conclusions

A variationally consistent and robust refined zigzag plate theory has been discussed and its predictive capability examined on laminated-composite and sandwich plates that exhibit a high degree of transverse shear flexibility, anisotropy, and heterogeneity. In this refined theory, a first-order shear deformation theory is used as a baseline for the kinematic assumptions with a set of novel piecewise-continuous zigzag displacements added to the in-plane displacement components. The resulting kinematic field is independent of the number of material layers, and the zigzag displacements are defined by requiring only partial lamina-interface continuity requirements of transverse shear stresses. The force equilibrium equations, boundary conditions, and strain-displacement relations are completely consistent with respect to the virtual work principle, and transverse shear correction factors are not required. The refined zigzag theory is better suited for engineering practice than previous similar theories because of its relative simplicity and its ability to model accurately the transverse shear and in-plane deformations of the individual laminae in a physically realistic manner. Unlike other similar theories, meaningful in-plane and transverse shear stresses are obtained directly from the constitutive equations, in a theoretically consistent manner. The new theory is devoid of a major shortcoming of other similar theories; namely, the new theory enables accurate modeling of clamped boundary conditions.

Results for several example problems were presented, highlighting the superior predictive capability attainable with the present theory and its ability to model correctly clamped boundary conditions. The critical quantitative assessment of the new theory, including analyses of highly heterogeneous sandwich laminates in bending, revealed that this refined zigzag theory is more accurate than previous similar ones.

An additional and important benefit is that the new zigzag theory lends itself well to finite element approximations. In particular, the theory is perfectly suited for the development of computationally efficient, C^0-continuous finite elements. Because of a wide applicability range that includes moderately thick laminated-composite and sandwich structures, such finite elements would be highly desirable for large-scale analyses and design studies of high-performance aerospace vehicles.

Appendix: Plate stiffness coefficients

The stiffness coefficients in (22) are computed from the following expressions using the constitutive coefficients given in (3):

- Matrix $\boldsymbol{A} \equiv \left[A_{ij}\right]$ $(i, j = 1, \ldots, 3)$, symmetric, 3×3:

$$\boldsymbol{A} \equiv \int_{-h}^{h} \boldsymbol{C}\, dz.$$

- Matrix $\boldsymbol{B} \equiv \left[B_{ij}\right]$ $(i = 1, \ldots, 3;\ j = 1, \ldots, 7)$, nonsymmetric, 3×7:

$$\boldsymbol{B} \equiv \int_{-h}^{h} \boldsymbol{C}\, \boldsymbol{B}_{\phi}\, dz.$$

- Matrix $\boldsymbol{D} \equiv \left[D_{ij}\right]$ $(i, j = 1, \ldots, 7)$, symmetric, 7×7:

$$\boldsymbol{D} \equiv \int_{-h}^{h} \boldsymbol{B}_{\phi}^{T}\, \boldsymbol{C}\, \boldsymbol{B}_{\phi}\, dz.$$

- Matrix $\boldsymbol{G} \equiv \left[G_{ij}\right]$ $(i, j = 1, \ldots, 4)$, symmetric, 4×4:

$$\boldsymbol{G} \equiv \int_{-h}^{h} \boldsymbol{B}_{\beta}^{T}\, \boldsymbol{Q}\, \boldsymbol{B}_{\beta}\, dz,$$

where

$$\boldsymbol{C} \equiv \begin{bmatrix} C_{11} & C_{12} & C_{16} \\ C_{12} & C_{22} & C_{26} \\ C_{16} & C_{26} & C_{66} \end{bmatrix}^{(k)}, \qquad \boldsymbol{B}_{\phi} \equiv \begin{bmatrix} z & \phi_1^{(k)} & 0 & 0 & 0 & 0 & 0 \\ 0 & 0 & z & \phi_2^{(k)} & 0 & 0 & 0 \\ 0 & 0 & 0 & 0 & z & \phi_1^{(k)} & \phi_2^{(k)} \end{bmatrix},$$

$$\boldsymbol{Q} \equiv \begin{bmatrix} Q_{22} & Q_{12} \\ Q_{12} & Q_{11} \end{bmatrix}^{(k)}, \qquad \boldsymbol{B}_{\beta} \equiv \begin{bmatrix} 1 & \beta_2^{(k)} & 0 & 0 \\ 0 & 0 & 1 & \beta_1^{(k)} \end{bmatrix},$$

List of symbols

a, b	Lateral dimensions of a rectangular plate.
$2h$	Total plate (laminate) thickness.
$2h^{(k)}$	Thickness of the k-th material layer (lamina).
(x_1, x_2)	Reference plate-coordinate axes positioned in the middle plane of the laminate.
z	Thickness coordinate axis.
N	Number of material layers (laminae) through the laminate thickness.
S_m	Reference middle plane of the laminate.
S_u, S_σ	Parts of the cylindrical edge surface of the laminate where displacements and tractions are prescribed, respectively.
C^0	Denotes a continuous function whose first-order derivative is discontinuous.
C_u, C_σ	Intersections of the cylindrical edge surfaces (S_u, S_σ) with the middle surface S_m where displacements and traction resultants are prescribed, respectively.
$\boldsymbol{s}$, $\boldsymbol{n}$	Unit outward tangential and normal vectors to the midplane boundary: see Figure 1.

q Applied transverse pressure [force/length^2]: see Figure 1.

$\bar{T}_1, \bar{T}_2, \bar{T}_z$ Prescribed in-plane and transverse shear tractions: see (14).

$u_1^{(k)}, u_2^{(k)}, u_z$ In-plane and transverse components of the displacement vector in the k-th material layer: see (1).

$u, v, w,$
$\theta_1, \theta_2, \psi_1, \psi_2$ Kinematic variables of the refined zigzag plate theory: see (1).

N_1, N_2, N_{12} Membrane stress resultants: see (16).

M_1, M_2, M_{12} Bending and twisting stress resultants: see (17).

M_1^{ϕ}, M_2^{ϕ} Bending stress resultants due to zigzag kinematics: see (17).

$M_{12}^{\phi}, M_{21}^{\phi}$ Twisting stress resultants due to zigzag kinematics: see (17).

Q_1, Q_2 Transverse shear stress resultants: see (18).

Q_1^{ϕ}, Q_2^{ϕ} Transverse shear stress resultants due to zigzag kinematics: see (18).

$\phi_1^{(k)}, \phi_2^{(k)}$ Zigzag functions: see (1).

$\beta_1^{(k)}, \beta_2^{(k)}$ Derivatives of zigzag functions with respect to the thickness coordinate: see (2b).

$\xi^{(k)}$ Dimensionless thickness coordinates of the k-th layer (lamina): see (5).

$z_{(k)}$ Thickness coordinate of the interface between the k-th and $(k+1)$-st layers: see Figure 1.

$u_{(k)}, v_{(k)}$ Dimensionless in-plane displacements along the interface between the k-th and $(k+1)$-th layers: see Figure 2.

$\varepsilon_{11}^{(k)}, \varepsilon_{22}^{(k)}$ In-plane in the k-th layer: see (3).

$\gamma_{12}^{(k)}, \gamma_{2z}^{(k)}, \gamma_{1z}^{(k)}$ Transverse strains in the k-th layer: see (3).

γ_1, γ_2 Average shear strains: see (2a) and (9).

η_1, η_2 Transverse shear strain measures: see (11).

ψ_1, ψ_2 Zigzag amplitude functions: see (1).

$\sigma_{11}^{(k)}, \sigma_{22}^{(k)}$ Normal stresses in the k-th layer: see (3).

$\tau_{12}^{(k)}, \tau_{2z}^{(k)}, \tau_{1z}^{(k)}$ Transverse stresses in the k-th layer: see (3).

$E_i^{(k)}$ Young's moduli of the k-th layer: see Table 1.

$G_{ij}^{(k)}$ Shear moduli of the k-th layer: see Table 1.

$\nu_{ij}^{(k)}$ Poisson's ratios of the k-th layer: see Table 1.

$A_{ij}, B_{ij},$
D_{ij}, G_{ij} Constitutive stiffness coefficients: see (22).

$C_{ij}^{(k)}, Q_{pq}^{(k)}$ In-plane and transverse shear elastic stiffness coefficients for the k-th layer: see (3).

G_1, G_2 Weighted-average, laminate-dependent transverse shear constants: see (12b).

δ Variational operator: see (9).

$\frac{\partial}{\partial x_\alpha}$ or $(\cdot)_{,\alpha}$ Partial differentiation.

k^2 Shear correction factor for FSDT.

Acknowledgments

The authors thank Dr. Scott Burton of Avago Technologies for providing the research code that was used to compute the 3D elasticity solutions for simply supported laminates. The first author is also very thankful to Prof. James G. Simmonds of the University of Virginia for a number of valuable technical discussions during the course of this research.

Di Sciuva and Gherlone acknowledge the Piedmont Region for the financial support of this research in the framework of Contract E57 "Multidisciplinary optimization of aeromechanical structural systems." The third author also gratefully acknowledges Politecnico di Torino for supporting his research in the framework of the Young Researchers Program (2007).

Finally, the authors thank the editorial committee of the Structural Mechanics and Concepts Branch of the NASA Langley Research Center, chaired by Dr. Michael P. Nemeth, for many valuable suggestions.

References

[Ambartsumyan 1961] S. A. Ambartsumyan, Теория анизотропных оболочек, State Publishing House for Physical and Mathematical Literature, Moscow, 1961. Translated in "Theory of anisotropic shells", NASA Technical translation TT F-118, 1964, http://tinyurl.com/NASA-TT-F-118.

[Arfken 1985] G. Arfken, *Mathematical methods for physicists*, 3rd ed., Academic Press, Orlando, FL, 1985.

[Averill 1994] R. C. Averill, "Static and dynamic response of moderately thick laminated beams with damage", *Compos. Eng.* **4**:4 (1994), 381–395.

[Averill and Yip 1996] R. C. Averill and Y. C. Yip, "Development of simple, robust finite elements based on refined theories for thick laminated beams", *Comput. Struct.* **59**:3 (1996), 529–546.

[Barut et al. 2002] A. Barut, E. Madenci, T. Anderson, and A. Tessler, "Equivalent single layer theory for a complete stress field in sandwich panels under arbitrary distributed loading", *Compos. Struct.* **58**:4 (2002), 483–495.

[Cho and Parmerter 1992] M. Cho and R. R. Parmerter, "An efficient higher-order plate theory for laminated composites", *Compos. Struct.* **20**:2 (1992), 113–123.

[Cho and Parmerter 1993] M. Cho and R. R. Parmerter, "Efficient higher order composite plate theory for general lamination configurations", *AIAA J.* **31**:7 (1993), 1299–1306.

[Cook and Tessler 1998] G. M. Cook and A. Tessler, "A {3, 2}-order bending theory for laminated composite and sandwich beams", *Compos. B Eng.* **29**:5 (1998), 565–576.

[Di Sciuva 1984a] M. Di Sciuva, "A refinement of the transverse shear deformation theory for multilayered orthotropic plates", in *Atti del VII Congresso Nazionale AIDAA* (Naples, 1983), edited by A. Marchese, ESA, Rome, 1984. Also in *Aerotecnica Missili e Spazio* **63** (1984), 84–92.

[Di Sciuva 1984b] M. Di Sciuva, "A refined transverse shear deformation theory for multilayered anisotropic plates", *Atti Accad. Sci. Torino Cl. Sci. Fis. Mat. Natur.* **118** (1984), 279–295.

[Di Sciuva 1985a] M. Di Sciuva, "Development of an anisotropic, multilayered, shear-deformable rectangular plate element", *Comput. Struct.* **21**:4 (1985), 789–796.

[Di Sciuva 1985b] M. Di Sciuva, "Evaluation of some multilayered, shear-deformable plate elements", pp. 394–400 in *A collection of technical papers: AIAA/ASME/ASCE/AHS* 26*th Structures, Structural Dynamics and Materials Conference* (Orlando, FL, 1985), vol. 1, AIAA, New York, 1985. Paper 85-0717.

[Di Sciuva 1986] M. Di Sciuva, "Bending, vibration and buckling of simply supported thick multilayered orthotropic plates: an evaluation of a new displacement model", *J. Sound Vib.* **105**:3 (1986), 425–442.

[Di Sciuva 1987] M. Di Sciuva, "An improved shear-deformation theory for moderately thick multilayered anisotropic shells and plates", *J. Appl. Mech.* (*ASME*) **54**:3 (1987), 589–596.

[Di Sciuva 1990] M. Di Sciuva, "Further refinement in the transverse shear deformation theory for multilayered composite plates", *Atti Accad. Sci. Torino Cl. Sci. Fis. Mat. Natur.* **124**:5–6 (1990), 248–268.

[Di Sciuva 1992] M. Di Sciuva, "Multilayered anisotropic plate models with continuous interlaminar stresses", *Compos. Struct.* **22**:3 (1992), 149–168.

[Di Sciuva et al. 2002] M. Di Sciuva, M. Gherlone, and L. Librescu, "Implications of damaged interfaces and of other non-classical effects on the load carrying capacity of multilayered composite shallow shells", *Int. J. Non-Linear Mech.* **37**:4–5 (2002), 851–867.

[Kim and Cho 2005] J.-S. Kim and M. Cho, "Enhanced first-order shear deformation theory for laminated and sandwich plates", *J. Appl. Mech.* (*ASME*) **72**:6 (2005), 809–817.

[Kim and Cho 2006] J.-S. Kim and M. Cho, "Enhanced modeling of laminated and sandwich plates via strain energy transformation", *Compos. Sci. Technol.* **66**:11–12 (2006), 1575–1587.

[Librescu et al. 1987] L. Librescu, A. A. Khdeir, and J. N. Reddy, "A comprehensive analysis of the state of stress of elastic anisotropic flat plates using refined theories", *Acta Mech.* **70**:1–4 (1987), 57–81.

[Liu and Li 1996] D. Liu and X. Li, "An overall view of laminate theories based on displacement hypothesis", *J. Compos. Mater.* **30**:14 (1996), 1539–1561.

[Lo et al. 1977a] K. H. Lo, R. M. Christensen, and E. M. Wu, "A higher-order theory of plate deformation, 1: Homogeneous plates", *J. Appl. Mech.* (*ASME*) **44** (1977), 663–668.

[Lo et al. 1977b] K. H. Lo, R. M. Christensen, and E. M. Wu, "A higher-order theory of plate deformation, 2: Laminated plates", *J. Appl. Mech.* (*ASME*) **44** (1977), 669–676.

[MSC 2006] *MD Nastran: reference guide*, Version 2006.0, MSC Software Corporation, Santa Ana, CA, 2006.

[Murakami 1986] H. Murakami, "Laminated composite plate theory with improved in-plane responses", *J. Appl. Mech.* (*ASME*) **53**:3 (1986), 661–666.

[Noor and Burton 1989] A. K. Noor and W. S. Burton, "Assessment of shear deformable theories for multilayered composite plates", *Appl. Mech. Rev.* (*ASME*) **42**:1 (1989), 1–12.

[Noor and Burton 1990] A. K. Noor and W. S. Burton, "Three-dimensional solutions for antisymmetrically laminated anisotropic plates", *J. Appl. Mech.* (*ASME*) **57**:1 (1990), 182–188.

[Pagano 1969] N. J. Pagano, "Exact solutions for composite laminates in cylindrical bending", *J. Compos. Mater.* **3**:3 (1969), 398–411.

[Reddy 1984] J. N. Reddy, "A simple higher-order theory for laminated composite plates", *J. Appl. Mech.* (*ASME*) **51**:4 (1984), 745–752.

[Reddy 1997] J. N. Reddy, *Mechanics of laminated composite plates: theory and analysis*, CRC Press, Boca Raton, FL, 1997.

[Reddy 2004] J. N. Reddy, *Mechanics of laminated composite plates and shells: theory and analysis*, 2nd ed., CRC Press, Boca Raton, FL, 2004.

[Reddy and Vijayakumar 1995] K. J. Reddy and K. Vijayakumar, "Lamination-dependent shear deformation models for cylindrical bending of angle-ply laminates", *Comput. Struct.* **55**:4 (1995), 717–725.

[Reissner 1984] E. Reissner, "On a certain mixed variational theorem and a proposed application", *Int. J. Numer. Methods Eng.* **20**:7 (1984), 1366–1368.

[Reissner 1985] E. Reissner, "Reflections on the theory of elastic plates", *Appl. Mech. Rev.* (*ASME*) **38**:11 (1985), 1453–1464.

[Sun and Whitney 1973] C.-T. Sun and J. M. Whitney, "Theories for the dynamic response of laminated plates", *AIAA J.* **11**:2 (1973), 178–183.

[Tessler 1993] A. Tessler, "An improved plate theory of {1,2}-order for thick composite laminates", *Int. J. Solids Struct.* **30**:7 (1993), 981–1000.

[Tessler et al. 2007] A. Tessler, M. Di Sciuva, and M. Gherlone, "Refinement of Timoshenko beam theory for composite and sandwich beams using zigzag kinematics", Technical report TP-2007-215086, NASA Langley Research Center, Hampton, VA, 2007, Available at http://tinyurl.com/NASA-TP-2007-215086.

[Tessler et al. 2009] A. Tessler, M. Di Sciuva, and M. Gherlone, "Refined zigzag theory for laminated composite and sandwich plates", Technical report TP-2009-215561, NASA Langley Research Center, Hampton, VA, 2009, Available at http://tinyurl.com/NASA-TP-2009-215561.

[Toledano and Murakami 1987] A. Toledano and H. Murakami, "A high-order laminated plate theory with improved in-plane responses", *Int. J. Solids Struct.* **23**:1 (1987), 111–131.

[Umasree and Bhaskar 2006] P. Umasree and K. Bhaskar, "Analytical solutions for flexure of clamped rectangular cross-ply plates using an accurate zig-zag type higher-order theory", *Compos. Struct.* **74**:4 (2006), 426–439.

[Vlachoutsis 1992] S. Vlachoutsis, "Shear correction factors for plates and shells", *Int. J. Numer. Methods Eng.* **33**:7 (1992), 1537–1552.

[Yu 2005] W. Yu, "Mathematical construction of a Reissner–Mindlin plate theory for composite laminates", *Int. J. Solids Struct.* **42**:26 (2005), 6680–6699.

[Yu et al. 2008] W. Yu, J.-S. Kim, D. H. Hodges, and M. Cho, "A critical evaluation of two Reissner–Mindlin type models for composite laminated plates", *Aerosp. Sci. Technol.* **12**:5 (2008), 408–417.

Received 23 Mar 2009. Revised 7 Aug 2009. Accepted 13 Aug 2009.

ALEXANDER TESSLER: alexander.tessler-1@nasa.gov
Structural Mechanics and Concepts Branch, NASA Langley Research Center, Mail Stop 190, Hampton, VA 23681-2199, United States

MARCO DI SCIUVA: marco.disciuva@polito.it
Department of Aeronautics and Space Engineering, Politecnico di Torino, Corso Duca degli Abruzzi 24, 10129 Torino, Italy

MARCO GHERLONE: marco.gherlone@polito.it
Department of Aeronautics and Space Engineering, Politecnico di Torino, Corso Duca degli Abruzzi 24, 10129 Torino, Italy

SUBMISSION GUIDELINES

ORIGINALITY

Authors may submit manuscripts in PDF format online at the Submissions page. Submission of a manuscript acknowledges that the manuscript is original and has neither previously, nor simultaneously, in whole or in part, been submitted elsewhere. Information regarding the preparation of manuscripts is provided below. Correspondence by email is requested for convenience and speed. For further information, write to one of the Chief Editors:

Davide Bigoni	bigoni@ing.unitn.it
Iwona Jasiuk	ijasiuk@me.concordia.ca
Yasuhide Shindo	shindo@material.tohoku.ac.jp

LANGUAGE

Manuscripts must be in English. A brief abstract of about 150 words or less must be included. The abstract should be self-contained and not make any reference to the bibliography. Also required are keywords and subject classification for the article, and, for each author, postal address, affiliation (if appropriate), and email address if available. A home-page URL is optional.

FORMAT

Authors can use their preferred manuscript-preparation software, including for example Microsoft Word or any variant of TEX. The journal itself is produced in LATEX, so accepted articles prepared using other software will be converted to LATEX at production time. Authors wishing to prepare their document in LATEX can follow the example file at www.jomms.org (but the use of other class files is acceptable). At submission time only a PDF file is required. After acceptance, authors must submit all source material (see especially Figures below).

REFERENCES

Bibliographical references should be complete, including article titles and page ranges. All references in the bibliography should be cited in the text. The use of BibTEX is preferred but not required. Tags will be converted to the house format (see a current issue for examples); however, for submission you may use the format of your choice. Links will be provided to all literature with known web locations; authors can supply their own links in addition to those provided by the editorial process.

FIGURES

Figures must be of publication quality. After acceptance, you will need to submit the original source files in vector format for all diagrams and graphs in your manuscript: vector EPS or vector PDF files are the most useful. (EPS stands for Encapsulated PostScript.)

Most drawing and graphing packages—Mathematica, Adobe Illustrator, Corel Draw, MATLAB, etc.—allow the user to save files in one of these formats. Make sure that what you're saving is vector graphics and not a bitmap. If you need help, please write to graphics@mathscipub.org with as many details as you can about how your graphics were generated.

Please also include the original data for any plots. This is particularly important if you are unable to save Excel-generated plots in vector format. Saving them as bitmaps is not useful; please send the Excel (.xls) spreadsheets instead. Bundle your figure files into a single archive (using zip, tar, rar or other format of your choice) and upload on the link you been given at acceptance time.

Each figure should be captioned and numbered so that it can float. Small figures occupying no more than three lines of vertical space can be kept in the text ("the curve looks like this:"). It is acceptable to submit a manuscript with all figures at the end, if their placement is specified in the text by means of comments such as "Place Figure 1 here". The same considerations apply to tables.

WHITE SPACE

Forced line breaks or page breaks should not be inserted in the document. There is no point in your trying to optimize line and page breaks in the original manuscript. The manuscript will be reformatted to use the journal's preferred fonts and layout.

PROOFS

Page proofs will be made available to authors (or to the designated corresponding author) at a Web site in PDF format. Failure to acknowledge the receipt of proofs or to return corrections within the requested deadline may cause publication to be postponed.

Journal of Mechanics of Materials and Structures

Volume 5, No. 2 February 2010